UNIVERSIDADE DE SÃO PAULO
ESCOLA POLITÉCNICA

ICARO AMORIM DE CARVALHO

Enhanced control of bluff-body wakes by the interference of rotating rods

São Paulo
2023

ICARO AMORIM DE CARVALHO

Enhanced control of bluff-body wakes by the interference of rotating rods

Revised version

Thesis presented to the Escola Politécnica da Universidade de São Paulo in fulfillment of the requirements for the Doctor of Science degree.

PhD candidate: Icaro Amorim de Carvalho

Supervisor: Prof. Gustavo Roque da Silva Assi

São Paulo

2023

Este exemplar foi revisado e corrigido em relação à versão original, sob responsabilidade única do autor e com a anuência de seu orientador.

São Paulo, __21__ de _____Junho_____ de __2023___

Assinatura do autor: _____

Assinatura do orientador: _____

Catalogação-na-publicação

Carvalho, Icaro Amorim de
Enhanced control of bluff-body wakes by the interference of r otating rods / I. A. Carvalho -- versão corr. -- São Paulo, 2023.
260 p.

Tese (Doutorado) - Escola Politécnica da Universidade de São Paulo. Departamento de Engenharia Mecânica.

1.Wake control 2.Drag reduction 3.Vortex-shedding suppression 4.Computational fluid dynamics 5.Suppressors I.Universidade de São Paulo. Escola Politécnica. Departamento de Engenharia Mecânica II.t.

To my family

"All you can do is your best. There's no reason to worry beyond that."

– Randall Wolansky

"Don't lose any sleep tonight
I'm sure everything will end up alright
You may win or lose
But to be yourself is all that you can do."

– Audioslave

Acknowledgements

I am privileged to have had such outstanding people around me throughout my career. Since my early studies, I have relied on the unconditional support from my parents, Mazarello and Domingos, and brother, Diego. They have always been a great source of inspiration to give my best. To them, my undescribable gratitude.

To my wife Ana Caroline, all my love for all the support and understanding even in the most stressful times. My relentless effort continues to be anchored in her optimism and encouragement.

To my tight-knit northwestern Brazilian family that has always instigated me in my studies: Edite, Cláudia, Claudete, Allan, Adolfo, Ingrid and Ingra. I also dedicate this thesis to Sandra Mara, Silvio, Silvia Gabrielle and Ludmila Krywoshejko Affonso.

To my supervisor Prof. Gustavo Assi, for the guidance and mentorship in this research in affable meetings. But beyond that, for his uplifting spirit. During pandemic times, I cannot express how his empathy and assistance were essential to pushing me forward.

To professors and colleagues from NDF-Poli (Fluids & Dynamics Research Group). In particular, I would like to thank Alexandre Olender ("*No final tudo dá certo!*") for the day by day productive and nonproductive conversations; and Felipe Maffei, Profs. Fabio Saltara and Reinaldo Orselli. To be in such a group has contributed greatly to my growth and achievements. I have found in this group a welcoming environment of ideas and fruitful discussions.

To my long-term friends Mike William, Lais "Baka" Toshye, Marina Alice, and Ivo Terek. Our friendship is priceless.

To professors that sparked my passion toward fluid dynamics, Prof. Gabriela Cantarelli Lopes at UFSCar, and Profs. Gwynn Elfring and Ali Vakil at UBC; and to Prof. Paulo Daniel Emmel at UFSCar for inspiring me into the path of academia.

To Prof. Assi's group members and group meetings.

This section would not end if I should be truly fair.

To God, $f$or everything.

ABSTRACT

Carvalho, I.A. **Enhanced control of bluff-body wakes by the interference of rotating rods**. 2023. Thesis (Doctorate in Mechanical Engineering) – Department of Mechanical Engineering at Escola Politécnica. University of São Paulo, São Paulo, 2023.

Bluff structures are affected by alternating vortices as a fluid flows past them. This phenomenon affects a multiplicity of applications, ranging from the vibration of chimney stacks, cooling towers, floating offshore wind turbines to massive oil rigs; and may cause significant damages when vortex-induced vibrations occur. In order to control the vortex wake, several techniques have been devised; most of which are susceptible to directionality or excessive power expenditure.

In the present work, we attempt to understand the underlying physics behind a wake control mechanism consisting of a larger body surrounded by eight slender rods of smaller diameter, distanced from the former by a gap. The relevance of these small elements in open-loop flow control was examined passively and actively, by spinning them around their own axis to inject momentum into the nearby flow. Finite volume simulations in laminar and turbulent regimes were employed at Reynolds numbers of 100 (2D) and 1000 (3D), respectively; for the assumptions of infinitely-long and finite bodies. In the former, end effects were disregarded. This simplification is reasonable when the the ratio of the length of the body by its diameter is high enough. For finite bodies, free-end and free-surface effects were considered. In the latter, wave effects were neglected, because the system was assessed at low Froude number. Inspired by the optimal state of potential flow, which configures a suppressed condition with null mean drag, angular velocities were compared, in viscous case, in two arrangements: one with potential-flow-inspired velocities, and another, with all rods spinning at the same rotation rate. Hydrodynamic loads, vortex dynamics and power expenditure are principally addressed here.

Our results show that to attach the small elements to the larger main body enhanced wake control; especially when end effects were ignored. In such setups, the spinning rods progressively weakened the vortex wake in vorticity magnitude, and promoted the increase in correlation of structures of the wake in the direction parallel to the cylinders' span. Each rod was individually assessed as to its importance to the entire system. For

sufficiently large angular velocities, the rods completely eliminated the vortex wake and led the flow into a steady condition. These effects were accompanied by the mitigation of the hydrodynamic loads, in particular, mean drag and root mean square of lift. The same effects were found to occur for finite bodies under the effect of a free surface (in subcritical regime in terms of Reynolds and Froude numbers). Under these conditions, the active mechanism eliminated the bulk of the vortex-wake that followed the formation mechanism proposed by Gerrard (1966), but not the part associated with tip-vortices. Side forces were still decreased, and we showed this to be related to ring-like vortices detaching from the tip region that drew in other smaller structures of the Bénard-von Kármán wake, that was eventually suppressed. In general, the active mechanism, inspired by potential-flow angular velocities proved to be more cost-effective based on the formulation of power-loss introduced by Shukla and Arakeri (2013); and effective in reducing loads relative to the case of uniform velocities. Furthermore, studies on the directionality of the system exhibited in potential-flow-inspired cases an omnidirectional behaviour, against the directional-prone setup of uniform angular velocities from past studies.

Keywords: Wake control. Drag reduction. Vortex-shedding suppression. Computational fluid dynamics. Suppressors.

RESUMO

Carvalho, I.A. **Controle aperfeiçoado da esteira de corpos rombudos pela interferência de cilindros de controle**. 2023. Tese (Doutorado em Engenharia Mecânica) – Departamento de Engenharia Mecânica da Escola Politécnica. Universidade de São Paulo, São Paulo, 2023.

Estruturas rombudas são afetadas por vórtices alternantes conforme o escoamento as contorna. Este fenômeno impacta diversas aplicações, desde a vibração de chaminés, torres de refrigeração, turbinas eólicas flutuantes *offshore* até enormes plataformas de petróleo; e podem causar danos significativos quando vibrações induzidas por vórtices ocorrem. Para controlar a esteira de vórtices, diversas técnicas foram desenvolvidas; a maior parte das quais é suscetíveis à direcionalidade ou dispêndio de potência excessivo.

Neste trabalho, buscamos entender a física subjacente por trás do mecanismo de controle da esteira que consiste em um grande corpo cercado por oito cilindros finos de menor diâmetro, distantes do anterior por um espaçamento. A relevância destes elementos no controle do escoamento com malha aberta é examinada passiva e ativamente, rotacionando-os em torno de seu próprio eixo para se injetar quantidade de movimento no escoamento próximo ao sistema. Simulações de volumes finitos em regimes laminar e turbulento foram empregadas em números de Reynolds 100 e 1000, respectivamente; para as suposições de corpos infinitamente longos e finitos. Na primeira suposição, efeitos de ponta foram ignorados. Esta simplificação é razoável quando a razão entre o comprimento do corpo e seu diâmetro é suficientemente alta. Para corpos finitos, efeitos de ponta e de superfície livre foram considerados. No último caso, efeitos de onda foram ignorados, pois o sistema foi avaliado em baixos números de Froude. Inspiradas pelo estado ótimo do escoamento potencial, que configura uma condição de supressão do escoamento com arrasto médio nulo, as velocidades angulares foram comparadas, no caso viscoso, em dois arranjos: um com velocidades inspiradas pelo escoamento potencial, e outro, com cilindros rotacionando com a mesma taxa de rotação. Forças hidrodinâmicas, dinâmica de vórtices e dispêndio de potência são principalmente abordados aqui.

Nossos resultados mostram que inserir estes pequenos elementos ao corpo maior principal aperfeiçoou o controle da esteira; principalmente quando efeitos de ponta foram ignorados. Em tais configurações, os cilindros rotativos progressivamente enfraqueceram

a esteira de vórtices em magnitude de vorticidade, e promoveram o aumento da correlação das estruturas da esteira na direção paralela à envergadura dos cilindros. Cada cilindro foi individualmente avaliado sobre sua importância relative ao sistema como um todo. Para velocidades angulares suficientemente altas, os cilindros eliminaram a esteira de vórtices completamente e conduziram o escoamento a adentrar uma condição de regime permanente. Estes efeitos foram acompanhados pela mitigação das forças hidrodinâmicas, em particular, arrasto médio e raiz quadrada média da sustentação. Os mesmos efeitos foram observados para cilindros finitos sob o efeito de uma superfície livre (em regimes subcríticos de números de Reynolds e de Froude). Sob estas condições, o mecanismo ativo eliminou a maior parte da esteira de vórtices que segue o mecanismo de formação de Gerrard (1966), entretanto, não eliminou a parte associada com vórtices de ponta. Forças laterais foram reduzidas, e mostramos que isto está relacionado a vórtices em formato de anel, que atraíam outras pequenas estruturas da esteira de Bénard-von Kármán, que eventualmente foi suprimida. Em geral, o mecanismo ativo de velocidades angulares inspiradas pelo escoamento potencial provou ser mais viável, com base na formulação de perda de potência introduzida por Shukla e Arakeri (2013); e efetivo na reduçao de forças, relativo ao caso de velocidades uniformes. Ademais, estudos de direcionalidade do sistema mostraram, no caso inspirado pelo escoamento potencial, um comportamento omnidirecional, distinto daquele do sistema de velocidades angulares uniformes de trabalhos anteriores, que é suscetível à direção do escoamento.

Palavras-chave: Controle de esteira. Redução de arrasto. Supressão do desprendimento de vórtices. Dinâmica dos fluidos computacional. Supressores.

List of Abbreviations

2P	Vibration mode with two pairs of vortices shed in a period
2S	Vibration mode with two single vortices shed in a period
CFD	Computational Fluid Dynamics
CFL	Courant–Friedrichs–Lewy condition
DES	Detached Eddy Simulation
DNS	Direct Numerical Simulation
FAPESP	São Paulo Research Foundation
LES	Large Eddy Simulation
LUST	Linear-Upwind Stabilised Transport scheme
MSBC	Moving Surface Boundary-layer Control
NDF	Núcleo de Dinâmica e Fluidos (Fluids & Dynamics Research) group
OpenFOAM	Open-source Field Operation And Manipulation
RANS	Reynolds-Averaged Navier-Stokes turbulence models
RMS	Root mean square
SGS	Sub-Grid Scale
SIMPLE	Semi-Implicit Method for Pressure-Linked Equations
SST	Shear Stress Transport
TVD	Total Variation Diminishing
URANS	Unsteady RANS simulations

USP	Universidade de São Paulo
VIM	Vortex-Induced Motion
VIV	Vortex-Induced Vibration

List of Symbols

Latin Alphabet

$\mathbf{a}$	Vector
$\mathbf{A}$	Matrix
$\mathbf{A}^\intercal$	Transpose of a matrix
C_D	Drag coefficient
C_{DES}	DES calibrating constant in Spalart-Allmaras model
C_L	Lift coefficient
C_N	Dimensionless power-loss coefficient due to shear on a spinning rod
C_p	Pressure coefficient
C_{PL}	Power-loss coefficient
C_S	Side force coefficient
D	Diameter of the main cylinder
d	Diameter of the peripheral rods
$\mathrm{d}S$	Infinitesimal element of the surface S of a control volume
d_{wall}	Distance from the wall in the Spalart-Allmaras model
$\hat{e}_i$	Unit vector in the i^{th} direction
F_D	Dimensional drag force
F_L	Dimensional lift force
F_S	Dimensional side force

f_S	Strouhal frequency
f_v	Shedding frequency
G	Gap between the main cylinder and the peripheral rods
i, j	Indices
k	Turbulent kinetic energy
k_∞	Free stream turbulent kinetic energy
L	Spanwise length of the cylinder
l_{DES}	Characteristic length in DES
ℓ_d	Mesh length downstream of the cylinder
ℓ_u	Mesh length upstream of the cylinder
m	Mass of the cylinder and the added mass
m^*	Mass ratio
m_f	Mass of displaced fluid due to the insertion of the cylinder
n	Index of the cylinders, $n = 0, \ldots, N$ (0 is the main cylinder)
N	Number of rods
p	Pressure
Pe	Péclet number
P_n	Reference to the n^{th} clockwise spinning rod
P'_n	Reference to the n^{th} anticlockwise spinning rod
p_N	Dimensional power-loss due to shear on a spinning rod
Q	Q-criterion
R	Distance from the centre of the main cylinder to the outmost point at the surface of any rod ($= D/2 + G + d$)
Re	Reynolds number based on the diameter D of the main body
Re_d	Reynolds number based on the diameter d of the rods

S	Surface of a body
S_t	Strouhal number
t	Time instant
T_S	Strouhal period
U	Velocity
U_∞	Free stream velocity
U_n	Tangential velocity of the spinning rods
U_R	Reduced velocity
x, y, z	Orthogonal coordinates
$\mathbf{x}$	Position

Greek Alphabet

$\mathrm{d}\Omega_n$	Volumetric infinitesimal element of the control volume Ω_n
μ	Dynamic viscosity
μ_t	Turbulent dynamic viscosity
ν	Kinematic viscosity
ν_∞	Free stream kinematic viscosity
ν_{SGS}	Kinematic eddy viscosity due to Sub-Grid Scale
ν_t	Turbulent kinematic viscosity
ν_{wall}	Kinematic viscosity on the wall
ω	Specific rate of dissipation
ω_n	Angular velocity of the n^{th} peripheral rod
Ω_n	Control volume
Ψ	Low-Reynolds function correction in the Spalart-Allmaras DES formulation

ρ	Fluid density
τ_n	Shear on the n^{th} cylinder
θ	Angle relative to frontal stagnation region
θ_n	Angular position of the n^{th} cylinder
$\tilde{\nu}$	Kinematic eddy viscosity parameter in the Spalart-Allmaras formulation
$\tilde{\nu}_{\text{wall}}$	Kinematic eddy viscosity parameter on the wall in the Spalart-Allmaras formulation
ξ	Damping of a vibrating system
ζ	Velocity gain parameter

Mathematical symbols

$\| \ \|$	L_2 norm of a vector
$\| \ \|$	Absolute value of a scalar
$\cdot$	Dot product
$[\ ,\ ]$	Closed interval (includes extremes)
$]\ ,\ [$	Open interval (excludes extremes)
∇	Del operator

Contents

Presentation

This thesis is presented in the format of a compilation of collected scientific articles published by the author during the research project. Each article in chapters 9 and 10 will articulate its own piece of knowledge in the format expected by each journal. Nevertheless, the next chapters summarise the contents common to all papers, which characterise the research project as a coherent body of scientific knowledge. We present the outline of the entire research in chapter 2, together with the main objectives. Consecutively, the literature review is given in chapters 3, 4 and 5, followed by the methodology in chapter 6. The main results are briefly discussed in chapter 7 and full discussion is left to the papers.

1 Introduction

The pursuit of new oil and gas exploration sites requires the development of ever more sophisticated offshore technologies, capable of reaching ultra deepwater wells, such as the monocolumn platforms (see figure 1.1a). These structures have in common a large bluff hull. It has become possible, by means of the development of these technologies, to explore new oil and gas reserves, such as that of the pre-salt layer, whose relevance has reflected in more than 70% of the total oil extracted from the Brazilian territory (Gandra, 2020). Currently there is a demand for new offshore systems based on bluff structures, such as offshore wind turbines and systems devoted to carbon capture and utilisation, to provide conditions for the offshore industry to become one of clean energy. This transformation will require new technologies with high efficiency.

Currently, the aforementioned units are remarkably costly and face severe challenges imposed by the adverse conditions under which they operate. Generally of circular cross-section, an intrinsic problem to their operation are the vortices that appear downstream of the body as the incoming flow attempts to circumvent the obstructing structure. *Vortex shedding*, as this phenomenon is termed, is rooted in the interplay of alternating vortices that originate in the near wake of the structure (see figure 1.1b). This exchange of vorticity promoted by the vortices emanated leeway is accompanied by a resulting force that changes its orientation, and thus anticipates vortex-induced vibrations (VIV) upon the structure.

Due to this succession of events, one of the main issues in exploring oil and gas in ultra deepwater wells is to preserve the stability of the platform under conditions of agitation (Morais, 2013). Severe conditions provided by the wind, ocean currents and waves, may interact with vortex shedding and VIV and foster the amplification of these phenomena.

The impact of this vortex dynamics upon the structure is clear in dimensioning anchor

(a) Spar platform. Extracted from Lindefjeld and Randulff (2020).

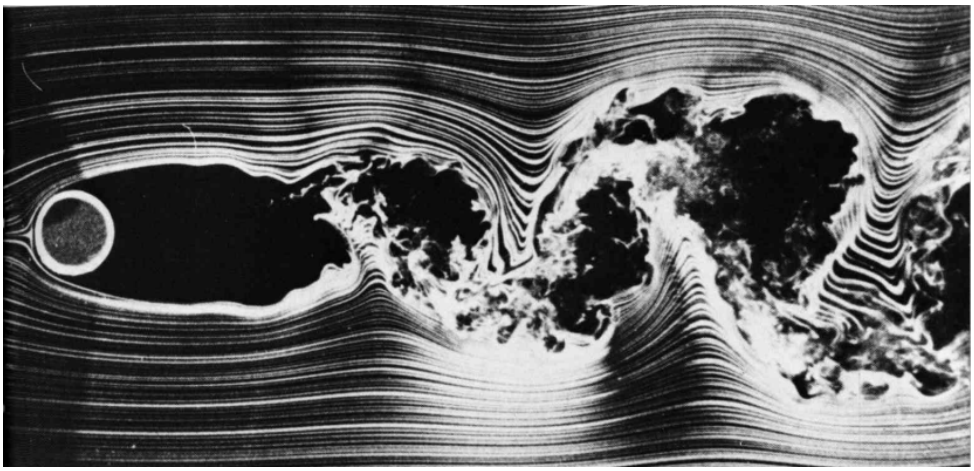

(b) Vortex shedding past a cylinder. Extracted from van Dyke (1982).

Figure 1.1: Example of a) a large cylindrically-shaped fluctuating platform, used for oil extraction and b) vortex shedding past a cylinder (like the bluff hull of the platform).

lines and risers. Accentuated forces and induced motion result in downright stress and strain; and the fatigue shortens the structures' lifespan. Furthermore, in critical cases, fluid-structure interaction resulting thereof may ultimately lead to utter failure of the oil rig.

At present, helical strakes configure the main solution adopted in the context of suppressors of vortex shedding and VIV, applied to risers and entire cylindrically-shaped platforms, such as spar. This solution has shown effective in reducing VIV, but leads to a drag increase. In fact, helical strakes come from the context of wind engineering, where the ratio of the mass of the entire system relative to that corresponding to the volume of air that it occupies is high; in contrast, when the fluid is water, this ratio is low (Assi, Bearman, and Kitney, 2009). Because low mass ratio systems are more responsive to VIV excitation, larger strakes are required in water, resulting in more drag (Korkischko and Meneghini, 2011).

To use one (Strykowski and Sreenivasan, 1990; Mittal and Raghuvanshi, 2001) or multiple secondary bodies (Mittal, 2001; Korkischko and Meneghini, 2012; Silva-Ortega and Assi, 2018; Assi, Orselli, and Silva-Ortega, 2018) near a main structure has shown to be a promising technology for flow control.

The main object of the present study is a system comprised by a main circular cylinder fitted with spinning rods, presented in figure 2.1. A certain degree of flow control may be achieved via this system to:

- attenuate the excitation due to vortex shedding, perhaps achieving its complete suppression;
- reduce the response amplitude in VIV of the entire system or the elimination of these vibrations;
- modify the entire flow topology, and alter the state of the flow, to enter an apparently different flow regime; and
- exert control over hydrodynamic loads. Indeed, it has been shown that such a system can not only reduce mean drag to null value, but also invert it to produce useful thrust.

In this sense, the development of suppressors that might eliminate or weaken vortex shedding – or, to put it in a broader sense, able to control the wake flow and hydrodynamic

loads – may be of strong interest to the offshore industry, that requires more efficient technologies. Moreover, the understanding of the flow over bluff bodies and associated control could help with the design of a multitude of applications, spanning simplified buildings, chimney stacks, cooling towers and floating offshore wind turbines.

This research is in agreement with the lines of investigation conducted at the Fluids & Dynamics Research group (NDF) at the University of São Paulo. The result of this work will enhance the understanding of vortex-shedding and wake-control mechanisms. We envision principally to contribute to the control of the fluctuating forces and vortex structures that act upon bluff bodies. This effort is justified in response to the lack of research developed for this purpose with a system such as that presented here.

2 Scope

In the present work we intend to advance on the matter of open-loop flow control, based on the system of figure 2.1, subject to the uniform incoming flow $\mathbf{U}_\infty = U_\infty [\cos(\alpha)\hat{x} + \sin(\alpha)\hat{y}]$, where α is the angle of attack and $\hat{x}$ and $\hat{y}$ are unit vectors. A main cylinder of diameter D and spanwise length L was fitted with eight slender rods of diameter $d = D/20$ with the same length. Upper rods P_1, P_2, P_3 and P_4 rotated clockwise, while the lower rods P_1', P_2', P_3' and P_4' spun counterclockwise. In terms of actuating power, the wake-control rods were employed passively (fixed, without rotation) and actively, with angular velocities given by $\omega_n = -\omega_n'$ for $n = 1, \ldots, 4$. In general, these were uniformly varied through the gain parameter $\zeta \geq 0$, yielding $\zeta\omega_n$ and $\zeta\omega_n'$. The gap $G = D/100$ between the walls separated the rods from the main body. Justification to the present arrangement of the control rods about the main body is given in section 6.1.

Our investigation comprised different levels of complexity of the flow and of the system. We first considered infinitely-long bodies in laminar and turbulent regimes at different α, ignoring the free water surface of figure 2.1. When finite cylinders (and thus end effects) were investigated, the system was considered first free from, and then under, the effect of the free water surface, at fixed α and passively ($\omega_n = 0$). Our more recent published works were concerned with the active mechanism for finite cylinders under the influence of free-end and free-surface effects with fixed $\alpha = 0$. In addition, we have evaluated the matter of omnidirectionality of the system, in laminar and turbulent regimes for the infinitely-long case.

It is a premise of this work that laminar regime studies should be pursued first because their simulations are less time consuming and provide insights into the more complex turbulent flows. Thus, in general, laminar regime studies were carried out before turbulent ones.

The different analyses conducted in this research may be summarised as follows:

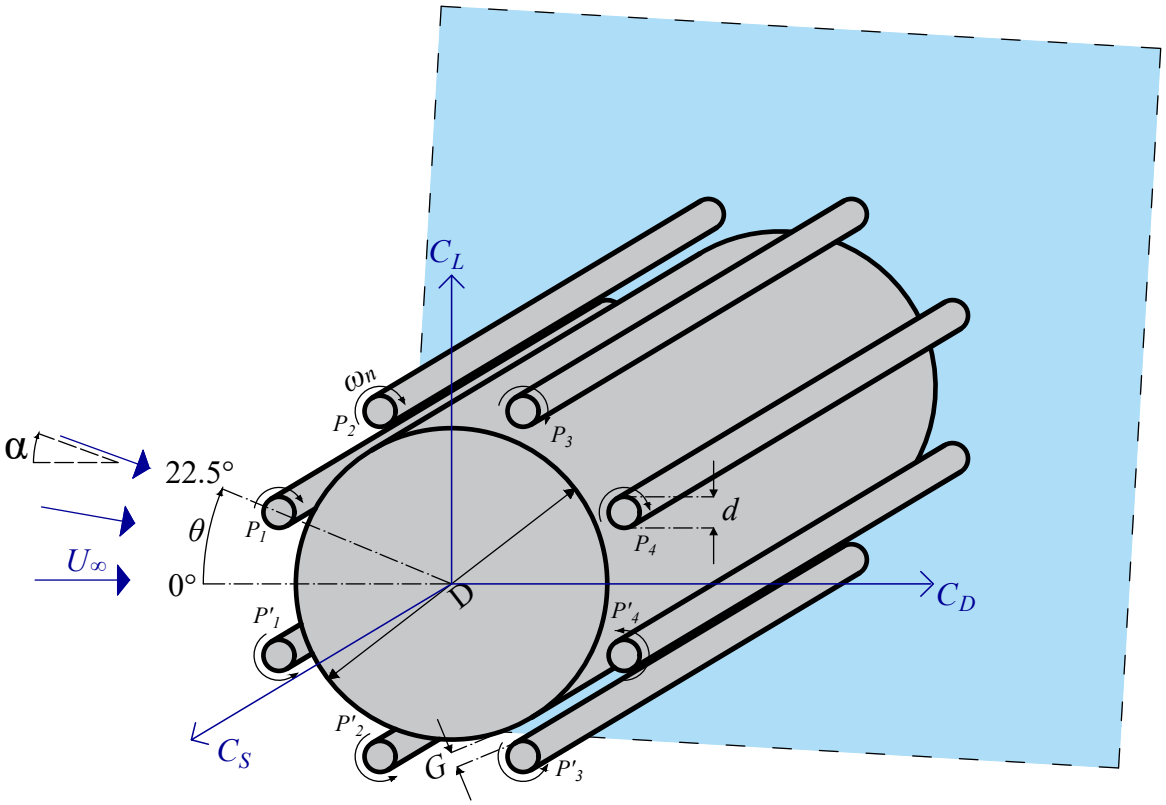

Figure 2.1: Configuration and parameters of wake-control cylinders.

- Infinitely-long bodies in laminar regime (Carvalho, Assi, and Orselli, 2021, section 9.1);
- Infinitely-long bodies in turbulent regime (Carvalho and Assi, 2022, section 9.2);
- Finite bodies in turbulent regime with a passive mechanism (Carvalho and Assi, 2023d, section 9.3);
- Finite bodies in turbulent regime with an active mechanism (Carvalho and Assi, 2023a, section 9.4).
- Omnidirectionality of the infinitely-long system in laminar regime (Carvalho and Assi, 2023b, section 10.1)
- Omnidirectionality of the infinitely-long system in turbulent regime (Carvalho and Assi, 2023c, section 10.2);

The Reynolds number based on the main cylinder's diameter, given by $Re = U_\infty D/\nu$ was equal to 100 in laminar and 1000 in turbulent (subcritical) flow regimes. A general overview of the research carried out in the present thesis can be visualised in figure 2.2.

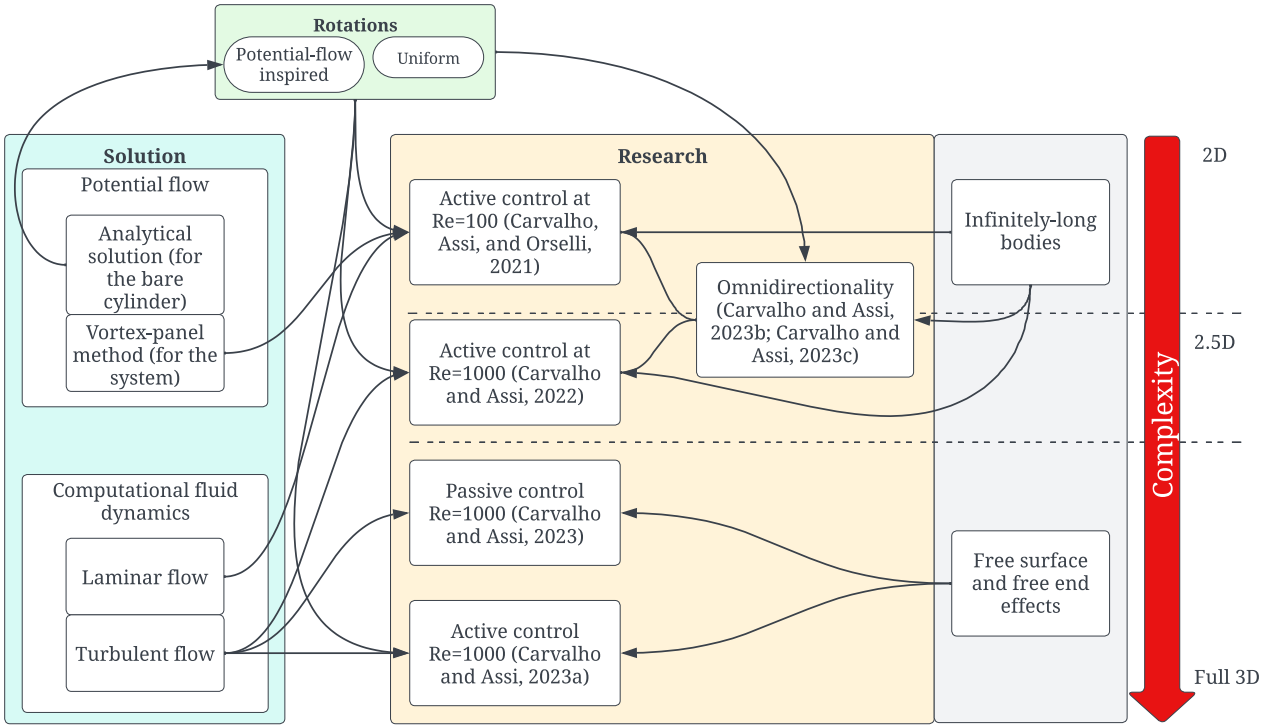

Figure 2.2: Outline of the research conducted in the present thesis. Larger boxes contain the analysed cases (centre, yellow) and associated assumptions (right, gray), solution methods (left, blue) and arrangement of rotations (top, green).

For infinitely-long bodies, an interesting aim and inspiration was the potential flow topology about a bare cylinder. In a state of complete vortex suppression, the flow topology should resemble that of a potential flow (although the physics of the problem is different). This perception was used to impose different angular velocities to the rods. We test the hypothesis whether these velocities are able to deliver greater flow control when compared with uniform velocities on the rods. One might expect that in an optimised configuration aiming at drag reduction with minimal power expenditure (akin to potential flow), the peripheral rods will be set to rotate at different speeds, related both to their positions and to local features of the flow. The capacity of the system to produce the same results when the angle of attack of the incoming flow is $\alpha \neq 0$ is also explored, and the role of each rod as α is changed. Direct comparison was also made with the potential flow about the system of figure 2.1 through the vortex-panel method.

For finite bodies, we first investigate the passive control of finite structures by studying free-surface and free-end effects on the vortex shedding mechanism and its suppression with interfering rods. We compare the flow behavior over infinitely long cylinders with two low-aspect-ratio cases: one in which the system is fully submerged and both ends are

free; and another, with one free end, and the other in contact with a free water surface. Finally, to assess the active mechanism, the system was evaluated only with a subset of the aforementioned study. We restrict the analysis to finite bodies wherein one end was under free-surface, while the other was under free-end effects. The goal is to comprehend, aside from the previous aspects, the extension of realisable flow control conveyed by this active mechanism against end effects and tip-vortex, and their suppression.

The level of complexity is also exhibited by the red arrow of figure 2.2, along with the dimension of the grid domain that was used for the simulations. It is worth briefly noting that two-dimensional (2D) simulations were employed strictly for laminar regime; three-dimensional (3D) for the finite cases; and the so-called "2.5D" refers to effectively three-dimensional simulations, but under the assumption of infinitely-long bodies (explained in chapter 6).

The relationship between the different aspects that were digressed above are represented through figure 2.2.

2.1 Objectives

We aim to understand the underlying physics behind the wake-control mechanism promoted by the set of slender rods surrounding the main body of figure 2.1. In general, we investigate how the hydrodynamic loads are affected by the suppressing device through vortex dynamics analysis. We principally address how the rods impact separation, wake width, formation length and vorticity distribution about the system; and how these aspects are affected when the system functions actively with rods spinning at progressively larger angular velocities, up to suppression. Analyses of the active mechanism regarding the efficiency of the system are conducted to broadly comprehend the balance between the energy consumption to rotate the rods against viscous action and the resulting drag mitigation. This information may be relevant to practical applications. In all cases, the system comprised of the main body and the control rods is compared with the reference configuration of the bare (or plain) cylinder, without the rods, to understand the effect of the rods (individually and collectively) and realisable potential of the system.

Specific objectives of this work entail to understand:

- how the system with rods compares with the bare cylinder (i.e., without rods).

- the effect of the non-uniform (potential-flow-inspired) setup of angular velocities upon the flow structure;
- the rods' contributions toward control of the hydrodynamic loads;
- whether the configuration of figure 2.1 sustains qualitative aspects under a different angle of attack of the incoming flow;
- the impact of free-end and free-surface effects, and tip-vortices on the control mechanism;

3 Literature review

Since the present thesis is composed of a compilation of published articles, each article will present its own literature review and discussion. However, a few concepts are succintly reviewed in this chapter concerning the main points of these matters in connection with the present research. References are provided for the interested reader.

3.1 Flow over bluff bodies

The flow over bluff bodies constitutes a canonical problem of fluid-structure interaction. Severe degree of complexity is found in its analysis, both in regard to the flow, and to the structure, providing a theme that for decades has largely captured the interest of the academic society (von Kármán, 1954).

Flow regimes about bluff bodies may be characterised by the Reynolds number, Re:

$$Re = \frac{\rho u D}{\mu} \tag{3.1}$$

which considers aspects of the body, of the flow, and of the fluid. This nondimensional number conveys the meaning of the relative importance of inertial over viscous effects. In equation 3.1, ρ and μ stand, respectively, for the density and viscosity of the fluid; and u and D correspond to characteristic velocity of the flow and length of the problem. Commonly, in external flows u matches the far-field incoming uniform flow velocity U_∞ (associated with the undisturbed flow sufficiently far from the body). In Blevins (1990), it is suggested through previous works, that if D is taken to be the distance between separation points (where the shear layers leave the bluff body), it may be part of the definition of a "universal" non-dimensional frequency for any bluff section (Strouhal frequency)[1]. For a circular cylinder, D can be reasonably approximated by the diameter of

[1]Henceforth, when mentioning "bluff bodies" we will be referring to circular cylinders.

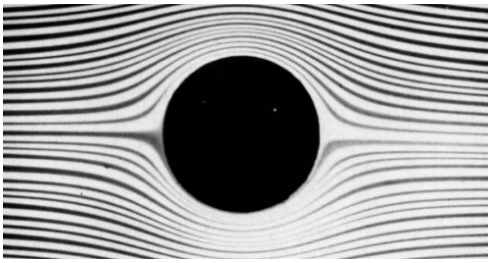

Figure 3.1: $Re \approx 5$ creeping flow. Extracted from van Dyke (1982).

the body (that we have already referred to by the same notation).

For low Reynolds numbers, i.e., $Re \lessapprox 5$, just away from the frontal stagnation point of the body (see figure 3.1), the boundary layer develops. Radially, an asymptotic velocity profile is formed within the boundary layer, from null (on the fluid-structure interface) to free stream value (away from the body), with favourable pressure gradient (see figure 3.3a). From the boundary-layer theory proposed by Ludwig Prandtl (Krazer, 1904), the so-called "no-slip condition" is met at the surface of the body, which means that the tangential velocity there is the same as the body's. Sufficiently distanced from the surface, the boundary layer gradually recovers the far-field condition. For such low Re, the boundary layer follows the curvature of the body and remains attached to it. This flow, wherein viscosity effects dominate and cause the dissipation of the vorticity, is denoted "creeping flow". An illustration is given in figure 3.1.

Coutanceau and Bouard (1977, apud Zdravkovich, 1998) shows through experimental data that downstream and for $Re \lessapprox 20$ the separation points move very slowly from the centreline of the cylinder to progressively lower values of $180° - \theta$ (see figure 2.1 for the θ-convention) with Re. After this range of Re, the separation points move faster toward the shoulders of the body, widening the wake of the cylinder, and two symmetrical bubbles appear downstream of the body and remain steadily in balance within the wake, increasing their streamwise lengths linearly up to $3D$ with Re (Blevins, 1990).

For $5 \lessapprox Re \lessapprox 47$, the curvature of the body affects the flow nearby in such a way that, under these circumstances, viscous action and adverse pressure gradient do not allow the flow to surmount enough kinetic energy to keep itself attached to the cylinder all the way downstream, ultimately leading to separation, see figure 3.3b.

It is now propitious to revisit the relation between pressure gradient and potential-flow theory, as well as pertinent terminology of figure 3.2, before proceeding to considerations of higher Re-regimes.

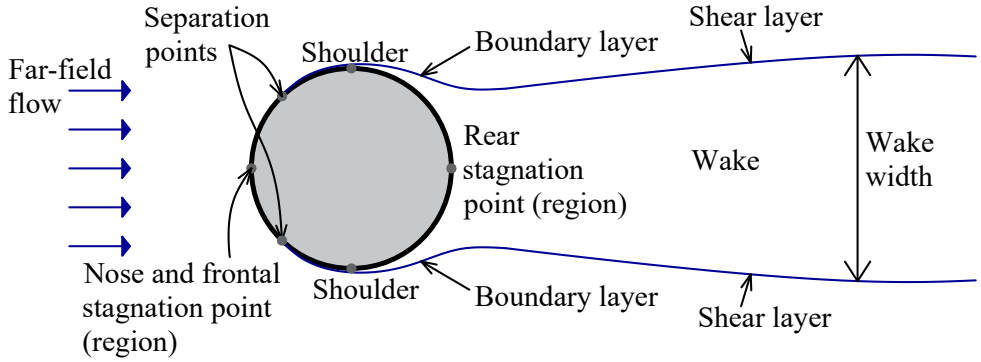

Figure 3.2: Reference terminology for the flow around a circular cylinder.

We recall that in viscous fluid the pressure gradient transverse to the boundary layer is very small compared with that longitudinally (that drives the flow). Hence, the pressure obtained from potential flow is imposed to and may be considered, to good approximation, constant across the boundary layer. As the incoming flow is impinged by the cylinder, the pressure on the front of the cylinder builds up to the most on the "nose" of the body, seen in figure 3.2, and a frontal stagnation region is established in the vicinity of this point. However, it is known from potential-flow theory that the flow runs about the structure and is accelerated by the confluence of the streamlines as it reaches the "shoulders" of the cylinder due to mass conservation (analogous to what is seen in the creeping flow of figure 3.1). From Bernoulli equation, as the velocity increases, the pressure decreases, and the entitled "favourable [or negative] pressure gradient" occurs in this piece of trajectory. Therefore, near the "shoulders" of the body, the pressure is low. Downstream of the cylinder an opposite sequence of events follows, such that now the velocity decreases as the streamlines move apart from one another and pressure develops about the circumference of the body up to a maximum toward the rear stagnation point, giving rise to what is termed an "adverse [or positive] pressure gradient".

In the viscous case, between the frontal stagnation point up to (about) the shoulder of the body, the flow within the boundary layer is driven by the favourable pressure gradient as in figure 3.3a. Contrarily, from (about) this point onward, the adverse pressure gradient leads to a retarding effect and to an inverse flow in the boundary layer, as depicted in figure 3.3b. The two velocity profiles resulting thereof are very different, insofar as their implications.

The inflexion point present in figure 3.3b leads to a region with a strong tendency toward rotation, that is, adds vorticity to the boundary layer. As the boundary layer sep-

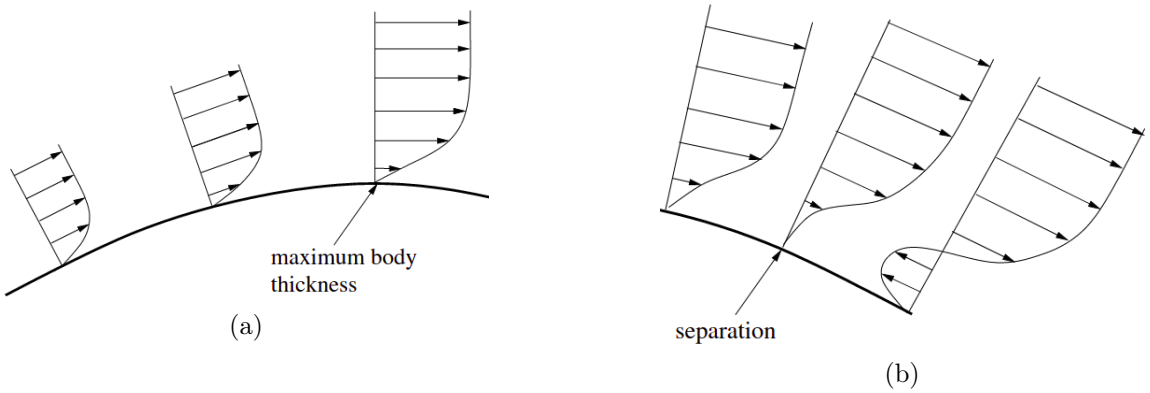

Figure 3.3: Boundary layer with (a) favourable and (b) adverse pressure gradient over a curvilinear surface. Extracted from Fielding (2005).

arates (upon occurrence of the velocity profile that contains the inverse flow in figure 3.3b) it detaches from the surface of the body and travels downstream. This symmetrically takes place both on the upper and on the lower part of the cylinder. Once this happens, the vorticity contained within the boundary layers and now carried by the shear layers eventually leads to the Kelvin-Helmholtz instability. The region comprehended between the two shear layers is termed the wake or vortex street. Therefore, besides the travelling shear layers on the interface between the wake and the free flow, the wake itself and the boundary layer are shear layers of the flow about bluff bodies (and make up for a rich vortex dynamics, Williamson and Govardhan, 2004).

Flow instabilities at $Re \approx 47$ lead to the imbalance of the aforementioned steady configuration. From the tail of the shear layers, the flow instability moves upstream, i.e., from the far-wake toward the posterior part of the body, introducing unsteadiness to the flow. The attached recirculation regions aft the body are affected, and one of the attached vortices is perturbed and grows. Later, it detaches from the body, ensuing a vortex-filled wake, denoted the *Bénard-von Kármán street*. After the first vortex is shed downstream, the other still attached gains vorticity and antisymmetrically replicates the former event, fostered by the rollup of the shear layers, thus contributing to the cyclic nature of vortex shedding. Consequently, a periodic load is imposed to the body and precedes the onset of VIV. The resulting force is commonly described in terms of the streamwise (F_D) and transverse (F_L) components, called drag and lift, respectively, which are represented in dimensionless form by coefficients respectively given by:

$$C_D = \frac{F_D}{\rho U^2 DL/2}, \qquad C_L = \frac{F_L}{\rho U^2 DL/2} \tag{3.2}$$

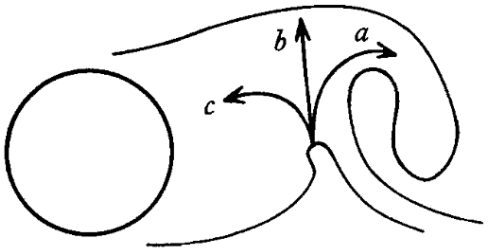

Figure 3.4: Fluid entrained into the wake (arrow c) and drawn across to the opposite shear layer (other arrows). Extracted from Gerrard (1966).

where the denominator stems from dimensional arguments, stating that the resulting force put in the form $F_D = \rho U^2 DL(C_D)/2$ is proportional to ρ, U^2, projected area DL and C_D. Variables embedded in Re are passed into $C_D = C_D(Re)$, such as the viscosity. Additionally, the denominator supplies the order of magnitude of the hydrodynamic loads on the projected area of the cylinder. (Of course, analogous thought may be followed for the lift).

Interaction of the detached shear layers, as in figure 3.4 results in the entrainment of the flow into the wake from either side of the cylinder, as well as fluid drawn across the centreline through to the opposite shear layer. The region that extends aft the body to the point where fluid from outside of the wake first crosses the axis (aligned with the flow direction, passing through the centre of the body) is termed the "formation region", and its length, the "formation length" (Gerrard, 1966). Alternatively, Williamson (1996) defined the formation length as the distance from the body to the point "where the velocity fluctuation has grown to a maximum and (thereafter decays downstream)".

With the increase in Re come further stages of the wake downstream and of the boundary layer, both ever more turbulent. According to Blevins (1990), between $150 \lessapprox Re \lessapprox 300$, the shed vortices become turbulent, while the boundary layer remains laminar. For $180 - 200 \lessapprox Re \lessapprox 3.5 \times 10^5$, the wake develops three-dimensionally, prevailing the laminar regime close to the body and turbulent regime away from it. Interestingly, in the subcritical regime ($300 < Re < 1.5 \times 10^5$) and even earlier than that, the shedding frequency f_v displays little variation. Its nondimensional counterpart – the Strouhal number, S_t:

$$S_t = \frac{f_S}{U_\infty / D}, \tag{3.3}$$

lies approximately equal to 0.2, and gives a rather precise estimate for the entire subcritical regime (see figure 3.5), so f_v is commonly taken to be equal to the Strouhal frequency f_S

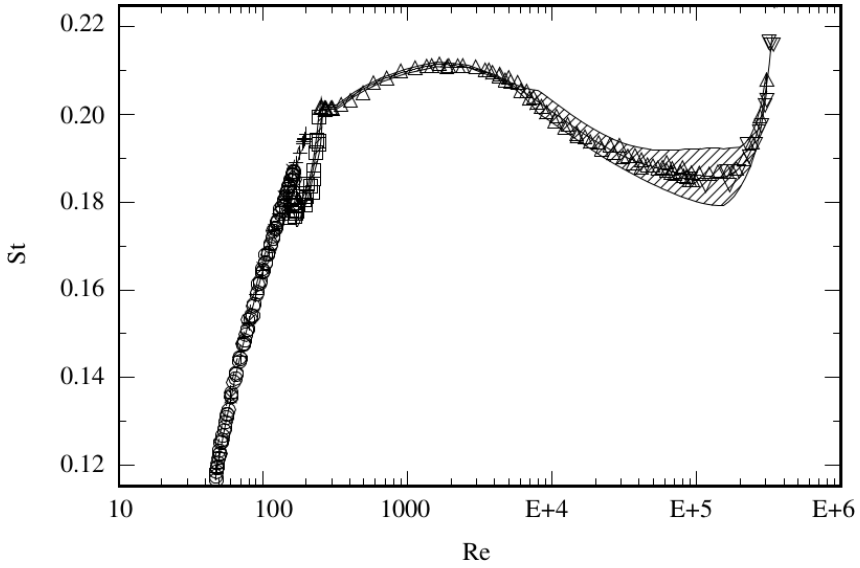

Figure 3.5: Strouhal number (S_t) verified by experiments and simulations from different authors for a wide range of Reynolds numbers (Re). Extracted from Norberg (2001).

at any Re in the subcritical regime.

$Re \approx 3.5 \times 10^5$ is associated with the transition of the boundary layer to turbulent regime. Then, the separation of the boundary layer is delayed rear of the cylinder, and θ moves from about 80° to 140°, shortening the wake width. The net result – commonly denominated "drag crisis" – is a substantial decrease in drag.

3.2 Vortex-induced vibrations (VIV)

Vortex-induced vibrations can be described as an auto-induced phenomenon of fluid-structure interaction of bluff bodies free to oscillate, caused by alternated vortex shedding in the Bénard-von Kármán street. Vortex shedding both causes and is the product of changes of the pressure distribution about the body, that sustains the entire phenomenon, as well as VIV.

VIV is described by transverse and longitudinal oscillations, and its effect depends on characteristic parameters, such as the Reynolds number, amplitude of oscillation of the body and reduced velocity, defined as $U_R = U_\infty/(f_v D)$. Bluff bodies subject to VIV present transverse oscillations that match the vortex shedding frequency and twice this frequency happens in the longitudinal direction.

The nature of the fluctuating forces is essentially the same as in the case of the fixed cylinder, rooted in pressure distribution about the body. Drag is predominantly due

to energy transfer from the mean flow to the body, as the bulk of the kinetic energy that drives the flow becomes potential energy at the nose of the cylinder, in the form of pressure; hence, a non-null component results from the pressure difference relative to the low-pressure wake. Lift adopts a cyclic behaviour about null value, as staggered rows of vortices are left interchangeably from either side of the cylinder.

Compared with a fixed cylinder, however, the dynamics of vortices in VIV follows a different behaviour. For sufficiently low reduced velocities, the cylinder emanates two rows of staggered vortices downstream during the oscillating motion. Following the terminology of Williamson and Roshko (1988), this mode of vortex shedding is called 2S, meaning that two single vortices are shed in a Strouhal period $T_S = 1/f_S$. This mode is alike that found for a fixed cylinder, see figure 3.6a. It has been observed that as the cylinder moves transversely to the flow, the spanwise correlation of the vortices increases, thereby resulting in an aspect of the wake progressively closer to a two-dimensional. For a circular cylinder, this becomes more relevant for amplitudes greater than $0.05D$ (Bearman, 1984). This feature leads to a strong increase in the lift coefficient compared with the case of a fixed cylinder. Moreover, the 2S mode eventually shifts to a 2P mode with the increase in U_R, so that two pairs of vortices detach from either side of the body (Feng, 1968), see figures 3.6b 3.6c. Analogously, shifting is also observed in the phase angle between the lift and the displacement of the body.

Measurements of the shedding frequency with the variation of the reduced velocity show that there is an interval in which the vortex-shedding frequency synchronises with the natural frequency of the body as the latter is approached, thereby giving rise to resonance.

To assume $f_v = f_S$ in the definition of U_R, along with the fact that $S_t \approx 0.2$, narrows down $U_R \approx 5$, the point about which VIV is more frequently noticed by researchers in the analyses of the amplitude, frequency, and hydrodynamic coefficients as functions of U_R. This interval of U_R was first denoted as the "range of synchronisation" (Bishop and Hassan, 1964), and it is also currently and predominantly referred to as the "lock-in regime", where the oscillation of the body controls the frequency of the shed vortices and the shedding frequency f_v departs from the Strouhal frequency f_S (which would be expected for a fixed cylinder, under otherwise the same conditions, according to Bearman, 1984). Once the lock-in regime is left, once again f_v is confused with f_S. Figure 3.7 shows the response

(a) 2S mode. Extracted from Griffin and Ramberg (1974).

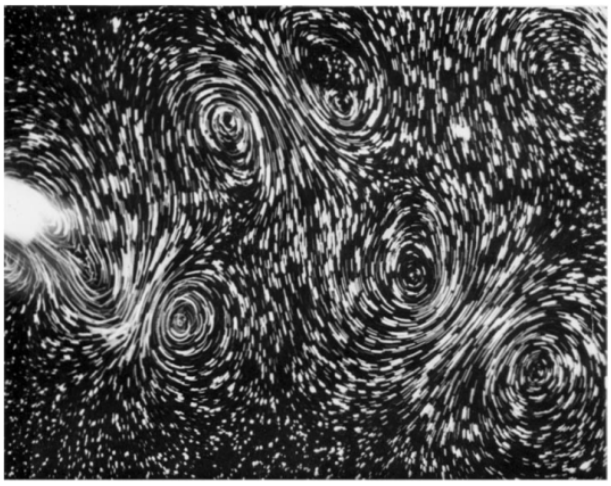

(b) 2P mode. Extracted from Williamson and Roshko (1988).

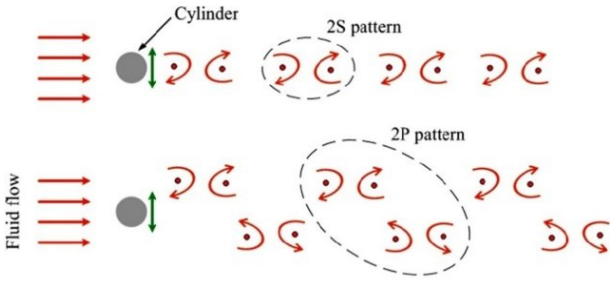

(c) Schematic representation of the 2S and 2P modes of the wake. Adapted from Ali et al. (2021).

Figure 3.6: Wake modes of vortex shedding. The cylinder is to the left and has been suppressed.

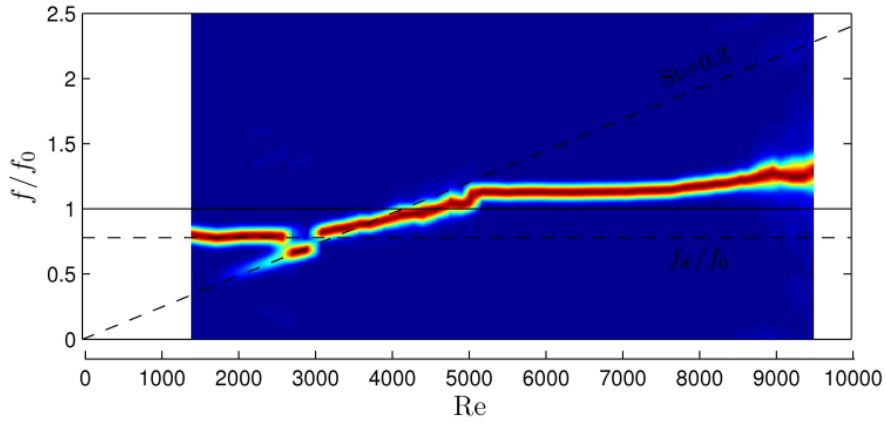

Figure 3.7: Frequency lock-in of a circular cylinder between $Re = 5 \times 10^3$ and $Re = 7.5 \times 10^3$. Adapted from Assi (2009).

frequency with Re of a circular cylinder free to oscillate crosswise; for $5000 < Re < 7500$, the frequency was unaltered.

The lock-in range of reduced velocities depends on the mass ratio $m^* = m/m_f$ between the structural mass (m) and the mass of fluid displaced due to the presence of the submerged body (m_f). At low Re, Willden and Graham (2006) showed through numerical simulations the effect of m^* on the range of U_R where lock-in and other transverse oscillation regimes occur. It was broadly shown that an increase in m^* shortens this interval. And within this range, the amplitude of the response varies with $m^*\,\xi$, the product of the mass ratio by the damping ξ (Khalak and Williamson, 1999).

3.3 Free-surface and free-end effects

Two other important matters in bluff body flows concern with free-surface and free-end effects. Much of the current state of information on bluff body flows neglects these effects and models cylinders as though they were infinitely-long and fully submerged[2]. To adopt the former assumption means that most studies to date still consider the vortex dynamics of vortex shedding dependent on the spanwise separation of the flow, although the subject of finite cylinders dates back to experiments made over a century ago concerning the finite length case (Wieselsberger, 1922). Further studies, predominantly belonging to a line of research on wall-mounted bodies (see figure 3.8 for an example) was born in the past century, and has improved the understanding of end effects. Yet, notably, even these

[2]Hereafter, the expressions "infinitely-long" and "infinite" shall refer to the flow over cylinders when end effects are disregarded, in opposition to the "finite" setup. We shall drop the quotes for succinctness.

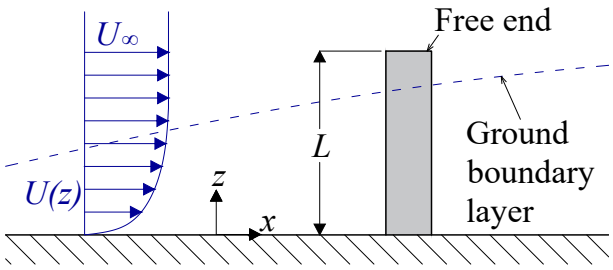

Figure 3.8: Example of wall-mounted cylinder. Extracted from Sumner, Heseltine, and Dansereau (2004).

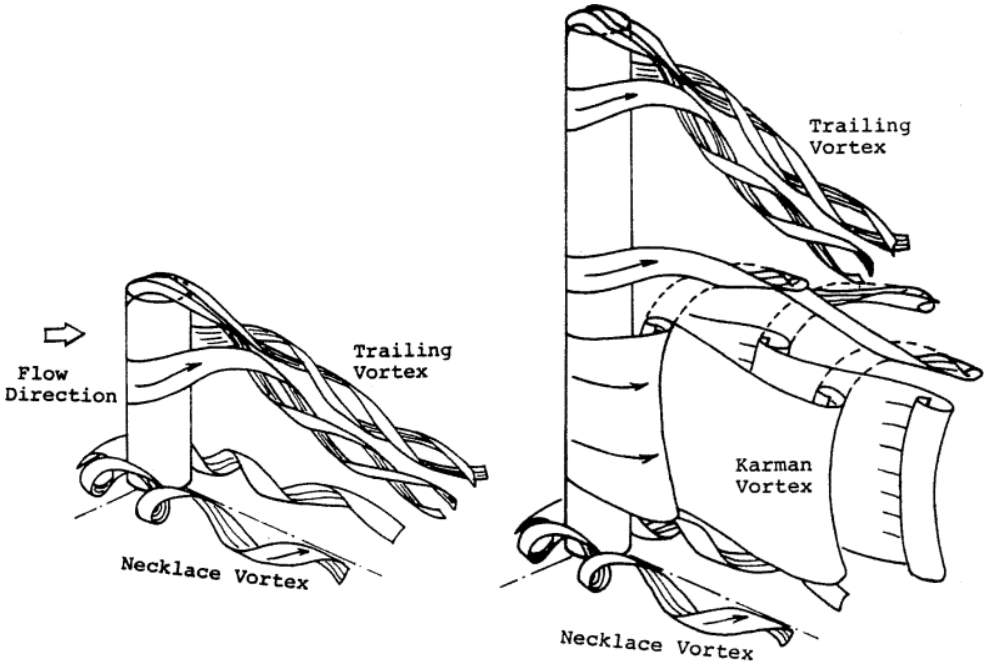

Figure 3.9: Vortex structures present for low (left) and high (right) slenderness parameter. In the former, the Bénard-von Kármán vortex street vanishes; only free-end trailing vortex and the necklace vortex (inherent to wall-mounted bodies) last. Extracted from Kawamura et al. (1984).

studies are still scarce when compared with those on infinitely-long bodies. Numerical computations that allow the analysis of the vortical content of the wake, for example, are represented by few studies (perhaps due to the high computational cost associated with the stringent discretisation of the flow domain, Palau-Salvador et al., 2010; Krajnović, 2011). Experiments seem to have explored the matter at greater depth, notwithstanding authors of relevant studies on this topic have converged, in published works, that there is still ample room to explore and open questions. In the forthcoming review, the flow about submerged, surface-mounted and bodies without end plates are jointly considered.

Incipient visualisation of the flow over wall-mounted bodies obtained by Okamoto and Yagita (1973) revealed the presence of complex streamwise vortex structures inherent to

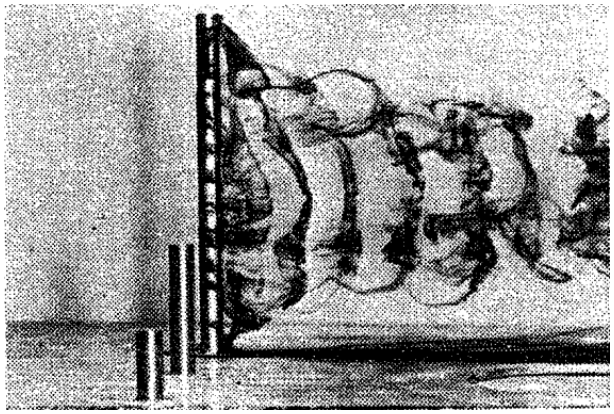

Figure 3.10: Shorter Bénard-von Kármán vortex street for a finite length cylinder at $Re = 550$, and long slenderness parameter $L/D = 15$. Adapted from Okamoto and Yagita (1973).

the ends of the bluff body, commonly referred to as the tip-vortices. Depending on the slenderness parameter (L/D), tip-vortices may result in specific topologies, as noted by these authors for L/D from 1 to 12.5 and by Kawamura et al. (1984) for L/D from 1 to 8 (see figure 3.9) and reviewed in Sumner (2013). Due to the presence of the free-end vortices, a noticeable aspect is that the mean drag upon finite structures is lower than in infinitely-long bodies, justified cumulatively by two factors: 1) lower separation velocity when the flow detaches from the structure; and 2) shorter extension of the vortex street along the span of the cylinder, as detected by Kawamura et al. (1984, see figure 3.10).

Farivar (1981) experimentally studied the turbulent flow at $Re = 7 \times 10^4$ about cylinders with finite length of slenderness ratio ranging from 2.78 to 12.5, focused on hydrodynamic loads and shedding frequency. In the same study, another setup was analysed, in which the submerged length of the body corresponded to the water depth, so the assumption of an infinitely-long cylinder could be made (in such case, $L/D = 15$). Supported by the work of Goldstein (1965) on the turbulent flow about a cylinder with different aspect ratios, Farivar (1981) attempted to describe the effect of the free end regarding mean and root mean square (RMS) of pressure fluctuation distributions about the cylinder, mean drag force and the vortex-shedding frequency. This study also searched for what the author called "suppressed" regions – those where the wake behaved two-dimensionally. (It is interesting to note that the author of this study associated the absence of end effects to a two-dimensional configuration of the flow; later it would be found out that the turbulent flow, including the Re assessed in Farivar's work, is three-dimensional regardless of end effects, Williamson, 1996). Amongst the relevant findings of Farivar (1981) are the identification of regions where the wake was better or worse correlated; the observation that the

mean drag was lower than in infinitely-long bodies due to end effects; the relevance, albeit small, of the viscous contribution to drag, observed in the discrepancy between measured mean drag and its computation through pressure integration over the surface of the body; and the fact that at sufficiently small aspect ratios it is rather difficult to observe any characteristic signature in Strouhal frequency, in clear contrast with the infinitely-long case.

The difficulty to detect a characteristic signature in frequency is associated with the verification made by Kawamura et al. (1984), where the authors noted that according to L/D, the Bénard-von Kármán wake could not form. Rather, for sufficiently low L/D, the trailing vortices dominated the wake. Later, Luo (1993) pointed out that the formation of a Bénard-von Kármán vortex street for finite cylinders was associated with a critical value of aspect ratio L/D that ranged between 1 and 7, depending on the influence of the ground boundary layer (see figure 3.8).

Working with different L/D, Sumner, Heseltine, and Dansereau (2004) produced time-averaged velocity and streamwise vorticity contours that showed tip-vortex structures, near-wake recirculations, and downwash[3]. It was found that the effect of the tip vortices extended into the wake downstream and scaled with the cylinder's length. The authors also reported that a coherent Kárman vortex street was not observed for $L/D \leq 3$. Instead, a symmetric "arch-vortex" (or "mushroom-vortex") dominated the near wake.

Older studies affirmed that tip-vortices originated along the span of the wall-mounted cylinder from just before its free end (Okamoto and Yagita, 1973; Kawamura et al., 1984), but fairly recent papers have converged in that the onset of tip-vortices actually occurs at the leading edge of the cylinder (Palau-Salvador et al., 2010; Krajnović, 2011; Rostamy et al., 2012). The nature of the recirculation zone generated by the free end lies in the obstruction of the end to the flow for any ratio L/D. As the flow attempts to circumvent the leading edge of the cylinder, the recirculation zone is locally established just near the tip of the cylinder. Reattachment of the flow occurs closer to the trailing edge the lower is the slenderness parameter (Rostamy et al., 2012, see figure 3.11 for this experimental verification for different slenderness parameters). Past the body, streamwise vortices interact with the tip-vortex. Collectively, these were shown able to disrupt the

[3]The term "downwash" refers to the flow that is deviated at the free end from its upstream course toward the centreline of the cylinder's wake. For a wall-mounted cylinder, vertically placed, as in Sumner, Heseltine, and Dansereau (2004), the term refers to the "downward directed local velocity field near the free end".

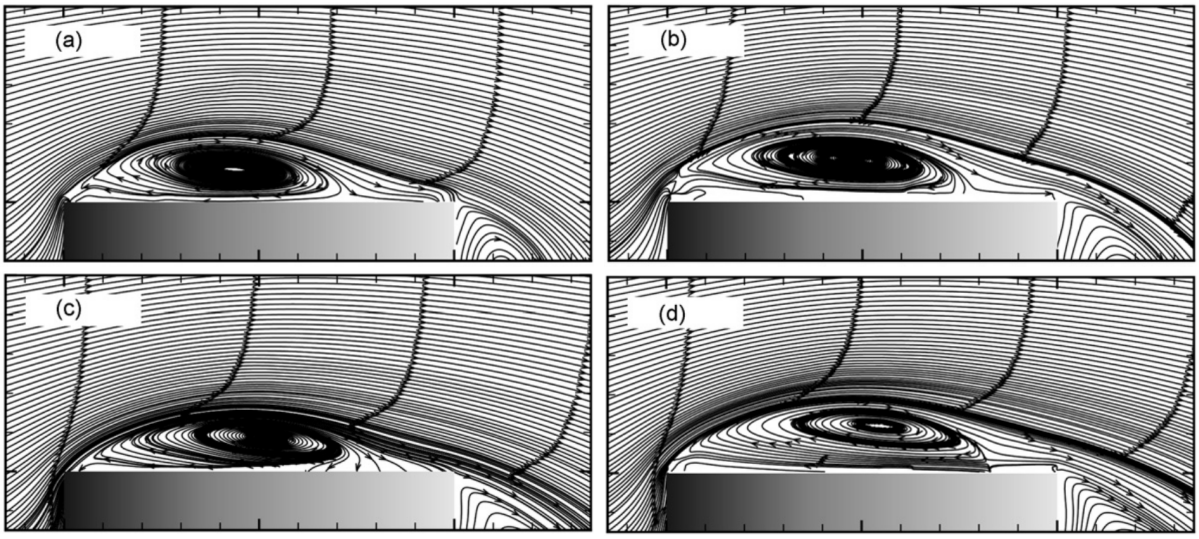

Figure 3.11: Recirculation zone at the tip of the cylinder for $L/D = 9$, 7, 5 and 3, respectively, from a) to d). Extracted from Rostamy et al. (2012).

regular Bénard-von Kármán wake in the end region in Park and Lee (2004), for $L/D = 6$, thereby locally suppressing the wake.

We now turn to studies that consider, instead of the ground, a free water surface. Amongst other features, free water surface setups are distinguishable from those on ground planes, because they do not lead to the formation of a boundary layer as the one shown in figure 3.8, that comprised the studies above on surface-mounted bodies; and when waves are generated, they may affect the body.

In free water surface studies, the Froude number, defined as $Fr = u/\sqrt{gL}$ is a dimensionless number concerning the relevance of wave effects. According to Newman (2018), for a subcritical regime of $Fr < 1$, the wave pattern is similar to that expected for deep waters. Generally, for $Fr < 0.5$ water elevation due to free surface effects is deemed negligible. According to Hay (1947, apud Gonçalves et al., 2015), in the upper limit $Fr = 0.5$ wave effects may be neglected, based on the investigation of low aspect ratio cylinders piercing through the free water surface. In such cases, the surface may be considered sufficiently well approximated by a slip-allowing plane. We remark that instead of the local flow velocity u, for the purposes of this work, we shall refer hereafter to $Fr = U_\infty/\sqrt{gL}$ based on the incoming flow velocity for a conservative estimation of Fr, and L as the cylinder's submerged (and spanwise) length (Hay, 1947, apud Gonçalves et al., 2015).

In the laminar regime of $Re = 180$, the numerical investigation (using volume-of-fluid method) of Reichl, Hourigan, and Thompson (2005) with a horizontal cylinder (parallel to

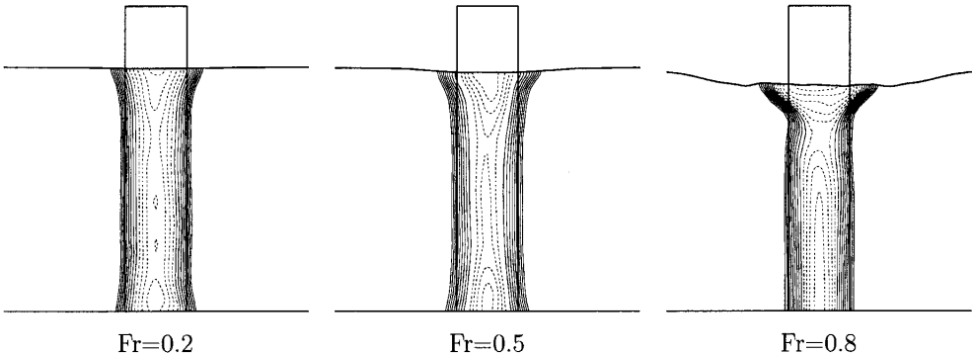

Figure 3.12: Vorticity contours at the location of one diameter downstream of the cylinder. At low Fr the surface waves are generally very small and negligibly affect the submersed flow dynamics. Extracted from Kawamura et al. (2002).

the water surface) varied the gap ratio[4] between the cylinder and the free surface from 0.1 to 5.0; and noted that for low Fr the flow behavior was similar in the case of free surface to that of a slip wall attached to the respective end, as in the surface-mounted bodies mentioned above. Up to $Fr = 0.6$, the free water surface was not intensely disturbed, although the wake formation differed strongly. Vertically-placed cylinders piercing through the free water surface investigated through LES simulations of Kawamura et al. (2002) in subcritical regime for $Fr = 0.2$, 0.5 and 0.8 rendered clear that up to this second value the free water surface could be approximated by a resistance-free plane, because the influence of the small-amplitude waves thereof was very weak on the wake, see figure 3.12.

More recently, the study of Gonçalves et al. (2015) advanced on the matter of VIV for very low aspect ratios (in the range $L/D = 0.1$ to 2.0), and evaluated, through particle image velocimetry method, the subcritical flow of $10^4 < Re < 5 \times 10^4$ about circular cylinders piercing through the water surface, also without end plates. In this setup, the spanwise axis of the cylinder was perpendicular to the free water surface. It was noted that from long to short cylinders, the wake passed from a dominated Bénard-von Kármán vortex street to another wherein vortex structures stemmed from the ends became predominant. The authors assessed the power spectrum density, and detected two major frequency components, as L/D was adjusted to different values: one, Re-independent associated with the Bénard-von Kármán street; and another, dependent on Re and independent of L/D, associated with the free end (with $S_t < 0.1$).

In spite of the advancements achieved with the past studies, free-end and free-surface effects are still not entirely understood. The influence of the aspect ratio and Re number,

[4]Ratio of the distance from the centre of the body to the free surface and the diameter of the cylinder.

for example, have been parametrically studied, but a complete understanding is still far from the current state of information (Sumner, 2013).

From the review above, it is easy to understand that the flow about bluff structures is marked by complexity. It is of interest to understand the interaction between finite bodies and to control such flows, and many studies have endeavored in this matter for infinitely-long bodies. Nevertheless, aside from the work of Luo, Gan, and Chew (1996) in the evaluation of the flow interaction between low aspect ratio cylinders of the same size (thus, not control-related), we are unaware of studies devoted to active flow control of finite circular cylinders. We review this subject in greater depth below.

3.4 Suppression of vortex shedding

Vortex shedding suppression is paramount to avoid fatigue in large offshore structures, and may prevent the onset of VIV at its root. Adverse effects upon the structure subject to vortex shedding are notably important when these endure VIV in the lock-in region. To counteract these phenomena, active and passive flow-control techniques have been devised for bluff bodies (Zdravkovich, 1981; Gad-el-Hak, 2000; Choi, Jeon, and Kim, 2008).

3.4.1 Passive control

Passive solutions aim at suppressing vortex shedding without power input. Common examples comprehend shrouds (Cicolin and Assi, 2017), near-wake stabilisers (such as control plates, as in Assi, Bearman, and Kitney, 2009 and fairings as in Assi, Bearman, and Tognarelli, 2014), geometrical modifications (such as surface protrusions, e.g., helical strakes, as seen in Korkischko and Meneghini, 2011 and Assi, Crespi, and Gharib, 2022, as well as spanwise or trailing edge waviness, etc. reviewed in Choi, Jeon, and Kim, 2008) and secondary smaller bodies, such as small rods positioned about the system (Strykowski and Sreenivasan, 1990; Patino, Gioria, and Meneghini, 2017). These examples are illustrated in figures 3.13, 3.14a, 3.14b and 3.15.

Currently, the most widely used passive technology for slender bodies of circular cross section are helical strakes in risers. According to Assi, Bearman, and Kitney (2009), the most rigorous way of evaluating the suppression of VIV from this passive mechanism is at low levels of $m^*\xi$ (where ξ is a fraction of critical damping), since it is inversely

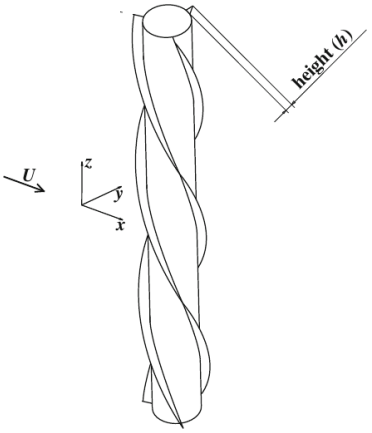

Figure 3.13: Helical strakes. These are mainly used to avoid VIV, however, their usage tends to increase drag over the main structure. This is a downside from its original application, that for the wind industry, where the fluid density (air) is much lower than in offshore applications (water). Extracted from Korkischko and Meneghini (2011).

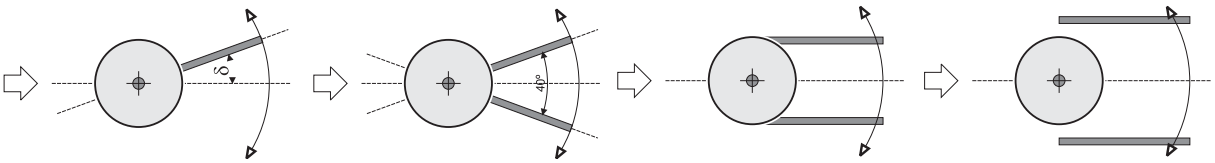

(a) Splitter plates. These structures are used to avoid the communication between shear layers and delay vortex shedding aft the body, to produce vortices of lower strength; and thus reduce mean drag. Extracted from Assi, Bearman, and Kitney (2009).

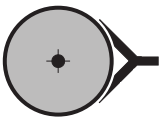

(b) Fairings. The fixed plates streamline the flow about the system comprised by the main body and passive device to avoid abrupt separation of the flow. Extracted from Assi, Bearman, and Tognarelli (2014).

Figure 3.14: Mean drag reduction is achieved for fairings and splitter plates; however, these fixed-plate devices are susceptible to the directionality of the flow and may be prone to galloping.

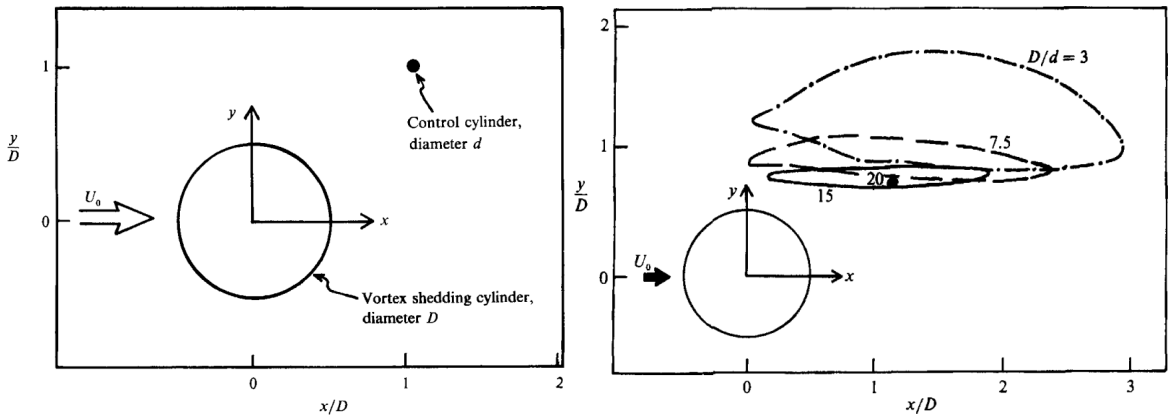

(a) (b)

Figure 3.15: Passive technology effective at low Reynolds numbers using a single slender rod of diameter d near the main body of diameter D. The mechanism here is to perturb the near flow, and to avoid growing instabilities that would otherwise lead to vortex shedding (left). On the right, sensitive regions for different ratios D/d where the insertion of the rod avoided vortex shedding. Extracted from Strykowski and Sreenivasan (1990).

proportional to the response amplitude for an elastically mounted cylinder. From this argument, it follows that helical strakes are poorly efficient for a fixed height with the reduction of $m^*\xi$ and their use increases drag (Zdravkovich, 1981). These assertions have been verified experimentally (Korkischko and Meneghini, 2011). In fact, helical strakes were designed for wind engineering purposes, where it effectively works, given that m^* in air is much greater than in water (due to differences in density). Therefore, there is room for improvement of passive technologies devoted to the mitigation of vortex shedding and VIV of circular cylinders.

On physical grounds, the class of passive solutions acts through different mechanisms. One way is through elimination or delay of vortex shedding away in the wake downstream, thus diffusing vorticity. It is known from the classical work of Gerrard (1966) that shear layers of circular cylinders replenish the wake with vorticity and their interaction is of utmost relevance to the shedding mechanism. Thus, some strategies will try to prevent shear layer interaction. The farther away vortex shedding occurs, the less intense are its effects on the body, because the viscosity acts on the shear layers, and thus attenuates their circulation. The insertion of a splitter plate rear of the body, aligned with its streamwise axis of symmetry, for example, effectively works against vortex shedding, because it blocks shear-layer interaction. Another measure is to insert splitter plates or fairings in appropriate configurations to smoothen the flow downstream (which can be thought of as a way to lessen the bluffness of the body, closing in the separation points at

greater downstream distance from the rear part of the body's surface). Such arrangements have been extensively studied in Assi, Bearman, and Kitney (2009) and Assi, Bearman, and Tognarelli (2014) and for 2D VIV in Assi et al. (2010). An interesting feature of these technologies is that vortex dynamics is mitigated accompanied by drag reduction (in contrast to helical strakes employed to long bodies).

In general, these technologies focus on the reattachment of the shear layers, reduction of their interaction or delay entrainment of fluid further downstream, so as to dissipate the vorticity of the communicating shear layers. It has also been verified in the literature that symmetry is important for the vortex dynamics. The breakdown of this quality in the flow structure past the body can entirely suppress the vortex street, as it was somewhat done by Strykowski and Sreenivasan (1990). Indeed, it has been detected by Mittal and Raghuvanshi (2001) with a control rod that, even if complete steadiness of the flow is not achieved, the presence of the this smaller body still affects vortex shedding significantly. Alternatively, to spin a bare cylinder may also impede the formation of vortices (at least in laminar regime at $Re = 200$, Mittal and Kumar, 2003).

This research concerns with the use of peripheral rods. In a seminal work, Strykowski and Sreenivasan (1990) verified that the insertion of a single small cylinder in an appropriate position was able to attenuate the growth of temporal instabilities and was able to not only reduce vortex shedding but also to banish its inception entirely in a limited range of Reynolds numbers. In a more general sense, their numerical and experimental results for $40 \leq Re \leq 100$ showed that local modifications led to global changes in the flow and that, in order to control the wake, interaction with the near field was of vital importance. These findings were later supported by the simulations performed by Mittal and Raghuvanshi (2001).

Based on the mechanism studied by Strykowski and Sreenivasan (1990), Silva-Ortega, Assi, and Cicolin (2015) used 2, 4 and 8 control rods uniformly with the same diameter $d/D = 0.06$; that were fitted to the main, larger, cylinder of diameter D in order to evaluate vortex shedding of a fixed system, and gaps $G/D = 0.05$ and 0.15 were used as well. The system with 8 rods is illustrated in figure 3.16.

These parameters were combined in the flow regime $5000 < Re < 50000$. The results showed that the setup of four control rods presented most suppression of drag and lift. An important consideration upheld by the authors of this study is that, in spite of their

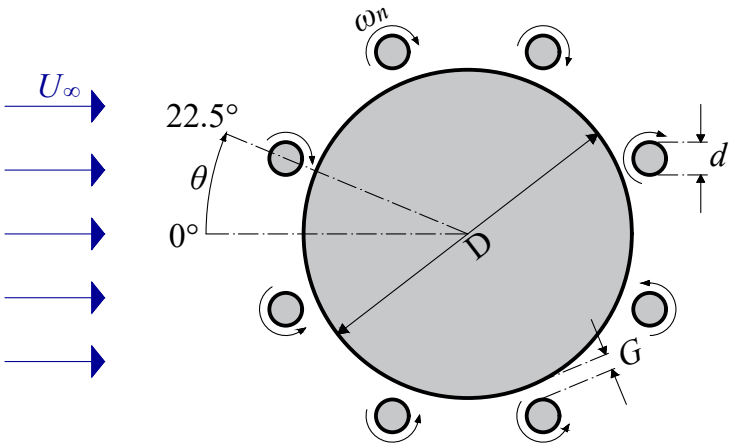

Figure 3.16: System with eight wake-control rods and associated parameters d, G and ω_n. This system was employed passively, i.e., $\omega_n = 0$; and actively in Assi, Orselli, and Silva-Ortega (2019) and in past works cited therein. This system corresponds to figure 2.1, simplified when free-end and free-surface effects are neglected (infinitely-long approximation) and for axial incoming flow $\alpha = 0$.

findings for a fixed system (that is, constrained not to oscillate), the same experiments could provide different results for a system free to vibrate under VIV.

To follow up on this, using the same number of rods about the main cylinder and additional geometrical parameters ($d/D = 0.04$ and 0.08; and $G/D = 0.10$ were also considered), Silva-Ortega and Assi (2017a) assessed VIV of the passive system. Two notorious outcomes were achieved: the mitigation of 99% of the peak amplitude of vibration, and the lowest drag for the configuration with 4 rods, although the latter was highly affected by VIV, in connection with the interrogation made by Silva-Ortega, Assi, and Cicolin (2015). Amongst the conclusions of this work, the sensitivity of the parameters was pointed out to, referring to the number of cylinders N, the diameters' ratio d/D, and the gap ratio G/D. The authors noted that care must be taken with such a passive device, which may not only increase hydrodynamic loads but also introduce galloping due to directional effects. With an adequate choice of parameters, only residual vibration due to VIV remained for a setup involving eight control rods.

3.4.2 Active control

It was remarked by Mittal and Raghuvanshi (2001) that suppression of vortex shedding by proper placement of a passive rod near the main cylinder was possible only at low Re. This is a common feature that pertains to passive control in general. It is deemed an adequate alternative to employ an *active* solution instead in such cases, that is, one in

which power is required, that allows for flow control at higher Re.

Active devices tend to be more expensive and complex in design, installation and maintenance, typically prohibiting their application in risers and other similar structures. But when larger systems are considered, such as huge floating platforms with bluff hulls, active VIV suppressors could play a significant role in mitigating the response with considerable reduction of hydrodynamic loads.

Amongst the techniques employed in this class of solutions are suction and blowing, vortex generators, forced (rotary, streamwise and transverse) oscillations, base bleed, spinning wake-control rods, etc. These technologies can be equipped with feedback control for more efficient power consumption (Choi, Jeon, and Kim, 2008). An interesting aspect is that to employ the active mechanism may enable the control of the wake and of vortex shedding at higher Re-flows. Besides, this class of solutions may allow an omnidirectional performance of the system, i.e., may enable a system to produce similar results regardless of the direction of the incoming flow, a feature that is lacking in most passive solutions (Zdravkovich, 1981).

Thus, a more advanced approach relative to the rods, in the context of this research, is to inject momentum into the near-wake flow by means of the same elements. To do so, the rods must spin with adequate angular velocities. This active technique is termed the Moving Surface Boundary-layer Control (MSBC, Modi, 1997), herein suggested with the use of the spinning elements of figure 2.1. MSBC is originally from the aerodynamics context. Modi (1997) employed MSBC with different arrangements of one and two control rods fitted to an airfoil and assessed the curve of lift versus angle of attack; and found that stall was delayed. The author also tested this technology in bluff bodies. In MSBC, momentum is injected into the near flow to delay separation. To provide the spinning elements with increasingly higher angular velocities has proven effective to reduce mean drag and fluctuating lift, and eliminate vortex shedding entirely.

Silva-Ortega and Assi (2017b) conducted experiments to assess mean drag and vortex-shedding frequency of a circular cylinder subject to VIV with a degree of freedom in the cross-flow direction, surrounded by 8 control rods (as in figure 3.16), under different arrangements[5] and angular velocity. The rods were constrained to spin uniformly at a

[5]All arrangements were configured so the rods were equally distant from one another, and none was positioned in front of a stagnation region. The angle between any of the stagnation points and nearest rods was half of that between rods.

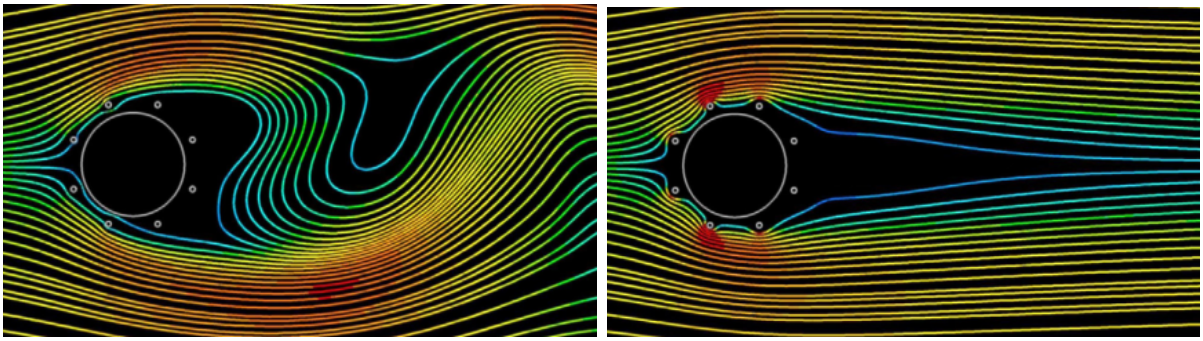

Figure 3.17: Streamlines of the system comprised by a main cylinder fitted with eight control rods fixed (left) and rotative (right) coloured by velocity magnitude. Extracted from Assi, Orselli, and Silva-Ortega (2019).

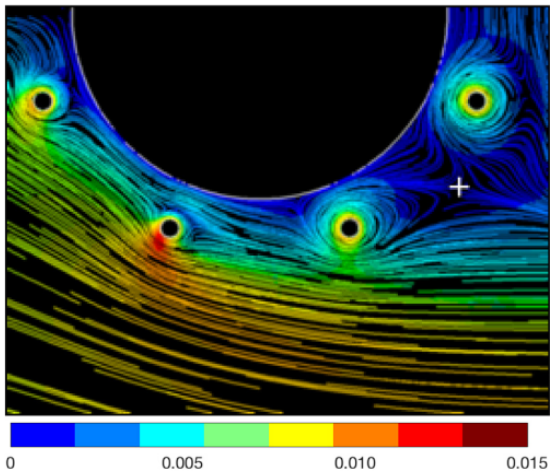

Figure 3.18: Suppression of VIV with eight fixed control rods. Streamlines coloured by velocity magnitude. Extracted from Silva-Ortega, Orselli, and Assi (2014).

single speed, and two distinct diameters were tested. Momentum was injected into the boundary layer by means of the rotating elements, delaying vortex formation, and the wake became thinner (figures 3.17 and 3.18). As a consequence of the suppression, mean drag and RMS of lift decreased.

Through numerical simulations, Assi, Orselli, and Silva-Ortega (2019) showed that to employ open-loop MSBC with sufficient actuating power gave rise not only to the results attained by Mittal and Raghuvanshi (2001, with one rod), but extended the results of Mittal (2001, with two rods) to produce thrust upon the entire system at $Re = 100$ with eight rods. Thus, the rotating mechanism promoted a mean drag inversion and released greater flow control than its passive counterpart and than the rotating mechanism with fewer spinning elements.

Although complete suppression was not attained in numerical simulations with such a system, Assi, Orselli, and Silva-Ortega (2018) were able to significantly impede the

growth of vortex tubes into large eddies in the wake at $Re = 10^4$. Essentially, the paper showed that only smaller eddies remained at the upper end of rotations of the wake-control rods. Previously, also at $Re = 10^4$, Mittal (2001) verified that the level of organisation in the wake was enhanced when two control rods were rotated. Building on this work, however through particle image velocimetry (PIV), Korkischko and Meneghini (2012) experimentally further allowed the system to vibrate in a water channel at $Re = 1600$ up to 7500, with rods spinning at increasingly higher rotation rates up to $5U_\infty$. They noted a narrower wake a circulation-free region that prevented vortex formation.

In terms of power expenditure, both the analysis of Assi, Orselli, and Silva-Ortega (2018) and Assi, Orselli, and Silva-Ortega (2019) showed that the system required relatively little power, considering that less power was spent to spin the rods than would have been lost due to drag otherwise. However, in both studies the cylinders were put in motion with uniform rotation, that is, with a single magnitude of angular velocities.

One might wonder: *in a suppressed condition of the flow, would each rod deliver the same contribution to the entire system?* It is a reasonable assumption that in a suppressed condition, different rods would represent different contributions to the system, because of their positions relative to the main body and to the vortex dynamics taking place nearby.

Indeed, more recently, experiments performed by Cicolin et al. (2021) with one rod at different locations surrounding a central cylinder employing particle-image velocimetry at $Re = 2 \times 10^4$ advanced on two matters: (i) on the details of the interaction between the control rod and the shear layer of the main body and (ii) on the influence of the control rod on separation. The authors remarked on a significant influence of the position of the separation point on drag and lift measurements in turbulent regime. The study showed that the insertion of the control rod within the recirculation zone had little effect upon the drag of the main body. For example, rods positioned within the wake and in stagnation regions are expected to be less relevant when one considers a fixed angle of attack (for simplicity, take the flow as in figure 3.16). In such cases, the intermediate rods might seem more relevant than the frontmost and rearmost rods. Indeed, the intermediate rods are positioned close to separation points of the otherwise plain cylinder; they also interact more with the shear layers before separation, thus might lead to a thinner wake through displacement of the separation points further aft the entire system. Of course, the best answer to this inquiry would be given through an optimisation (more precisely,

minimisation) problem with objective functions such as power-loss, mean drag or RMS of lift. A simple and significantly less costly procedure is to visually compare the resemblance between suppressed condition in viscous fluid with the easily-computed and optimal setup of potential-flow (in terms of mean drag). And to use an analogy, wherein the velocities of the latter become inputs of the former, as explained in chapter 6.

A pertinent question that lies within this context is the following: *would such a system be sensitive to the angle of attack of the incoming flow?* If so, then the results found so far for flow-control in general, and consequently to hydrodynamic loads could differ significantly once α of figure 2.1 was altered. Otherwise, one might say that the system behaved omnidirectionally (in the same sense formulated by Zdravkovich, 1981).

Finally, it is worth noting the absence of research concerning both mechanisms for finite cylinders subject to end effects. For example, the inquiries: *How well would the system of figure 2.1 work for flow control in finite bodies fully submerged? What impact would a free surface have on passive and active mechanisms? What impact would free ends have on the flow control mechanism? Efficiencywise, would the power expenditure to spin the rods compensate the mitigated drag?* all remain unanswered. As a matter of fact, flow control for bluff bodies of low aspect ratio is a matter that, to the author's best of knowledge, has not been explored[6].

[6]The paper of Luo, Gan, and Chew (1996) is one of few studies that evaluated interference between low aspect ratio cylinders, however, the authors were not concerned with a mechanism of (active) flow control as described above. Rather, focus was given to the interference between two bodies of the same scale.

4 Finite volume method

4.1 Governing equations

The finite volume discretisation is one of the methods used to solve the governing equations of motion and mass conservation.

The Navier-Stokes equations correspond to Newton's second law applied to an infinitesimal fluid element, together with i) the hypothesis of a Newtonian fluid, in order to properly describe the stress tensor, which ii) consecutively requires the postulation of a rate of strain (Stokes hypothesis) and iii) the assumption of an isotropic character of the viscous stresses. Continuity is derived purely from a mass balance over all faces of a control volume. The resulting Navier-Stokes and continuity equations are given, respectively, by equations 4.1 and 4.2 where incompressibility was considered:

$$\rho\left(\frac{\partial U_i}{\partial t} + U_j\frac{\partial U_i}{\partial x_j}\right) = -\frac{\partial p}{\partial x_i} + \mu\frac{\partial^2 U_i}{\partial x_j \partial x_j} \tag{4.1}$$

$$\frac{\partial U_j}{\partial x_j} = 0 \tag{4.2}$$

Einstein notation is used above, whereby repeated indices in a product represent the summation over all terms carrying the same index (i.e., U_iU_i denotes what could be redundantly represented by $\sum_{i=1}^{i=M} U_iU_i$, for any upper index M).

Regarding the equations above, it is adequate to acknowledge that another equation is frequently used in fluid dynamics, that of the transport of energy, but, throughout this work the flow is assumed incompressible (low Mach number), under no heat transfer. Another relevant consideration is that body forces were neglected. As it is remarked in section 6, wave effects were deemed negligible here (in view of a low Froude number, in the context of free-surface effects).

Deduction of such equations is found in several texts in the literature. Anderson (1995)

and Versteeg and Malalasekera (2007) offer a rather intuitive and physically appealing derivations, also concerned with the frame of reference used in the derivation of these equations. More general and advanced description is discussed in Bird, Stewart, and Lightfoot (2006), along with explicit expressions in cylindrical and spherical coordinate systems.

Analytical solution of this set of partial differential nonlinear equations is not a trivial task. Rather, it is considered one the greatest unsolved challenges at present. Currently, these equations are only solved numerically; and yet, many difficulties arise.

4.2 Discretisation schemes

General properties

In the finite volume method, discretisation is made of the equations and of the physical domain into a numerical domain comprised of finite volumes through which the balance between incoming and outgoing fluxes is respected (Patankar, 1980). Equations 4.1 and 4.2 are integrated over the surface of the fluid element and subsequently discretised. To approximate the flow by an ever more refined grid would ideally lead to a better representation of the flow[1]. However, due to feasibility constraints, the balance between grid refinement and accuracy is often the prime goal in CFD computations.

The nonlinear aspect of the Navier-Stokes equations render their solution difficult. It appears to be due to the convective and nonlinear term $U_j \partial U_i / \partial x_j$ of equation 4.1. Some regions of the flow might behave differently from others. To impose a single discretisation scheme for the solution of the flow thus becomes inaccurate. Customarily, discretisation schemes use many forms of interpolants, because they must comply with desired properties, such as conservativeness, boundedness and transportiveness (Versteeg and Malalasekera, 2007).

Conservativeness refers to the capacity of the discretisation scheme to preserves fluxes across cell faces.

Boundedness refers to the ability of the discretisation scheme to represent intermediate quantities bounded by boundary values in a problem without sources. An example is a one-dimensional bar whose temperature is measured along its length, with fixed

[1]This is the property of consistency of the discretisation scheme.

(a) Asymptotically diffusive flow, $Pe \to 0$. (b) Asymptotically convective flow, $Pe \to \infty$.

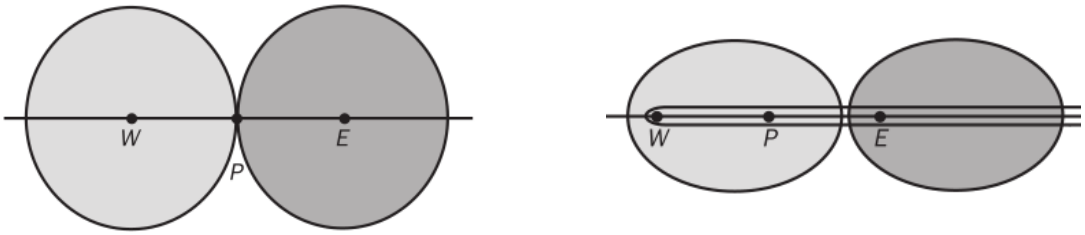

Figure 4.1: Transportivity effects. Below, sources are placed on points W and E. Extracted from Versteeg and Malalasekera (2007).

temperatures at its ends. It is expected that the computed intermediate values will be comprehended between those of the ends (Versteeg and Malalasekera, 2007). From a computational standpoint, this is related to the ease of reaching a convergent solution, or, alternatively, with the proximity of the resulting system of equations to a more diagonally dominant. Scarborough (1958) states that this property is associated with the algebraic coefficients of the system of equations resulting after the discretisation. Versteeg and Malalasekera (2007) points to the connection between boundedness and a non-converging solution, as well as the appearance of "wiggles" in what should be monotone solutions.

Transportiveness refers to the property of an interpolation scheme to consider the effect of a source on points of its surroundings. Roache (1976, apud Versteeg and Malalasekera, 2007) describes this property in terms of the Péclet number (Pe), a nondimensional quantity that assesses the importance of convective effects relative to diffusive ones. For an asymptotically diffusive flow ($Pe \to 0$, see figure 4.1a), sources placed on points W and E of figure 4.1 lead to omnidirectional effects on surrounding points; whereas the same sources put into an asymptotically convective flow ($Pe \to \infty$, see figure 4.1b) will affect just the immediate neighbours crosswise, and will have a much stronger effect upon points downstream relative to the purely diffusive flow. Other aspects will be discussed through the text, such as stability and convergence. A fuller discussion on these matters, as well as other properties, is found in Ferziger, Perić, and Street (2002).

Discretisation of the equation of motion

The Eulerian term $\partial U_i/\partial t$ of equation 4.1 is generally accurately discretised by means of central differences, providing second-order accuracy. The same does not hold for the convective term, unless for low Péclet number. Central differencing is an inadequate

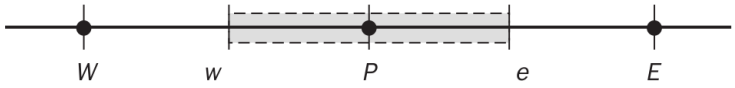

Figure 4.2: Cell scheme containing faces e and w of the control volume (or cell) P, and neighbour cells W and E. Extracted from Versteeg and Malalasekera (2007).

scheme for the convective term in highly convective flows because it is oblivious to flow direction, requiring $Pe < 2$ for accuracy. This creates the need for another scheme, such as the upwind, which weights the contributions of the point being solved in the numerical grid, and the point upstream. Originally, this form of discretisation was proven too diffusive, as a result of its first-order truncation error. This led to the need of the Total Variation Diminishing (TVD) schemes.

The concept of total variation is explained in Sweby (1984). It suffices to say that a monotone scheme is TVD; and TVD schemes preserve monotonicity. This means that "undershoots" and "overshoots" shall not appear in the solution, supplying numerical stability to the solution procedure. Furthermore, second-order accuracy is attained. Therefore, the best characteristics of the upwind and of the central differencing are absorbed in TVD schemes. There is a variety of these, that are pointed out in Versteeg and Malalasekera (2007) and in the references therein; this text shall strictly deal with the linear upwind and its variant, the Linear-Upwind Stabilised Transport (LUST) scheme. Both are improved versions of the upwind scheme for convective flows.

The linear upwind scheme is formulated as the following:

$$\phi_e = \phi_P + \frac{1}{2}(\phi_P - \phi_W) \tag{4.3}$$

where the symbol ϕ, commonly used in finite volume texts, represents some general scalar quantity to be solved (it can be either pressure, a component of velocity, temperature, etc). East and west faces of the cell associated with the (uppercase) point P are denoted (lowercase) e and w. Accordingly, the neighbouring east and west cell centres are E and W, respectively (see figure 4.2). The LUST scheme is a blend of 25% linear upwind and 75% central differencing.

With respect to the unsteady term $\partial U_i/\partial t$ of equation 4.1, different schemes have been suggested. Those that only use past information (explicit schemes), and those that also include the contribution of the current time-level (implicit schemes), into the system. Generally, implicit schemes are preferred in view of their better stability, allowing greater

time steps. Good examples are Crank-Nicolson (semi-implicit) and backward second-order scheme (fully implicit). Although both ensure second-order accuracy, the backward scheme is more stable and it is represented by:

$$\frac{\partial \phi}{\partial t} = \frac{1}{\Delta t}\left(\frac{3}{2}\phi - 2\phi^{0} + \frac{1}{2}\phi^{00}\right) \tag{4.4}$$

where ^{0} refers to the time level just before the one under consideration (that is, one time step size Δt before the current time instant), and ^{00} refers to that twice before (that is, $2\Delta t$ before the current time instant). Explicit schemes generally establish an upper limit to the time step size to respect the Courant–Friedrichs–Lewy (CFL) condition: It states that the Courant number, $Co = u/(\Delta x/\Delta t) < 1$ for negligibly diffusive flows, where u describes the velocity crossing the cell and Δx is the characteristic grid size. One interpretation to this condition is that the time step Δt should be small enough to capture the convective flow that crosses Δx, otherwise information is lost. Because of this condition, explicit schemes have limited use in incompressible flows. Detailed derivation of CFL condition is found in Ferziger, Perić, and Street (2002).

Now, for gradient terms such as the first term of the right hand side of equation 4.1, linear interpolation works well for structured gradients; while for unstructured grids the least squares gradient reconstruction is a popular choice (Versteeg and Malalasekera, 2007). In least squares the gradient is obtained indirectly through a second-order Taylor expansion of ϕ for neighbouring cells around a cell (say, P). A system of equations is obtained that allows for the calculation of the gradients in all directions determined by P and adjacent cells.

The same procedure may be conducted for the Laplacian term, since it can be interpreted as the divergence of the gradient. The divergence part is commonly conducted with a linear interpolant.

Once discretisation of the equations and of the domain is concluded a linear system of equations is derived.

Before further discussion, it is worth recalling that the general CFD solution procedure does not start with a given (converged) flow-field, with which the solution is merely marched on. Indeed, the solution may actually be unknown beforehand. Rather, arises the urge of an iterative procedure to transport boundary and initial conditions across the domain by means of transport equations iteratively until a state of convergence is

reached. This is a form of iteration present in finite volume schemes. Another concern is with pressure-velocity coupling.

4.3 Pressure-velocity coupling

One can see in equations 4.1 and 4.2 that p is absent in the second equation, and that it does not possess a transport equation (as U does). Actually, the velocity field is not univocally fixed by a single pressure; rather, it depends on the pressure gradient. The aforementioned equations depend only on the pressure gradient; thus, they are oblivious to the pressure field itself which is carried along. However, if the correct pressure field is applied, then the correct velocity field is obtained. Thus, the continuity equation establishes a constraint for the solution procedure.

Pressure-velocity coupling is commonly dealt with by means of the Semi-Implicit Method for Pressure-Linked Equations iterative algorithm (SIMPLE, Patankar and Spalding, 1972) and its variants. In a nutshell, Patankar and Spalding (1972) suggest that a merely guessed pressure field should be used initially to solve the Navier-Stokes equations in order to find the *guessed* velocity field. Then, expressions in the form below are to be assumed:

$$U = U_{guessed} + U_{correction} \tag{4.5}$$

$$p = p_{guessed} + p_{correction} \tag{4.6}$$

for U and p. The continuity equation is then rewritten in terms of pressure correction terms $p_{correction}$, so this quantity can be determined. Once the correction is found, it is applied to find the new pressure and later the new, consequent velocity and further scalars of interest (such as turbulent ones). In order to find the new velocity field, a correction term is plainly dropped in the Navier-Stokes equations, whose effect is null in a converged situation (because the correction terms would be zero). The solution procedure then continues, until the iteratively corrected pressure field is such that the velocity field resulting thereof satisfies continuity to a tolerance criterion.

To accurately use SIMPLE, Patankar and Spalding (1972) suggest the use of a staggered grid in order to avoid jigsaw patterns that may arise from the concurrent use of a collocated grid arrangement and finite differences, in the so-called *checker-board ef-*

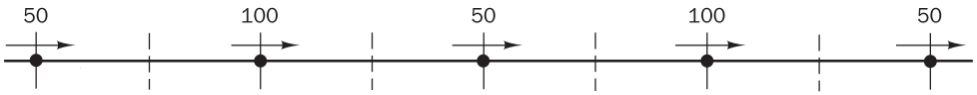

Figure 4.3: Checker-board effect on a pressure or velocity field, giving rise to unrealistic results. Gradients considering straddling points to 50 (or 100) give null result, indicating an incorrect uniform field with collocated grids. Extracted from Versteeg and Malalasekera (2007).

fect (Patankar, 1980). This effect is prompted by the dependence of pressure gradients on straddling points of P, but not on P itself. As an example, a non-uniform (and incorrect) pressure field may be treated as though it were uniform, when incorporated into the momentum equations with a collocated grid. The net result is an unrealistic velocity and pressure fields, such as the one shown in figure 4.3. Convergence is still achieved, although inappropriately.

This research uses Rhie and Chow's (1983) interpolation, whereby a third-order pressure term is included for the computation of face velocities, so the pressure itself is incorporated in the resolution, thus avoiding the aforementioned spurious oscillations. Amongst the advantages of this procedure, collocated and body-fitted grids can be used, storage is more efficient, and second-order accuracy is ensured. The proposed software of this project, Open-source Field Operation And Manipulation (OpenFOAM, Weller et al., 1998), performs this algorithm (and its implementation is described in Kärrholm, 2006).

It is worth highlighting that the SIMPLE algorithm corresponds to a steady condition of the flow. In comparison with the unsteady case, the steady SIMPLE must be applied within a time-step in internal iterations, and then the unsteady version (which takes into account the unsteady term in the momentum equations) is used to move the solution to the new time step in outer iterations. More details are found in Ferziger, Perić, and Street (2002) and Versteeg and Malalasekera (2007).

4.4 Solution scheme of the linear system

As it has been pointed out, iterative methods are abundantly used in finite volume methods. As a matter of fact, these are preferred over direct methods, as their memory overhead is lower. As an example, the vortex-panel method used in section 9.1 (detailed in appendix A), consumed over 15 gigabytes of RAM[2] to solve for the potential flow over a system as the one in figure 3.16 with a flow domain comprised of the order of

[2]Random access memory.

10^4 grid points using a direct method. In CFD applications the number of grid points commonly surpasses this number of grid points by at least one order of magnitude for three-dimensional (3D) applications (that, in addition, are generally time-dependent).

Ferziger, Perić, and Street (2002) point out to the character of slow convergence of iterative methods in fine grids. It is ascertained that the spectral radius of a matrix, which corresponds to the greatest absolute eigenvalue, directly impacts on the rate of convergence of an iterative process. Such a value can be measured by taking the error iterative matrix (Versteeg and Malalasekera, 2007).

We do not delve deeply into such matters. It suffices to state that iterative methods such as Gauss-Seidel lead to smoothing of error functions, annihilate rapidly-varying components of the error, and thus allow for faster convergence over the iterations. From one iteration to the next, the update of the error matrix is easier. This qualitative aspect, however, prevails strictly on coarser grids, because the long-wavelength errors are just about the order of the size of the elements. As a comparative note, Ferziger, Perić, and Street (2002) refer to the decrease in computational effort (as number of iterations) to be proportional to the square of the number of grid points, to clarify the motivation for the use of such a method. On the other hand, for fine grids, the convergence rate is much slower, as a result of the much greater long-wavelength errors compared with the characteristic size of small cells.

Methods like Gauss-Seidel in a coarser grid smoothen the error function and attain fast convergence. Some consideration must be given to ensure accuracy. This is accomplished by means of a multigrid method, through which different levels of refinement are applied. First a number of iterations is performed on the finest grid. The results are transported to the next, coarser, mesh by means of interpolation, where the residual is found (*restriction* operation). After successive restriction operations, the residual is returned in a backward operation, from the coarsest mesh to the consecutive finer mesh, interpolating where necessary.

The advantage of this method is that most of the effort is performed on coarser grids, where the solution is attained faster. Another feature is that the number of iterations on the finest grid is not a function of the number of points for a given convergence criterion. Usually, refinement and coarsening is made by a factor of two, by simply removing lines, and coefficient matrices are calculated by linear interpolation for the coarse grid from the

refined one, in what is called the *algebraic* multigrid method. OpenFOAM performs a more complex algorithm, called GAMG – Geometric Agglomeration Algebraic Multigrid, where coarsening is made through *agglomeration*, however the basic idea is the same as the one above.

5 Turbulence

One of the greatest challenges in the solution of fluid flows is to tackle turbulence modelling. The very description of the nature of turbulence is a difficult task. In the literature, authors tend to describe qualitative aspects of turbulent flows, rather than to depict turbulence itself, referring to its nature as diffusive, a continuum medium, comprised of random fluctuations, three-dimensional, dissipative, constituted by multiple scales; and so on (Tennekes and Lumley, 1972). In spite of its complexity, turbulence is the mainstream, not the particularity when one considers fluid flows. Correspondingly, laminar flows constitute exceptions.

Turbulence ubiquity draws strong interest to its understanding. Commonly, two parts are assumed to comprise quantities of the flow ($U,\ p$ in equations 5.1 and 5.2) in the so-called *Reynolds decomposition*: the first part is the mean flow ($\overline{U},\ \overline{p}$), and the other is the fluctuating part ($U',\ p'$).

$$U_i = \overline{U_i} + U_i' \tag{5.1}$$

$$p = \overline{p} + p' \tag{5.2}$$

(the different components are indexed by i.) Other turbulent quantities can be formulated analogously. For application purposes, one is frequently interested in the average behaviour of the flow over time rather than in the time history. As it is widely known in the literature, substitution of these relations into the Navier-Stokes equations (see equations 4.1) followed by their statistical averaging, lead to the formulation of the *Reynolds-Averaged Navier Stokes* (RANS) equations. A closure problem emerges, whereby the number of variables surpasses that of equations, due to the inclusion of turbulent fluctuations. Terms of the sorts of $-\rho U_i' U_j'$ appear in the equations. Physically, these additional terms correspond to turbulent (normal, for $i = j$ and shear, $i \neq j$) stresses, denoted

Reynolds stresses, which inherently come from the effect of turbulent fluctuations.

Ideally, an accurate model in the spirit of Newton's law – that relates stress strain and viscous stresses – would be desired to represent Reynolds stresses. Nevertheless, such *unique* model has not been found, in the sense that numerical results with the turbulence models at hand do not usually agree with experimental data to high precision. However, the analogy that turbulent stresses and rate of strain would be related as in viscous stresses was undertaken in 1877, resulting in the Boussinesq hypothesis,

$$-\rho\overline{U_i'U_j'} = \mu_t\left(\frac{\partial\overline{U_i}}{\partial x_j} + \frac{\partial\overline{U_j}}{\partial x_i}\right) - \frac{2}{3}\rho k\delta_{i,j} \tag{5.3}$$

still predominantly used nowadays to solve unsteady RANS equations embedded in closure models. In equation 5.3, μ_t, $\delta_{i,j}$ and k correspond, respectively, to the turbulent dynamic viscosity, to the Kronecker delta[1] and to the turbulent mean kinetic energy per unit mass ($=\overline{U_i'U_i'}/2$). The last term on the right-hand side of equation 5.3 is a correction term. It must be discerned that μ_t is a property of the flow, whereas μ corresponds to a property of the fluid. This difference constitutes one of the core difficulties in the use of the Boussinesq hypothesis as fluid flows vary case-by-case. As a side note, better hypotheses than Boussinesq's do exist, however, they do not generally provide the same level of numerical stability (e.g., Reynolds stress tensor models, Versteeg and Malalasekera, 2007).

We now present only a subset of the multitude of closure models that have been developed in the literature to tackle the difficulty of representing μ_t. We emphasise below seminal ones, including the SST k-ω, that was used in turbulence modelling to solve the closure problem in a URANS formulation; and the Spalart-Allmaras model, that beyond the latter aim, comprised a relevant part of the Detached Eddy Simulations employed in turbulent regime simulations.

5.1 Turbulence modelling

Tennekes and Lumley (1972) presented the mixing-length model, a one-equation model with severe difficulties, namely due to its assumption of one-scale-structured turbulence. This is not realistic, as turbulence necessarily contains several scales. The authors subsequently included the dynamics of turbulence, directly deriving equations for the transport

[1] $\delta_{i,j} = 1$ if $i = j$ and zero otherwise.

equation of turbulent kinetic energy k with the Reynolds decomposition and the Boussinesq hypothesis, which led to fruitful physical insights into turbulent processes. Analogous procedure was followed for the dissipation rate of turbulent kinetic energy. Nonetheless, the overwhelming mathematical complexity of the derived equation frustrates any attempt to use it for CFD purposes, or to measure some of the terms therein for calibration of models.

Turbulence closure models[2] usually replace these transport equations by more convenient approximations to handle numerically or measure experimentally (for the calibration of numerical models); and incorporate the best of qualitative knowledge of turbulent processes into them, including production, dissipation, diffusion and convection. Equilibrium in production and destruction of turbulent kinetic energy is also often assumed, even though it is unrealistic for boundary layers under adverse pressure gradient. This is carried out in the k-ϵ model just as much as in more advanced models, such as k-ω, Shear Stress Transport (SST) k-ω model, and so on. ϵ is the rate of dissipation and ω is proportional to ϵ/k. An eddy viscosity expression is obtained by dimensional analysis considering length scales of the flow (Tennekes and Lumley, 1972).

Some constants are also incorporated into the model equations, in order to calibrate models to benchmark experimental data, usually conducted over different turbulent flows. A pertinent limitation of the success of this procedure is pointed out in Versteeg and Malalasekera (2007) for cases with adverse pressure gradient. Under these circumstances, closure models usually overpredict levels of turbulent shear which become especially problematic in curved surfaces. In such cases, separation of the boundary layer is forcefully and incorrectly delayed, due to the increased diffusion of momentum. This is the cornerstone problem of RANS, because as the problem steers away from that of a zero pressure-gradient flow over a flat plate (where such models usually work well), the models tend to fall short of accuracy.

The k-ω model follows the same derivation as the k-ϵ model. However, a different length scale is formulated, using the specific rate of dissipation instead of the rate of dissipation. Menter (1992) observed that the k-ϵ and the k-ω models complemented each other. The k-ϵ model solves well the flow away from the walls; but requires the placement of the first node sufficiently far from the wall to avoid $\mu_{t,\text{wall}} \to \infty$ from the definition of μ_t

[2]We shall refer to these models as "closure models" or "turbulence models".

(suppressed here). Generally, there is great appeal to resolve the near-wall region, because of the boundary layer, so, to require this specification on the location of the first node is a downside of the model. The k-ω model allows the imposition that the turbulent kinetic energy zeroes in on the wall, however the model strongly affects the results depending on free-stream initial and boundary conditions, as once again singularity shows up from the imposition of null values for the turbulent kinetic energy and for the turbulent frequency. The SST k-ω model brings together the advantages of the k-ϵ and k-ω models, so that the transport equation for the rate of dissipation leans toward the k-ω model close to the wall, whereas in the far-field the k-ϵ capacity is retrieved. This is presented in a series of papers, started in Menter (1992).

One of such papers is that of Menter (1994) where the blending is presented. In the viscous sublayer and logarithmic region of the boundary layer the k-ω model is used; and, away, the formulation allows switching to the altered k-ϵ model. One of the constants' main goals within the blending function is to promote this switch of models in the wake region of the boundary layer, to achieve more accurate separation. Another constant, according to the author, is "to account for the transport of the principal turbulent shear stress in adverse pressure gradient boundary layers" and such "principal shear stresses" correspond to those proportional to the turbulent kinetic energy. In terms of computational cost, the SST k-ω model demands just as much time as the reformulated k-ω version of Wilcox (2008). Appropriate boundary conditions are given by the following (including updates of Menter, Kuntz, and Langtry, 2003):

$$U_\infty/L < \omega_\infty < 10U_\infty/L \tag{5.4}$$

$$10^{-5}U_\infty^2/Re < k_\infty < 0.1U_\infty^2/Re \tag{5.5}$$

$$\omega_{\text{wall}} = 10\frac{6\nu}{\beta_1(\Delta d_1)^2} \tag{5.6}$$

$$k_{\text{wall}} = 0 \tag{5.7}$$

where $\beta_1 = 0.075$ and Δd_1 is the size of the first cell next to the wall.

Another important model is that of Spalart and Allmaras (1992), a one-equation model for the turbulent viscosity, mostly dedicated to external aerodynamics. Spalart-Allmaras model was built "from scratch", as the authors referred to it, and calibrated thereafter in a sequential manner, starting from the less complex case of shear-layer flows up to viscous

flows with laminar regions, nesting one after another. This procedure is not trivial by any means. In this process, the authors adjusted new terms, functions and constants, leading to the following equation:

$$\frac{D\tilde{\nu}}{Dt} = c_{b1}(1-f_{t2})\tilde{S}\tilde{\nu} + \frac{1}{\hat{\sigma}}\left\{\frac{\partial}{\partial x_k}\left[(\nu+\tilde{\nu})\frac{\partial\tilde{\nu}}{\partial x_k}\right] + c_{b2}\frac{\partial\tilde{\nu}}{\partial x_k}\frac{\partial\tilde{\nu}}{\partial x_k}\right\} - \left(c_{w1}f_w - \frac{c_{b1}}{\kappa^2}f_{t2}\right)\left(\frac{\tilde{\nu}}{d_{\text{wall}}}\right)^2 \tag{5.8}$$

where d_{wall} is the distance from the wall, with constants given by:

$$\begin{aligned} &\tilde{\sigma} = 2/3,\ \kappa = 0.41,\ c_{b1} = 0.1355,\ c_{b2} = 0.622,\ c_{w2} = 0.3,\ c_{w3} = 2,\ c_{v1} = 7.1 \\ &c_{w1} = c_{b1}/\kappa^2 + (1+c_{b2})/\tilde{\sigma},\ c_{t3} = 1.2,\ c_{t4} = 0.5,\ c_s = 0.3 \end{aligned} \tag{5.9}$$

In the expressions below, f_{v2} and f_w are damping functions:

$$\chi = \tilde{\nu}/\nu,\ f_{t2} = c_{t3}\exp(-c_{t4}\chi^2),\ f_{v1} = \chi^3/(\chi^3 + c_{v1}^3),\ f_{v2} = 1 - \chi/(1+\chi f_{v1}) \tag{5.10}$$

$$\tilde{S} = \max\left\{\left|\frac{\partial U_i}{\partial x_j} - \frac{\partial U_j}{\partial x_i}\right| + \frac{\tilde{\nu}}{\kappa^2 d_{\text{wall}}^2}f_{v2},\ \ c_s\left(\frac{\partial U_i}{\partial x_j} - \frac{\partial U_j}{\partial x_i}\right)\right\} \tag{5.11}$$

$$f_w = g\left[\frac{(1+c_{w3}^6)}{(g^6+c_{w3}^6)}\right]^{1/6},\ g = r + c_{w2}(r^6 - r),\ r = \min(\tilde{\nu}/\tilde{S}\kappa^2 d^2,\ 10) \tag{5.12}$$

The following equation retrieves the relationship between the turbulent dynamic viscosity (ν_t) and the turbulent dynamic viscosity parameter ($\tilde{\nu}$):

$$\nu_t = \tilde{\nu} f_{v1} \tag{5.13}$$

In Spalart and Allmaras (1992), the authors included an additional tripping term to force transition. In time, it was found that its usage is not advisable in general; and has been avoided since then (Travin et al., 2000; Vatsa, Lockard, and Spalart, 2017). Furthermore, the equation of $\tilde{S}$ did not contain the right term within the max function or this function at all; this is rather a numerical adjustment for stability.

This model captures well boundary layers with adverse pressure-gradient and considers the decay of eddy viscosity away from the surfaces. Wilcox (1998) shows that the Spalart-Allmaras model provides good results for mixing-layer and far-wake; this is in agreement with the purpose of Spalart Allmaras' model – aerodynamic applications. Versteeg and Malalasekera (2007) warn against the use of this model in general flows where

the characteristic length scale is not easily defined.

Besides the "standard" version (Spalart and Allmaras, 1992), other variants of the Spalart-Allmaras model were created. A variant of the standard version which neglects both the trip term and its correction provided by the f_{t2} term (imposing $c_{t3} = 0$ in equation 5.12) is often used, embedded in a DES formulation (see below).

The appropriate boundary conditions are those of Spalart (2000) and Vatsa, Lockard, and Spalart (2017) for $\tilde{\nu}$:

$$\tilde{\nu}_{\text{wall}} = 0 \tag{5.14}$$

$$3 < \tilde{\nu}_{\infty}/\nu_{\infty} < 5 \tag{5.15}$$

5.2 URANS limitations and the drive for LES and DES

In spite of all the efforts toward turbulence modelling, the use of the Boussinesq hypothesis implies isotropy of the eddy viscosity, in disagreement with experimental validation: Accentuated limitations can be placed on RANS modelling for flows over bluff bodies, where the geometry of the body leads to a strong pressure gradient, separation and a wide spectral distribution of turbulent structures. The resulting large eddies contribute most to the production of turbulent kinetic energy. Indeed, in this case, the scale of the large eddies is proportional to the distance between separation points (roughly equal to the characteristic length of the body D) and are quite anisotropic. These structures' behaviour is distinct from the universal features of small scales.

Emphasis must be placed on the misrepresentation supplied by 2D URANS applications for the flow about cylinders, where perfect correlation of the eddies impart overestimation of the lift and drag, ruling out spanwise effects. In fact, adequate correlation falls short even in 3D URANS formulation, as it is shown in figure 5.1 with Q-contours[3].

Large-scale eddies carry the gross of the budget of kinetic energy, retain low vorticity content, behave inviscidly and anisotropically, and depend on the boundary conditions of the mean flow, from which energy is extracted. The contrary to all these assumptions prevail for the small scales. Viscous dissipation occurs at the smallest scales, also termed the *Kolmogorov microscales*.

[3]As a side note, we simply surmise that the Q-criterion captures well gradients of the velocity, and thus allow for the detection of turbulent structures. Its use and formulation are reviewed in Freire (2015).

Figure 5.1: 2D (top) and 3D (bottom) SST k-ω URANS modelling. Excessive levels of correlation are reported in turbulent structures in the wake. Adapted from Spalart (2009).

Vortical dynamics dictates that spectral energy transfer occurs from the large scales to the small ones through a nonlinear mechanism (Tennekes and Lumley, 1972). Spectral energy transfer starts with the large scales, which extract energy from the mean flow by means of vortex stretching. Since they behave inviscidly – because their Reynolds number, based on appropriate characteristic scales is high – viscous dissipation does not occur significantly. But they roll up, and due to conservation of angular momentum, their characteristic length reduces, thus resulting in the spectral energy transfer from large eddies to small ones ("inviscid dissipation", Tennekes and Lumley, 1972). About the order of the Kolmogorov microscales, viscous dissipation finally occurs, since the local Reynolds number is then low. This is to say that appropriate resolution of turbulent large scales on the flow over bluff bodies is of vital importance, as it affects the whole flow structure. One of the shortcomings of closure models used in RANS is that all eddies are considered to behave in the same way. Alternative formulations to tackle the solution of the flow, without losing the physics of large scales are provided by Large Eddy Simulation (LES) and Detached Eddy Simulation (DES).

The motivation for LES is frequently regarded to principally account for the behaviour of different scales and to achieve accuracy with reasonable computational costs (when compared with Direct Numerical Simulation, DNS). In order to do so, the formulation takes advantage of the universal behaviour of small scales, which are mostly isotropic and locally invariant. As a consequence, the Kolmogorov microscales, for example, are not resolved in LES, in order to avoid excessive refinement and the longer run time resulting thereof that would otherwise be required (as in DNS), but modelled instead. A schematic representation of scales resolved by LES and DNS are shown in figure 5.2.

Large Eddy Simulations involve the spatial filtering of the turbulent scales. The inspiration for doing so is to filter in scales that must be resolved as it would in DNS, but to dispense with the computation of scales smaller than some cutoff. Small-scale effects are considered by means of Sub-Grid Scale (SGS) modelling. The resolved part of the Navier-Stokes equations is derived in Versteeg and Malalasekera (2007) and the process to model the SGS stresses is found in Wilcox (1998). In the latter, an example is given of a backward facing step that LES required 3% of grid points and 2% of the time required by DNS. Amongst the normalised filter kernels used, a simple one is the box-filter, along with a cut-off volume, which has to be at least greater than the minimum cell size. Scales

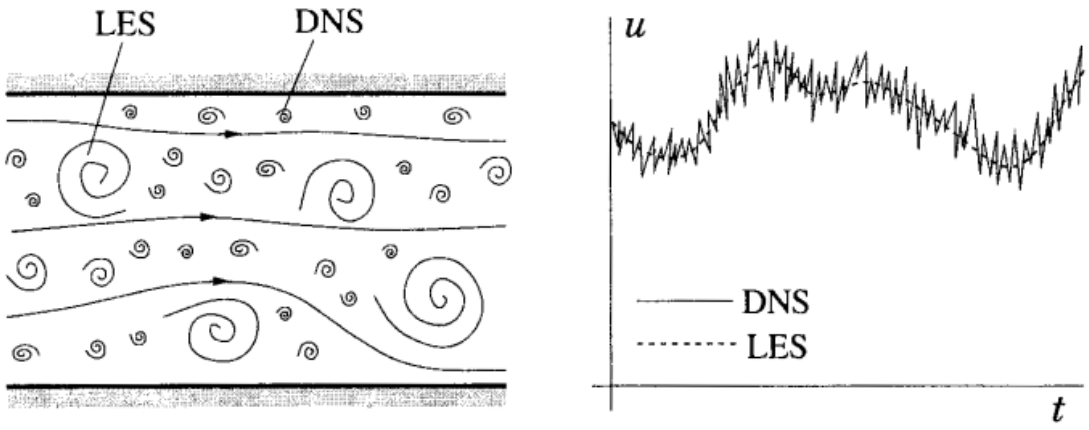

Figure 5.2: Comparison between LES and DNS. The former resolves medium and large scales, while the latter concerns even with the Kolmogorov microscales (left) regarding low-scale fluctuations in variables of the flow (right). Extracted from Ferziger, Perić, and Street (2002).

lower than this cutoff fall into the modelled SGS Reynolds stresses, which translate the effect of small eddies.

One of the most famous SGS models, elaborated by Smagorinsky (1963), states that SGS Reynolds stresses are proportional to the strain rate of the large eddies through the eddy viscosity (which is modelled by dimensional arguments). Guidelines for obtaining expressions for the Smagorinsky model are found in Ferziger, Perić, and Street (2002). Limitations and alternatives to this SGS model are also in the same reference. The main problems are related to i) calibation of the model, that depends only on a constant to describe turbulent viscosity, and ii) to its purely dissipative nature for the resolved eddies, because the model assumes that turbulent kinetic energy is transferred only from large resolved eddies to SGS ones, and does not incorporate backscatter effects.

Appropriate calibration of the Smagorinsky's model posed a case-by-case requirement that is not fulfilled, and has been reported to result in inaccuracy (as in any other empirical formulation, such as the ones above for other purposes), because it was based on a single universal constant. Amongst the attempts made to improve the Smagorinsky coefficient (the calibrating constant in the SGS model) that determines the eddy viscosity, the most successful so far has been the Dynamic SGS model of Germano et al. (1991), whereby this coefficient is computed dynamically along with the simulation. Through the use of two filtering operators, the grid filter and the test filter, the authors devised a model independent of *ad hoc* damping or intermittency functions, that were used to adjust the classical model of Smagorinsky (1963) near the wall. Additionally, the modelled SGS eddies' dissipation of turbulent kinetic energy matched that of resolved eddies, thus dealt

with backscatter, an often neglected phenomenon in previous models.

Despite considerable mitigation of the computational cost provided by LES against DNS, LES is still a demanding formulation due to the requirement of very refined meshes, its strongest disadvantage.

Spalart et al. (1997) criticised LES and closure models, on the basis of a conservative estimation of grid points and precision required for the computation of the flow over an airliner wing. LES requires a refined mesh and short time steps. URANS simulations, on the other hand, even in the idealised case of an overly refined grid still leads to pathological results, due to its inherently modelled nature. DES was then presented in the paper, a solution that is midway between turbulence modelling of RANS and LES. In this new formulation, the detached eddies (away from the boundary layer) are resolved by means of LES, inasmuch as the attached eddies fall into RANS turbulence models.

The idea presented by the author is to use the Spalart-Allmaras one-equation turbulence model instead of the Smagorinsky's SGS model for the determination of the turbulence in the near-wall region. By scaling arguments, it is shown that the eddy viscosity parameter $\tilde{\nu}$ is analogous to the SGS version ν_{SGS}. The difference between the two is that Smagorinsky's model uses the filter length scale, whereas Spalart Allmaras' model uses the distance from the wall. To adjust this, it is suggested to use then a length scale (l_{DES}, equation 5.16) which switches from one to the other, appropriately. Besides this, Spalart et al. (2006) included a low-Reynolds correction (Ψ, equation 5.17):

$$l_{DES} = \min(\Psi C_{\mathrm{DES}}\Delta,\ d_{\mathrm{wall}}) \tag{5.16}$$

$$\Psi = \min\left\{10^2, \left[1 - \frac{1-c_{b1}}{c_{w1}\kappa^2 f_w^*}(f_{t2} + (1-f_{t2})f_{v2})\right][f_{v1}\max(10^{-10}, 1-f_{t2})]^{-1}\right\} \tag{5.17}$$

where Δ is the largest dimension of the cell and the calibrating constants are given by

$$\begin{aligned} C_{\mathrm{DES}} &= 0.65 \\ f_w^* &= 0.424 \end{aligned} \tag{5.18}$$

in addition to equations 5.9 and 5.12.

Spalart et al. (1997) work specified the usage of the Spalart-Allmaras model close to the wall, and Smagorinsky's SGS model away from it. Only one constant is used, which is related to Smagorinsky's SGS part, that ideally would be set conforming to homogeneous

turbulence. It is also to be noted that, unlike URANS, and alike LES, DES with more refined meshes tend toward DNS, as it is illustrated in figure 5.3. In another respect, it is important to emphasise the use of the Spalart-Allmaras model as the "closure model part" for DES, for its capability to resolve flows with separation and adverse pressure gradient boundary layers, its most relevant strength.

The main detrimental aspects of DES formulation with the Spalart-Allmaras model were reviewed as (Spalart, 2009):

1. when the distance from the wall closes in to Smagorinsky's cut-off size, eddies might be confusedly resolved either by URANS or LES formulation, creating a "nonmonotonic response of DES to grid refinement" in what is called the *grey area*;

2. large separation regions are not well captured by URANS (in general, not only with the Spalart-Allmaras model[4]);

3. modelled-stress depletion, a situation such that the grid does not allow URANS resolution of the boundary layer, yet eludes a LES solution, leading to grid-induced separation;

4. slow switch from URANS to LES in mixing-layers in cells of high aspect ratio.

However, in view of the extensively discussed unrealistic results provided by URANS, and the more demanding requirements of LES, DES prevails as a promising formulation for general CFD, and a valid approach toward the solution of the flow over bluff bodies.

[4]We have not detected this to be a problem in our results.

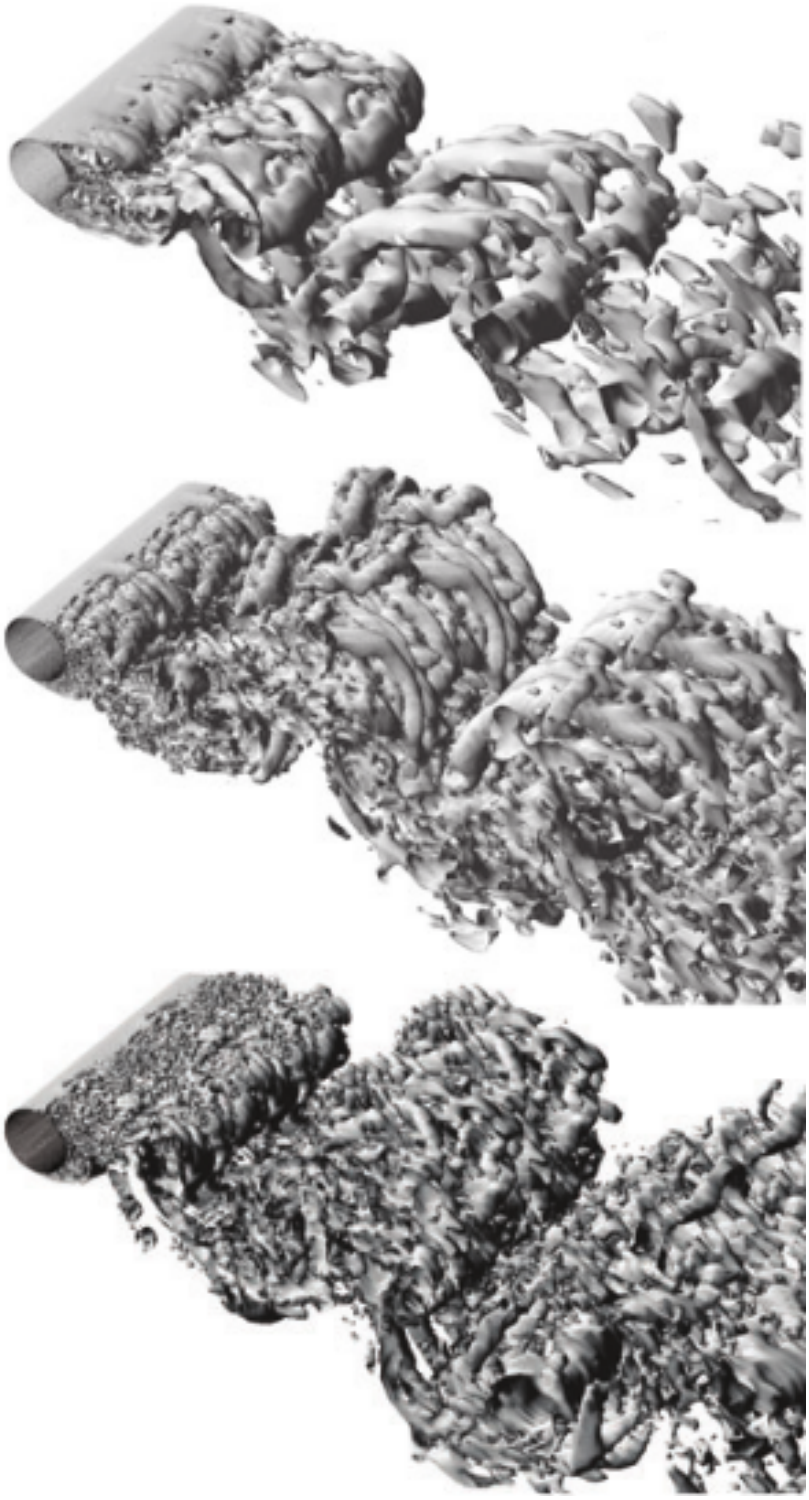

Figure 5.3: Increasing levels of refinement from top to bottom, accentuating DES tendency toward DNS with shortening of cell sizes. Adapted from Spalart (2009).

6 Methodology

The present research focuses on the system of figure 2.1 with different levels of simplifying assumptions, displayed in figure 6.1. In general, laminar regime at $Re = 100$ was considered first in simulations (without free-end or free-surface effects, represented in figure 6.1a) because of the lower requirements in terms of grid refinement, domain size, number of relevant state variables and faster analysis. Indeed, in such geometries, the flow is 2D, its solution hinged only on the velocity and pressure, and the flow complexity is much lower than in turbulent regime. These simulations were stepping stones toward infinitely-long, turbulent, ones at $Re = 1000$, which involved three-dimensional domains[1], as depicted in figure 6.1b, and involved variables associated with turbulence modelling. The attribute of omnidirectionality of these two cases was also explored (with different α). After these setups, finite cases were considered. The passive mechanisms of figures 6.1c and 6.1d were evaluated. The former refers to a setup with two free ends of a fully submerged body; the latter to a case where one end was free, while the other was attached to a free surface. Finally, the active mechanism was assessed, but only for the latter finite case of the geometry exhibited by figure 6.1d.

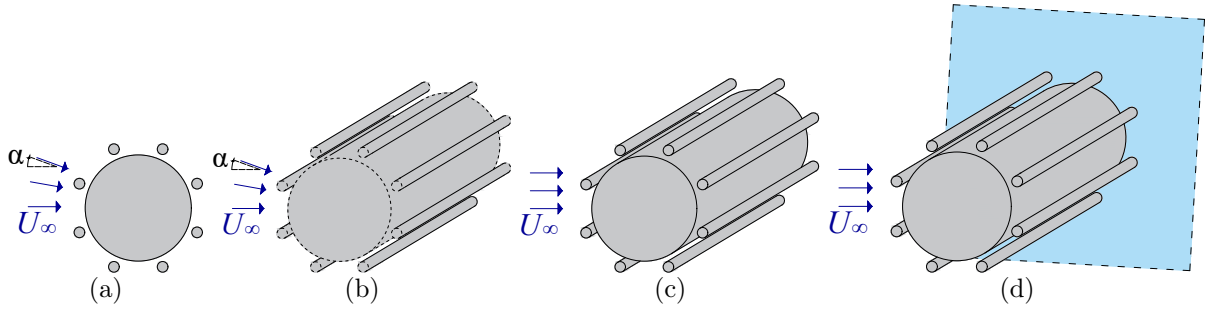

Figure 6.1: Different geometries. Infinitely-long cases were considered in a) 2D laminar, and b) 3D turbulent regimes. Finite bodies were considered in turbulent regime under c) free-end, and d) also free-surface effects. Different angles of attack α were investigated in a) and b).

[1]It is common to refer to these infinitely-long simulations as "two-and-half dimensional", or "2.5D" because the grid is entirely made in a 2D domain, that is then extruded spanwise.

6.1 Problem description

An incoming flow U_∞ reached the arrangement comprised of a main body P_0 of diameter D fitted with an active-control device. The control mechanism was exerted through eight slender rods of diameter $d = D/20$, that spun about their respective axes with angular velocities ω_n to inject momentum into the outer flow about the entire system. These rods were distant from the wall of the main body by the gap $G = D/100$. Upper rods P_1, ..., P_4 spun clockwise with the same magnitude, but opposite direction to that of the lower rods P_1', ..., P_4', so that $\omega_n = -\omega_n'$, $n = 1, \ldots, 4$. Wake-control rods were deliberately positioned away from stagnation regions by 22.5° and uniformly distributed, so consecutive rods were separated by a 45° angle.

The number $N = 8$ of control rods followed the most successful configuration in VIV suppression found by Silva-Ortega and Assi (2017a). The selected gap was that of greatest mitigation of VIV response and drag carried out in the parametric study by Silva-Ortega and Assi (2017b). The chosen diameter d was based on the work of Korkischko and Meneghini (2012), which produced enough interaction with the shear layers of the central body at a local low Re based on the rod diameter.

Figures 6.1a and 6.1b refer to infinitely-long bodies in laminar and turbulent regimes. In the former, the bodies were modelled with $L/D = 1$, while in the latter, $L/D = \pi$. We emphasise that these quantities, in these specific cases, were not related to physical meaning, but rather to numerical requirements. $L/D = 1$ was used in laminar regime simulations, because OpenFOAM considers all simulations as three-dimensional, whereas this laminar regime flow is actually 2D. Any other ratio $L/D > 0$ could have been used. For infinitely-long, but turbulent cases, $L/D = \pi$ has shown to be a good compromise between size mesh (and thus computational effort) and adequate results (Travin et al., 2000; Assi, Orselli, and Silva-Ortega, 2018). For finite cases, all cylinders were modelled as finite bodies of low aspect ratio, with length $L/D = 2$, thus end effects were considered, and in this case the length was indeed physically meaningful.

Regarding possible wave interactions on a real free surface, we verified beforehand that the Froude number based on the cylinder's length (given by $Fr = U_\infty/\sqrt{gL}$, where g is the gravitational acceleration) for the finite cases was inferior to 0.23. As seen in section 3, wave effects are not significant at this Fr; thus, they were disregarded.

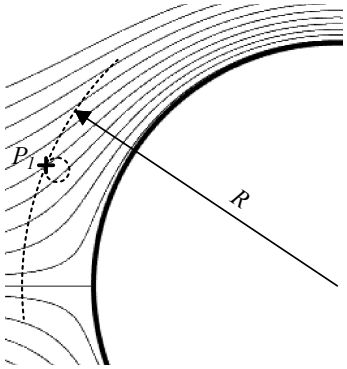

Figure 6.2: Potential flow about a bare cylinder: Within this flow configuration, streamwise velocities were computed at positions corresponding to the outmost point (relative to the centre of the system) that would be located on the surface of the rods. We emphasise that in this flow, the rods were not placed; thus justifying the representation of P_1 by a dashed line.

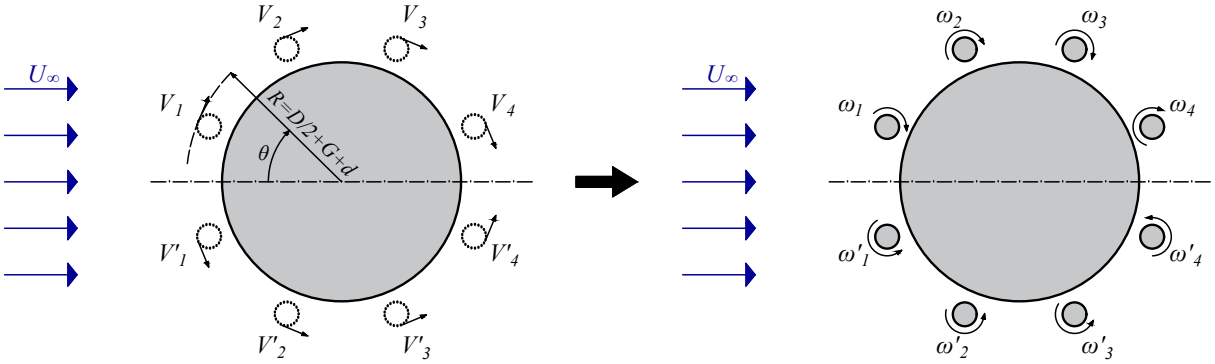

Figure 6.3: Velocity vectors computed from the potential-flow field (left) at points located in polar coordinates $r = R = D/2 + G + d/2$, $\theta = \pm 22.5° \pm (n-1)45°$, with $n = 1, \ldots, 4$ were assigned as equivalent angular velocities to the rods (right).

6.2 Definition of rotation rates

The angular velocities imposed to the rods were obtained from a potential-flow analogy. For this derivation, we considered the polar coordinates $\theta = \theta_n = \pm 22.5° \pm 45°(n-1)$ (see the convention for θ in figure 2.1) and $r = R = D/2 + G + d$ that mark the farthest point located on the surface of the rods relative to the centre of the entire system, depicted by figure 6.2. At these points, the streamwise velocity components V_1, V_1', ..., V_4, V_4' were calculated from the potential flow about a bare cylinder, as illustrated in figure 6.2 (that is a closed-in view of figure 6.3). Note that figures 6.2 and the left of figure 6.3 *strictly* contain the plain cylinder (the rods were represented by dashed lines solely for clarity sake of the aforementioned outmost point on their surfaces). These same velocities, obtained in *potential* flow for a *bare* cylinder, were consecutively imposed in *viscous* flow for the *entire system* to the control rods in two ways (see the right of figure 6.3).

- For the study on the active mechanism for finite bodies (section 9.4) and those on the omnidirectionality of the system (sections 10.1 and 10.2), these potential velocities matched the angular velocities $\omega_n = V_n/(d/2)$ of the rods. For the latter infinitely-long cases a further constraint was imposed, so the system inspired by potential-flow velocities (hereby denoted "case 1") and another, with uniform angular velocities (hereby denoted "case 0"), had the same input kinetic energy. These two constraints together fixed the angular velocities of case 0, while case 1 was based directly on the potential-flow velocities.

  Since in general,

$$\mathbf{V}_n = U_\infty \left\{ \hat{r}\left[\cos\left(\theta_n\right)\right]\left[1 - \frac{(D/2)^2}{\left(D/2+G+d\right)^2}\right] + \hat{\theta}\left[-\sin\left(\theta_n\right)\right]\left[1 + \frac{(D/2)^2}{\left(D/2+G+d\right)^2}\right]\right\}, \tag{6.1}$$

  and the equalities

$$\|\mathbf{V}_1\| = \|\mathbf{V}_1'\| = \|\mathbf{V}_4\| = \|\mathbf{V}_4'\| \tag{6.2}$$

$$\|\mathbf{V}_2\| = \|\mathbf{V}_2'\| = \|\mathbf{V}_3\| = \|\mathbf{V}_3'\|. \tag{6.3}$$

  held in infinitely-long setups due to symmetry and $\omega_2/\omega_1 = \omega_3/\omega_4 = 2.42$. The input kinetic energy constraint was given by:

$$\left[8\omega_0^2\right]_{\text{case 0}} = \left[\sum \omega_n^2\right]_{\text{case 1}} \tag{6.4}$$

  fixed the velocities of case 0. For finite bodies, only case 1 was considered.

- For infinitely-long bodies with fixed angle of attack, $\alpha = 0$ (of sections 9.1 and 9.2), the ratio between velocities was considered instead in case 1 (while the two cases were kept with the same input kinetic energy as explained above). Now, however, the velocities of case 0 were proportional to the incoming flow; and the velocities of case 1 were adjusted according to these constraints (that is, same input kinetic energy and following the proportionality from potential flow), so that

$$\left[\sum \omega_n^2\right]_{\text{case 1}} = \left[8\omega_0^2\right]_{\text{case 0}} \tag{6.5}$$

  fixed the velocities of case 1.

It may be noted that the computation of the velocities in potential flow introduced only two magnitudes of velocities due to the symmetry, specified by equations 6.2 and 6.3. To modify the rotation rates proportionally (for any setup with the active mechanism), the parameter ζ, a "velocity gain", was employed, so that instead of $V_n/(d/2)$, the velocities became $\zeta V_n/(d/2)$ for ζ ranging from 0.0 (passive setup) to 5.0 depending on the analysis. Numerical details are presented next.

6.3 Vortex-panel method - inviscid simulations

The potential flow about the main cylinder and the 8 peripheral control rods was calculated by means of the vortex panel method in section 9.1. The classical vortex panel method commonly applied to lifting bodies Stevens et al. (1971) allows one to solve the flow over multiple bodies in a cost-effective manner. Based on the work of Hess and Smith (1967), the surface of the cylinders were discretised into closed polygons of vortex panels over which the circulation density varied linearly and was continuous across the vertices of the panels (boundary points). The strength of the vortices over each panel met the following criteria: (i) the no-penetration boundary condition was satisfied at the midpoint of each panel (control points), so the surface of the body was approximated by a streamline of the flow; and (ii) the sum of the circulations over the panels that make up each body delivered the total circulation of the respective body, related to its angular velocity.

The velocity potential at a single control point was defined by the superposition of the uniform flow and the effect of the vortices located at all panels representing the main cylinder and the control rods. As the circulation varied linearly over the panels, its effect was conveyed to a single control point by means of integration over the entire panel. Null velocity was imposed to every control point in the normal direction to the panel so that the no-penetration condition could prevail. The produced circulation was associated with the angular velocities of the control rods. All these boundary conditions, put together with the velocity potential, allowed for the solution of an algebraic system, delivering the circulation at the boundary points. Note that this modelling differs from that generally adopted, as in Kuethe, Chow, and Fung (1987). Broadly speaking, panel methods are usually applied to aerofoils, where a Kutta condition can be imposed at the trailing edge.

Finally, the Biot-Savart Law was applied to solve for the entire velocity field induced by the circulations acting over the panels. Fluid forces acting on the elements were calculated by integrating the pressure field obtained from the Bernoulli equation on the surfaces.

6.4 Finite volume - viscous simulations

Essentially the same numerical scheme was applied to the different simulations employed in this work, except by the nuanced differences explicited otherwise. We anticipate that the numerical scheme of the laminar regime simulations is described in section 9.1 and references therein, so it will be not be repeated here.

The governing equations 4.1 and 4.2 were solved through a finite-volume discretisation with OpenFOAM, an open-source C++ library, at Reynolds numbers $Re = U_\infty D/\nu = 100$ and 1000 based on the main cylinder diameter D. We note that this nondimensional based on the rods' diameter was given by $Re_d = U_\infty d/\nu = 5$ and 50 (about the onset of vortex shedding), respectively. It may be anticipated that, as it will be explained in the papers, vortex shedding did not occur in the wake of the rods, as expected, considering the active mechanism of rotation studied by Mittal and Kumar (2003).

In order to ensure quality results, all terms hereby discretised followed second-order accuracy interpolants. A fully implicit backward scheme was employed for the (Eulerian) transient term $\partial U_i/\partial t$ of the left-hand side of equation 4.2, while for the (Lagrangian) convective term $U_j \partial U_i/\partial x_j$ a blend of the linear upwind and central scheme was employed (based 25% on the former, and 75% on the latter) in turbulent regime, called LUST (see section 4.2) in the aforementioned library, except for the O-grid simulations in laminar regime of section 10.1, where the linear upwind scheme was used. Gradients were obtained based on a least squares method. Because our numerical scheme was cell-centred, interpolation of values to the surface of the cells was carried out with linear interpolation. Both structured and unstructured regions contained elements whose centres were not aligned perpendicularly relative to the interface between them, thus, it was necessary to impart a non-orthogonality correction to the surface normal gradient (along with the Gauss theorem) to solve for the skewness of the mesh. This procedure also allowed computation of the Laplacian term.

A known issue in the solution of incompressible flows is the coupling of velocity and

pressure, described in section 4.3. To avoid this issue, these variables were solved together through the unsteady version of the SIMPLE algorithm. Residue tolerances of 10^{-4} for the solution of the pressure and 10^{-8} for the velocity components and other scalars were required for convergence at each time step, with the further requirement of at least 10 outer loops at each time step. For infinitely-long turbulent simulations a tighter tolerance of 10^{-6} was employed for the solution of the pressure for the flow over the plain cylinder. Significant difference was not noted between this tighter criterion and the former, so for simulations of the entire system, 10^{-4} was deemed acceptable and required in the simulations for convergence (except for those of section 9.1, where 10^{-6} was maintained). Rhie and Chow's interpolation was used to prevent the *checker-board effect*.

In order to avoid information loss from one time step to another, time step size restrictions were enforced based on i) the rotation rate of the rods and ii) on the reference vortex shedding cycle of a bare cylinder. In such cases, the Strouhal period is specified with $T_S = (D/U_\infty)/St$ and the Strouhal number $St \approx 0.2$ in subcritical regime. Time steps were thus limited from above by 1/70 of the revolution of the rods and by 1/100 of the timespan of a shedding cycle.

A linear system was obtained after discretisation of all terms. After the solution of the linear system, the resultant forces were obtained through integration of viscous effects and pressure distribution over the surface of each body, and the components thereof, lift (F_L), side force (F_S) and drag (F_D) were obtained. Normalisation was made by $1/2\rho U_\infty^2 DL$ to get the lift, side force and drag coefficients C_L, C_S and C_D

$$\begin{aligned} C_L &= \frac{F_L}{\frac{1}{2}\rho U_\infty^2 DL} \\ C_D &= \frac{F_D}{\frac{1}{2}\rho U_\infty^2 DL} \\ C_S &= \frac{F_S}{\frac{1}{2}\rho U_\infty^2 DL} \end{aligned} \tag{6.6}$$

illustrated in figure 2.1.

6.4.1 Boundary conditions and meshing

Symmetry boundary conditions (no flow across) were imposed on the sides of the domains and on the free surface for finite bodies. This condition allows a non-null tangential

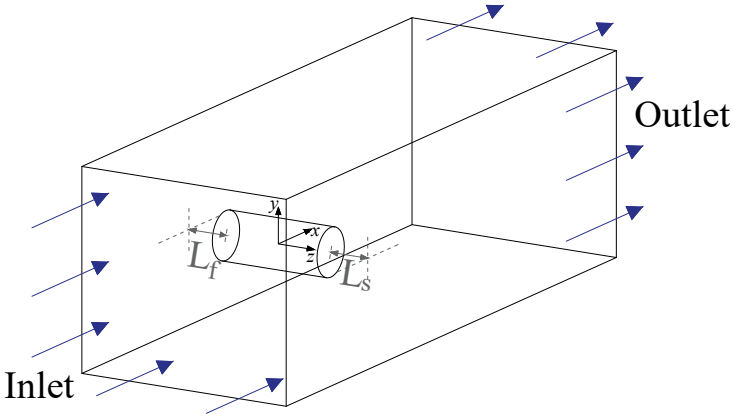

Figure 6.4: Simplified numerical domain. Only the main cylinder is represented for clarity.

velocity on the surface, so it is also termed a "slip" condition, but does not allow the flow to cross the respective side. For infinitely-long bodies, a periodic (or cyclic) condition was required to ensure this approximation on appropriate ends, so the flow leaving a side of the domain corresponding to an end of the cylinder entered the other side, corresponding to the other end. The walls of the rods adopted the rotation rates explained in section 6.2 for $\zeta \neq 0$, and no-slip condition was applied to their surfaces in all configurations of $\zeta = 0$ and $\zeta \neq 0$. For the main body, the no-slip condition with null velocity was ensured throughout the simulations. The inflow was specified by a Dirichlet condition[2], the far-field flow of fixed velocity U_∞, and a Neumann condition[3] corresponded to fully developed pressure gradient. Conversely, the outflow was prescribed by a Neumann condition on the velocity and Dirichlet's for the pressure. The simplified geometry of the domain, together with the indication of inlet and outlet patches is given by figure 6.4, in which L_s represents the distance from the system free end to the side of the domain. For the infinitely-long cases (in which $L_f = 0$ and $L_s = 0$) the sides of the cylinders (and the flow domain there) were linked by the periodic condition.

From the free end to the farthest side of the numerical domain, an adequate distance $L_s/D = 8$ was imposed to avoid blockage effects in the case involving a free water surface. For fully submerged bodies, $L_s/D = 8$ and $L_f/D = 8$. The centre of the main cylinder was distant $8D$ from the top and bottom surfaces, and from the inlet. A greater distance of $20D$ was applied between the main cylinder's centre and the outlet downstream. These dimensions for the grid geometry corroborated with the work of Behr et al. (1995), Behr

[2]The Dirichlet condition is such that the quantity under consideration is specified.

[3]The Neumann condition is such that the derivative of the quantity under consideration is specified, here in the direction perpendicular to the respective surface.

et al. (1991), and Kim and Mohan (2005) for infinitely-long bodies. A wider domain was investigated in section 9.2, and no significant changes were observed.

Hexahedral and prismatic elements covered the flow domain for finite bodies, and the mesh was the more refined the nearer it was to the bodies or to the wake region, to capture typical gradients of the flow directly associated with vortices and eddies. Away from the cylinders and from the wake were located regions where gradients typically approach null value and the flow asymptotically assumes fixed and fully developed boundary conditions. Toward these gradient-free locations the cells were enlarged. Expansion of the cells adopted ratios lower than 1.10 and 1.14 for the bare cylinder and system grids, respectively.

When end effects were considered, triangular-faced elements comprised part of the lateral surface of the main cylinder and of the rods. The extrusion of the side wall of these cylinders led to the need of unstructured, prismatic, cells away from the ends and into the free stream. While for infinitely-long bodies, only structured hexahedral elements were employed. Nevertheless, predominantly structured and hexahedral elements were used for finite-bodies analyses. Near the wall, this choice of element is appropriate because the boundary layer contains a strong velocity gradient transversely to the wall (although weak longitudinally).

For the simulations assessing omnidirecionality (sections 10.1 and 10.2), an O-grid geometry was preferred to allow different angles of attack α. In such cases, a no-slip condition was imposed on the walls of passive and rotating cylinders (here, the flow adopted the velocity of the spinning rod). For the inflow, a Dirichlet condition for the velocity and Neumann's for the pressure were specified; and the opposite for the outflow. This is expanded in the respective sections.

Considerations of grid convergence are in order. Mesh convergence study was carried out in all studies, both for the bare cylinder and for the entire system. Generally, mean drag and root mean square of fluctuating lift were the monitored parameters. In particular, we also verified mean pressure curves about the midsection of the main or bare cylinder; and the Strouhal number. We fixed the first cell in the radial direction near the bare cylinder to a size $D/1000$ as in Saltara, Neto, and Lopez (2011); whereas for the system, near the main body the same cell measured $1.54 \times 10^{-3}D$, and near the rods was $3.77 \times 10^{-3}d$. Away from the wall, the mesh was coarsed at different expansion rates and the

monitored quantities were assessed. We broadly regarded mesh convergence successful if the monitored quantities varied less than 10%, but this was not feasible for the RMS of lift, because it fluctuates strongly (both in numerical and experimental measurements, see Norberg, 2001).

In hindsight, we recognize, after personal communication with Prof. Dr. Leandro Salviano, that mesh convergence following Roache (1997) would have been a better and more systematic convergence criterion. Still, considering i) the present verification and validation, ii) qualities of the mesh, such as low values of maximum skewness and iii) aspect ratio; and iv) that we generally concerned more with the *tendencies* of the hydrodynamic loads and wake topology rather than the specific values associated to particular sets of angular velocities, we deem the present results valid. We also remark that for the larger meshes employed here, the aforementioned criterion would have been highly demanding in terms of computational resources. Nuances of grid convergence are given in papers presented in chapters 9 and 10. A final note is made here that the nondimensional parameter y^+ was kept under 1, so we dispensed with wall functions in turbulence modelling.

6.4.2 Turbulence models

It follows from the work of Carmo and Meneghini (2006) that 3D simulations are vital to properly incorporate the effects of vortical structures on the fluid loads for $Re > 190$. For cost-effective 3D simulations involving turbulence scales, the Detached Eddy Simulation (DES) formulation was elected (Spalart et al., 1997) for a good compromise between physical results and reasonable computational effort. This approach resolved the large (detached) eddies, while for the boundary layer RANS was employed. For small scales away from the boundary layer, the classical SGS model of Smagorinsky (1963) was used, whereas for the closure model part, the one-equation model of Spalart and Allmaras (1992) allowed for the transport of the turbulent viscosity parameter and related it to the turbulent viscosity. Moreover, this model allowed to capture separation and reversed pressure gradient.

A major problem in the DES formulation for the flow about cylindrical structures in subcritical regime is that the boundary layer is laminar whereas the wake is already turbulent (Williamson and Roshko, 1988), and the RANS formulation for the boundary layer is intrinsically turbulent. This downside was circumvented by a low-Reynolds correction

(Ψ, by Spalart et al., 2006).

Turbulence modelling was given by equations 5.9, 5.12, 5.13, 5.17 and 5.16 with parameters of equation 5.18. This full approach is shown to have worked well in section 9.2. It also exhibited satisfactory results at $Re = 10^4$, and in supercritical regime of $Re = 10^6$, see appendix B. Blockage effects were also assessed in the same appendix.

7 Main results

This thesis adopts the format of a compilation of thesis. We understand that it might be bothersome to refer to the results of each paper individually. Thus, in this section we summarise the results that are thoroughly described in chapters 9 and 10.

All active mechanism analyses started with a passive configuration, and then the rotation speeds were progressively increased. In a nutshell, this work may be described by figures 7.1 and 8.1.

In section 9.1, departing from a passive configuration, potential-flow-inspired angular velocities progressively larger were imposed to the system (that we denoted "case 1"). As a result, the spinning rods caused the formation of a progressively longer formation length and narrower wake width. Prolongation of the unrolled shear layers further downstream was also a detected effect. This caused the vorticity concentrated in the shear layers to be dissipated by viscous action. Upon roll-up of these shear layers, the vortices resulting thereof were thus weaker. Vortex-shedding was steadily suppressed, thereby accompanied by the attenuation of mean drag, mean lift and RMS of lift.

In comparison with an analogous setup akin to that of Assi, Orselli, and Silva-Ortega (2019), whereby the velocities were uniformly imposed on the rods (termed "case 0") at the same Reynolds number (Re) of 100, the system of case 1 required less input kinetic energy to suppress vortex shedding entirely; thus rendering this system more efficient. Faster vortex-shedding suppression was accompanied by lower oscillating loads generated upon the structure. In particular, under any configuration of the same input kinetic energy, case 1 consistently led to the production of lower mean drag upon the entire system, compared with case 0.

According to Patino, Gioria, and Meneghini (2017) following the analysis of Marquet, Sipp, and Jacquin (2008), by means of sensitivity analysis, an optimised distribution of

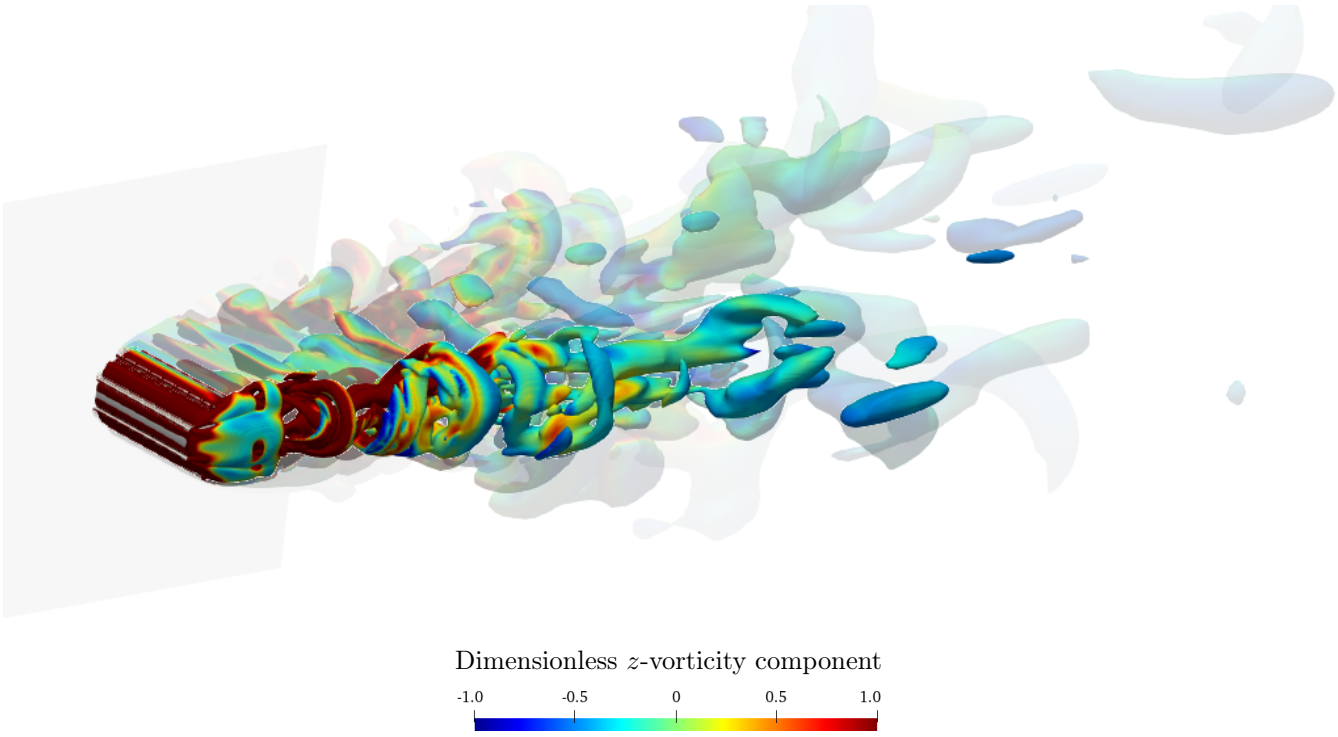

Figure 7.1: Our published results showed that this wake-control mechanism was capable of attenuating Kármán vortices even in finite bodies under the effect of a free surface. I.e., even in those setups where free-end and free-surface effects were present and led to a more complex wake than that found in infinitely-long bodies, the wake-control mechanism was capable of reducing hydrodynamic loads, in spite of the lasting tip vortices. Growing levels of opaqueness refer to sets of higher angular velocities.

control rods may reduce drag. Even though the *Re* based on the rods' diameter was still within that where Föppl vortices lied in the wake (Blevins, 1990) for a non-rotating rod, in agreement with the suppressing mechanism described by Mittal and Kumar (2003) intrinsically due to rotation, they did not emanate vortices. Yet, they collectively caused about a quarter of the total mean drag upon the entire structure. But their spinning mechanism was able to not only offset this uprise in mean drag, but also to lead the entire system to a downturn of the hydrodynamic forces that encompasses dampening of lift fluctuations. In fact, using the analysis of Shukla and Arakeri (2013), the decay of mean drag was such that it compensated the power spent to spin the rods. The system was able to produce a total power loss (comprised of that due to mean drag and due to mean shear on the wall) below that of the plain cylinder for infinitely-long bodies of sections 9.1 and 9.2 for laminar and turbulent regimes, respectively. Different from Assi, Orselli, and Silva-Ortega (2019), the mean drag was not reversed to become propulsion, but the observed steady downtrend leaned into this tendency. Nevertheless, to lower, and eventually to reverse the mean drag into propulsion, was bound to require a much greater power than to spin the rods against vortex shedding; in this fashion, case 1 lowered the power loss beyond case 0, related, principally, to the preference of case 1 to spin intermediate rods much faster than frontmost and rearmost rods, and much faster than the corresponding rods in case 0.

Thus, results showed that in any respect, the potential-flow-inspired arrangement of angular velocities for infinitely-long bodies in laminar regime enabled greater flow control than its counterpart with uniform velocities. Indeed, it was shown that this superior behaviour was due to the emphasis of case 1 given to the intermediate rods, that is, to those elements placed on the "shoulder"-regions (see figure 3.2) of the main body. Since these rods were placed adjacent to separation regions, to the shear layer detachment point and to the location of the onset of formation of the wake of the otherwise unsuppressed plain cylinder, they were within a region of utmost relevance to the vortex dynamics. Of course, all these shear layers are abundant in vortical content; to interact with them directly impacted the interplay of the opposite vortices (furthermore, in this 2D case the vortex formation followed closely the "bi-dimensional mechanism" of vortex formation explained by Gerrard, 1966).

Our paper of section 9.1 also exhibited slight similarities between viscous and potential

flows. Particularly, the potential flow anticipated the inversion of the mean drag (into thrust) upon the frontal rods and frontal intermediate rods. This was due to the increase in the speed within the gap that reduced the pressure there (directly verified through Bernoulli's relation).

These laminar regime simulations were vital to assess the flow response to this active mechanism. In view of these results, turbulent regime of $Re = 1000$ was also assessed for infinitely-long bodies in the paper of section 9.2. It was demonstrated that the three-dimensional turbulent effects affected the influence of the active mechanism on the nearby flow. Nevertheless, some similarities were observed. For example, the active mechanism of case 1 (with analogous definition to that used in papers of sections 9.2, 10.1, 9.4 and 10.2) was more efficient in reducing hydrodynamic forces and in achieving vortex-shedding suppression at lower requirements of power expenditure and input kinetic energy than case 0. Emphasis on specific control rods was the same as mentioned above, noted from the computation of the resulting hydrodynamic loads upon each individual rod. In this paper, we also found that the Strouhal number was affected. It was noticeable that the Strouhal number generally adopted higher values with faster rotations, up to suppression. This was linked to the fact that a shorter formation length and narrower wake diminished the distance between forming vortices. Thus, interaction between vortices occurred more intensely, although they contained lower levels of vorticity, compared with the plain cylinder.

Detached Eddy Simulations considering low-Reynolds correction were employed. Through Q-contours coloured by turbulent viscosity, it was noted that the active mechanism directly impacted this quantity, and led to the elimination of the eddies. Indeed, this turbulent-control mechanism led to the formation of ever more spanwise-correlated flow structures (a "laminarisation effect" through which the wake resembled a two-dimensional topology) with increasing rotation rates prior to suppression. This was further corroborated by visualisation of spanwise strucures; that enabled to observe the interference of the rods with the mechanism of streamwise vorticity transfer of vortex dislocations. These were expected to occur in a wake-transition regime ($230 < Re < 250$, Williamson, 1996), not in a subcritical one as it happened with the addition of the spinning elements.

In terms of power expenditure in turbulent regime, for these cases of infinitely-long bodies at a fixed angle of attack (aligned with the centreline of the system), the power-

loss coefficient remained below that of the plain cylinder (see the *Corrigendum* of section 9.2.1), in agreement with the study conducted in laminar regime. Yet, while case 1 presented a power-loss coefficient of 0.596 that of the bare cylinder, case 0 exhibited one just slightly below, of 0.963 that of reference case (thus much larger than case 1). Obviously, comparing the paper of section 9.1 with that of 9.2 (together with the *corrigendum* of section 9.2.1), the second required greater power to weaken the Bénard-von Kármán street.

The quality of omnidirectionality[1] of this system brought up by Assi, Orselli, and Silva-Ortega (2018), had not been studied prior to the present thesis. The study given in sections 9.1 and 9.2 remarked on the possibility that the frontmost and rearmost rods could perhaps be removed from the system for a fixed incoming flow direction aligned with the centreline of the system. However, care was advised, because this could impair the system response to other angles of attack. We tackled this issue in sections 10.1 and 10.2 in laminar and turbulent regimes of $Re = 100$ and 1000, respectively. It was shown that case 0 indeed was susceptible to the directionality of the flow; while case 1 demonstrated a "more omnidirectional" behaviour, as it retained its capability to suppress vortex shedding and reduce hydrodynamic loads consistently, provided the angular velocities were those determined in potential flow and increased proportionally. In the arrangement of case 0, when the angle of attack was maintained fixed, suppression was still achieved in laminar regime with sufficiently high angular velocities due to the mechanism alluded by Mittal (2001), but the hydrodynamic loads were not attenuated. Rather, mean lift tended to increase for sufficiently high angle of attack due an imbalanced pressure distribution past the system. In case 1, there was an interchange of relevance between frontmost and rearmost rods as the angle of attack increased that was important to maintain a symmetrical mean vorticity distribution past the system to ensure null mean lift and lower mean drag. In general, we observed that mean lift was eliminated for infinitely-long structures in case 1.

Now, free-end and free-surface effects should be incorporated into the analysis to understand to which extent the rods could affect vortex formation; and what representativeness could be associated with the tip-vortices. Firstly, the passive mechanism was assessed and compared within the assumptions of infinitely-long bodies (case i), fully submerged bodies

[1] By "omnidirectionality" one must understand that lift and vortex shedding are suppressed at different angles of attack for the same system.

without free-surface effects (case ii); and another, where free-surface effects were considered as well (case iii); all at $Re = 1000$. This is given in section 9.3. It was verified that even though the hydrodynamic coefficients upon the finite structures were significantly lower than under the infinitely-long assumption, due to end effects, the passive mechanism was incapable of inhibiting vortex shedding or reducing force coefficients; rather, the contrary was noted for the latter, in the increase of these loads. Vortex shedding was weakly affected, with prolonged formation length. Even spanwise, the vortex dynamics presented a behaviour distinct from the Bénard-von Kármán street, as instead, a rather very small part of one shear layer was responsible for the cut-off of its opposite, and a major fraction of the shear layer was entrained and dissipated, contributing little to the interaction and formation of stronger vortices. Furthermore, these vortices became stronger in the presence of end effects; and even more, when the free surface was also present.

In contrast with the infinitely-long studies above, greater relevance of the frontal rods and negligible importance of the rear ones were remarked in regard to individual contributions of the different slender bodies comprising the passive mechanism.

Finally, the active mechanism was addressed for finite bodies (see sections 9.4 and the *Erratum* in section 9.4.1). In this paper, the active mechanism effect was corroborated: from time-averaged contours, we detected that the reduction of the wake width, formation length, and intensity of the velocity fluctuations, with utter elimination of the part of the wake associated with the Bénard-von Kármán street. As a consequence, the mean drag and RMS of lift of the entire system were reduced to values below that of the bare cylinder. In general, we observed that mean and RMS lift were not eliminated, but remained near zero for finite structures subjected to free-surface effects using this potential-flow-inspired set of angular velocities.

In spite of these achievements in flow control, tip-vortices shaped like rings, and the corresponding side force remained, even at the upper end of the fastest rotation rates. Although the active mechanism did not consistently affect these ring-like vortices, when one compares them before and after suppression of the bulk of the wake, a decay of 5.5% in side force became evident. While turbulent eddies lost vorticity by viscous dissipation, they were able to draw vorticity from smaller structures that were carried along. This mechanism was interrupted partially as the Bénard-von Kármán wake was suppressed.

The mechanism of formation of these ring-like vortices is expanded in section 9.4 with further details. We just emphasise that at the upper end of the angular velocities assessed in this study, the free-end vortices were "induced" to a reversed motion as the active mechanism injected sufficient momentum into the near flow; that was transmitted to free-end vortices by viscous traction.

Efficiency of the entire system, analysed on the basis of power-loss coefficient (Shukla and Arakeri, 2013), rendered clear that in order to mitigate mean drag, power expenditure was key to counteract mean drag for finite structures. Our analysis also corroborated with previous studies, in that the component of power loss associated with wall shear stress was the main source of power-loss, and became dominant as the rods spun fast enough. Power-loss coefficient was 27% and 98% above that of the bare cylinder to reduce in 57% and 66% the mean drag, respectively.

8 Conclusion

This thesis adopts the format of a compilation of thesis. Here we present in a nutshell the results expanded by the papers of chapters 9 and 10.

We have advanced on the matter of wake control for infinitely-long and finite bodies, subject to free-end and free-surface effects in laminar and turbulent regimes of Reynolds 100 and 1000, respectively. In order to do so, we carried out finite volume simulations to assess the flow about a system consisting of a circular cylinder of diameter D, fitted with eight slender rods of diameter $d/D = 1/20$. The rods were placed distant from the main body by the gap $G/D = 1/100$. Rods and main body were of equal spanwise length. Passively, these rods were fixed to the body, while actively, they rotated about their own axis at their fixed position.

One might speculate that in an optimal setup of angular velocities, suppression of the wake in viscous fluid would be achieved closing in a potential-flow state: The flow about the entire system would be steady and unaffected by mean drag. This insight allowed for the determination of potential-flow-inspired angular velocities for the rods ("case 1").

To evaluate the active device supplied with increasingly larger actuating power, the rods were put in faster motion, proportionally. Two setups were evaluated: one in which the rods spun with case 1 velocities and another, with uniform rotation speeds ("case 0"), analogous to Assi, Orselli, and Silva-Ortega (2019). We evaluated simulations at different angles of attack to assess the directionality of this system.

The active mechanism was capable of controlling vortex-shedding, but restricted to the vortex formation mechanism proposed by Gerrard (1966); and better control was found in case 1, with higher efficiency, in comparison with case 0. Under different angles of attack, case 1 also demonstrated to behave omnidirectionally, a finding that is particular to this research. Previous studies neither considered the present system under different

directions of the incoming flow nor the set of potential-flow-inspired rotations.

In general, we have found that intermediate rods play a crucial role in the active mechanism, principally because they interact with the most relevant regions of the outer flow; and regions of high concentration of vorticity of the otherwise plain cylinder. Frontmost and rearmost rods relevance was found in the exchange of their contributions to the hydrodynamic loads acting on the entire system as the angle of attack increases; this allowed the potential-flow-inspired system to sustain null mean lift and consistent reduction in mean drag. This was not previously observed. In fact, we verified that these systems (akin to case 0) caused the increase of mean lift and drag depending on the combination of angular velocities and angle of attack, although suppression was attained either way, provided the rods were imparted with sufficiently fast revolutions.

Novel studies on finite bodies with such active mechanism were also conducted, to find that the proposed wake-control mechanism did not have the same impact in tip-vortices or in the part of the wake generated by them, as it was detected for the Bénard-von Kármán street. For the passive case relative to the infinitely-long one, end effects lowered mean drag and root mean square lift; led to a less coherent wake topology; the frontal rods concentrated most of the hydrodynamic loads; the formation length was increased; and, although all cases developed larger hydrodynamic loads when the rods were fitted to the main body compared to the plain cylinder, the finite cases produced a lower increase.

As for the active mechanism of finite bodies, steady reduction of mean drag, and less significant mitigation of root mean square of lift and mean side force were verified to occur for the entire system and for the central body. However, the side force proved less affected by the wake-control mechanism. We demonstrated this to be associated with a novel ring-like vortex that prevailed throughout the simulations. As in the infinitely-long case, vortices were better correlated with larger angular velocities, notwithstanding this novel vortex structure was not eliminated.

In all cases, we can surmise that to fit the passive rods to the main body causes an increase in mean drag upon the entire system due to the wider wake, and to provide the system with spinning rods leads to stronger wake control, insofar as it concerns with the suppression of the Bénard-von Kármán street component of the wake. For finite bodies, end effects were not harnessed by either passive or active mechanisms, because the vortex-formation mechanism differed to far greater measure from the classical vortices

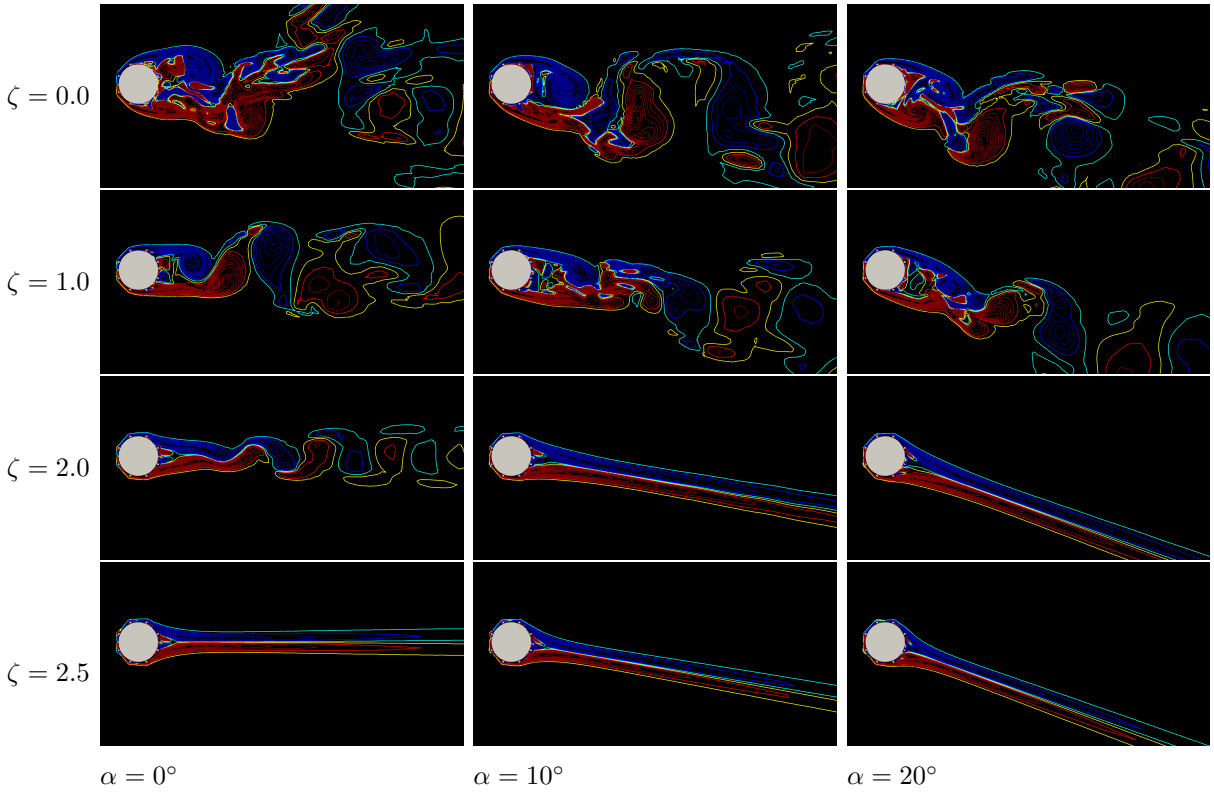

Figure 8.1: The wake-control mechanism not only showed able to attenuate vortex shedding, but also to provide consistent results when the angle of attack of the incoming flow was modified.

of infinitely-long bodies; and requires further study. Future works should concern with optimisation of the angular velocities to fully understand the realisable potential of the present system.

8.1 Future work

Future work should concern with the optimisation of this system to reach solutions of minimal mean drag and complete vortex suppression. Such a study could also be performed to produce useful mean lift. Such optimisation studies are bound to require massive computational resources, or adequate experimental apparatus, as it was done by Bingham et al. (2018) with a single rod. However, Bingham et al. (2018) did not deepen into the understanding of the vortex dynamics; an analysis that reserves merit and would add to the current state of information. A cheaper, but valid approach is to pursue the enhancement of such a system through artificial intelligence. Indeed, Fan et al. (2020) conducted such a study, also with one rod. To employ machine learning to the present system of eight rods could lead perhaps to a result that was not attained at present, that

of lower power loss for the system relative to the bare cylinder in turbulent regime for a finite system. Sensitivity studies concerning such optimal device would also attract attention of the scientific community.

Albeit VIV is rooted in vortex-shedding, the impact of the active wake-control rods upon a system subject to VIV could extend the understanding of this thesis to a flexibly-mounted system free to vibrate, that cannot be directly inferred from a fixed system, as it has been detected by Dolci and Carmo (2019), particularly depending on the reduced velocity.

The sensitivity of the present system yawed relative to the incoming flow would also be interesting; and would allow to put together the present results and those of Franzini et al. (2013).

Zhu et al. (2021) studied a quasi-active control method, that instead of requiring an external power input, extracts energy from the flow through two impellers. Such system could employ eight impellers; and an analogous study such as the present could be conducted upon it, or with a miscellaneous of the previous ideas.

Acknowledgement

The support of CAPES Brazilian Ministry of Education for the author's PhD scholarship is acknowledged under Finance Code 001. The author is also grateful for the support of FAPESP, Brazil (2011/00205-6) and CNPq, Brazil (306146/2019-3), and the RCGI Research Centre for Gas Innovation, hosted by the Universidade de São Paulo, Brazil and sponsored by FAPESP (2014/50279-4) and Shell Brasil. The HPC resources of the SDumont supercomputer at the National Laboratory for Scientific Computing (LNCC/MCTI, Brazil) are also gratefully acknowledged.

9 Published papers

Journal of Fluids and Structures 106 (2021) 103385

Contents lists available at ScienceDirect

Journal of Fluids and Structures

journal homepage: www.elsevier.com/locate/jfs

Wake control of a circular cylinder with rotating rods: Numerical simulations for inviscid and viscous flows

I.A. Carvalho [a], G.R.S. Assi [b,*], R.M. Orselli [c]

[a] Department of Mechanical Engineering, EPUSP, University of São Paulo, São Paulo SP, Brazil
[b] Department of Naval Architecture & Ocean Engineering, EPUSP, University of São Paulo, São Paulo SP, Brazil
[c] Department of Aerospace Engineering, Federal University of ABC, São Bernardo SP, Brazil

ARTICLE INFO

Article history:
Received 12 March 2021
Received in revised form 7 May 2021
Accepted 16 August 2021
Available online 8 September 2021

Keywords:
Vortex shedding
Suppression
Wake control
Drag reduction

ABSTRACT

This paper investigates the suppression of vortex shedding of a system comprised of a main circular cylinder surrounded by eight small rotating rods. Numerical simulations for an inviscid flow and a viscous flow at a Reynolds number of 100 have been performed. The rotation of each rod was controlled to promote the injection of momentum into the boundary layer and to mitigate the formation of vortices in the wake. Two cases have been investigated regarding the rotation speeds: case 0, in which all rods rotated at the same rate; and case 1, in which the rotation speeds were inspired by the potential-flow velocity field around a bare cylinder. Results showed that given enough rotation speed, both cases completely suppressed the formation of vortices, reducing the mean drag coefficient below that of a bare cylinder and mitigating fluctuating lift. Case 1 was the most efficient in reducing drag. Considering the system's total power loss, there is a range of rotation speeds capable of reducing the overall drag with minimum power spent to rotate the rods. It is worth noting that simulations with the inviscid flow captured an inversion of lift acting on the rotating rods that has not been verified to occur for the viscous flow.

1. Introduction

Offshore exploration of oil and gas in ultra-deepwater requires unconventional technologies to counteract the harsh operational conditions in the ocean. Some of the offshore structures employed for this purpose, such as risers and floating platforms (monocolumn and spar platforms, for example), comprise circular cross-sections. The fluid–structure interaction generated by the flow around such bluff structures leads to the well-known phenomenon of vortex shedding, possibly causing vortex-induced vibrations (VIV) depending on the dynamic characteristics of the systems.

The physical mechanisms of VIV have been investigated in many studies in the literature, summarised in the comprehensive review of Williamson and Govardhan (2004) and others. The present research suffices to recall that vortices shed behind a bluff body are convected downstream to form a Kármán wake, generating alternating fluid forces conveniently projected as lift and drag. These cyclic loads can excite the body into flow-induced vibrations with adverse effects such as undesirable high-amplitude oscillations, increased drag and structural fatigue. Active and passive methods to suppress or mitigate such phenomena are constantly under development. Some devices try to mitigate the response by tuning the structural parameters of the body, while others tackle the excitation mechanism at its root, interacting with the vortex-shedding process to prevent VIV.

* Corresponding author.
E-mail address: g.assi@usp.br (G.R.S. Assi).

https://doi.org/10.1016/j.jfluidstructs.2021.103385
0889-9746/

Passive methods commonly take the form of surface protrusions in risers and other cylindrical structures; helical strakes being the typical example. Strakes are quite effective in suppressing VIV from production risers, but their major drawback is a considerable increase in overall drag (Zdravkovich, 1981; Korkischko and Meneghini, 2011; Assi et al., 2021). Other passive VIV suppressors that interact with the formation of vortices (free-to-rotate fairings, for example) have been widely tested and optimised with the objective of reducing drag (Assi et al., 2009, 2014a,b). Active suppressors, in contrast, use energy to interact with the vortex formation mechanism and mitigate VIV. The balance between energy input and the energy saved due to vibration and drag reduction is an essential factor when evaluating the efficiency of the device. Active devices tend to be more expensive and complex in design, installation and maintenance, typically prohibiting their application in risers and other similar structures. But when larger systems are considered, such as huge floating platforms with bluff hulls, active VIV suppressors could play a significant role in mitigating the response with considerable drag reduction.

Strykowski and Sreenivasan (1990) showed (through simulations and experiments at $Re = 80$) that placing a smaller cylinder at an adequate location around the main cylinder can eliminate vortex shedding by properly reattaching the shear layers. This effect has also been verified by the numerical simulations of Mittal and Raghuvanshi (2001) and experiments with flexible shrouds performed by Cicolin and Assi (2017). More recently, Silva-Ortega and Assi (2017a) have investigated the efficiency of arrangements of 2, 4 and 8 peripheral rods in the range of Reynolds numbers from 5×10^3 to 5×10^5, varying their diameters and gap. These experiments revealed a 99% suppression of peak amplitude of vibration with an increase in drag of about 12%. Among active methods, a technique called "moving surface boundary-layer control" (MSBC) actuates in the wake of a circular cylinder by injecting angular momentum into the shear layers, imparted by the rotation of peripheral rods surrounding the main body. Mittal (2001) verified that the level of organisation in the wake at $Re = 10^4$ is enhanced when two control rods are applied, while a steady wake without alternating vortices is achieved at $Re = 10^2$. Assi et al. (2019) performed simulations of open-loop MSBC with eight rotating rods varying their rotation speed. They reported that a controlled wake without vortex shedding was obtained at $Re = 100$ when the rotating rods' tangential velocity was greater than 3 times that of the incoming free stream.

Most previous studies investigating MSBC with rotating control rods have imposed a uniform rotation speed upon all the peripheral rods. Assi et al. (2019) achieved wake control with all 8 control rods spinning at the same rate and observed that the topology of the flow around the main body resembled that of the potential flow around a circular cylinder. It is rather intuitive to think that the optimal rotation speed for each control rod will be different depending on its angular position around the main body. If one considers that the optimal flow configuration is that of a potential flow around a circular cylinder (with zero drag and no unsteady vortices), perhaps the tangential velocity of the control rods would have to be adjusted to induce a "potential-flow-like" velocity field around the main body. That is the hypothesis for the present investigation.

1.1. Objective

In the present work, we investigate the effect on the wake of different rotation speeds of 8 control rods placed around the main circular cylinder. Potential flow theory offers useful insight into the relationship between the rotation speeds that may suppress the formation of a vortex wake with minimum drag and energy consumption. The present study aims at understanding the physical mechanisms behind a different control strategy for such a device.

The hypothesis is that the optimal rotation speed of the peripheral control rods is not the same for all of them but depends on the angular position of the rod, aiming at producing a velocity field as similar as possible to that of a theoretical potential flow around a circular cylinder. Our objective is to evaluate if applying different rotation speeds to the control rods (inspired by the theoretical potential flow) the device is able to achieve wake control with drag reduction and less energy consumption when compared to the case in which all 8 peripheral rods are spinning at the same rotation speed. Hence, wake topology, drag reduction and energy consumption are the critical parameters in the present study.

2. Method

A main circular cylinder of diameter D is surrounded by 8 control rods of diameter $d = D/20$, equally spaced 45 degrees apart around the perimeter; a gap of $G = D/100$ separates the peripheral rods from the wall of the main cylinder (Fig. 1). The degree of flow control realisable by introducing rotating control rods relies on various parameters, as studied earlier by Korkischko and Meneghini (2011), Silva-Ortega and Assi (2017a,c), among others. Silva-Ortega and Assi (2017b) showed that amongst passive configurations with two, four and eight rods, that with eight control rods provided suppression of VIV under minimal effect of galloping, thus highlighting an omnidirectional property of the system. The ratio d/D has been chosen based on the previous experimental work of Assi et al. (2019). The incoming flow with velocity U is aligned with the frontal stagnation point so that no control rod sits at 0°. Each rod spins at a rate ω_n (defined in rad/s for the nth rod) and the direction represented by the arrows in Fig. 1(a). The tangential velocity (U_n) induced on the wall of the control rods is non-dimensionalised by the incoming flow speed producing the velocity ratio

$$\frac{U_n}{U} = \frac{\omega_n d}{2U}. \tag{1}$$

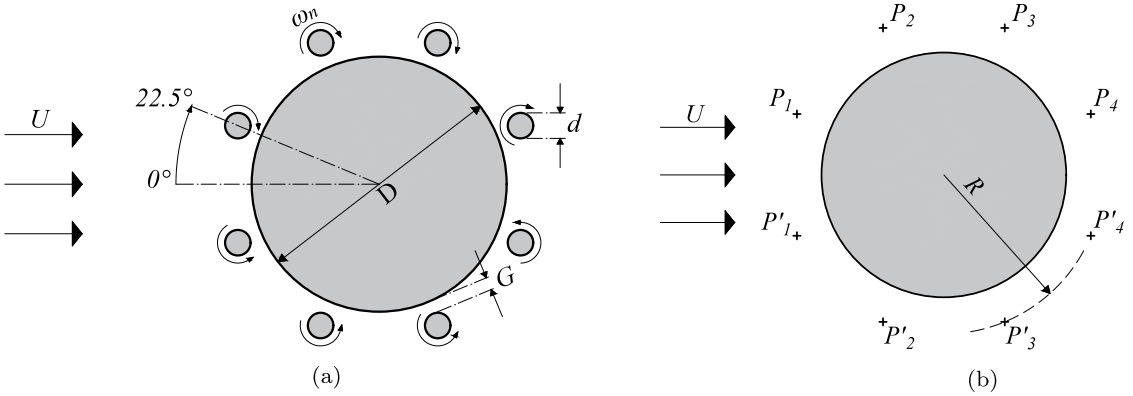

Fig. 1. (a) Geometric parameters of the main cylinder with 8 rotating peripheral rods. (b) Position of the reference points (P_n) for the potential-flow analogy.

Rotation speeds ω_n were set so that the tangential velocity on the wall of the control rods at the maximum radial distance ($R = D/2 + G + d$) from the centre of the main cylinder would respect the ratios obtained from the potential velocity field calculated for the flow around a bare cylinder with diameter D. Additionally, the total kinetic energy due to ω_n in cases 0 and 1 was the same. To investigate the overall variation of velocity magnitude over the flow, the rotation speeds ω_n have been multiplied by a "velocity gain" ζ, keeping constant the ratio ω_1/ω_2 that is equal to ω_4/ω_3, by symmetry.

The present paper now presents the canonical potential flow around a bare cylinder as a reference, followed by the inviscid flow solution for the system with control rods, and the viscous flow solution for the system with control rods at $Re = 100$.

2.1. Reference case: potential flow analogy

The canonical solution for the potential flow around the main cylinder was calculated yielding the reference velocities at a radial distance R and angles $\theta_n = \pi/8 + (n-1)\pi/4$ for $n = 1, 2, \ldots, 8$ (corresponding to the positions of the rods). The flow was modelled by the superposition of potential functions, imposing no penetration at the wall and far-field boundary conditions. The computed velocities are generally expressed in a polar coordinate system $(\hat{r}, \hat{\theta})$ by

$$\vec{v}_{P_n} = U\left\{\hat{r}\left[\cos\left(\theta_n\right)\right]\left[1 - \frac{(D/2)^2}{(D/2+G+d)^2}\right] + \hat{\theta}\left[-\sin\left(\theta_n\right)\right]\left[1 + \frac{(D/2)^2}{(D/2+G+d)^2}\right]\right\}, \tag{2}$$

where $\theta_1 = \pi/8$, $\theta_2 = 3\pi/8$, verifying the equalities

$$|\vec{v}_{P_1}| = |\vec{v}_{P'_1}| = |\vec{v}_{P_4}| = |\vec{v}_{P'_4}| \tag{3}$$

$$|\vec{v}_{P_2}| = |\vec{v}_{P'_2}| = |\vec{v}_{P_3}| = |\vec{v}_{P'_3}| \tag{4}$$

Due to symmetry, the relevant velocities to the problem are reduced to only two different magnitudes, corresponding to the absolute values of $\vec{v}_{P_1}$ and $\vec{v}_{P_2}$. Considering the $\hat{\theta}$-component of these velocities results in the ratios between rotation speeds $\omega_2/\omega_1 = \omega_3/\omega_4 = 2.41$.

2.2. Inviscid-flow solution: vortex panel method

The inviscid flow around the main cylinder and the 8 peripheral control rods has been calculated by the vortex panel method. Of course this could be achieved with simpler methods, but the implementation of a robust algorithm that can be employed with more complex geometries, multiple bodies, oscillatory and transient motions, for example, will contribute to the ongoing research effort.

Restricted to the inviscid problem, the classical vortex panel method commonly applied to lifting bodies (Stevens et al., 1971) allows one to solve the flow around multiple bodies in a cost-effective manner. Based on the work of Hess and Smith (1966), the surface of the cylinders has been discretised into closed polygons of vortex panels over which the circulation density varied linearly and was continuous across the vertices of the panels (boundary points). The strength of the vortices over each panel met the following criteria: (i) the no-penetration boundary condition was satisfied at the middle of each panel (control points), so the surface of the body was approximated by a streamline of the flow; and (ii) the sum of the circulations over the panels that make up each body delivered the total circulation of the respective body, related to its angular velocity.

The velocity potential at a single control point was defined by the superposition of the uniform flow and the effect of the vortices located at all panels representing the main cylinder and the control rods. As the circulation varied linearly over

the panels, its effect was conveyed to a single control point by means of integration over the entire panel. Null velocity was imposed to every control point in the normal direction to the panel so that the no-penetration condition could prevail. The produced circulation was associated with the angular velocities of the control rods. All these boundary conditions, put together with the velocity potential, allowed for the solution of an algebraic system, delivering the circulation at the boundary points. Note that this modelling differs from that generally adopted, as in Kuethe et al. (1987). Broadly speaking, panel methods are usually applied to aerofoils, where a Kutta condition can be imposed at the trailing edge.

Finally, the Biot–Savart Law was applied to solve for the entire velocity field induced by the circulations acting over the panels. Fluid forces acting on the elements were calculated by integrating the pressure field obtained from the Bernoulli equation around the surfaces.

2.3. Viscous-flow solution: finite volume method

Viscous-flow simulations were carried out employing the commercial code ANSYS Fluent 13.0 to solve the incompressible Navier–Stokes equations. The unsteady finite volume equations for the conservation of mass and momentum, presented here in integral form, are respectively given by

$$\int_S \vec{v} \cdot \hat{n}\, \mathrm{d}S = 0 \tag{5}$$

$$\int_\Omega \frac{\partial \vec{v}}{\partial t}\, \mathrm{d}\Omega + \int_S \vec{v}(\vec{v} \cdot \hat{n})\, \mathrm{d}S = -\int_S \frac{p}{\rho}\hat{n}\, \mathrm{d}S + \int_S \nu \nabla \vec{v} \cdot \hat{n}\, \mathrm{d}S, \tag{6}$$

where $\vec{v}$ is the flow velocity, p is pressure, t is time, ν is the kinematic viscosity, Ω represents control volumes of the system and S are the external surfaces of the control volumes with outward unit normal $\hat{n}$. Infinitesimal elements of the control volume and of the surface under consideration are represented, respectively, by $\mathrm{d}\Omega$ and $\mathrm{d}S$.

A cell-centred finite-volume method (FVM) was employed to discretise the equations in a computational mesh. The solution was based on an implicit pressure-based scheme, and the PISO (pressure-implicit with splitting of operators) algorithm was employed to couple pressure and velocity, which is known for its efficiency in solving unsteady problems. To obtain the pressure on the surfaces of the control volumes, an interpolation scheme based on a staggered grid arrangement (Patankar, 1980; Versteeg and Malalasekera, 2007) was assigned (this is known in ANSYS Fluent as PRESTO, pressure staggering option). Upwind second-order spatial differencing method was applied for the convective terms (following Barth and Jespersen, 1989) and the diffusive terms were discretised by central differences. The solution was advanced in time via an implicit second-order accurate scheme that implemented three-time levels incorporated within the PISO algorithm. All equations have been solved iteratively, for a given time-step, until convergence criteria were met. All residuals for each algebraic equation were less than 10^{-4} and 20 internal iterations were executed per time step.

A rectangular computational domain surrounded the cylinders with upstream, lateral and downstream boundaries located, respectively, at $8D$, $8D$ and $30D$ away from the main cylinder's centre, shown in Fig. 2. Despite its influence over the hydrodynamic coefficients (Behr et al., 1995), the computational domain was devised to minimise this effect upon the cylinders, offset by reasonable computational costs. The present mesh counted 89,310 cell volumes; similar but smaller computational domains have been successfully used in the literature (Mittal, 2001; Young et al., 2001; Goodarzi and Dehkordi, 2017). Moreover, a structured mesh fine enough to resolve the details of near-wall flow for all cylinders (including the rotating rods) was employed, and mesh convergence tests were conducted to evaluate mesh quality (omitted here for briefness).

Boundary conditions were specified for the velocity on the surface of the cylinders (*no-slip* condition), and free-stream values were assigned for the velocity at the upstream boundary. On the lateral boundaries, the component of the velocity normal to and the component of stress vector along these boundaries were set to zero. In contrast, for the downstream boundary, all variables were prescribed zero gradients. The numerical simulations were performed for enough time so at least six cycles of vortex shedding had occurred in a fully developed wake.

As seen in Fig. 1(a), the peripheral rods were disposed to preserve the symmetry of the flow and avoid the presence of a control rod at the frontal stagnation region. Their rotation directions and their rotation speeds were calculated as described in the sections above. Lift, drag and pressure coefficients were obtained by integrating the pressure field and viscous forces on the surfaces of the bodies, all normalised by $\frac{1}{2}\rho U^2 D$.

3. Results for an inviscid flow

The potential flow around a circular cylinder served as the idealised reference for the present investigation. The inviscid flow was solved by the vortex panel method and compared with the canonical analytical solution to validate the algorithm. The bare cylinder was discretised with 400 vortex panels, for which a residual of less than 10^{-6} was achieved for C_D and 10^{-5} for C_L. The pressure coefficient over the cylinder's surface ($C_p(\theta)$) showed good agreement with the analytical results.

Subsequently, the inviscid flow over eight peripheral rods fitted about the main cylinder at a gap $G = 0.01D$ was solved by the same vortex panel method. First, the rotation of the control rods was set to zero (no spin), then it was increased in steps keeping the ratio between the rotations inspired by the potential flow, as described above (case 1). Hence, the

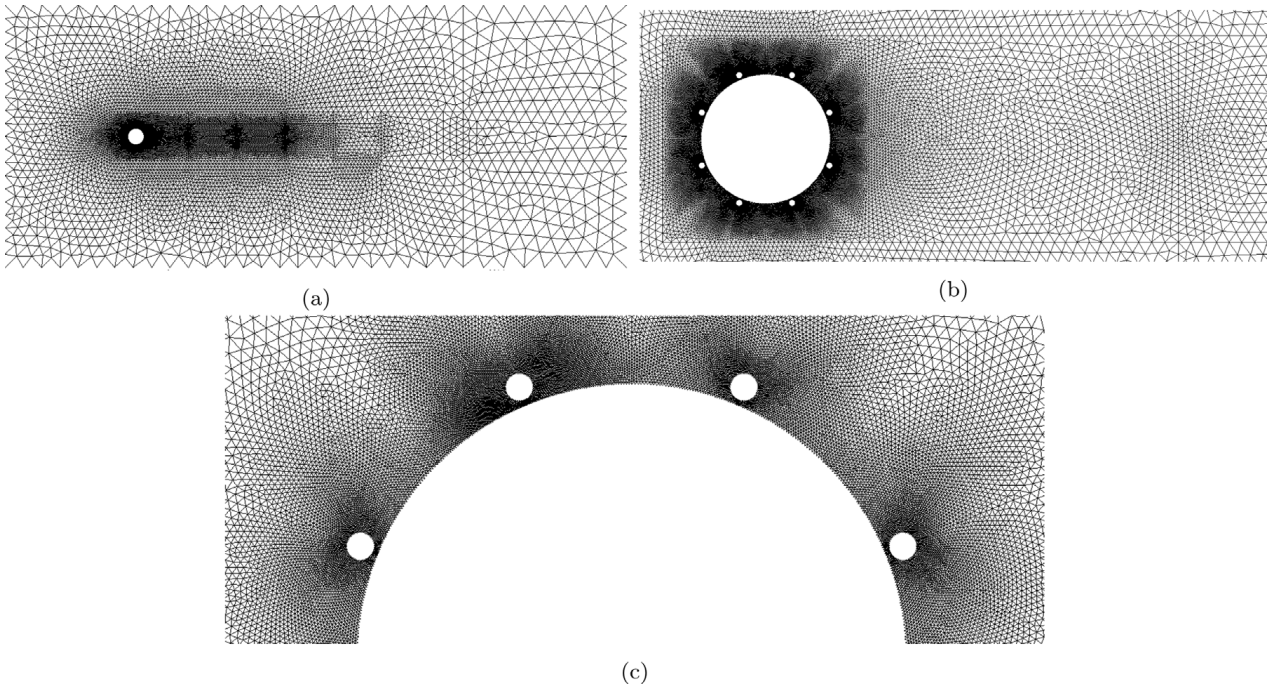

Fig. 2. (a) Mesh of the entire domain; (b) detail around the system of cylinders; (c) and detail around the upper peripheral rods.

rotation of the peripheral rods was controlled by setting the multiplier ζ from 0 to 3.5, a type of velocity gain, producing the tangential velocity $\zeta U_n/U = \zeta\omega_n d/2U$ for each rod.

The system was discretised with 2000 vortex panels for the main cylinder and 2000 panels for each rod. Convergence analysis was performed, and an error of 0.4% for the C_L of the entire system and a residual of 0.01% for the lowest value of C_p of the main cylinder were verified.

Fig. 3 presents the results in terms of streamlines coloured by velocity magnitude varying the velocity gain from $\zeta = 0$ to 3.5. As ζ was increased, regions of higher flow speeds appeared in the vicinity of the control rods induced by their rotation. The overall streamlines around the whole system remained symmetric, but a considerable change occurred around the rotating rods. Fig. 4 shows a detailed view of the flow around the control rod positioned at P_1. For $\zeta = 0$ the flow around the rod is only confined by the wall of the main cylinder, producing two stagnation points (marked by red dots) located on the wall of the rod. The lower pressure due to the compressed streamlines in the gap produced an inward radial force on the rod, represented by the small vectors acting on the rods for $\zeta = 0$ in Fig. 3.

Given enough rotation gain, say for $\zeta = 2.0$, the kinematic energy provided by the rotation of the rods was sufficient to reverse the flow in the gap (Fig. 4(b)), moving the two stagnation points away from the wall of the control rod, as marked by the two red dots. The velocity in the gap was reduced compared with the outer velocity field around the rod, increasing local pressure and producing an outward force on the rod. This is noticeable by the small vectors acting on the rods for $\zeta = 0.5$ to 3.0 in Fig. 3.

Finally, as ζ was further increased, the higher local velocity of the reversed flow in the gap reduced local pressure even further, as seen for $\zeta = 3.5$ in Fig. 4(c). The force on the rods turned inwards again, as illustrated by the vectors for $\zeta = 3.5$ in Fig. 3. This double change in the direction and magnitude of the lift force acting on the rods is evident for the inviscid flow regime as ζ increased from 0 to 3.5. The resultant force upon the whole system (comprised of the main cylinder and the peripheral rods) was negligible, as expected considering the symmetry of the system's inviscid flow field.

Now, if the gap between the control rods and the cylinder wall is increased, this double change in the direction of lift acting on the rods is affected. Fig. 5 presents similar results for a system of cylinders in which G/D was increased to 0.075. The general behaviour of the flow is rather similar to that observed for the smaller gap, with negligible overall drag and lift acting on the whole system. But the behaviour of the local flow around the rotating rods is substantially different. For $\zeta = 0$ the radial force acting on the rods points inwards, as the confined flow between the walls reduces the local pressure. However, as soon as the rods start to rotate, a region of lower pressure appears on the opposite side of the rods, resulting in an outward radial force that increases in magnitude from $\zeta = 0.5$ to 3.5. In other words, the larger $G/D = 0.075$ is too wide for the rotation of the rods alone to create enough lower pressure in the gap. It is reasonable to think that the second inversion might occur for higher rotation speeds for this specific gap.

Results obtained for the inviscid flow with the vortex panel method, especially those presented in Fig. 3, will be compared with those for the viscous flow simulations presented below.

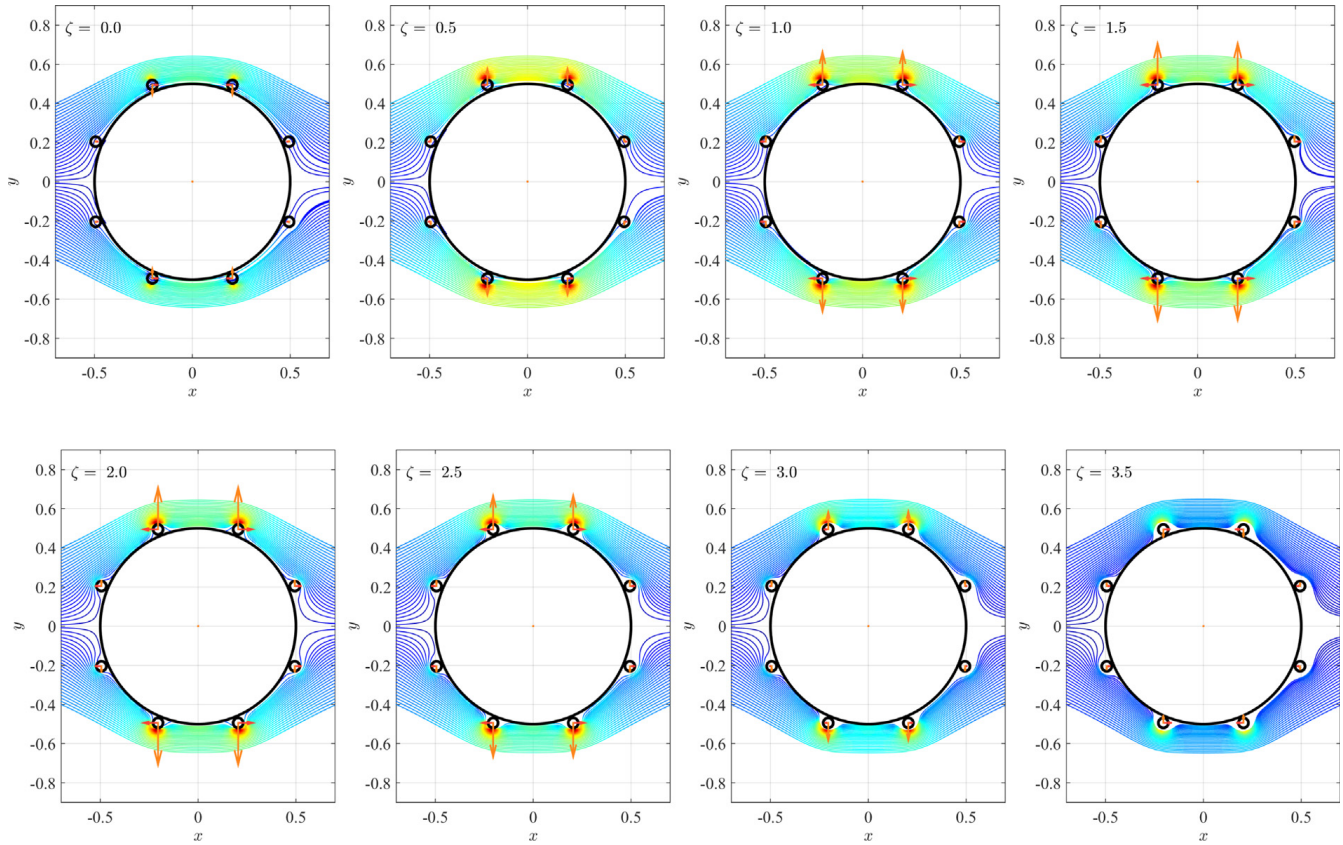

Fig. 3. Streamlines of inviscid flow (coloured by velocity magnitude) and forces on the rotating rods. $G/D = 0.01$. (For interpretation of the references to colour in this figure legend, the reader is referred to the web version of this article.)

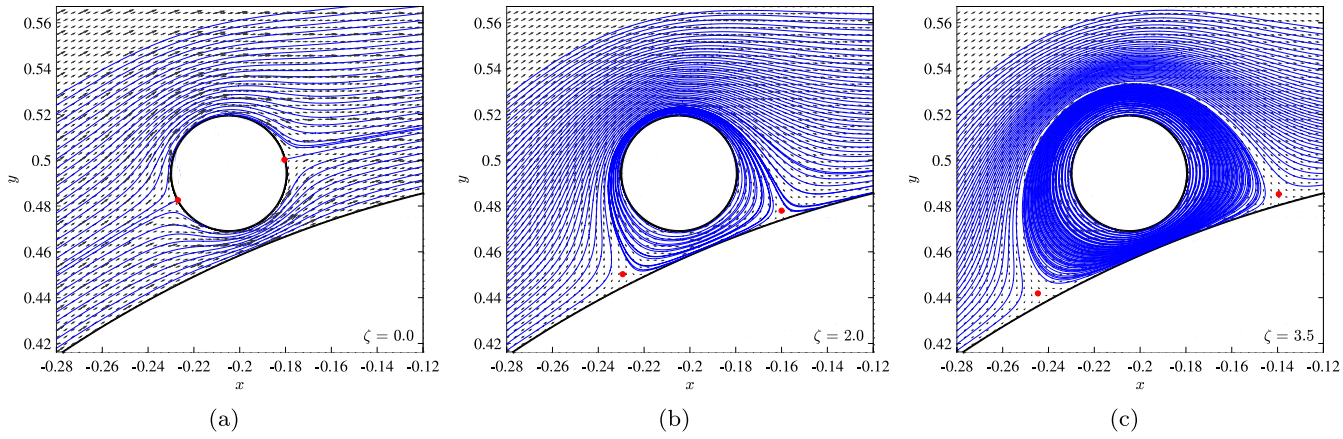

Fig. 4. Detail of streamlines and stagnation points around rotating rod P_1 for $\zeta = 0$, 2.0 and 3.5. $G/D = 0.01$.

4. Results for a viscous flow at $Re = 100$

Preliminary simulations have been performed with the finite volume method at $Re = 100$ for the case of a bare cylinder under uniform flow. Time series of C_L and C_D, as well as vorticity contours and streamlines, were collected with enough samples to evaluate the periodic flow regime. Verification of these results with the same numerical scheme was made in Assi et al. (2019), and will not be repeated here for brevity. It suffices to show a sample of the developed wake in Fig. 6 and point out that the methodology was validated adequately against other results in the literature.

The present work now focuses on the effect of the rotating rods over the viscous flow at $Re = 100$ for a system with $G/D = 0.01$. Two different cases have been simulated as far as the rotation of the rods is concerned:

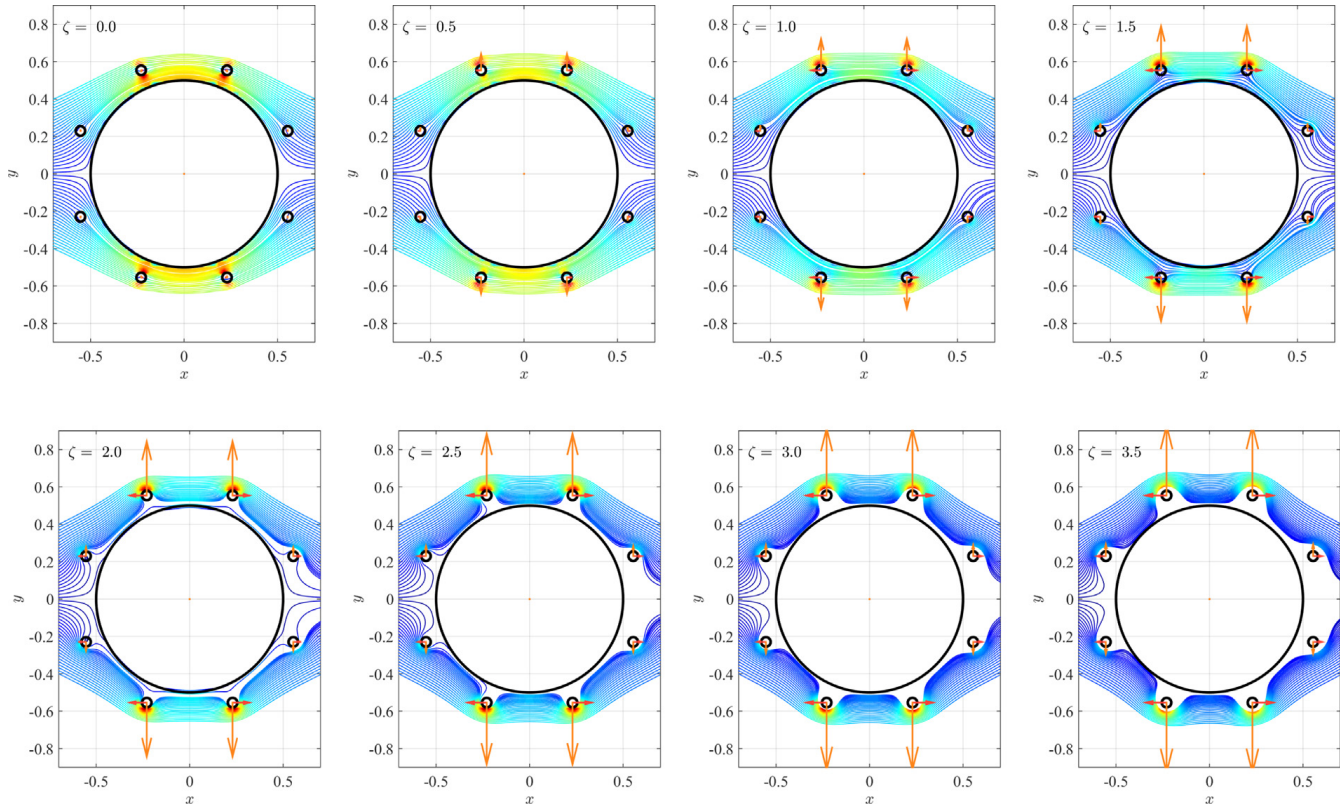

Fig. 5. Streamlines of inviscid flow (coloured by velocity magnitude) and forces on the rotating rods. $G/D = 0.075$. (For interpretation of the references to colour in this figure legend, the reader is referred to the web version of this article.)

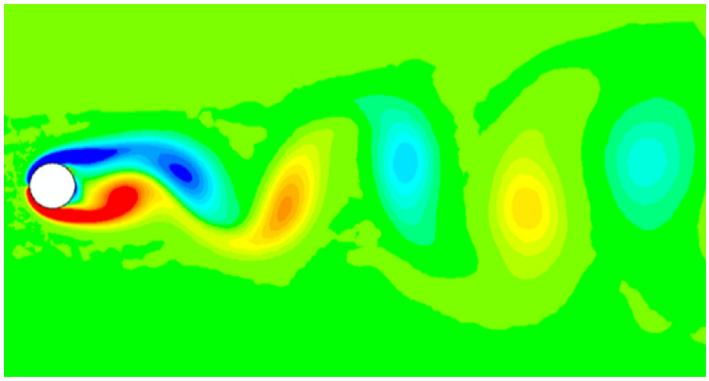

Fig. 6. Vorticity contours showing a developed vortex street for the bare cylinder at $Re = 100$. The vorticity range is from $-1.2s^{-1}$ (blue) to $1.2s^{-1}$ (red). (For interpretation of the references to colour in this figure legend, the reader is referred to the web version of this article.)
Source: Reproduced from Assi et al. (2019).

Case 0: All control rods rotated at the same speed $|\omega_0|$, with the directions indicated in Fig. 1. This case is analogous to Assi et al. (2019), where $G = 0.1D$, differing only in gap to this paper. Thus, new data had to be generated for comparison purposes.

Case 1: The rotation $|\omega_n|$ of the nth rod was inspired by the potential flow field around a bare cylinder but constrained to the input kinetic energy of case 0. Therefore, the proportionality between the rotation speeds found in the reference points in the potential flow was preserved, although the angular velocities are not the same. The same direction and ratio of rotation speeds applied to the rods in the inviscid flow problem ($\omega_2/\omega_1 = \omega_3/\omega_4 = 2.41$) have been repeated here for the viscous flow.

To allow for direct comparison between these two cases, ω_0 in case 0 was chosen so that the overall kinetic energy of the whole system would match that of case 1, thus

$$\left[\sum \omega_n^2\right]_{\text{case 1}} = \left[8\omega_0^2\right]_{\text{case 0}}. \tag{7}$$

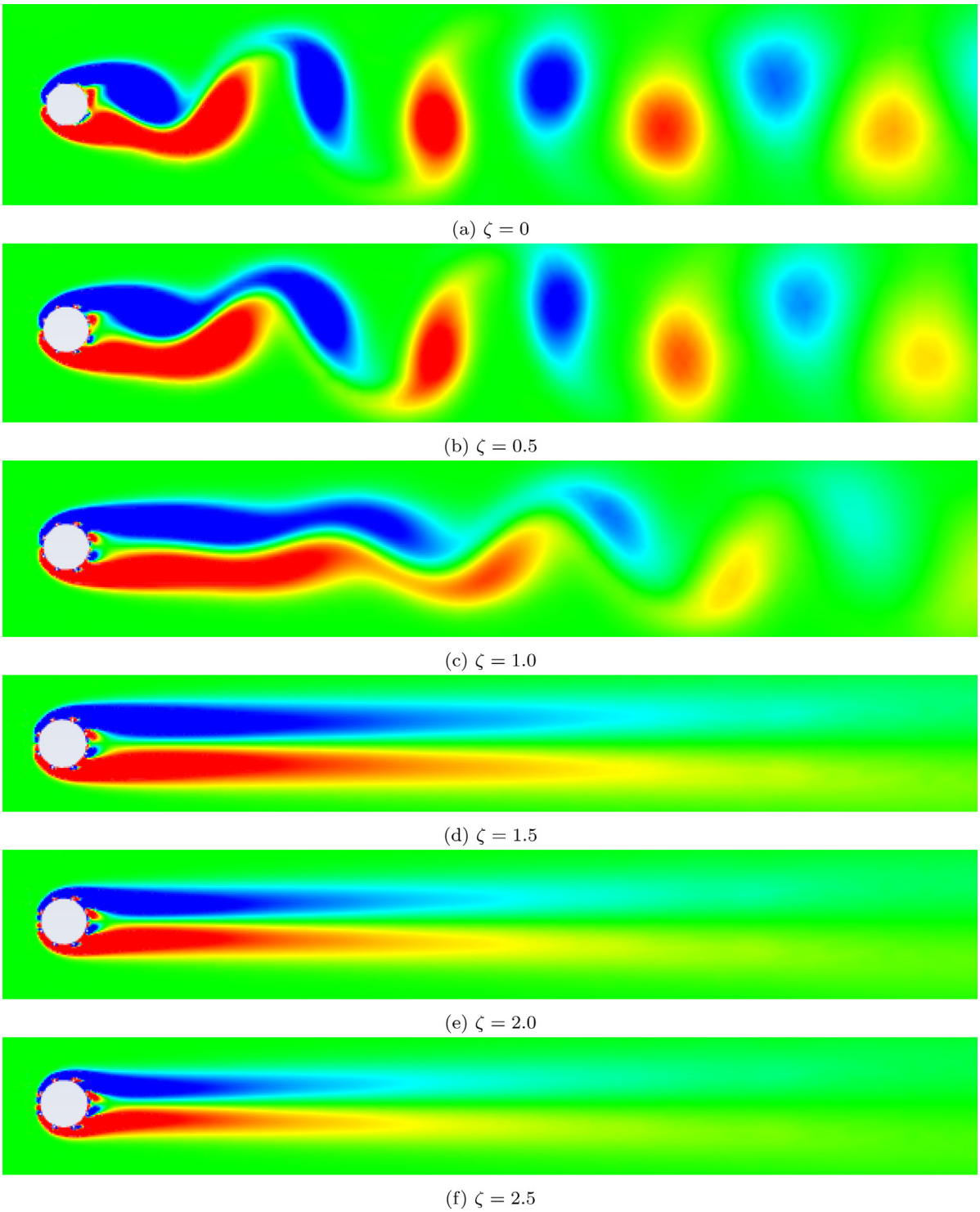

Fig. 7. Case 1. Instantaneous vorticity contours for $\zeta = 0$ to 2.5. The vorticity range is from $-1s^{-1}$ (blue) to $1s^{-1}$ (red). $G/D = 0.01$ and $Re = 100$. (For interpretation of the references to colour in this figure legend, the reader is referred to the web version of this article.)

Fig. 7 presents the instantaneous vorticity field for the developed wake of case 1 varying ζ. For $\zeta = 0$, the typical pattern of alternating vortices shed downstream of the bluff system is clearly observed. The wake is wider compared to that of a bare cylinder (Fig. 6), which is expected given the shrouding effect of the static rods around the main body. It is worth noticing that the Reynolds number based on the diameter of the rods was only $Re_d = 5.02$, hence in the brink of formation of a pair of Föppl vortices, but below the onset of the shear layer instability (which is expected to occur for $Re_d \approx 45$). Therefore, the resulting wake developed downstream of the whole system did not show traces of smaller vortices shed from the peripheral rods.

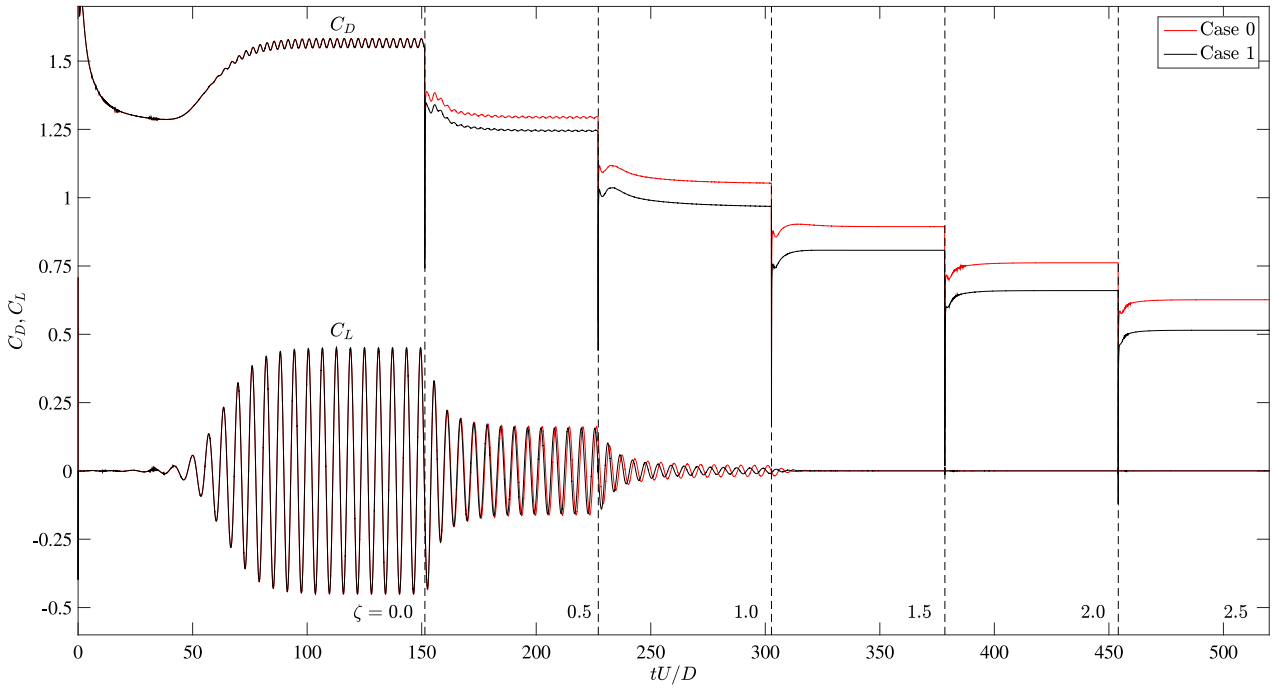

Fig. 8. Time histories of lift and drag coefficients of the entire system for cases 0 and 1.

As the rotation of the peripheral rods was increased, the vortex-formation length was increased, as seen for $\zeta = 1.0$ until the unsteady interaction between the shear layer and consequent vortex shedding disappeared for $\zeta \geq 1.5$. Given enough rotation, the unsteady mechanism was mitigated, and vortex shedding was completely suppressed for the higher ζ of Fig. 7.

4.1. Oscillating fluid forces

The viscous-flow simulations have been performed in a sequence, starting at $\zeta = 0$. After a sufficient number of cycles of vortex shedding had been obtained, ζ was increased in 0.5 steps up to $\zeta = 2.5$. The same procedure was successfully applied by Mittal (2001) and Assi et al. (2019), and resulted in the time histories of lift and drag coefficients presented in Fig. 8. The vertical dashed lines indicate when ζ was changed in the normalised time scale (tU/D).

As the peripheral rods increased rotation, the fluid forces acting on the system also changed. The overall drag on the system and the amplitude of fluctuating lift decreased with increasing ζ, which was expected since the vortex wake was being suppressed as ζ increased. But Fig. 8 also shows that the rotation speeds in case 1 resulted in less drag being generated on the system when compared to case 0.

The mean drag coefficient ($\overline{C}_D$) and the RMS (root mean square) of lift coefficient ($\hat{C}_L$) for cases 0 and 1 are presented in Fig. 9 as a function of ζ. It becomes clear that both cases were very similar in suppressing the fluctuation of lift (Fig. 9(b)), but case 1 was more efficient in mitigating vortex shedding and reducing drag for the whole range of ζ (as seen in Fig. 9(a)). More importantly, the enhancement brought by the potential-flow-inspired speed ratios became more pronounced as ζ reached higher values. This was due to the narrowing of the wake downstream of the system, thus reducing drag. One should remember that the input kinetic energy spent to rotate all the rods in both cases is the same for each ζ. Note that additional simulations have been run for ζ between 0.5 and 1.0 to populate the curves and clarify the smooth transition for $\hat{C}_L$ as it asymptotically approached zero in Fig. 9(b).

The mean drag coefficient for a bare cylinder at the same conditions is $\overline{C}_D = 1.4$, reproduced from Assi et al. (2019) (in good agreement with the numerical results of Blanchard et al., 2019). As seen in Fig. 9(a), the system with non-rotating rods ($\zeta = 0$) produced $\overline{C}_D = 1.57$, representing a 12% increase in the mean drag when compared with that of the bare cylinder. This drag increase was expected due to the shrouding effect of the peripheral bodies. (Note: One should acknowledge that an optimised distribution of shrouds may reduce drag, as shown by Patino et al. (2017) employing sensitivity analysis.) As soon as the rods started to rotate and more momentum was injected into the flow, $\overline{C}_D$ dropped below the level found for a bare cylinder. This is in agreement with the findings by Assi et al. (2019), even though negative values of $\overline{C}_D$ were not observed in the present investigation (case 1) for ζ between 0 and 2.5.

The fluctuation of lift (Fig. 9(b)) also started with a $\hat{C}_L = 0.32$ higher than that of a bare cylinder ($\hat{C}_L = 0.23$), and quickly dropped as vortices were suppressed for higher values of ζ. $\hat{C}_L$ asymptotically approached zero for $\zeta > 1.5$.

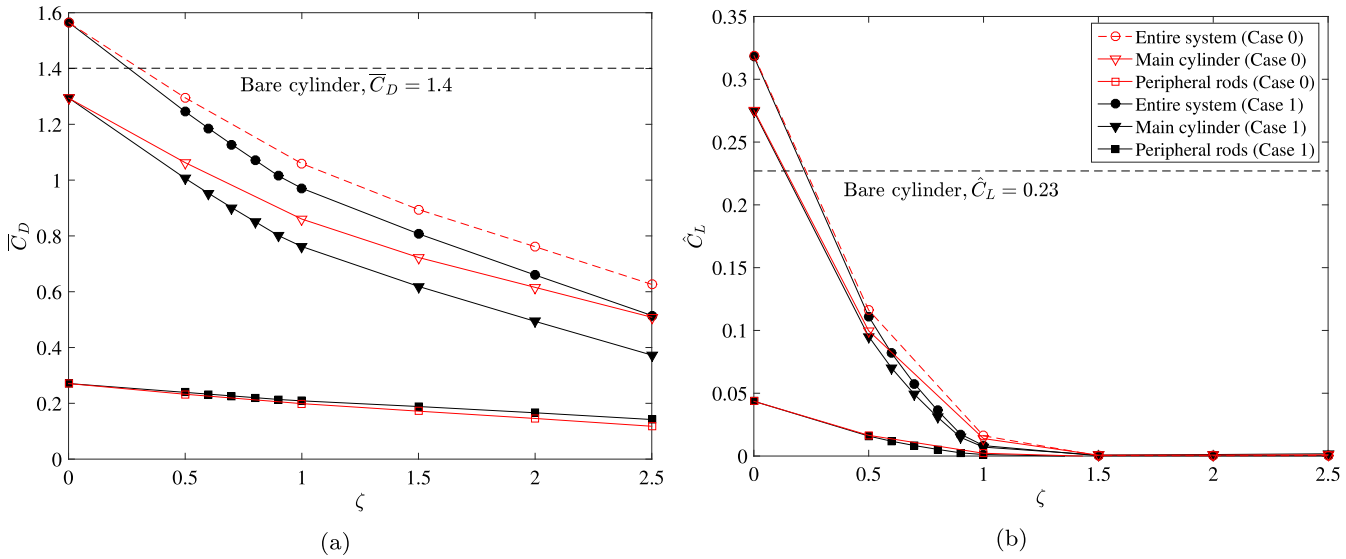

Fig. 9. Mean drag ($\overline{C}_D$) and RMS of lift ($\hat{C}_L$) coefficients for cases 0 and 1.

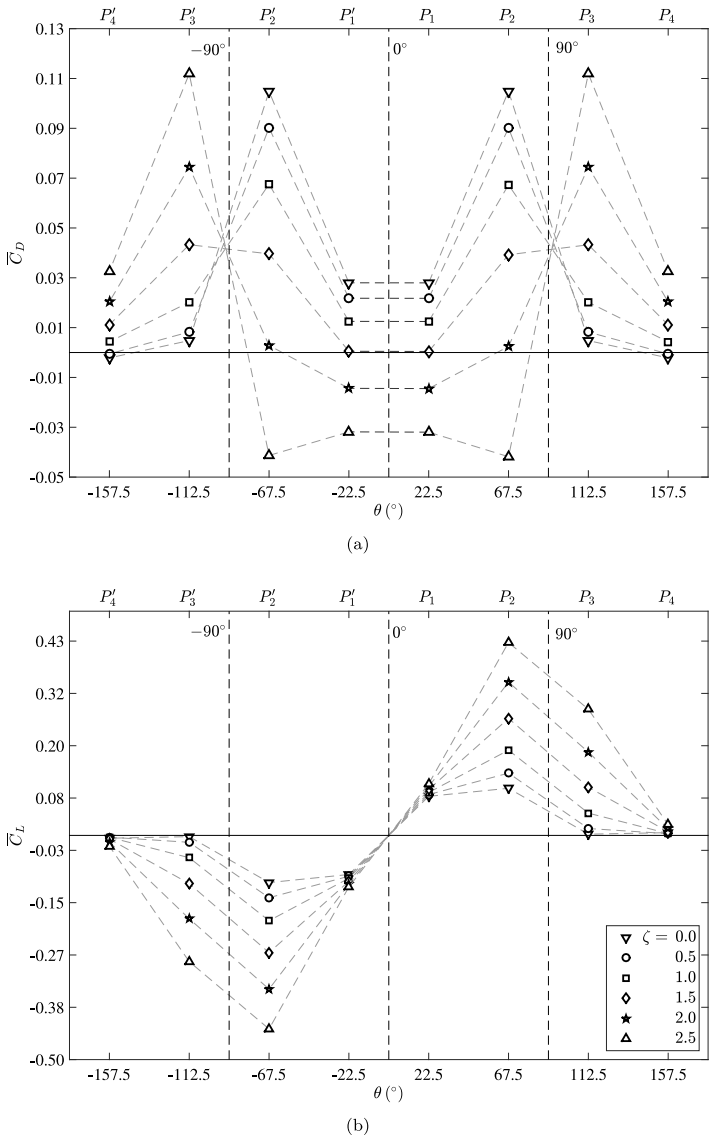

Fig. 10. Contribution of wake-control cylinders to $\overline{C}_D$ (above) and $\overline{C}_L$ (below).

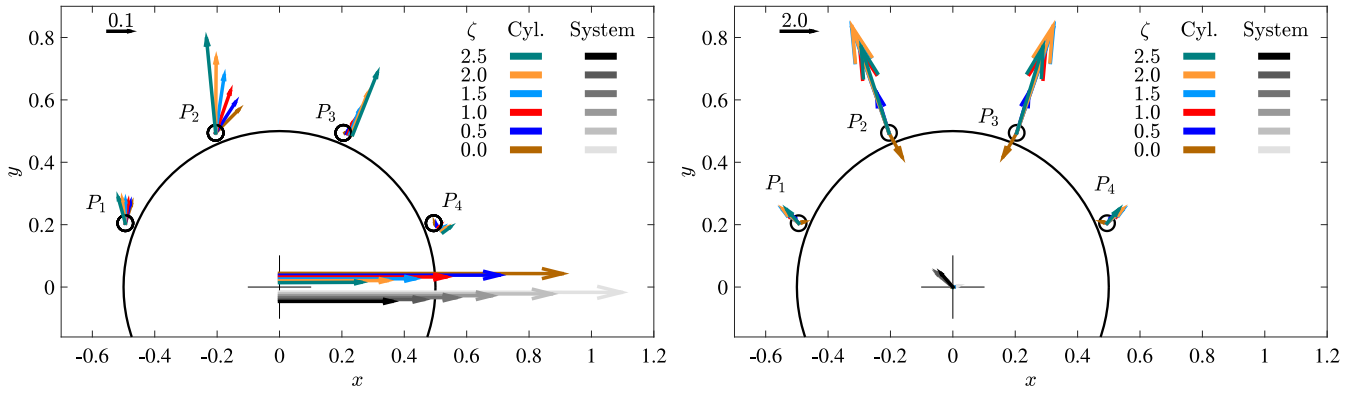

(a) Viscous flow, $Re = 100$. (b) Inviscid flow.

Fig. 11. Vectors of the resultant force coefficients on the system for case 1 (scales shown on the upper left side of each diagram). Coloured arrows represent the force acting on each element. Grey arrows represent the overall force acting on the entire system. (For interpretation of the references to colour in this figure legend, the reader is referred to the web version of this article.)

4.2. Loads on the peripheral control rods

Fig. 9 also splits lift and drag acting on the entire system in two parts: (1) acting on the main cylinder and (2) acting on the peripheral rods only. It becomes clear that most of the drag on the system is generated on the main cylinder (Fig. 9(a)) with only about 25% of the overall $\overline{C}_D$ being generated by the peripheral rods. The same behaviour is verified for the fluctuating lift (Fig. 9(b)), with only a small portion of $\hat{C}_L$ being generated by the rotating rods before the wake is suppressed.

We now turn to the contribution of each rotating rod to the hydrodynamic loads on the system obtained from the viscous-flow simulations of case 1. Fig. 10(a) presents $\overline{C}_D$ on each individual peripheral rod varying ζ. As ζ increased from 0 to 2.5, the frontal rods (located at P_1, P_1' and P_2, P_2') decreased drag, eventually reaching negative values of $\overline{C}_D$ for $\zeta = 2.5$. This inversion of drag could have been anticipated from the inviscid simulations, which revealed that the presence of reversed flow in the gap led to the inversion of drag on the rods (although for higher ζ). Interestingly, this effect only appeared on the frontal cylinders, where the attached boundary layer around the main cylinder resembled the potential flow.

The rear rods (located at P_3, P_3', P_4 and P_4'), on the other hand, produced very little drag for $\zeta = 0$, but showed an increase of $\overline{C}_D$ as ζ increased to 2.5. As a general conclusion, one may verify that the overall drag's dominant contribution changed from the front to the rear rods as ζ increased from 0 to 2.5.

Now looking at the cross-flow direction, Fig. 10(b) shows the mean lift coefficient ($\overline{C}_L$) acting on each rod varying ζ (by convention, $\overline{C}_L$ is positive upwards in Fig. 1). As expected, the behaviour of $\overline{C}_L$ is antisymmetric in relation to the centreline, so that the top rods (P_1, P_2, P_3 and P_4) presented positive $\overline{C}_L$, while the bottom rods (P_1', P_2', P_3' and P_4') showed negative $\overline{C}_L$. The second rotating rods (P_2 and P_2') produced the highest magnitude of lift for all $\zeta > 0$. Curiously enough, the first and fourth rods (P_1, P_1' and P_4, P_4') showed almost no variation of $\overline{C}_L$ over ζ.

Inversion of lift was not observed for ζ between 0 and 0.5 when $\overline{C}_L$ in Fig. 10(b) is compared with the results obtained for the inviscid fluid in Fig. 5. This might be attributed to the effect of viscosity acting within the gap, not allowing the same difference in pressure that would lead, on its own, to the inversion of lift.

By combining $\overline{C}_D$ and $\overline{C}_L$, it is possible to deduce the resultant force acting on the individual rotating rods. This is represented schematically in Fig. 11 by the force vectors acting on each element of the system for the viscous and inviscid simulations of case 1. Note that coloured vectors correspond to the force acting on each element for different ζ, while greyscale vectors represent the total force on the entire system. Also, some vectors have been slightly moved away from their respective axes for visibility purposes.

It can be seen that the greatest force magnitudes corresponded to rods P_2 and P_3 for both viscous and inviscid flows (Figs. 11(a) and 11(b), respectively). As expected, the inviscid flow did not generate drag on the main cylinder and all the force vectors acting on the peripheral rods showed a radial direction in Fig. 11(b), only varying magnitude as ζ was increased.

For the viscous simulations, shown in Fig. 11(a), the vectors on rods P_1 and P_2 highlighted the inversion of drag as well as the distinct variation of lift on rod P_2 as ζ was increased. The mean drag on the main cylinder and that overall drag acting on the entire system was also reduced with an increase in ζ, as qualitatively illustrated by the arrows.

The vector plots in Fig. 11 offer an intuitive way to identify which element presented the most pronounced variation in hydrodynamic forces as a function of ζ. Hence, one could speculate whether rotating rods P_1, P_1' and P_4, P_4' had any influence on wake control whatsoever, since their contributions to $\overline{C}_D$ and $\overline{C}_L$ are minimal. This should be further

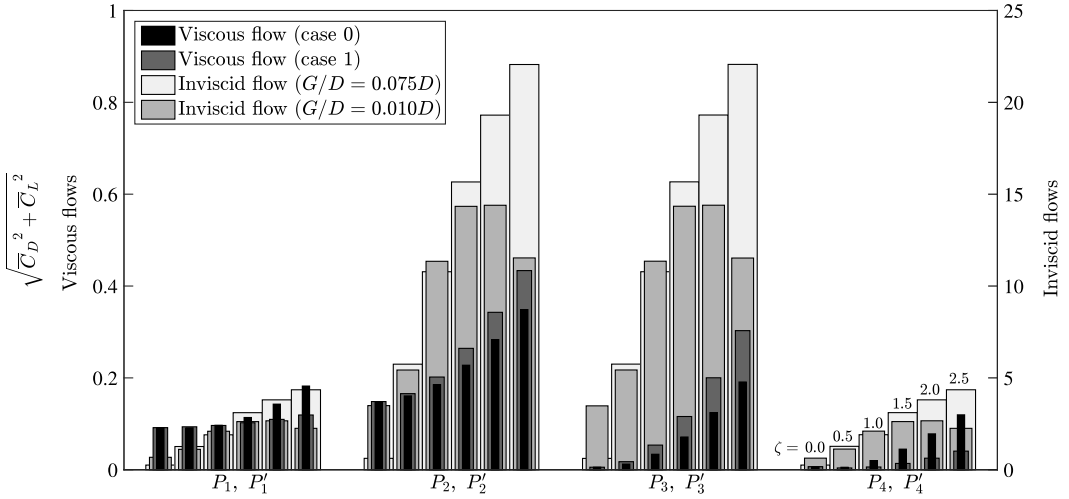

Fig. 12. Contributions of wake-control cylinders to the resultant force on the system.

investigated during an optimisation study. Of course, by removing these rods, one would eliminate the omnidirectional characteristic of the system, which is a fundamental aspect of this research considering practical applications.

A comparison is now made with the inviscid flow. Fig. 12 shows the effect of increasing speeds on the magnitude of the resultant force coefficient ($\sqrt{\overline{C}_D{}^2 + \overline{C}_L{}^2}$) for control rods P_1, P_2, P_3 and P_4, both in viscous and in inviscid conditions. One may notice that differently from viscous flow, the aforementioned double-inversion effect in lift and drag was detected for the smaller gap for the inviscid flow. In contrast, for the same range, the larger gap $G/D = 0.075$ produced a monotonic increase in the resultant coefficient, as in the case of viscous flow. Additionally, in the absence of viscosity, inviscid flow produced much larger resultant forces on the peripheral rods, ranging in the order of 25 times that of the viscous flows (check two different vertical axis in Fig. 12).

Incidentally, the downturn of the resultant coefficient for the inviscid flow started at $\zeta = 1.5$, where the suppression of vortex shedding was observed in Fig. 7, recalling the connection between the inviscid case and that of a viscous case in a suppressed vortex-shedding condition. One may argue that the two cases are linked by approaching an optimal state with minimum drag, after which an increase in rotation speeds in the viscous case may generate thrust on the entire system, as in Assi et al. (2009), thus leading to more energy expenditure without drag mitigation. Such a state was not detected in this work for our range of ζ values.

Furthermore, the least significant contribution of P_4, P_4' is more clearly shown against the other cylinders in Fig. 12, as it was anticipated qualitatively by Figs. 10 and 11.

4.3. Pressure coefficients

The comparison between the viscous and inviscid cases can be extended to the pressure coefficients (C_p) around the main cylinder for varying ζ, as illustrated in Fig. 13. C_p around a bare cylinder, obtained from the canonical potential flow, is repeated as a black line in both Figs. 13(a) and 13(b) as a reference. For clarity when comparing results for case 1, only curves for $\zeta = 0$, 1.0 and 2.5 are plotted, contrasting results before and after wake suppression was achieved.

Pressure coefficients for inviscid and viscous cases broadly follow the same sinusoidal behaviour, highlighted as a pure sine wave for the bare cylinder in potential flow. Since C_p was calculated on the wall of the main cylinder, the flow interaction with the peripheral rods produced an abrupt jump in C_p near the P_n and P_n' positions (θ_n marking the angular position of the nth rod). The difference between the inviscid and viscous flows on the C_p jump is quite remarkable, suggesting that viscosity is relevant to change the topology of the flow in the gap.

To evaluate the overall C_p around the main cylinder disregarding the local effect of the rods, data points in between rods were marked with circles in Fig. 13(a) and plotted in Fig. 13(b) interpolated with splines.

For the inviscid flow and $\zeta = 0$, the incoming flow found a confined region in the gap between the main cylinder and the control rods through which it accelerated, dropping C_p. A similar behaviour was observed for $\zeta = 1.0$ and 2.5, with only a difference in magnitude in C_p. The stagnation points marked in Fig. 4 for $\zeta = 2.0$ provided a sensible idea of how C_p varied around the cylinder wall as the flow is constrained in the gap by the rotating rod.

With no-slip flow on the wall and viscosity, C_p took a different behaviour in the gap for the viscous flow. For $\zeta = 0$ and 1.0 the flow separated and a vortex street was formed downstream of the system, as seen in Fig. 7. This reflected on a reduction of C_p near the base of the cylinder, that remained flat within the region of separated flow, producing pressure drag. Given enough rotation to suppress the wake formation, as for $\zeta = 2.5$, C_p recovered the sinusoidal behaviour typical of a reattached flow around a bluff body, reducing drag. The level of C_p is different than that observed for the potential flow around the bare cylinder, but the general behaviour of the curves are rather similar. Pressure drag was not eliminated, but considerably reduced.

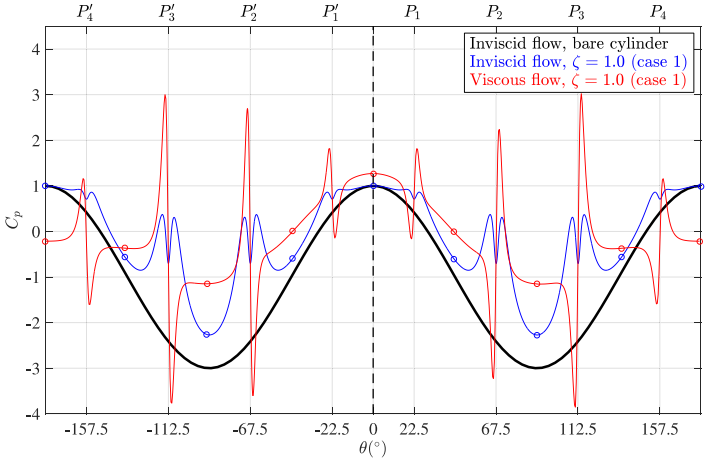

(a) Peaks correspond to the effect of the insertion of the peripheral rods.

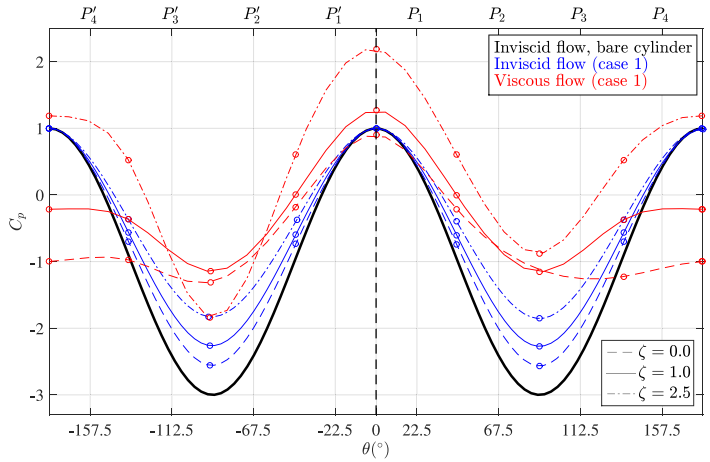

(b) Splines approximate the points marked by circles, obtained from figure 13a.

Fig. 13. Pressure coefficients for viscous and inviscid flows of case 1 and typical curve for a bare cylinder. Fig. 13(a) corresponds to $\zeta = 1.0$ and Fig. 13(b) refers to $\zeta = 0.0$, 1.0 and 2.5.

5. Driving power

Finally, keeping in mind the technological applications that might appear from this investigation, it is worth evaluating the energy spent to rotate the control rods compared with the energy saved in drag reduction. Following the model for driving power employed by Assi et al. (2019) and Shukla and Arakeri (2013), the power (p_n) spent to rotate a single control rod is that required to overcome the effect of pressure and viscous stresses on its wall. Adding up the contributions of all the N control cylinders results in

$$C_N = \sum_{n=1}^{N} \frac{p_n}{\rho U^3 D/2}, \tag{8}$$

the coefficient of power spent to drive all the rods into spinning motion, where the power

$$p_n = U_n \int_0^{2\pi} \tau_\theta \, \frac{d}{2} \, \mathrm{d}\theta \tag{9}$$

driving each rod represents the integration of the wall shear stress τ_θ over the surface of the small cylinder, and U_n corresponds to its tangential velocity. The total power-loss coefficient

$$C_{PL} = \overline{C}_D + C_N. \tag{10}$$

is a means of evaluating the energy efficiency of the system, obtained by adding the mean drag acting upon the entire system to the energy expended to rotate the rods.

Fig. 14 presents the breakdown of C_{PL} into $\overline{C}_D$ and C_N as a function of ζ for cases 1 and 0. For non-rotating rods ($\zeta = 0$), all the power-loss of the system was due to drag, which was higher than the $\overline{C}_D$ of a bare cylinder for both cases. As ζ was

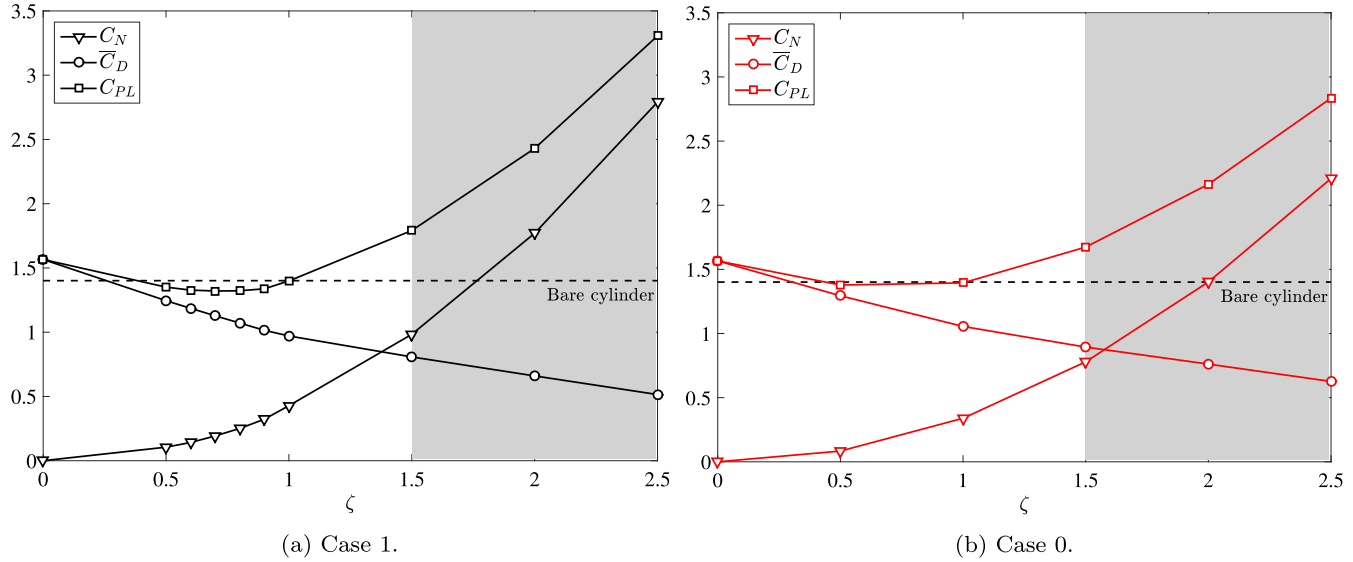

Fig. 14. Breakdown of the power-loss coefficient (C_{PL}) into $\overline{C}_D$ and C_N. The areas shaded in grey represent suppression of vortex shedding.

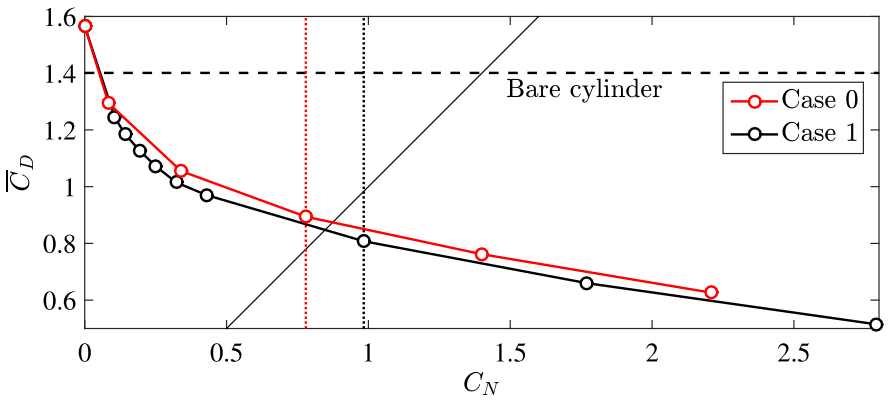

Fig. 15. $\overline{C}_D$ as a function of C_N. Vertical dotted lines mark the minimum C_N for which vortex shedding was suppressed.

increased, power was spent to rotate the control rods, but the stronger reduction in $\overline{C}_D$ dominated over the behaviour of C_{PL}.

The intersection of $\overline{C}_D$ and C_N curves mark ζ in which the energy spent to rotate the rods is equal to that lost due to drag. For case 1, the intersection occurred at $\zeta \approx 1.38$ (Fig. 14(a)), whereas for case 0 it happened at $\zeta \approx 1.62$ (Fig. 14(b)). For higher values of ζ, the energy was mostly spent spinning the control rods, although concurrently, the entire system's mean drag was reduced. By comparing C_{PL} for both cases, it appears that the minimum-energy operating point lies between $\zeta = 0.5$ and 1.0. Note that the few extra points produced for case 1 between $\zeta = 0.5$ and 1.0 may give the impression that case 1 presented a minimum C_{PL} value lower than that of case 0, but this is not conclusive given the available data.

The shaded areas in Fig. 14 represent ζ for which the effect of the rotating rods has suppressed vortex shedding. We believe that more data points are required between $\zeta = 1.0$ and 1.5 to evaluate which case achieves effective wake suppression with less power-loss. So far, considering that at $\zeta = 1.5$ both cases completely mitigated vortex shedding, we can conclude that case 1 produced less drag but spending slightly more energy than case 0 ($C_{PL} = 1.79$ and 1.67, respectively, at $\zeta = 1.5$ in Figs. 14(a) and 14(b)).

Finally, by plotting $\overline{C}_D$ versus C_N in Fig. 15 it is possible to evaluate the efficiency of the systems regarding drag reduction as a function of power spent to rotate the rods. Overall, case 1 appeared to be more efficient than case 0 because it produced less drag with the same power consumed in rotation. Note that if C_N is greater than $\overline{C}_D$ more power is spent to rotate the rods than the equivalent power lost in the flow due to drag ($\overline{C}_D = C_N$ is represented by the diagonal line in Fig. 15).

The two vertical, dotted lines indicate the minimum C_N recorded in this investigation for which vortex shedding has been entirely suppressed in the wake. Even though more data is required to evaluate with better accuracy the minimum C_N for vortex suppression, it is interesting to note that this controlled-wake condition was achieved with $\overline{C}_D > C_N$ for case 0 and with $\overline{C}_D < C_N$ for case 1. For the suppressed condition, the actuating system of case 0 provided a reduction in

energy consumption, to which C_N relates, offset by a greater drag. On the other hand, case 1 showed a tendency of drag reduction, at the expense of greater power requirement, as far as our range of ζ values showed. For both cases, the same C_{PL} was quantified, equal to that of a bare cylinder, as it is captured by Fig. 14.

6. Conclusion

In the present work, we have investigated the effect of 8 control rods arranged around the main cylinder and rotating at different speeds on suppressing vortex shedding and reducing the overall drag of the system. For case 0, all rods rotated at the same rate (uniform $|\omega_n|$). In case 1, the control rods were set to rotate at different $|\omega_n|$ inspired by the condition of the potential-flow velocity field around a bare cylinder, constrained to the same input kinetic energy of case 0.

Both cases 0 and 1 completely suppressed the formation of vortex shedding for a speed ratio greater than $\zeta = 1.5$, bringing the mean drag coefficient below that of a bare cylinder. Case 1, however, achieved that wake suppression producing less drag than case 0. The simulations performed at $Re = 100$ showed that, given enough rotation of the control rods, sufficient momentum is injected into the boundary layer, delaying flow separation and eventually attenuating the interaction of the separated shear layers in shedding vortices.

This "potential-flow-inspired" arrangement of $|\omega_n|$ (case 1) appeared to be more efficient than a system with uniform $|\omega_n|$ (case 0) in mitigating the formation of vortices with a reduction in the mean drag and fluctuating lift. Keep in mind that both configurations employed the same overall input kinetic energy. Regarding the contribution of each rotating rod, we conclude that the two upstream rods (P_1 and P_1') and the two downstream rods (P_4 and P_4') had only a minor effect in reducing drag and lift when compared with the other four rods positioned near the wider portion of the main cylinder (P_2, P_2', P_3 and P_3'). Hence, there is room for optimisation.

It is interesting to note that the simulations with inviscid flow performed with the vortex panel method captured inversion of the lift acting on the rotating rods as ζ was increased. This phenomenon has not been verified to occur for the viscous flow.

Considering the total power-loss coefficient (C_{PL}), it became evident that there is a range of rotation speeds ($0.5 < \zeta < 1.0$) capable of reducing the overall drag with minimum power spent to rotate the rods so that the total power spent and that lost due to drag remains below the equivalent mean drag for a bare cylinder. In other words, regarding energy efficiency, it is worth spending that amount of energy to rotate the rods to reduce drag. Now, in order to completely mitigate vortex shedding, more energy will have to be spent spinning the rods.

Finally, considering a technological application of such a device, one should consider some desirable objectives: (i) mitigate vortex shedding with minimum energy consumption; (ii) reduce drag without spending more power than that lost due to drag on a bare cylinder; (iii) reduce drag to a minimum on the expense of more acting power; or (iv) generate a lateral force (lift) to manoeuvre the body; among others. To efficiently achieve those objectives, the system can be optimised considering the rotation speed of each rod without changing their equal distribution about the main cylinder, which confers the omnidirectional characteristic of the system. As the paper shows, the frontal and rear cylinders are much less relevant to flow control than the intermediate ones. We believe that even at different incidence angles over 8 rods, the control strategy of the intermediate rods would prevail in suppressing vortex-shedding.

Moving from a uniform $|\omega_n|$ (proposed by Assi et al., 2019) to the "potential-flow-inspired" distribution of $|\omega_n|$ of the present work represents an improvement as far as power expenditure and drag reduction are concerned. Future work should deal with a multi-variable and multi-objective optimisation of the system.

CRediT authorship contribution statement

I.A. Carvalho: Conception and design of study, Acquisition of data, Analysis and/or interpretation of data, Writing – original draft, Writing – review & editing. **G.R.S. Assi:** Conception and design of study, Acquisition of data, Analysis and/or interpretation of data, Writing – original draft, Writing – review & editing. **R.M. Orselli:** Acquisition of data, Analysis and/or interpretation of data, Writing – review & editing.

Declaration of competing interest

The authors declare that they have no known competing financial interests or personal relationships that could have appeared to influence the work reported in this paper.

Acknowledgements

IAC is grateful to CAPES Brazilian Ministry of Education for his PhD scholarship. GRSA acknowledges the support of FAPESP, Brazil (2011/00205-6) and CNPq, Brazil (306146/2019-3). We gratefully acknowledge the support of the RCGI Research Centre for Gas Innovation, hosted by the University of São Paulo, Brazil and sponsored by FAPESP, Brazil (2014/50279-4) and Shell Brasil. Gustavo R.S. Assi approved the version of the manuscript to be published.

References

Assi, G.R.S., Bearman, P.W., Kitney, N., 2009. Low drag solutions for suppressing vortex-induced vibration of circular cylinders. J. Fluids Struct. 25 (4), 666–675.
Assi, G.R.S., Bearman, P.W., Tognarelli, M.A., 2014a. On the stability of a free-to-rotate short-tail fairing and a splitter plate as suppressors of vortex-induced vibration. Ocean Eng. 92, 234–244.
Assi, G.R.S., Crespi, T., Gharib, M., 2021. Experiments with novel geometries of serrated helical strakes to suppress vortex-induced vibrations. Ocean Eng. Accepted for Publications.
Assi, G.R.S., Franco, G.S., Vestri, M.S., 2014b. Investigation on the stability of parallel and oblique plates as suppressors of vortex-induced vibration of a circular cylinder. J. Offshore Mech. Arct. Eng. 136 (3), 031802.
Assi, G.R.S., Orselli, R.M., Silva-Ortega, M., 2019. Control of vortex shedding from a circular cylinder surrounded by eight rotating wake-control cylinders at Re=100. J. Fluids Struct. 89, 13–24.
Barth, T., Jespersen, D., 1989. The design and application of upwind schemes on unstructured meshes, in: 27th Aerospace Sciences Meeting, pp. 366.
Behr, M., Hastreiter, D., Mittal, S., Tezduyar, T., 1995. Incompressible flow past a circular cylinder: dependence of the computed flow field on the location of the lateral boundaries. Comput. Methods Appl. Mech. Engrg. 123 (1–4), 309–316.
Blanchard, A., Bergman, L.A., Vakakis, A.F., 2019. Vortex-induced vibration of a linearly sprung cylinder with an internal rotational nonlinear energy sink in turbulent flow. Nonlinear Dynam. 99, 593–609.
Cicolin, M.M., Assi, G.R.S., 2017. Experiments with flexible shrouds to reduce the vortex-induced vibration of a cylinder with low mass and damping. Appl. Ocean Res. 65, 290–301.
Goodarzi, M., Dehkordi, E.K., 2017. Geometrical parameter analysis on stabilizing the flow regime over a circular cylinder using two small rotating controllers. Comput. & Fluids 145, 129–140.
Hess, J., Smith, A., 1966. Calculation of potential flow about arbitrary bodies. Prog. Aeronaut. Sci. 8.
Korkischko, I., Meneghini, J.R., 2011. Volumetric reconstruction of the mean flow around circular cylinders fitted with strakes. Exp. Fluids 51 (4), 1109.
Kuethe, A.M., Chow, C.-Y., Fung, Y., 1987. Foundations of Aerodynamics, Bases of Aerodynamics Design. John Wiley & Sons, Inc.
Mittal, S., 2001. Control of flow past bluff bodies using rotating control cylinders. J. Fluids Struct. 15 (2), 291–326.
Mittal, S., Raghuvanshi, A., 2001. Control of vortex shedding behind circular cylinder for flows at low Reynolds numbers. Internat. J. Numer. Methods Fluids 35 (4), 421–447.
Patankar, S.V., 1980. Numerical Heat Transfer and Fluid Flow. Hemisphere Publishing Corp., Washington, DC, p. 210.
Patino, G.A., Gioria, R.S., Meneghini, J.R., 2017. Evaluating the control of a cylinder wake by the method of sensitivity analysis. Phys. Fluids 29 (4), 044103.
Shukla, R.K., Arakeri, J.H., 2013. Minimum power consumption for drag reduction on a circular cylinder by tangential surface motion. J. Fluid Mech. 715, 597–641.
Silva-Ortega, M., Assi, G., 2017a. Flow-induced vibration of a circular cylinder surrounded by two, four and eight wake-control cylinders. Exp. Therm Fluid Sci. 85, 354–362.
Silva-Ortega, M., Assi, G.R.S., 2017b. Flow-induced vibration of a circular cylinder surrounded by two, four and eight wake-control cylinders. Exp. Therm Fluid Sci. 85, 354–362.
Silva-Ortega, M., Assi, G.R.S., 2017c. Suppression of the vortex-induced vibration of a circular cylinder surrounded by eight rotating wake-control cylinders. J. Fluids Struct. 74, 401–412.
Stevens, W., Goradia, S., Braden, J., Morgan, H., 1971. Mathematical model for two-dimensional multi-component airfoils in viscous flow, in: 10th Aerospace Sciences Meeting, pp. 2.
Strykowski, P., Sreenivasan, K., 1990. On the formation and suppression of vortex shedding at low Reynolds numbers. J. Fluid Mech. 218, 71–107.
Versteeg, H.K., Malalasekera, W., 2007. An Introduction To Computational Fluid Dynamics: The Finite Volume Method. Pearson education.
Williamson, C., Govardhan, R., 2004. Vortex-induced vibrations. Annu. Rev. Fluid Mech. 36, 413–455.
Young, D., Huang, J., Eldho, T., 2001. Simulation of laminar vortex shedding flow past cylinders using a coupled BEM and FEM model. Comput. Methods Appl. Mech. Engrg. 190 (45), 5975–5998.
Zdravkovich, M., 1981. Review and classification of various aerodynamic and hydrodynamic means for suppressing vortex shedding. J. Wind Eng. Ind. Aerodyn. 7 (2), 145–189.

Journal of Fluids and Structures 113 (2022) 103652

Contents lists available at ScienceDirect

Journal of Fluids and Structures

journal homepage: www.elsevier.com/locate/jfs

Enhanced control of the turbulent flow past a circular cylinder with rotating rods inspired by an inviscid solution

I.A. Carvalho [a,*], G.R.S. Assi [b]

[a] Department of Mechanical Engineering, EPUSP, University of São Paulo, Brazil
[b] Department of Naval Architecture & Ocean Engineering, EPUSP, University of São Paulo, Brazil

ARTICLE INFO

Article history:
Received 13 January 2022
Received in revised form 10 May 2022
Accepted 3 July 2022
Available online xxxx

Keywords:
Vortex-shedding suppression
Wake control
Drag reduction
Bluff body

ABSTRACT

This paper examines an active mechanism of wake control for a turbulent flow regime of Reynolds number 1000 through finite volume, three-dimensional DES simulations. Eight peripheral rods equally spaced about a central body are forced to spin around their axes in two arrangements: case 0, with uniform rotation speed and case 1, with rotation rates inspired by the solution of the potential flow around the body. The two cases were constrained to the same input kinetic energy for every set of rotations. We have found case 1 to be more effective to control the wake, eliminate turbulent structures, and attenuate mean drag and fluctuating lift. The interference of the rods in the flow past the main body resulted in a steady wake in both cases, provided enough rotation was supplied to the system. This result was previously achieved only in laminar regime. Novel to such a system, rotations midway between a vortex wake and a steady wake led streamwise vortices to show a mode-B-like mechanism of vorticity transfer. Case 1 generally suppressed vortex shedding with lower input kinetic energy and required less power than case 0, thus resulting in a more efficient configuration to suppress vortices in the wake.

1. Introduction

Oil and gas exploration in ultra-deep waters has motivated the design of large offshore marine structures of circular cross-section, such as monocolumns and spar platforms (Gonçalves et al., 2011), that allow for the exploration of reservoirs in ultra-deep waters. These platforms are subjected to the effect of sea currents, whereby the interaction with the bluff structure leads to alternate vortex shedding in the wake past the body, generating the so-called *Kármán vortex street*.

The cyclic loads produced by the phenomenon of *vortex shedding* may cause the structure to respond with *vortex-induced vibrations* (VIV), a periodic motion both streamwise and in the transverse direction, caused by the components of the resultant force, respectively denoted drag and lift. As the vortex-shedding frequency nears and locks onto the natural frequency of the body, progressively larger amplitudes of motion develop. Fatigue and failure of slender structures have been reported as some of the adverse outcomes of VIV. This rather minute overview of VIV can be expanded by the comprehensive review of Williamson and Govardhan (2004) and the references therein. Considering the response of large floating structures, the same physical mechanism has been termed *vortex-induced motion* (VIM) due to its low-frequency characteristics (Fujarra et al., 2012; Gonçalves et al., 2011).

* Corresponding author.
E-mail address: amorim.icaro@usp.br (I.A. Carvalho).

https://doi.org/10.1016/j.jfluidstructs.2022.103652
0889-9746/

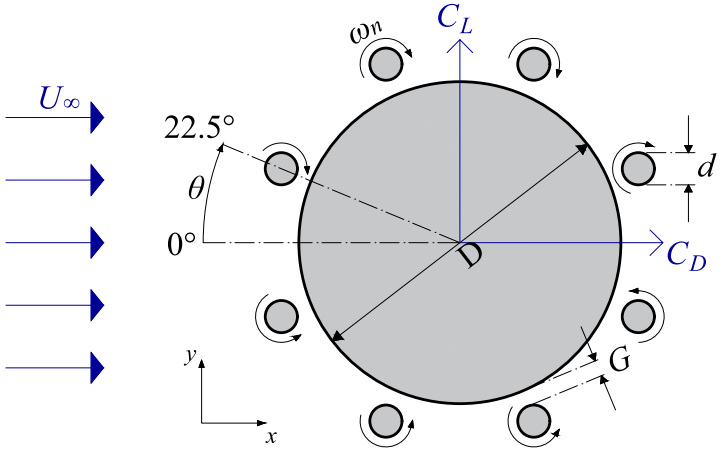

Fig. 1. Uniform flow past a system comprised by a main cylinder and rotating control rods.

Techniques to suppress vortex-shedding, reduce oscillating loads and avoid VIV have been fostered by a wealth of studies. The seminal paper of Strykowski and Sreenivasan (1990) elucidated, through experiments and numerical simulations, that the proper placement of a single control cylinder (a smaller rod near the main, larger body) could suppress entirely the instabilities that otherwise led to vortex shedding at low Reynolds numbers (*Re*). Later, Mittal and Raghuvanshi (2001) conducted numerical investigations and found that this passive mechanism reduced the mean drag even in the turbulent regime of $Re = 10{,}000$, although it could not prevent vortex shedding or the formation of three-dimensional structures in the wake.

More recently, experiments performed by Cicolin et al. (2021) with one rod at different locations around a central cylinder employing particle-image velocimetry at $Re = 20{,}000$ advanced on two matters: (i) on the details of the interaction between the control rod and the shear layer of the main body and (ii) on the influence of the control rod on separation. The authors remarked on a significant influence of the position of the separation point on drag and lift measurements in turbulent regime. Interestingly, the insertion of the control rod within the recirculation zone had little effect upon the drag of the main body.

Complex systems involving multiple rods can be engineered to achieve greater flow control. Axisymmetric arrangements with 2, 4 and 8 rods around the main cylinder, as in Fig. 1, were tested by Silva-Ortega and Assi (2017a) varying rod diameter and gap at *Re* between 5×10^3 and 5×10^4. The authors revealed that a galloping-like response was produced using 4 rods, and a decrease in drag was obtained. For 8 rotating rods, an omnidirectional-like system strongly reduced VIV, also generating negative drag for higher rotation speeds. Under any configuration, it was reported that, in general, the presence of the rods around the main cylinder reduced the response amplitude. Building on the vortex-shedding mechanism proposed by Gerrard (1966) one can infer that this interference with control rods might be disrupting the communication between the shear layers. Through sensitivity analysis, Patino et al. (2017) referred to the stabilising effect of the (passive and active) rods as a consequence of the cutback in circulation being supplied to the near-wake region.

The passive mechanism in conjunction with power input to spin the rods, and thus to impart momentum into the shear layers, gave rise to the active mechanism of Moving Surface Boundary-layer Control (MSBC). Active and passive control techniques were thoroughly reviewed by Zdravkovich (1981) and Choi et al. (2008). We simply surmise that MSBC has been proven effective to mitigate drag in bluff bodies (Modi et al., 1990) and to reduce the total variance in the cylinder wake, as well as to render the streamwise velocity profile more uniform (Korkischko and Meneghini, 2012). Some of the previous works in this matter employed a system such as that of Silva-Ortega and Assi (2017a) with 8 rods.

In laminar regime, Assi et al. (2019) demonstrated through two-dimensional, finite volume simulations at $Re = 100$ that the setup of eight control rods spinning at a uniform speed (equal to three times that of the free stream) could suppress vortex shedding. Sufficient spinning beyond this critical value gave rise to thrust (negative drag) on the entire system. With a similar setup, however, in turbulent flow regime, the MSBC technique allowed Assi et al. (2018) to extend the interval of Reynolds numbers where reduction in the fluctuating loads was obtained up to $Re = 10{,}000$, even though full vortex-shedding suppression was not achieved. Silva-Ortega and Assi (2017a) investigated the active interference of the rods with crosswise VIV and reported lowered hydrodynamic loads and peak amplitude in the oscillatory motion for the same setup of 8 rods and *Re* range as Silva-Ortega and Assi (2017a), but suppression was not achieved either.

In line with these previous works, Carvalho et al. (2021) approached the same problem in a laminar regime with a methodology inspired by potential-flow theory that defined the rotation rates of the rods (to be explained in detail in Section 2). Surely, different rods relative to the main body and to the separation of the flow differed in relevance with respect to one another. Comparing the work of Carvalho et al. (2021) with that of Assi et al. (2019), the new setup – with the same input kinetic energy – seemed to present lower drag obtained by a slightly greater power requirement.

It seems, to the best our knowledge, that there is still room for the investigation of a setup such as that of Silva-Ortega and Assi (2017a) (with 8 rods) in regards to complete suppression of vortex shedding in turbulent regime and to

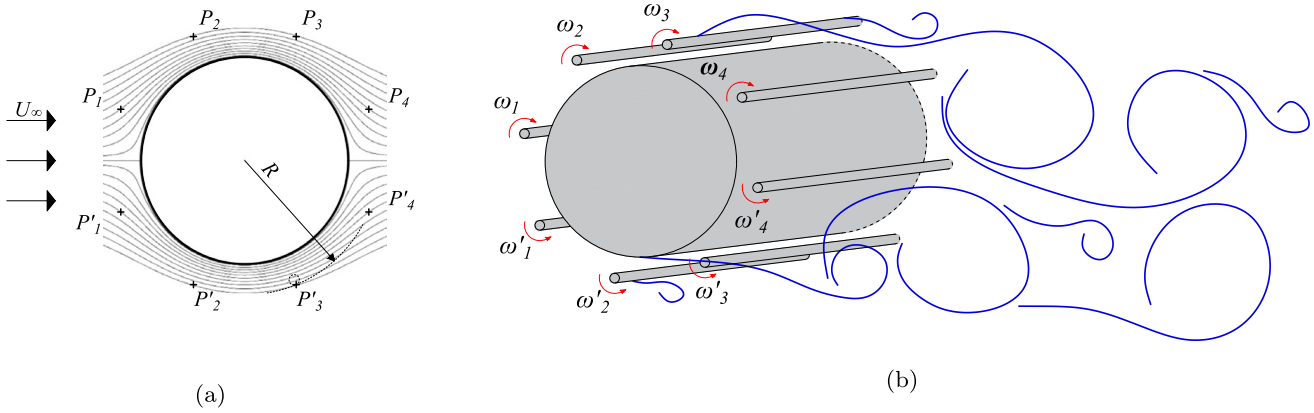

Fig. 2. (a) Streamlines of the potential flow around a bare cylinder providing velocity magnitudes at positions P_n. (b) The ratio between these velocities was imposed on case 1 to control the turbulent wake.

considerations of streamwise vorticity, which are lacking in previous analyses. We now follow this thread and retain the potential-flow-inspired angular speeds, but for a turbulent regime (as opposed to laminar regime in Carvalho et al., 2021) and seek to evaluate how the system of Fig. 1 responds in turbulent flows.

1.1. Objective

The present paper focuses on the flow response to a progressive increase in the angular velocities of the eight control rods placed around the main body, as shown in Fig. 1. Our motivation is to explore this active mechanism for wake control and suppression of vortex shedding. More specifically, we are concerned with the effect of imposing rotation speeds inspired by the solution of the inviscid flow around the main body, and its impact on turbulent flow at $Re = 10^3$. This setup is compared with another, constrained to the same input kinetic energy, where all rods spin at an uniform rate. Hydrodynamic loads, wake dynamics and power expenditure are principally addressed.

From previous studies, the role of the individual control rods in vortex-shedding suppression is known to differ regarding their position relative to the main body and of their spinning motion. It is taken as a premise that an optimised setup will require different contributions from each rod, thus it is of interest to comprehend if a potential-flow-inspired configuration may lead the system closer to an optimal operating condition.

2. Method

Fig. 1 illustrates the object of this study: the main circular cylinder of diameter D is fitted with eight peripheral rods of diameter $d = D/20$, distanced by a gap $G = D/100$ from the central body. Angular velocities are denoted ω_n and $\omega'_n = -\omega_n$ ($n = 1$ to 4), corresponding, respectively, to the upper rods at positions P_n (that spin clockwise) and to the lower rods at P'_n (which rotate counter-clockwise). The entire system was subjected to an incoming flow of velocity U_∞. The rods were uniformly separated from each other and neither of them rested on the stagnation regions. The convention adopted for the angle θ, as displayed in Fig. 1, used a positive orientation clockwise with $\theta = 0°$ at the frontal stagnation point.

The number of $N = 8$ control rods in this study followed the most successful configuration in VIV suppression found by Silva-Ortega and Assi (2017a). The selected gap was that of greatest mitigation of VIV response and drag carried out in the parametric study by Silva-Ortega and Assi (2017b). The chosen diameter d was based on the work of Assi et al. (2019), which produced enough interaction with the shear layers of the central body at a local low Re based on the rod diameter (also employed by Korkischko and Meneghini, 2012).

In the present work, two cases have been considered:

- **Case 0 - "uniform"**: All 8 rods were forced to rotate at the same angular velocity given by $|\omega_0|$ (considering their local clockwise and counter-clockwise directions). This case followed the approach employed by Assi et al. (2019), but with a different gap and flow regime.
- **Case 1 - "potential"**: The rods were forced to rotate at different angular velocities ω_n, specified in analogy to the solution of the potential flow over a bare cylinder, following Carvalho et al. (2021). The overall kinetic energy was the same as for case 0.

Rotation rates of case 1 were defined in the following manner: The velocity field from the potential flow about a plain cylinder was solved for positions $R = D/2 + G + d$ away from the axis of the main cylinder, as marked in Fig. 2(a) by small crosses. Consecutively, the rods were placed around the main body and the system was inserted in the turbulent flow at Reynolds number $Re = U_\infty D/\nu = 10^3$, where ν is the kinematic viscosity of the fluid and D is the diameter of the

main body, as shown in Fig. 2(b). Note that the wake becomes turbulent for $Re > 200$, as highlighted by Williamson and Roshko (1988).

In doing so, it was considered that: (i) ω_n were set so that the input kinetic energy of cases 0 and 1 were the same for every ζ (defined later). (ii) A fixed rotation ratio of $\omega_2/\omega_1 = \omega_3/\omega_4 = 2.41$ was determined by the potential flow around a bare cylinder, meaning that the tangential velocity on the spinning rod was that from the inviscid velocity field at the marked positions.

In order to spin all the rods faster at once, their angular velocities were multiplied by the parameter ζ, which varied from 0 to 5. For case 0, ζ directly represented the tangential velocities of all rods normalised by the far-field velocity, i.e., U_n/U_∞. More details on this potential analogy (in a laminar regime) are found in Carvalho et al. (2021).

2.1. Numerical scheme

The numerical scheme allowed for the resolution of the Navier–Stokes equations of momentum transport and the continuity equation, respectively given by

$$\rho\left(\frac{\partial U_i}{\partial t} + U_j\frac{\partial U_i}{\partial x_j}\right) = -\frac{\partial p}{\partial x_i} + \mu\frac{\partial^2 U_i}{\partial x_j \partial x_j}, \tag{1}$$

$$\frac{\partial U_j}{\partial x_j} = 0. \tag{2}$$

These equations were discretised and integrated over control volumes by means of the finite volume formulation. Simulations were carried out with the OpenFOAM library. The Eulerian time-transient term was discretised with a fully implicit backward scheme. The divergence scheme was comprised of a blend made up of 25% of the linear upwind scheme and 75% of the central scheme. For turbulent quantities, the linear upwind scheme was used. Gradients were obtained from a cell-based least squares method. Laplacian terms were discretised according to unbounded Gauss theorem, together with linear interpolation. Correction for non-orthogonality (between a cell interface and the line connecting cell centres) was also applied. Discretisation of all the aforementioned terms involved second-order truncation error (Versteeg and Malalasekera, 2007).

For pressure–velocity coupling required in incompressible flows, the unsteady version of the SIMPLE algorithm (Patankar, 1980) was used for all simulations, and 10 corrector steps were considered without relaxation. The reference simulation of a plain cylinder was iterated to a maximum tolerance of 10^{-6} for the pressure. However, for the entire system of cases 0 and 1, a more relaxed 10^{-4} tolerance was imposed to the same field. These two levels of tolerance were simulated and generated the same results (omitted here for briefness), so for faster run times the 10^{-4} maximum residual was kept for the pressure. For all other fields, a 10^{-8} tolerance was met at the end of every time step.

Time steps were set to concomitantly capture at least 100 parts of the Strouhal period $T_S = (D/U_\infty)/St$ (where the Strouhal number $St \approx 0.2$ in sub-critical regime) and 70 parts of every revolution of the rods. In this matter, two points must be acknowledged: (i) The small rods were on the threshold of vortex shedding (which occurs around $Re = 50$, precisely equal to the Reynolds related to the rods' diameter, $Re_d = Ud/\nu = 50$), therefore T_S is based on the main body. (ii) *A priori*, it can be assured that for configurations with high rotation rates the three-dimensional, small-scale vortical flow structures were weakened as vortex shedding was suppressed, thus justifying the lower requirement for capturing the rotations.

Convergence was obtained for all simulations, and the last 30 cycles of vortex shedding were considered for mean and root mean square (RMS) computations. In order to comply with CFL conditions, the restrictive condition of a maximum Courant number of 0.98 was imposed. It was usually this condition that limited the time step sizes (over other less stringent time step conditions mentioned above).

It follows from the work of Carmo and Meneghini (2006) that 3D simulations are vital to properly incorporate the effects of vortical structures on the fluid loads for $Re > 190$. For cost-effective 3D simulations involving turbulence scales, the Detached Eddy Simulation (DES) formulation was elected (Spalart, 1997) for a good compromise between physical results and reasonable computational effort. This approach resolved the large (detached) eddies, while the boundary layer was modelled by means of the unsteady Reynolds-Averaged Navier–Stokes (URANS) equations. For small scales away from the boundary layer, the classical SGS model of Smagorinsky (1963) was used, whereas for the URANS-part, the one-equation model of Spalart and Allmaras (1992) allowed for the transport of the turbulent viscosity parameter and related it to the turbulent viscosity. Moreover, this model allowed to capture separation and reversed pressure gradient.

A major problem in the DES formulation for the flow about cylindrical structures in sub-critical regime is that the boundary layer is laminar whereas the wake is already turbulent (Williamson and Roshko, 1988), and the URANS formulation for the boundary layer is intrinsically turbulent. This downside was circumvented by a low-Reynolds correction (Spalart et al., 2006).

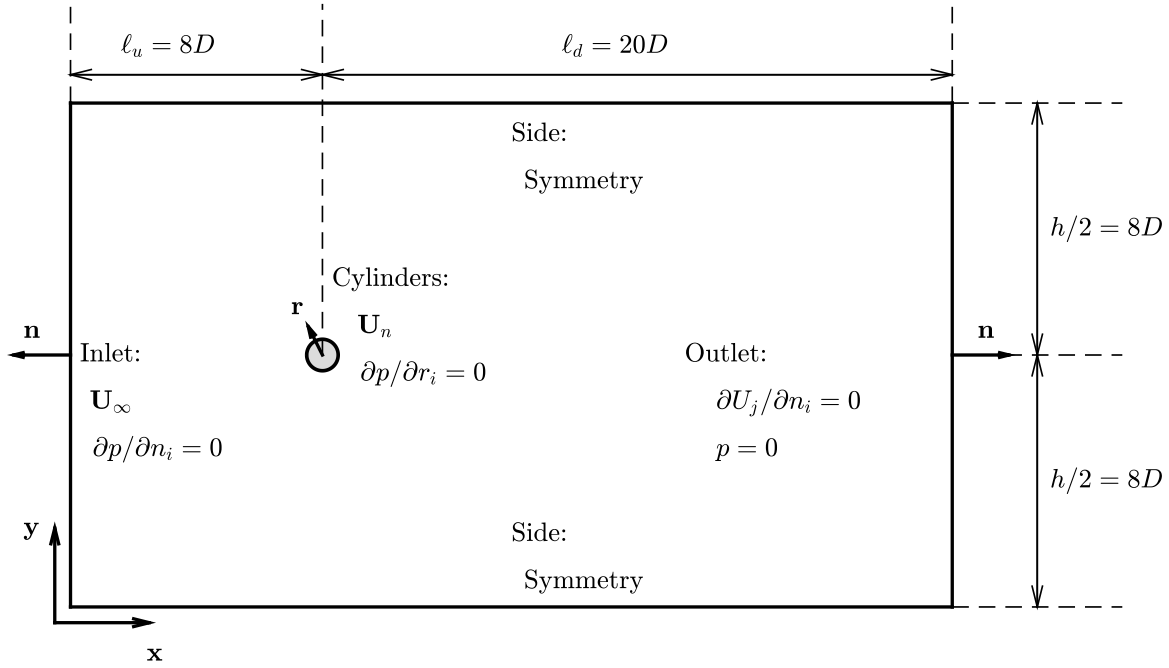

Fig. 3. Flow domain and boundary conditions. Control rods are not represented for clarity.

Table 1
Grid information. The total number of cells corresponds to that resulting from the spanwise extrusion of the cross-sectional grid. The smallest element size relates to y^+.

	Number of cells		Smallest element
	Cross-section	Total	
Bare cylinder	49,204	2,361,792	$1.00 \times 10^{-3}D$
System	130,004	6,500,200	$1.54 \times 10^{-3}D$ (main body) $3.77 \times 10^{-3}d$ (control rods)

2.2. Boundary conditions and meshes

Boundary conditions are introduced schematically in Fig. 3 for the cross section (x–y plane) of the extruded grid, both for the reference simulation of a plain cylinder and for the entire system.

Free stream velocity (uniform and constant) and zero pressure gradient were applied to the inlet; conversely, a Dirichlet condition was imposed to the outlet pressure, and Neumann's to the velocity. On the upper and lower sides, a symmetry condition prevailed. On the surface of the cylinders, the flow velocity matched the tangential velocity of the cylinders $U_n = \omega_n\, d/2$. Finally, the pair of front and back faces generated by the extrusion of the mesh (in the z-direction) were coupled by means of a periodic condition. The appropriate boundary conditions used for the turbulent quantities were those of Spalart (2000) and Vatsa et al. (2017), respectively, $\tilde{\nu}_{\text{wall}} = 0$ and $3 < \tilde{\nu}_\infty/\nu_\infty < 5$.

The structured meshes used in this work had lateral ($h/2$) and upstream (ℓ_u) boundaries distanced $8D$, and ample outflow distance $\ell_d = 20D$, away from the centre of the cylinder to avoid blockage effects (see Fig. 3). These values are in agreement with (Behr et al., 1995, 1991). Sizes of the smallest elements – related to boundary layer refinement – sitting on the surfaces of the main body and rods are supported by Table 1 along with further information. All simulations preserved $y^+ < 1$, the non-dimensional distance away from the walls of the cylinders. Figs. 4 and 5 expose the cross-section of the meshes, focused on the fluid domain and on close-ups, respectively.

The meshes were extruded for a spanwise length $L = \pi D$ following Assi et al. (2018) for a system similar to the one here. The number of layers in this direction for the case of the plain cylinder (48) came from the work of Saltara et al. (2011). For the entire system 50 layers were used. Fig. 6 portrays the extruded mesh (the extrusion of the rods is not represented for clarity).

2.3. Grid independence, verification and validation

Mesh convergence analysis, validation and verification procedures were performed for the reference case of a plain cylinder subjected to oncoming uniform flow at $Re = 10^3$. For the same Re, only mesh convergence was verified for

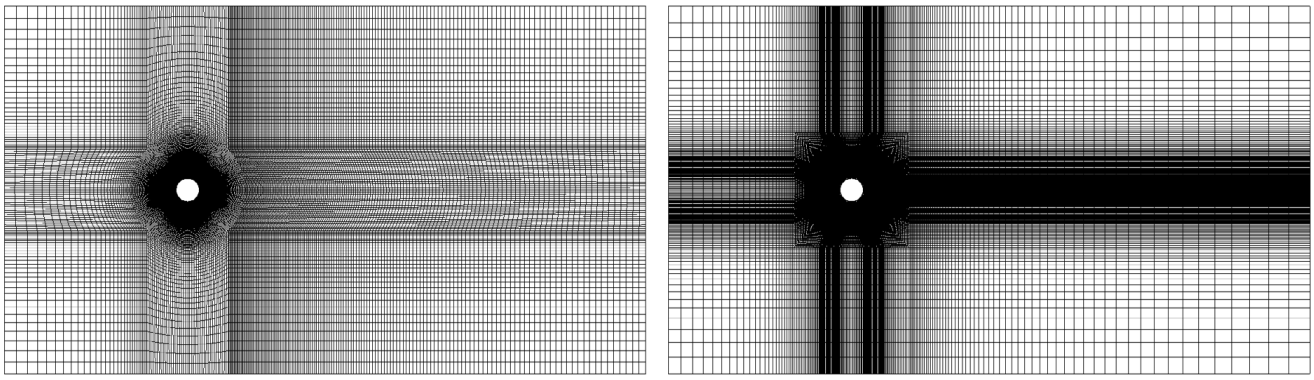

Fig. 4. Grids used for the simulation of the bare cylinder (left) and of the entire system (right).

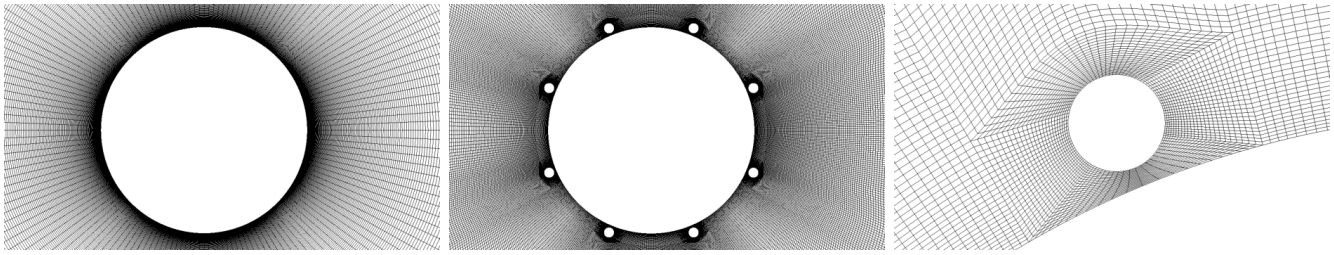

Fig. 5. Close-up grids around (a) the bare cylinder, (b) the entire system, and (c) a control rod.

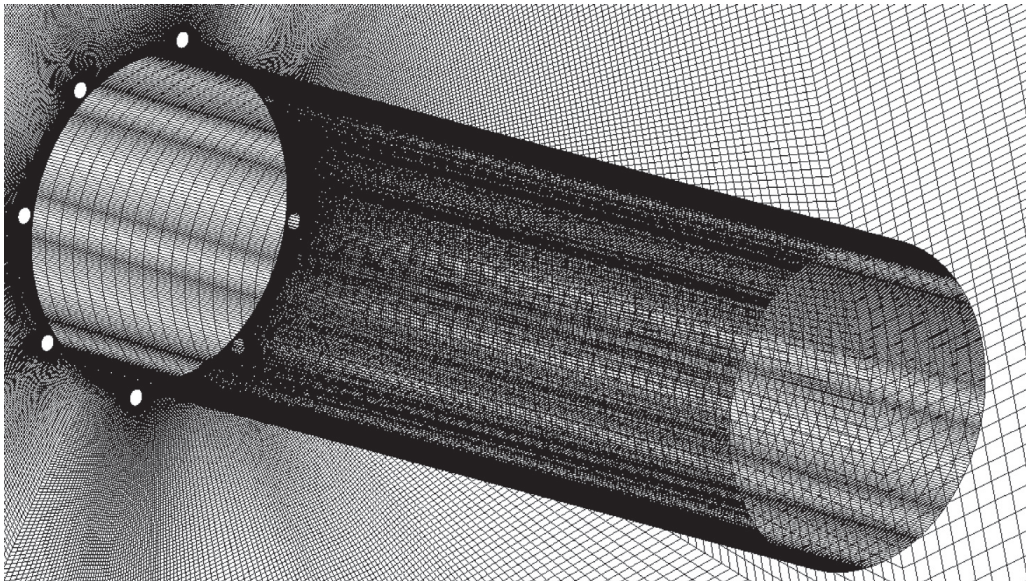

Fig. 6. Extrusion of the grid. Only the main cylinder's extrusion is depicted for ease of visualisation.

the entire system. Simulations were conducted for at least $50T_S$ (for the more refined mesh), and $20T_S$ were awaited for convergence. Mean and RMS quantities were computed thereafter.

All meshes of Table 2 were constrained to a first element of size $D/1000$ orthogonal to the surface of the cylinder (as presented in Table 1). It was noted that (i) data displayed by Tables 2 and 3 (the latter shall be discussed shortly) brought close values with mesh refinement. This was more pronounced for the mean drag ($\overline{C}_D$), which is of utmost interest to this paper, with variance below 3%. And (ii) the mesh used in the work of Saltara et al. (2011) was coarser than the ones invested in this paper and they all shared the same size of the first cell near the wall. In view of these two remarks, we deem the present convergence analysis sufficient for the bare cylinder case and select the mesh with 49,204 elements as reference for the forthcoming comparisons.

Table 2
Mesh convergence in terms of the mean drag ($\overline{C}_D$) and RMS of the fluctuating lift ($\hat{C}_L$). Percentages in parentheses refer to the comparison of a given mesh with the most refined one hereby analysed. Only the number of cells in the cross section (x–y plane) is disclosed, which was extruded for 48 layers in the spanwise z-direction.

Number of cells	$Re = 10^3$		$Re = 10^4$	
	$\overline{C}_D$	$\hat{C}_L$	$\overline{C}_D$	$\hat{C}_L$
27,854	1.00 (0.0%)	0.14 (16%)	1.10 (0.90%)	0.17 (19%)
39,224	1.00 (0.0%)	0.11 (8.3%)	1.13 (1.8%)	0.23 (9.5%)
49,204	1.00 (0.0%)	0.12 (0.0%)	1.11 (–)	0.21 (–)
67,504	1.00 (–)	0.12 (–)		

Table 3
Validation of the reference simulation of a bare cylinder. The maximum value of y^+ was 0.16.

	$\overline{C}_D$	$\hat{C}_L$	St
Jordan and Fromm (1972)	1.24		0.21
Braza et al. (1986)	1.1–1.2		0.21
Norberg (2001)		0.10–0.30	0.21
Cantwell and Coles (1983)	1.00		
Wieselsberger (1921)	1.00		
Present work (3D DES)	1.13	0.24	0.21

Table 4
Assessment of blockage effects for a wider flow domain.

ℓ_d/D	h/D	$\overline{C}_D$	$\hat{C}_L$	St	$y^+_{\max}$
20	16	1.13	0.24	0.22	0.16
30	32	1.08	0.22	0.22	0.15

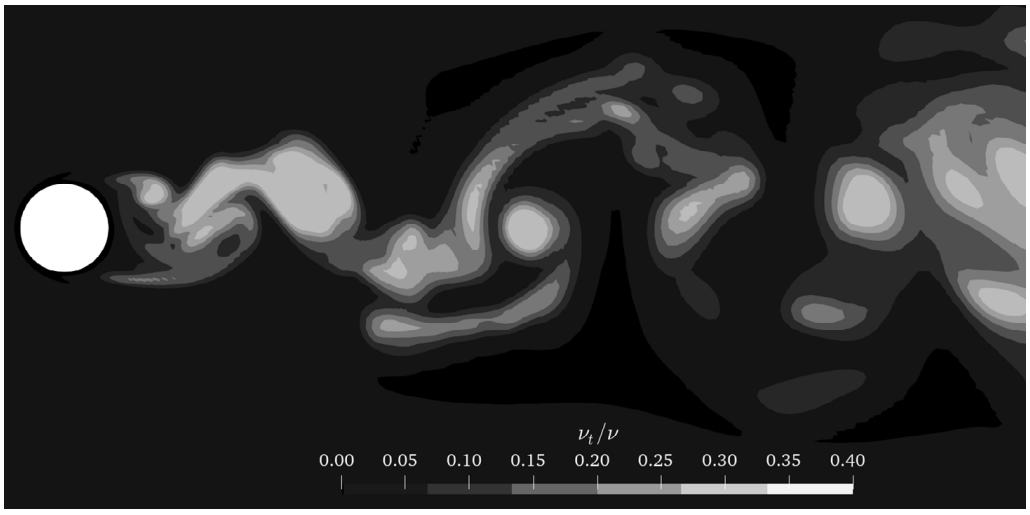

Fig. 7. The ratio ν_t/ν shows a negligible value of ν_t near the wall and the expected wake transition downstream of the system.

Verification and validation of this mesh confirms through Table 3 that the reference simulation agreed well with both numerical (first two references of the table) and experimental data (other references) in regard to mean drag ($\overline{C}_D$), RMS of the fluctuating lift ($\hat{C}_L$) and Strouhal number (St). Although $\overline{C}_D$ was a little overestimated when contrasted with experimental values, it agreed well with numerical works.

Blockage effects were not extensively evaluated. Instead, results from previous studies concerned specifically with the adequate size of the domain (Behr et al., 1995, 1991) were used. The same simulation was run for a wider domain with $l_d/D = 30$ and $h/D = 32$. As Table 4 points out, no significant difference was perceived.

The effect of the low-Re correction applied in this DES formulation became evident in light of Fig. 7, where a laminar boundary layer is revealed ($\nu_t/\nu \approx 0$), while transition to turbulence occurred downstream in the wake.

Additional simulations, omitted here for conciseness, were run the bare cylinder for $Re = 10^4$ and 10^6. We simply outline that the results, in terms of the featured quantities of Table 3, corroborated to the validity of our meshing and numerical scheme.

Table 5
Mesh convergence in terms of $\overline{C}_D$ and $\hat{C}_L$ for the entire system. Percentages in parentheses refer to the comparison of the respective mesh with the most refined grid hereby analysed. The number of cells in the cross section was extruded for 50 layers in the spanwise z-direction.

Number of cells (in the x–y plane)	$\overline{C}_D$	$\hat{C}_L$
53,632	1.79 (2.2%)	0.597 (3.5%)
61,828	1.87 (2.2%)	0.691 (12%)
99,092	1.87 (2.2%)	0.692 (12%)
130,004	1.83 (0.0%)	0.616 (0.44%)
150,544	1.83 (–)	0.618 (–)

For the entire system, only grid independence was investigated, due to the lack of data for this setup in the literature for validation and verification. The same numerical scheme and grid refinement were employed as in the simulations of the bare cylinder. As compiled by Table 5, the results converged in terms of $\overline{C}_D$ and $\hat{C}_L$, with largest discrepancy between the more refined meshes just over 3%. In any simulation of this table, y^+ remained below 0.8 and Courant number below 0.99. The grid with 130,004 cells on the 2D plane (and 6,500,200 in total) was favoured for all simulations involving control rods. Results from a parallel grid evaluation, conducted in laminar regime for this same grid, supported the present analysis and agreed with the unstructured mesh of Carvalho et al. (2021) (suppressed here for conciseness).

3. Results

3.1. Effect of the control rods on vortex shedding

Simulations were run for 50 Strouhal periods (T_S) during each ζ-regime of cases 0 and 1, except for $\zeta = 0.0$ where $65T_S$ were considered. Transition from one regime to the next was allowed such that the flow field at the end of one simulation was mapped as startup for the subsequent one, thus providing lower iteration count at the beginning of each regime, as it was previously done by Mittal (2001). Time histories shown in Fig. 8 illustrate the effect of reducing both drag and lift coefficients as the control rods spun faster. Numerical transients at the start of the simulations were disregarded for mean and RMS computations. Fig. 8 also highlights a distinctive aspect between the cases: The mean drag acting on the system in case 1 was clearly lower than in case 0, and vortex-shedding suppression was achieved with lower input kinetic energy in case 1 ($\zeta = 3.0$) compared with case 0 ($\zeta = 4.0$).

Fig. 9 shows the wakes of the reference case (bare cylinder) and that of the system with the peripheral devices in case 1 starting from a passive condition in which the rods were fixed, $\zeta = 0.0$, up to rotations able to suppress the vortex street, represented by $\zeta = 3.0$. Simply fitting the static control rods around the main cylinder produced a wider wake and the shortening of the vortex-formation length. Larger vortical structures were convected to the far wake when compared to the reference case, where smaller vortices were discernible downstream in Fig. 9.

However, as the rods started to spin, the wake narrowed from $\zeta = 1.0$ onwards and the vortex-formation region was elongated. Prolongation of the shear layers downstream led vortices to emanate farther away from the system. Consequently, the vortex wake lost strength due to viscous dissipation of vorticity concentrated in and carried by the shear layers.

Similar analyses to this one were made in laminar (Assi et al., 2019; Carvalho et al., 2021) and turbulent regimes (Assi et al., 2018). Strictly focused on the hereby denoted *case 0*, Assi et al. (2018) obtained reduction in vortex shedding at $Re = 10^4$, but did not suppress it.

The shedding frequency f_s, represented by the Strouhal number $St = f_S/(U_\infty/D)$ in Fig. 10, quantified the behaviour illustrated in Fig. 9. For $\zeta > 0.5$, St increased for both cases due to narrower wakes with longer vortex-formation lengths. As pointed out by Williamson (1996), St scales inversely with wake width and formation length. As ζ approached 0.9, St for the entire system of case 1 approached that for a bare cylinder, whereas for case 0 this only happened after $\zeta = 1.0$. This increase of shedding frequency was detected up to $\zeta = 3.0$, and $\zeta = 2.5$, respectively, for cases 0 and 1.

A steeper rise of St occurred in case 0 beyond $\zeta = 2.5$, reaching $St \approx 0.67$ for $\zeta = 3.0$. For $\zeta \geq 4.0$ vortex shedding was completely suppressed producing $St = 0$, which is marked by the dark-grey area in the plot. Case 1 achieved vortex suppression ($St = 0$) for $\zeta \geq 3.0$, marked by the light-grey area Fig. 10. Perhaps a sharp increase of St could also have been found for case 1 if another data point were produced between $\zeta = 2.5$ and 3.0. Vortex shedding is not expected to return for ζ higher than these critical values.

3.2. Active control of the three-dimensional wake

Fig. 11 presents a three-dimensional visualisation of the turbulent structures in the flow by means of the Q-criterion (following Hunt et al., 1988, here$Q = 0.1$). A gradient ranging from black to white points to the relative importance of the turbulent viscosity against the molecular one, ν_t/ν. Firstly, the figure recalls the aspect portrayed

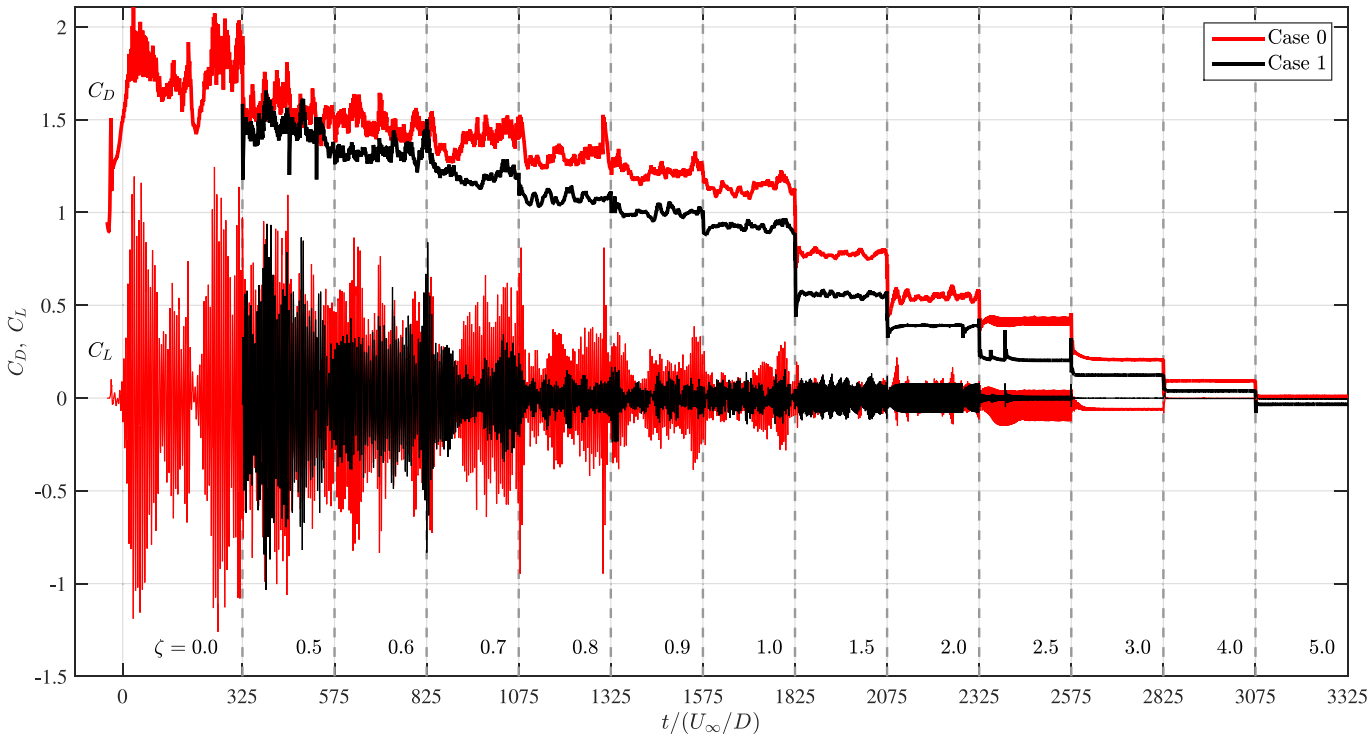

Fig. 8. Time histories of lift (thin line) and drag (thick line) acting on the entire system for cases 0 and 1. Each rotation was run for $50T_S$. The different rotation regimes are distinguished by dashed vertical lines.

by Fig. 9, i.e., vortex-shedding suppression. Secondly, transition of the wake past the system stands out, highlighting white-coloured eddies (greater ν_t/ν) being formed closer to the system with the passive mechanism, compared with the reference case. At the same time, the presence of smaller structures away from the system was reduced.

One must bear in mind that, with the presence of the passive rods, the wake was correspondingly shortened lengthwise, so turbulence was produced earlier. However, as the rods started to spin, turbulence was dissipated, as shown by the white-coloured eddies gradually fading into black and ν_t/ν approached 0. As a matter of fact, $\zeta = 1.5$ depicted the suppression of almost all small-scale turbulent structures, and anticipated the highly correlated, two-dimensional flow condition verified for $\zeta \geq 2.0$. Higher rotation speeds achieved complete suppression of vortex shedding; at $\zeta = 3.0$ the Q-contours were only marginally visible in the neighbourhood of the rods. Suppression of vortex shedding was verified for ζ up to 5.0, not shown here for briefness.

Vortex dynamics is further illustrated in Fig. 12 for case 1 configurations in which the rods were progressively rotated at $\zeta = 0.0$, 1.0, 2.0 and 2.5. The summary of this figure is that with faster spinning of the rods, the wake transitioned from a rich three-dimensional state to another stated dominated by coherent, two-dimensional vortex tubes (succeeded by complete suppression verified for $\zeta = 3.0$, not shown in this figure). For the four ζ-regimes in each column, the evolution of a vortex tube can be followed in time through the white stars as it is convected downstream from the body (grey body on the left of each snapshot).

Beyond this general description, two others aspects are worth attention. The first is that for $\zeta = 0.0$ and $\zeta = 1.0$, respectively, the first and second columns of Fig. 12 capture an easily-presumed spectral distribution of a turbulent wake, represented by the smaller scales in the near wake in random-like motion, promptly dissipated; and larger scales in the far wake, travelling in close alignment with the free stream direction. Of course, the colour gradient announces a vorticity distribution that is also within expectation. Ranging from blue to red (see colour key), it depicts respectively, low to high vortical content found, correspondingly, in large to small scales.

The second aspect is that $\zeta = 2.0$ allows one to appreciate a different wake development (third column of Fig. 12). As the vortices were convected downstream, *'vortex dislocations'* were observed. These vortex structures reminded the wake dynamics associated with the *mode B* instability, as denoted by Williamson (1996), with "finer-scale streamwise vortices". In their formation, a downstream row of vortices feeds back on the upstream row by means of these *vortex pairs* until their elimination by viscous dissipation. This mechanism of vorticity transfer between streamwise vortices can be seen in Fig. 13, reminiscent of the direct simulation of Zhang et al. (1995) apud Williamson (1996).

Interestingly, Williamson (1996) located this topology in the *wake-transition regime* of a bare cylinder ($230 \leq Re \leq 250$) with spanwise wavelength of the order of $1D$, whereas the present results were obtained on the intersection with a *shear-layer transition regime* ($10^3 \leq Re = 2 \times 10^5$) with wavelength of about $0.7D$. Longer formation length than that of Unal and Rockwell (1988) would be expected in the reference case for the same *Re*, but the opposite is observed here for the

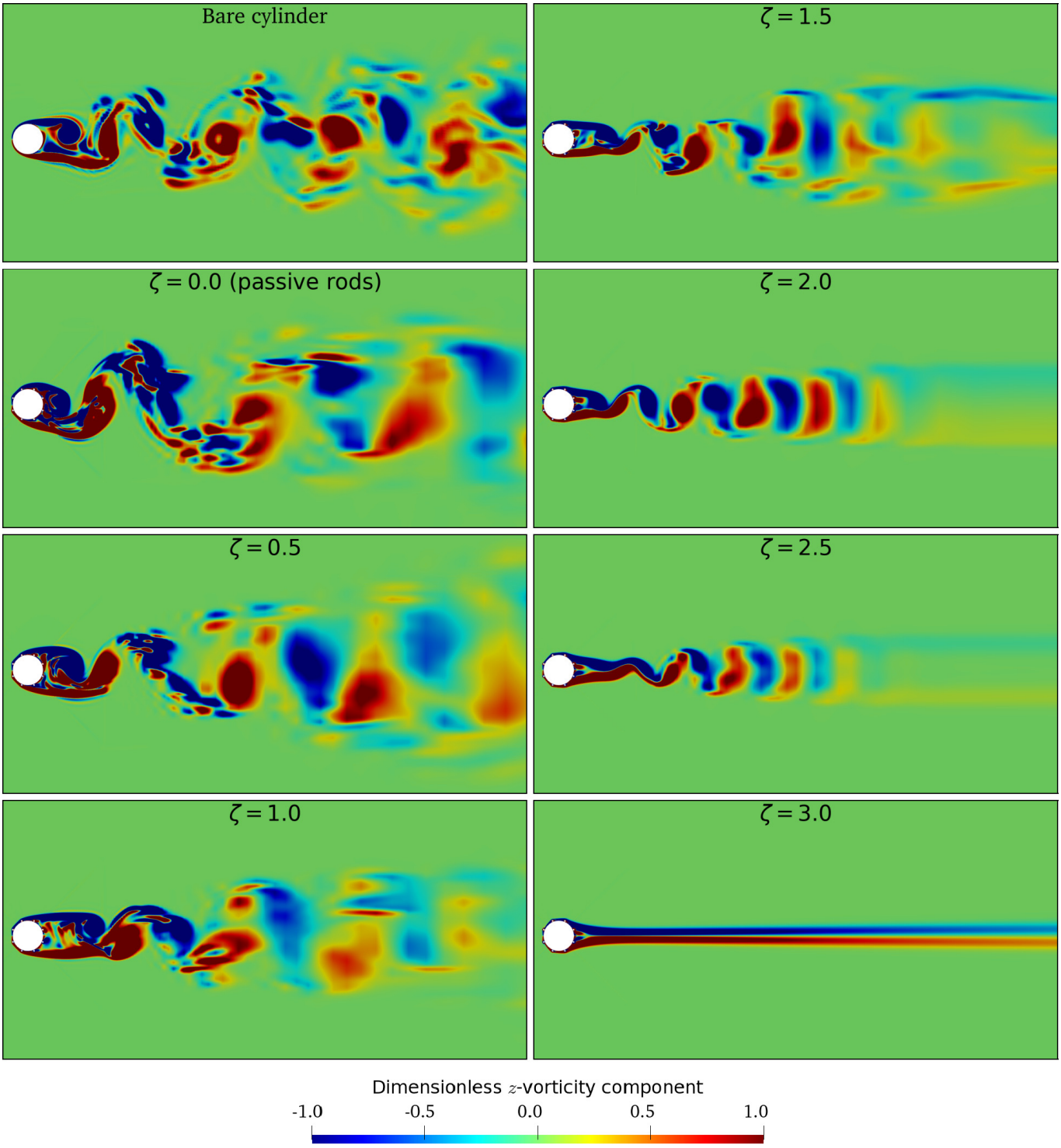

Fig. 9. Contours of dimensionless z-vorticity component (normalised by U_∞/D) for the reference case (head figure) and for the system with wake-control rods of case 1.

entire system (Fig. 14). Also in opposition is the growing St, as previously verified in Fig. 10. This pattern of streamwise vortices was not observed earlier for systems such as the present.

It appears that the rods effectively "lower the *Re*-regime". For the present flow regime they not only prevented shear layer transition, but also wake transition, given enough power input. High ζ-regimes resemble the visual character of low-*Re* flow past circular cylinders.

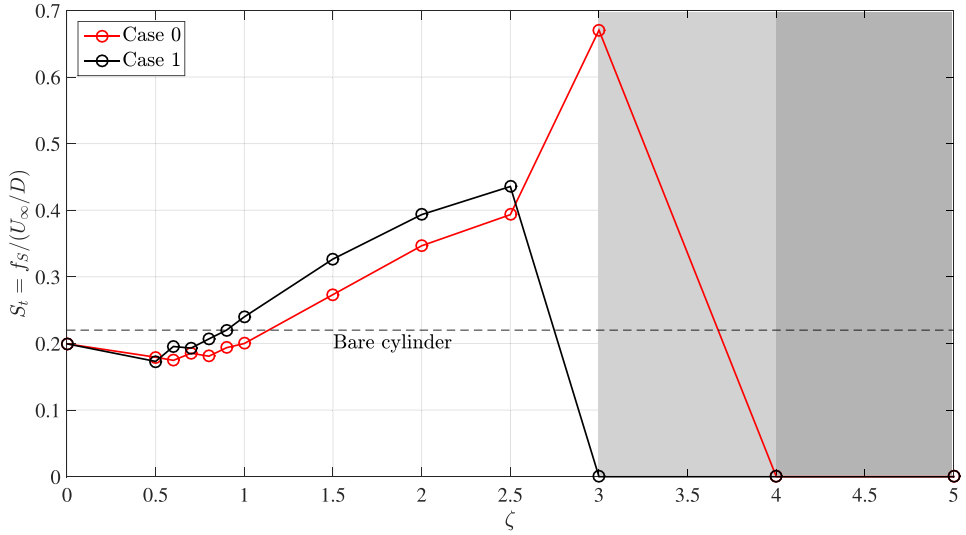

Fig. 10. Variation of the dimensionless frequency with angular velocities. The onset of suppression for case 1 is represented by the lighter shading, while the darker one corresponds to that of case 0.

3.3. Decrease in hydrodynamic loads

Mean drag and RMS of the fluctuating lift on the peripheral rods altogether, on the main cylinder and on the entire system are presented in Fig. 15. The rods behaved collectively oblivious to the shift from the setup of case 0 to the potential-flow-inspired case 1, aside from the following nuances: higher $\overline{C}_D$ (less negative) in case 1 for $\zeta \geq 2.0$, and lower $\hat{C}_L$ in case 1 for $0.5 \leq \zeta \leq 1.0$ and $2.0 \leq \zeta \leq 4.0$.

In contrast, the analysis differs for the main cylinder and for the entire system: The new setup (case 1) reduced mean drag for the entire ζ-range. As for the lift, case 1 was either comparable to case 0 ($\zeta = 1.5$ and 2.0) or presented lower $\hat{C}_L$ (other values within $\zeta \geq 0.5$). A rather curious deviation from sheer decay in case 0 took place in $\hat{C}_L$, at $\zeta = 0.7$ (see Fig. 15(b)). This was previously reported in Assi et al. (2018) (there, also in regard to $\overline{C}_D$) and invites further investigation. Incidentally, it was at this value of ζ for the main cylinder of case 1 that $\overline{C}_D = 1.16$ roughly equalled the baseline case and $\hat{C}_L = 0.059$ was lower.

We now focus on the loads acting on the entire system. An increase in the angular speeds to $\zeta = 2.5$ led to merely residual vortex-shedding for case 1 accompanied by almost zero fluctuating lift, whereas for case 0 there was a rise in the $\hat{C}_L$ that gradually fell to 0 as ζ approached 4.0. Fig. 15 also renders three further remarks: (i) A setup with $\zeta = 0.7$ already attenuated $\hat{C}_L$ to approximately half of the value of the reference case (Fig. 15(b)), while $\overline{C}_D$ remained virtually at the same value (1.19 against 1.13, see Fig. 15(a)). A similar behaviour was observed for case 0 only after $\zeta = 1.0$; (ii) Suppression of vortex shedding was succeeded by complete elimination of the mean drag at the upper end of the ζ range. (ii) Sufficient rotation of the control rods slightly inverted the drag and thus produced thrust on the entire system, as verified for $\zeta = 5.0$ with $\overline{C}_D = -0.034$. For the present system, drag inversion was previously observed only for laminar regimes (Assi et al., 2019).

3.4. Resultant forces

Now our attention is directed to the total force applied on every rod of case 1. Fig. 16 represents only the upper part of the entire system, since the other half is symmetric by design. In this figure, the radial forces are probably due to the Magnus effect, as the spinning motion altered the pressure distribution on the surface of the rotating rods. The figure schematically reveals that the strongest individual contributions (coloured arrows) distinctly came from the intermediate rods P_2 and P_3, followed in much less magnitude by P_1 and P_4. Departing from the reference case, one might argue that P_1 was located close to a stagnation region, and P_4 was placed within the wake, hence their lower contributions to wake control (Cicolin et al., 2021). Contrarily, P_2 and P_3 strongly interacted with the separation region, comprehended between them (Thompson and Hourigan, 2005; Cao et al., 2010), as they surrounded the (upper) 'shoulder' of the bluff body. Moreover, P_2 and P_3 interacted with the incipient shear layer. Therefore, P_2 and P_3 bore most of the hydrodynamic loads supported by the rods to control the wake that would otherwise form between them, and they further displaced the separation point aft the entire system.

Furthermore, drag inversion is apparent for P_2 and P_3 in Fig. 16. Propulsion of P_1 and P_2 developed with sufficient angular velocity, and led to an imbalance between left- (P_1 and P_2) and right-meridian (P_3 and P_4) rods in terms of streamwise force component. Eventually, this difference built up into thrust on the entire system, as can be interpreted from the respective arrows in greyscale acting on the main body. For this range of values of ζ, the same phenomenon

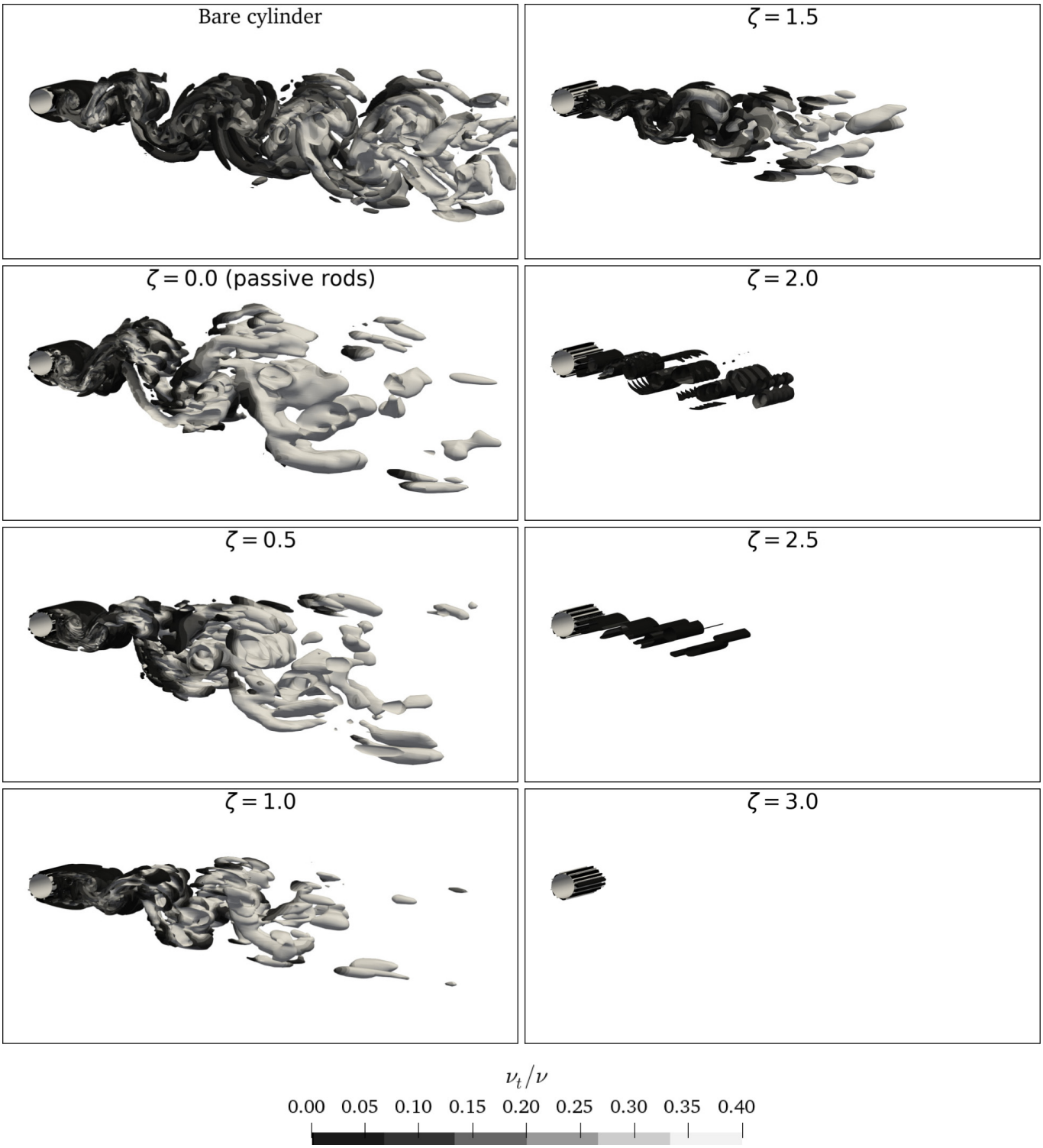

Fig. 11. Q-criterion for vortex visualisation of case 1. Contours of $Q = 0.1$ are coloured according to ν_t/ν. From the passive ($\zeta = 0.0$) to the most active mechanism ($\zeta = 3.0$) the mitigation of turbulent structures becomes evident.

was not exhibited by case 0 (as shown in Fig. 15(a)). For both main cylinder and the entire system, the magnitude of the resultant force was reduced with larger ζ. It is interesting to note, from Figs. 15(a) and 16, that a negative $\overline{C}_D$ was obtained for the entire system of case 1 when $\zeta = 5.0$ (shown by a small reversed arrow in Fig. 16), meaning that so much energy was put into the system to generate a small propulsion on the system. This phenomenon was also observed in the experimental investigation performed by Silva-Ortega and Assi (2017b) at moderate *Re*.

Of course, considerations made here also apply to the symmetrical counterparts, i.e., P_1', P_2', P_3' and P_4' and the same behaviour was followed in case 0 (not shown here for briefness).

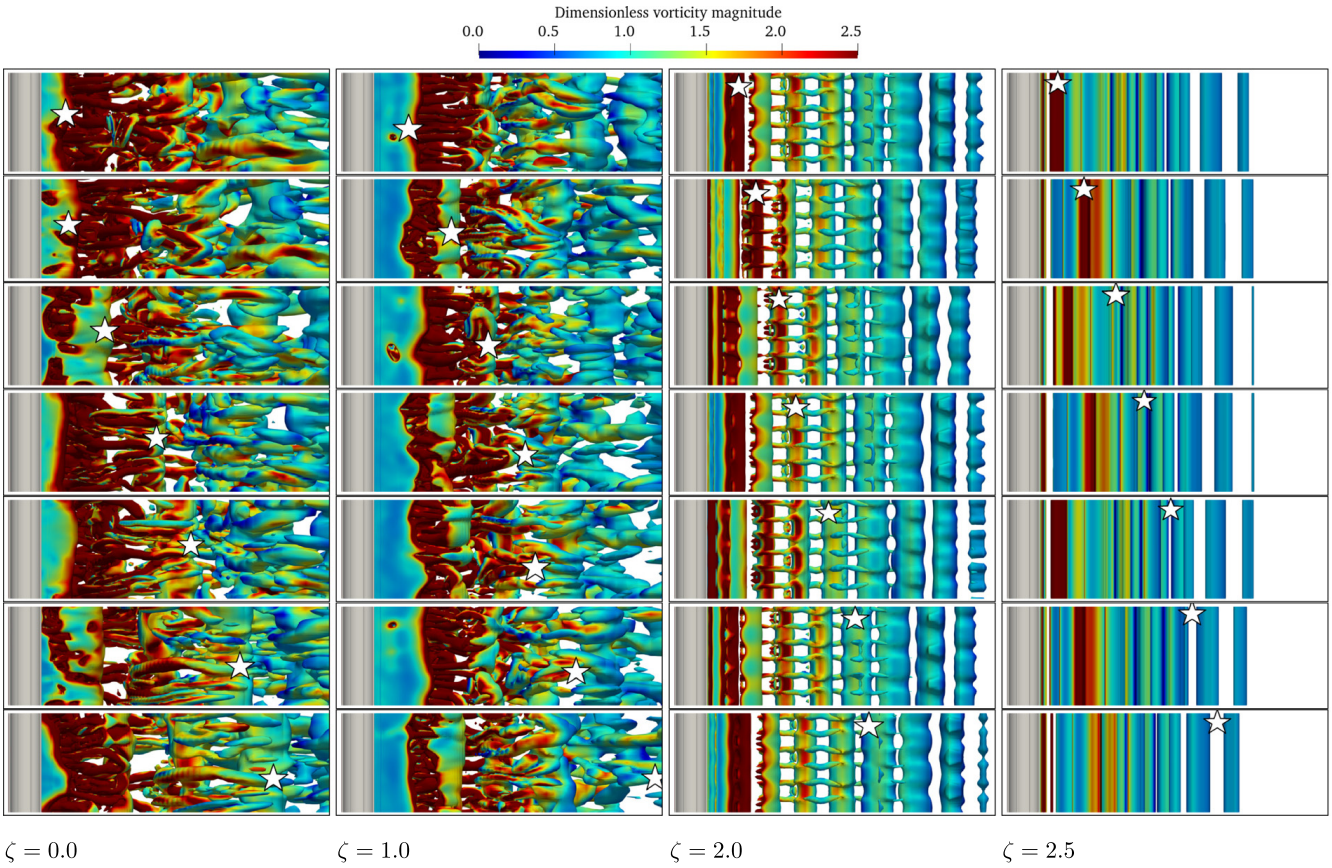

Fig. 12. Q-contours ($Q = 0.1$) coloured by dimensionless vorticity magnitude (normalised by U_∞/D). From left to right, the columns corresponding to ζ show progressive organisation of the wake. From top to bottom, the white stars mark the motion of a typical turbulent structure travelling downstream in time (snapshots were taken at unequal time intervals). (For interpretation of the references to colour in this figure legend, the reader is referred to the web version of this article.)

This result is aligned with the similar numerical study at laminar-flow regime by Carvalho et al. (2021), inasmuch as with other works in laminar and turbulent regimes that comprised analysis only of what is denoted here *case 0* (Assi et al., 2019, 2018). Notwithstanding the confirmation of these papers, the present result further corroborates with previous hypothesis of Carvalho et al. (2021) whether a potential-inspired setup could indeed lead to the decrease in hydrodynamic loads even in turbulent regime. Indeed, the above discussion positively supports that idea.

Fig. 17 shows that case 1 produced more intense loads on the intermediate cylinders in comparison to case 0. Indeed, these cylinders responded to a much stronger combination of lift and drag in case 1 than in case 0; the greater the value of ζ, the greater was the difference between the cases. On the other hand, end rods of case 1 faced ever less representative loads relative to case 0, despite their gradual increase. For P_4, the results are in agreement with the work of Cicolin et al. (2021) for the main cylinder, even though the negative drag reported by these authors was not detected here. This may be justified in view of the different *Re* ranges, as well as on account of the near-rod flow dynamics resulting from the spinning effect, not present in Cicolin et al. (2021).

It is now of interest to examine how longitudinal and transverse components of these loads impacted every rod for higher rotation rates.

3.5. Individual and collective contributions of the control rods

Mean drag and lift coefficients are referred to in Fig. 18 for every rod. The angle θ is associated to the frontal stagnation region and its positive orientation is given clockwise (as indicated in Fig. 1), such that opposing rods are marked by opposite angles, e.g., P_1 ($\theta = 22.5°$) and P_1' ($\theta = -22.5°$), etc.

First and foremost, the figure ascertains expected behaviours from theory and previous works, such as the symmetry in mean drag (Fig. 18(a)) and antisymmetry in mean lift (Fig. 18(b)) provided by opposing rods. The general growth in magnitude can also be noted (Assi et al., 2019; Carvalho et al., 2021). Short variation in drag and lift for the end rods, and correspondingly wider change for the intermediate ones with ζ quantitatively substantiate the overall discussion of the past section.

Another aspect brought by this figure is the inversion of mean drag with an increase in ζ. This occurred for rods P_2, P_2' and P_3, P_3' (Fig. 18(a)). For the former pair of symmetrically-positioned rods, this was observed for the change in ζ from

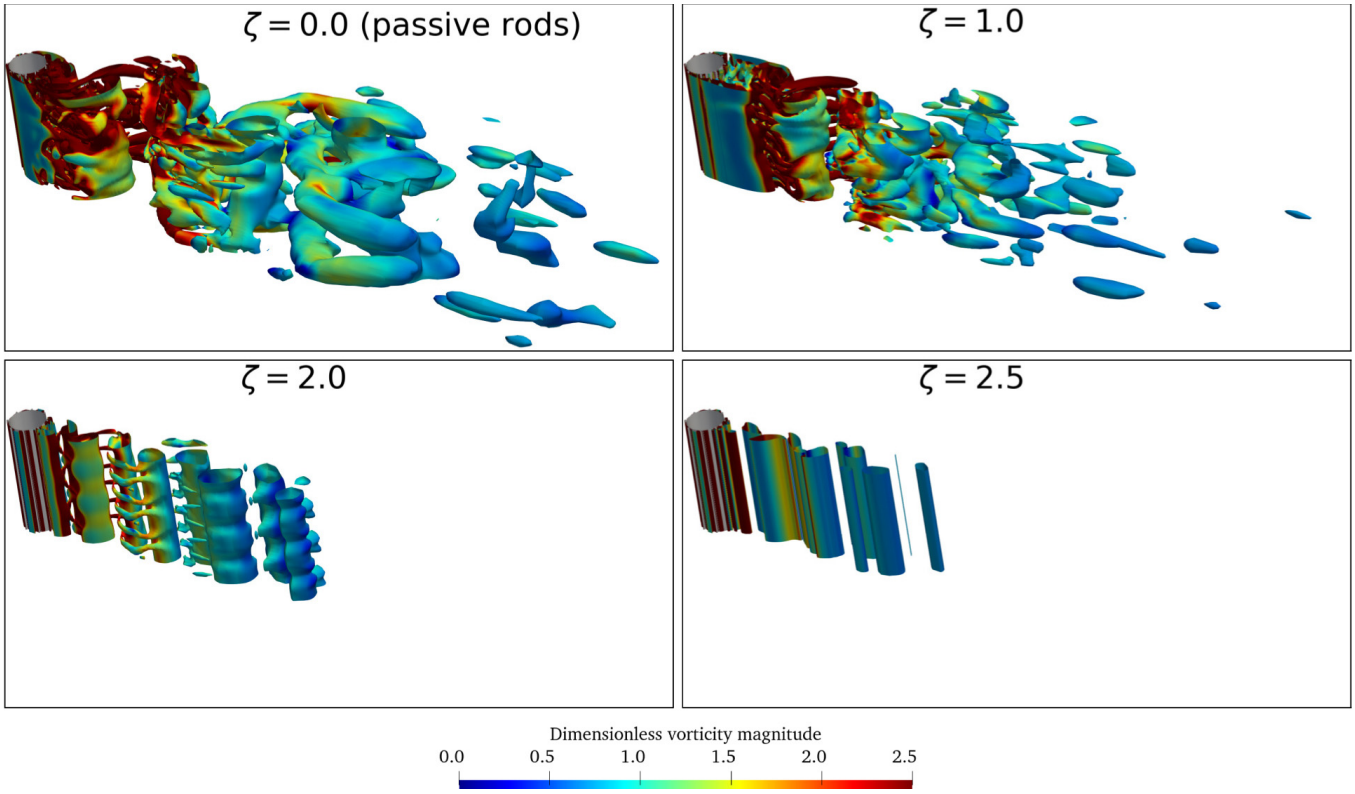

Fig. 13. Vortices shed by the system underwent progressive organisation and elimination of small turbulence scales as the rods spun faster. $\zeta = 2.0$ instigated the occurrence of *mode B* (Williamson, 1996) and triggered the formation of *vortex pairs* as a means of vorticity transfer between rows of vortices.

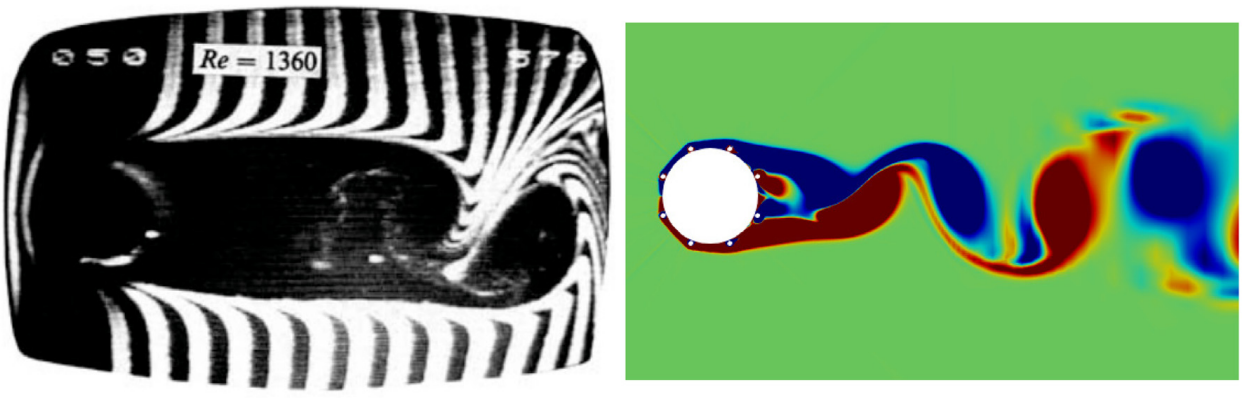

(a) (b)

Fig. 14. Control rods alter the *Re*-regime and its corresponding wake features. Both figures (a) at $Re = 1360$ from Unal and Rockwell (1988) and (b) the present case at $Re = 1000$ refer to sub-critical regime, and yet show different formation lengths.

0.5 to 1.0 and for the entire range of ζ the mean drag decreased monotonically. For the latter pair, drag inversion took place in the transition from $\zeta = 1.5$ to 2.0, and absolute values of mean drag did not match a monotonic tendency; they rather followed a descending trend between $\zeta = 0.0$ and 1.0. Outside of these intervals, $\overline{C}_D$ values accompanied ascending trends for ever greater values of ζ: P_1, P_1' and P_2, P_2' adopted negative, while P_3, P_3' and P_4, P_4' led to progressively positive values.

As expected, the rods were insensitive to the suppression of vortex shedding of the entire system in both cases, since no alteration was noted in mean drag or lift past the corresponding ζ. The Reynolds number based on the rods' diameter was merely $Re_d = 50$, on the brink of vortex shedding. Even if vortices were shed from the fixed rods for such small Re_d, the rotation would have eliminated this phenomenon at its root. Asymmetry produced by rotation of the cylinder was suggested as a means of attaining a steady wake in Badr et al. (1990).

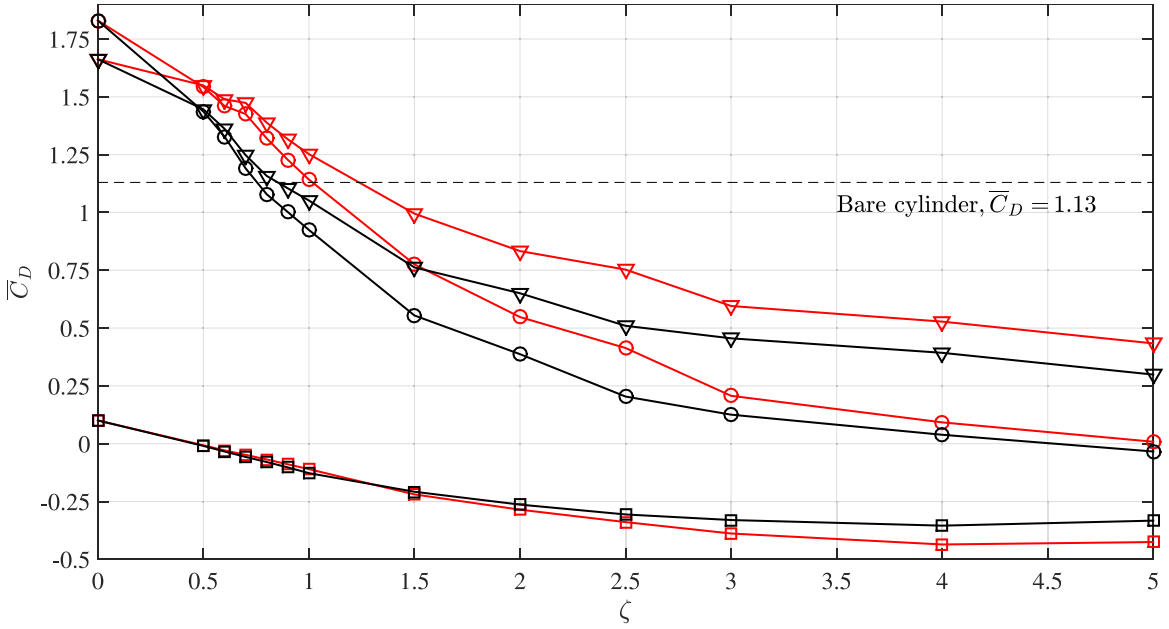

(a) Mean drag ($\overline{C}_D$).

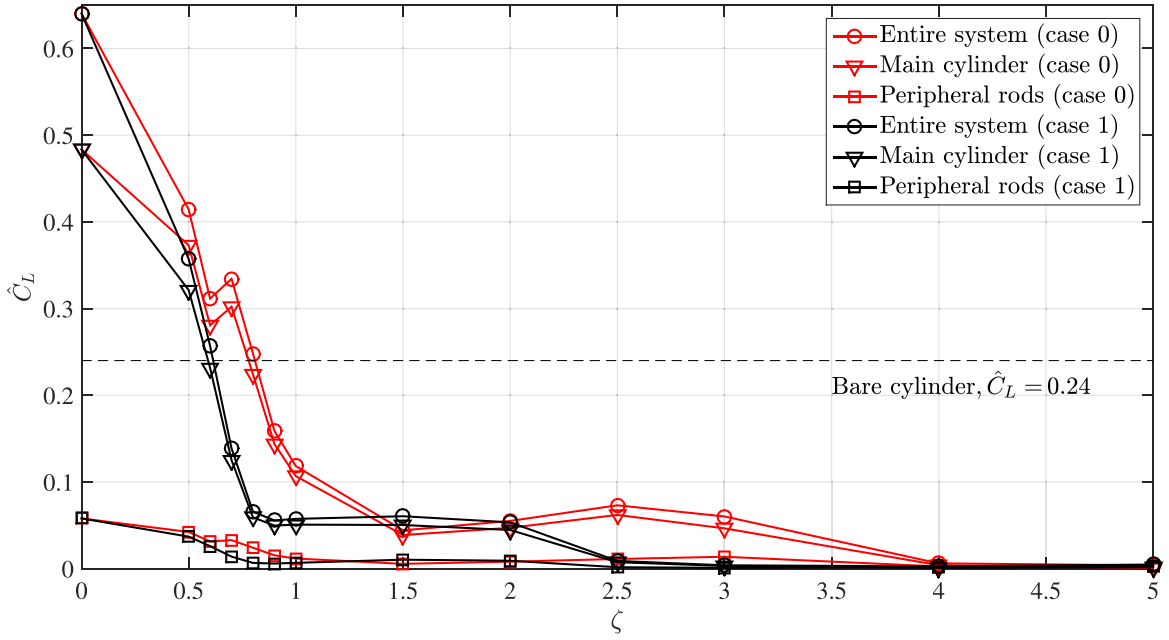

(b) Root mean square (RMS) of the fluctuating lift ($\hat{C}_L$).

Fig. 15. (a) Mean drag and (b) RMS of the fluctuating lift on the entire system, on the main cylinder and that resulting from the collective effect on the peripheral rods.

3.6. Power expenditure

Both circulation and injection of momentum resulting from the placement of the spinning elements surrounding the main body resulted in power expenditure required by MSBC. Following the formulation proposed by Shukla and Arakeri (2013), the power-loss coefficient, given in time-averaged form by

$$\overline{C}_{PL} = \overline{C}_D + \overline{C}_N, \tag{3}$$

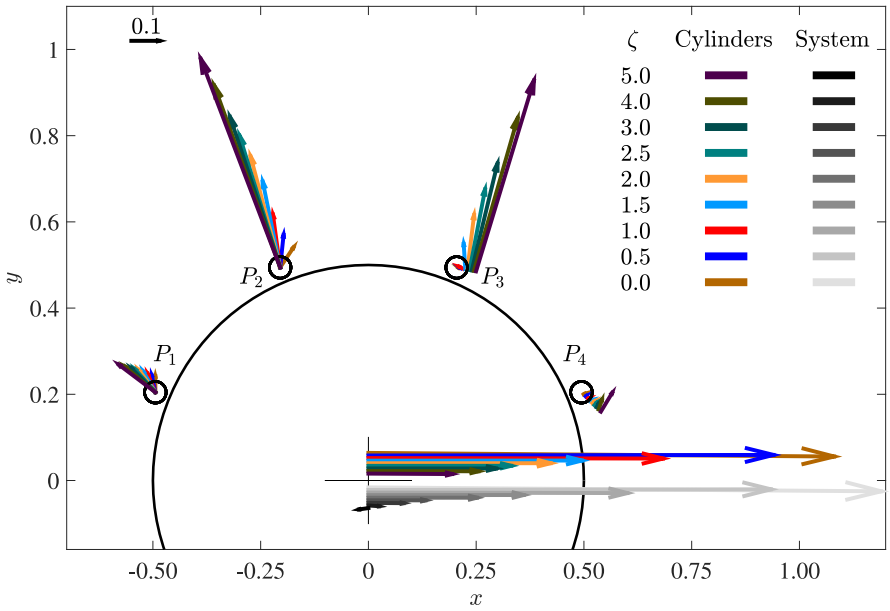

Fig. 16. Resultant forces acting on each cylinder (coloured) and on the entire system (grey) of case 1 for $\zeta = 0$ to 5.0. The radial vectors were deliberately moved from the axis of their respective cylinders whenever necessary for better visualisation. On the upper left, 0.1 unit of non-dimensional force is exemplified. (For interpretation of the references to colour in this figure legend, the reader is referred to the web version of this article.)

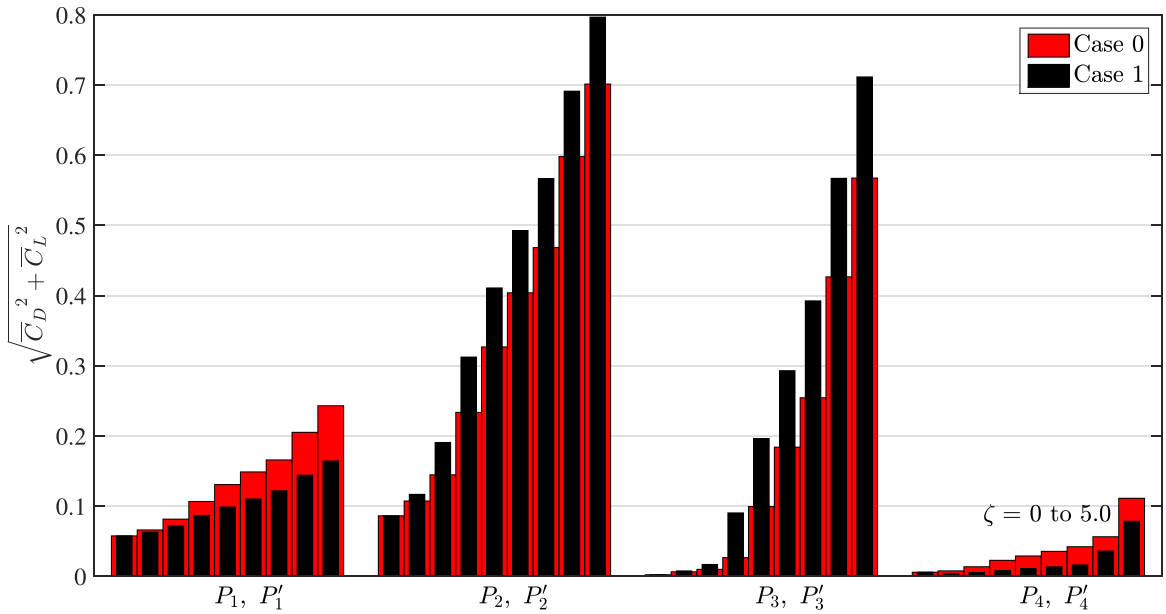

Fig. 17. Variation of the resultant force acting on each rod with increasing angular velocities, for $\zeta = 0.0$, 0.5, 1.0, 1.5, 2.0, 2.5, 3.0, 4.0 and 5.0.

quantifies the effort made by the control system to attenuate mean drag, $\overline{C}_D$, and to counteract shear forces on the $N = 8$ rotating rods

$$C_N = \sum_{n=1}^{N} \frac{p_n}{\rho U_\infty^3 D/2}, \tag{4}$$

in which

$$p_n = U_n \int_0^{2\pi} \tau_n(\theta)\, \frac{d}{2}\, \mathrm{d}\theta, \tag{5}$$

where $\tau_n(\theta)$ and U_n correspond, respectively, to the shear stress over the surface of the nth rod and U_n to its tangential velocity. Overlined quantities indicate time-averaging (as described in Section 2).

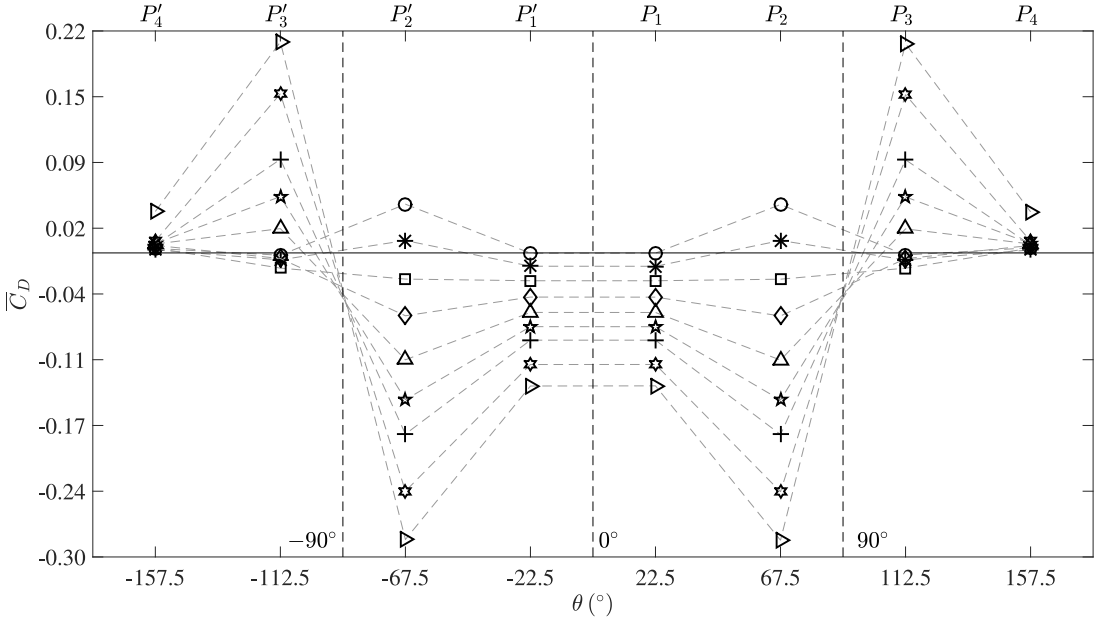

(a) Mean drag on each rod.

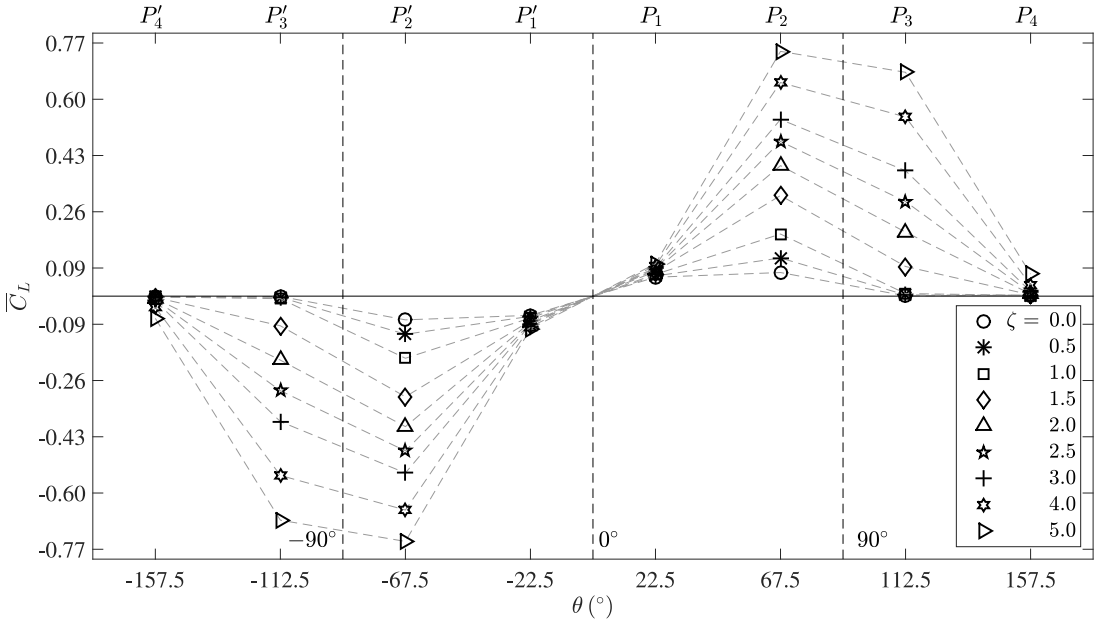

(b) RMS of the fluctuating lift on each rod.

Fig. 18. Mean drag (a) and RMS of the fluctuating lift (b) on control rods varying ζ. General monotonic tendencies followed $\zeta > 1.0$.

Fig. 19 presents $\overline{C}_{PL}$ and its components, $\overline{C}_N$ and $\overline{C}_D$. Shaded areas demarcate the region of complete elimination of vortex shedding, highlighting an earlier occurrence in case 1. The figure anticipates the more power-demanding feature of this new setup, as the curve of $\overline{C}_N$ surpassed that of $\overline{C}_D$ at $\zeta = 1.67$ and 1.38 for cases 0 and 1, respectively.

It becomes evident that in either case, the value of the power-loss coefficient was never below that of the mean drag of the reference case. This contrasts with the previous study of Carvalho et al. (2021) in laminar regime, where C_{PL} found lower values than $\overline{C}_D$ of a plain cylinder. Additional data are required in Fig. 19 to understand if such an event could happen between $\zeta = 1.0$ and 1.5 in case 1, but an educated guess likely points otherwise. Even in the occurrence of such an event, suppression of vortex shedding would not have been attained within this interval of ζ.

In a suppressed-wake condition, comparison against the reference case of a bare cylinder shows that the ratio $(\overline{C}_{PL}/\overline{C}_{D,\text{Bare}})_{\text{case 0}} = 2.85$ at $\zeta = 4.0$, and $(\overline{C}_{PL}/\overline{C}_{D,\text{Bare}})_{\text{case 1}} = 1.63$ at $\zeta = 3.0$, proving the more efficient suppression

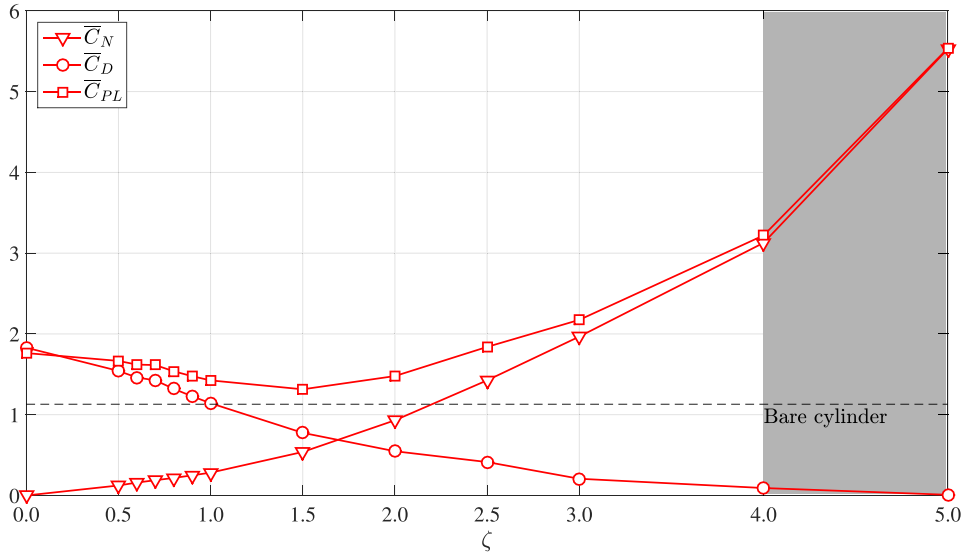

(a) Case 0.

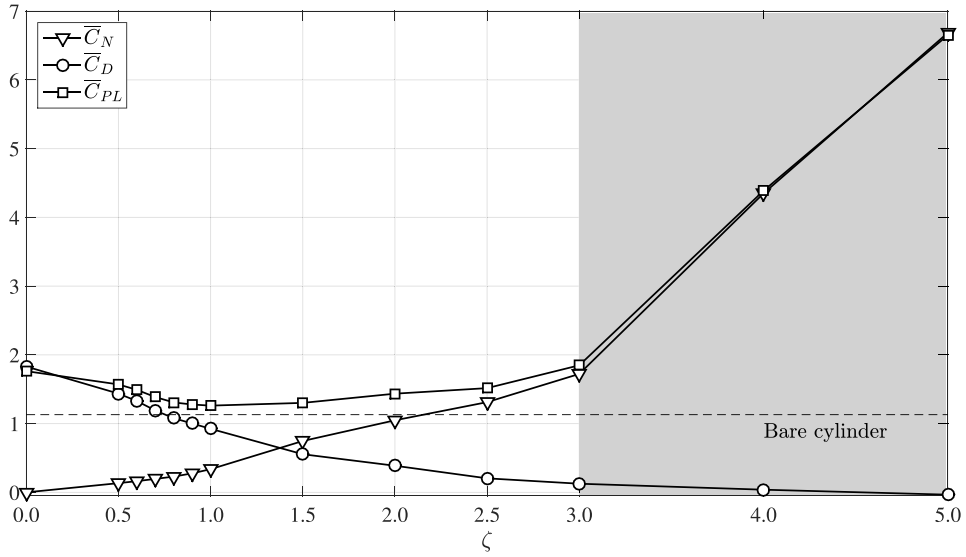

(b) Case 1.

Fig. 19. Mean values of the total power-loss coefficient ($\overline{C}_{PL}$) and of its constituents – power-loss due to shear ($\overline{C}_N$) and to drag ($\overline{C}_D$) – for cases 0 and 1. Shading indicates regions of vortex-shedding suppression.

of vortex shedding provided in case 1. Another aspect that must be retrieved here is that for the same ζ, cases 0 and 1 spent the same input kinetic energy. This enhances the appeal to case 1 for cost-effective vortex-shedding suppression, since $\zeta = 4.0$ required more kinetic energy than $\zeta = 3.0$.

Finally, Fig. 20 presents the components of $\overline{C}_{PL}$. Dotted vertical lines indicate where the wake was already suppressed. In terms of drag reduction, at the same ζ, case 0 reduced the mean drag to 0.092 (at $\zeta = 4.0$), whereas case 1 reached 0.13 (at $\zeta = 3.0$). This shows a downside of the new configuration for the incipient elimination of the vortex formation (although at lower requirement of input kinetic energy). Comparison of $\overline{C}_D$ and $\overline{C}_N$ outlined in the figure highlights that any suppressed condition demanded power expenditure. Furthermore, the frontier $\overline{C}_D = \overline{C}_N$ divides the figure into drag- and shear-dominated regions. At higher ζ, $\overline{C}_N$ dominated the composition of $\overline{C}_{PL}$ as it can be promptly noted for $\zeta = 5.0$. Unless propulsion is desired, started for $\zeta = 5.0$ in case 1, limiting $\zeta < 5$ as in the scope of this work aptly fulfils the purpose of suppression of vortex shedding with drag reduction.

4. Conclusion

A system comprised of a main cylinder fitted with 8 rotating peripheral rods distanced radially by a gap from the central body was analysed in this paper. DES simulations were conducted in turbulent regime at $Re = 10^3$. Two cases

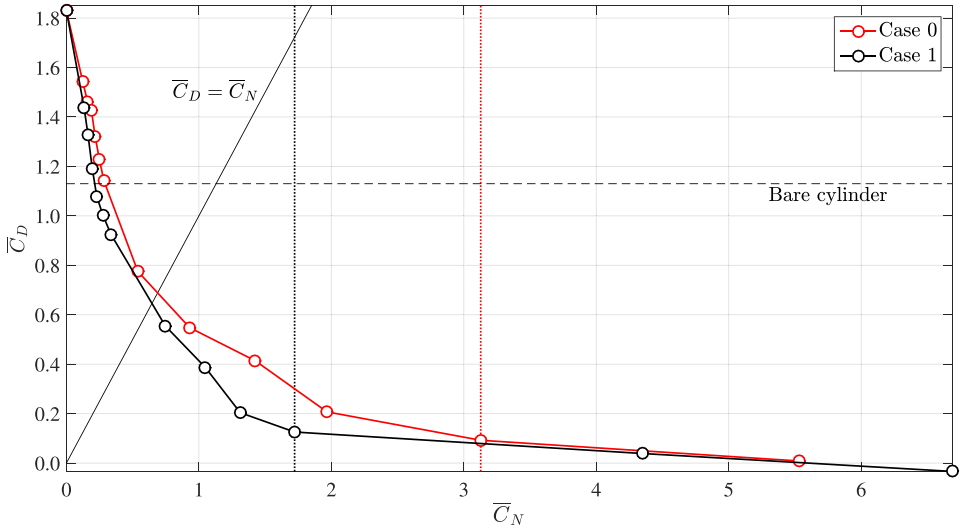

Fig. 20. $\overline{C}_D$ vs $\overline{C}_N$. Dotted vertical lines point to the onset of a controlled, steady-wake condition.

were assessed: case 0, where all rods adopted a uniform absolute speed value $|\omega_n|$; and case 1, where the angular velocities ω_n of the rods were inspired by potential-flow theory, thus weighting the relative position of the rods. The two cases were constrained to the same input kinetic energy. The parameter ζ multiplied the speed of all rods at once to evaluate the effect of the active devices for different rotation rates.

Vortex dynamics showed that the use of the potential-flow-inspired system produced a more effective way to mitigate vortex shedding. In general, mean drag ($\overline{C}_D$) and RMS of the fluctuating lift ($\hat{C}_L$) acting upon the entire system were significantly reduced using the new configuration compared with the uniform setup. This result was associated with a narrower wake and an elongated formation length, leading to increased shedding frequency prior to the transition of the wake to a steady condition.

Besides, it was demonstrated by means of Q-contours of turbulent viscosity that the spinning rods led to a two-dimensional "laminarised" state of the flow, that progressively eliminated turbulent structures. *Vortex dislocations*, in the sense of the vortex-shedding *mode B* of vorticity transfer were detected streamwise, provided the system was supplied with enough actuating power (sufficiently high ζ). One might wonder whether the spinning rods' effect was to "lower the effective *Re*-regime", taking in consideration that mode B was reported by Williamson (1996) in a wake-transition regime, rather than in a sub-critical regime as in the present work.

Although the loads acting on the group of rods made up by P_n (or, alternatively, by P_n') seemed insensitive to the distinction between cases 0 and 1, analysis of the individual contributions of the rods showed preference of case 1 to concentrate the effort on the intermediate rods (P_2 and P_3) more intensely than in case 0 for greater ζ, discerning case 1 from case 0 in greater power expenditure. Nevertheless, this behaviour at the upper limit of the velocities hereby analysed was offset by lower $\hat{C}_L$ and $\overline{C}_D$ throughout most ζ-regimes and a more efficient control of the wake. Indeed, because the end rods (P_1 and P_4) were located near stagnation regions, they were expected to interact less with boundary and shear layers. Hence, case 1 anticipated vortex-shedding suppression relative to case 0, thus required lower input kinetic energy and actuating power to control the vortex street.

Concerning the entire system, the present study showed that the power-loss coefficient (that includes power spent to counteract shear and effort to reduce drag) – resulting either from the new configuration or from the uniform-speed one – was not enough to lower the power-loss coefficient below the value of the mean drag of the reference case of a plain cylinder (a contrast with the result at a laminar regime foundby Carvalho et al., 2021).

Finally, we were able to show that potential-flow-inspired angular velocities are effective even in turbulent, three-dimensional regime to reduce hydrodynamic loads, and beyond, to suppress vortex shedding entirely. Future work should concern with the system free to respond to vortex-induced vibrations and with multi-objective optimisation of the angular velocities.

CRediT authorship contribution statement

I.A. Carvalho: Conception and design of study, Acquisition of data, Analysis and/or interpretation of data, Writing – original draft, Writing – review & editing. **G.R.S. Assi:** Conception and design of study, Acquisition of data, Analysis and/or interpretation of data, Writing – original draft, Writing – review & editing.

Declaration of competing interest

The authors declare that they have no known competing financial interests or personal relationships that could have appeared to influence the work reported in this paper.

Acknowledgements

IAC is grateful to CAPES Brazilian Ministry of Education for his Ph.D. scholarship and to the National Laboratory for Scientific Computing (LNCC/MCTI, Brazil) for providing HPC resources of the SDumont supercomputer. GRSA acknowledges the support of FAPESP, Brazil (2011/00205-6) and CNPq, Brazil (306146/2019-3). We gratefully acknowledge the support of the RCGI Research Centre for Greenhouse Gas Innovation, hosted by the University of São Paulo, Brazil and sponsored by FAPESP (2020/15230-5) and Shell Brasil. Approval of the version of the manuscript to be published: I.A. Carvalho.

Appendix A. Supplementary data

Supplementary material related to this article can be found online at https://doi.org/10.1016/j.jfluidstructs.2022.103652.

References

Assi, G.R.S., Orselli, R.M., Silva-Ortega, M., 2018. Suppression of vortex shedding with rotating wake-control cylinders: Numerical investigation at a moderate Reynolds number. In: International Conference on Offshore Mechanics and Arctic Engineering, Vol. 51210. American Society of Mechanical Engineers, V002T08A060.
Assi, G.R.S., Orselli, R.M., Silva-Ortega, M., 2019. Control of vortex shedding from a circular cylinder surrounded by eight rotating wake-control cylinders at Re=100. J. Fluids Struct. 89, 13–24.
Badr, H.M., Coutanceau, M., Dennis, S.C.R., Menard, C., 1990. Unsteady flow past a rotating circular cylinder at Reynolds numbers 103 and 104. J. Fluid Mech. 220, 459–484.
Behr, M., Hastreiter, D., Mittal, S., Tezduyar, T., 1995. Incompressible flow past a circular cylinder: Dependence of the computed flow field on the location of the lateral boundaries. Comput. Methods Appl. Mech. Engrg. 123 (1–4), 309–316.
Behr, M., Liou, J., Shih, R., Tezduyar, T., 1991. Vorticity-streamfunction formulation of unsteady incompressible flow past a cylinder: Sensitivity of the computed flow field to the location of the outflow boundary. Internat. J. Numer. Methods Fluids 12 (4), 323–342.
Braza, M., Chassaing, P.H.H.M., Minh, H.H., 1986. Numerical study and physical analysis of the pressure and velocity fields in the near wake of a circular cylinder. J. Fluid Mech. 165, 79–130.
Cantwell, B., Coles, D., 1983. An experimental study of entrainment and transport in the turbulent near wake of a circular cylinder. J. Fluid Mech. 136, 321–374.
Cao, S., Ozono, S., Tamura, Y., Ge, Y., Kikugawa, H., 2010. Numerical simulation of Reynolds number effects on velocity shear flow around a circular cylinder. J. Fluids Struct. 26 (5), 685–702.
Carmo, B.S., Meneghini, J.R., 2006. Numerical investigation of the flow around two circular cylinders in tandem. J. Fluids Struct. 22 (6–7), 979–988.
Carvalho, I.A., Assi, G.R.S., Orselli, R.M., 2021. Wake control of a circular cylinder with rotating rods: Numerical simulations for inviscid and viscous flows. J. Fluids Struct. 106, 103385.
Choi, H., Jeon, W.P., Kim, J., 2008. Control of flow over a bluff body. Annu. Rev. Fluid Mech. 40, 113–139.
Cicolin, M.M., Buxton, O.R.H., Assi, G.R.S., Bearman, P.W., 2021. The role of separation on the forces acting on a circular cylinder with a control rod. J. Fluid Mech. 915.
Fujarra, A.L.C., Rosetti, G.F., de Wilde, J., Gonçalves, R.T., 2012. State-of-art on vortex-induced motion: A comprehensive survey after more than one decade of experimental investigation. In: Proceedings of the OMAE International Conference on Offshore Mechanics and Arctic Engineering, no. 44915. pp. 561–582.
Gerrard, J.H., 1966. The mechanics of the formation region of vortices behind bluff bodies. J. Fluid Mech. 25 (2), 401–413.
Gonçalves, R.T., Rosetti, G.F., Fujarra, A.L.C., Nishimoto, K., 2011. An overview of relevant aspects on VIM of spar and monocolumn platforms. J. Offshore Mech. Arct. Eng. 134 (1), 014501.
Hunt, J.C.R., Wray, A., Moin, P., 1988. Eddies, stream, and convergence zones in turbulent flows. In: Studying Turbulence using Numerical Simulation Databases-I1, Vol. 193.
Jordan, S.K., Fromm, J.E., 1972. Oscillatory drag, lift, and torque on a circular cylinder in a uniform flow. Phys. Fluids 15 (3), 371–376.
Korkischko, I., Meneghini, J., 2012. Suppression of vortex-induced vibration using moving surface boundary-layer control. J. Fluids Struct. 34, 259–270.
Mittal, S., 2001. Control of flow past bluff bodies using rotating control cylinders. J. Fluids Struct. 15 (2), 291–326.
Mittal, S., Raghuvanshi, A., 2001. Control of vortex shedding behind circular cylinder for flows at low Reynolds numbers. Internat. J. Numer. Methods Fluids 35 (4), 421–447.
Modi, V., Fernando, M.S.U.K., Yokomizo, T., 1990. Drag reduction of bluff bodies through moving surface boundary layercontrol. In: 28th Aerospace Sciences Meeting. p. 298.
Norberg, C., 2001. Flow around a circular cylinder: aspects of fluctuating lift. J. Fluids Struct. 15 (3–4), 459–469.
Patankar, S.V., 1980. Numerical Heat Transfer and Fluid Flow. Hemisphere Publishing Corp., Washington, DC, 1980. 210 P.
Patino, G.A., Gioria, R.S., Meneghini, J.R., 2017. Evaluating the control of a cylinder wake by the method of sensitivity analysis. Phys. Fluids 29 (4), 044103. http://dx.doi.org/10.1063/1.4979482.
Saltara, F., Neto, A., Lopez, J., et al., 2011. 3D CFD simulation of vortex-induced vibration of cylinder. Int. J. Offshore Polar Eng. 21 (03).
Shukla, R.K., Arakeri, J.H., 2013. Minimum power consumption for drag reduction on a circular cylinder by tangential surface motion. J. Fluid Mech. 715, 597–641. http://dx.doi.org/10.1017/jfm.2012.537.
Silva-Ortega, M., Assi, G.R.S., 2017a. Flow-induced vibration of a circular cylinder surrounded by two, four and eight wake-control cylinders. Exp. Therm Fluid Sci. 85, 354–362.
Silva-Ortega, M., Assi, G., 2017b. Suppression of the vortex-induced vibration of a circular cylinder surrounded by eight rotating wake-control cylinders. J. Fluids Struct. 74, 401–412.
Smagorinsky, J., 1963. General circulation experiments with the primitive equations: I. The basic experiment. Mon. Weather Rev. 91 (3), 99–164.
Spalart, P.R., 1997. Comments on the feasibility of LES for wings, and on a hybrid RANS/LES approach. In: Proceedings of First AFOSR International Conference on DNS/LES. Greyden Press.
Spalart, P., 2000. Trends in turbulence treatments. In: Fluids 2000 Conference and Exhibit. p. 2306.
Spalart, P., Allmaras, S., 1992. A one-equation turbulence model for aerodynamic flows. In: 30th Aerospace Sciences Meeting and Exhibit. p. 439.
Spalart, P.R., Deck, S., Shur, M.L., Squires, K.D., Strelets, M.K., Travin, A., 2006. A new version of detached-eddy simulation, resistant to ambiguous grid densities. Theor. Comput. Fluid Dyn. 20 (3), 181–195.
Strykowski, P.J., Sreenivasan, K.R., 1990. On the formation and suppression of vortex shedding at low Reynolds numbers. J. Fluid Mech. 218, 71–107.

Thompson, M.C., Hourigan, K., 2005. The shear-layer instability of a circular cylinder wake. Phys. Fluids 17 (2), 021702.
Unal, M.F., Rockwell, D., 1988. On vortex formation from a cylinder. Part 1. The initial instability. J. Fluid Mech. 190, 491–512.
Vatsa, V.N., Lockard, D.P., Spalart, P.R., 2017. Grid sensitivity of SA-based delayed-detached-eddy-simulation model for blunt-body flows. AIAA J. 55 (8), 2842–2847.
Versteeg, H.K., Malalasekera, W., 2007. An Introduction To Computational Fluid Dynamics: The Finite Volume Method. Pearson education.
Wieselsberger, C., 1921. Recent statements on the laws of liquid and air resistancy. Phys. Z 22, 321–328.
Williamson, C.H.K., 1996. Vortex dynamics in the cylinder wake. Annu. Rev. Fluid Mech. 28 (1), 477–539.
Williamson, C.H.K., Govardhan, R., 2004. Vortex-induced vibrations. Annu. Rev. Fluid Mech. 36, 413–455.
Williamson, C.H., Roshko, A., 1988. Vortex formation in the wake of an oscillating cylinder. J. Fluids Struct. 2 (4), 355–381.
Zdravkovich, M.M., 1981. Review and classification of various aerodynamic and hydrodynamic means for suppressing vortex shedding. J. Wind Eng. Ind. Aerodyn. 7 (2), 145–189.
Zhang, H.Q., Fey, U., Noack, B.R., König, M., Eckelmann, H., 1995. On the transition of the cylinder wake. Phys. Fluids 7 (4), 779–794.

The following *corrigendum* was sent to the Journal of Fluids and Structures.

Corrigendum to "Enhanced control of the turbulent flow past a circular cylinder with rotating rods inspired by an inviscid solution" [J. Fluids Struct. 113 (2022) 1-21]

I. A. Carvalho[a,*], G. R. S. Assi[b]

[a] *Department of Mechanical Engineering, EPUSP, University of São Paulo, Brazil*
[b] *Department of Naval Architecture & Ocean Engineering, EPUSP, University of São Paulo, Brazil*

In the paper, instead of computing C_N per unit length, given by

$$C_N = \sum_{n=1}^{N} \frac{p_n}{\rho U_\infty^3 DL/2} \tag{1}$$

we computed, incorrectly,

$$C_N = \sum_{n=1}^{N} \frac{p_n}{\rho U_\infty^3 D/2}. \tag{2}$$

So C_N was overestimated, because it was computed for a body with spanwise length $L/D = \pi$ matching that of our grid, instead of per unit length, following the approximation of an infinitely-long body. $\overline{C}_{PL} = \overline{C}_D + \overline{C}_N$ was thus including $\overline{C}_D$ calculated per unit length and $\overline{C}_N$ for the entire length of the body. We apologise to the reader for the inconvenience. The revised sections 3.6 with the correct computation of C_N, and section 4 are presented below. In actuality, the system functioned more efficiently than formerly addressed.

3.6. Power expenditure

Both circulation and injection of momentum resulting from the placement of the spinning elements surrounding the main body resulted in power expenditure required by MSBC. Following the formulation proposed by Shukla and Arakeri (2013), the power-loss coefficient, given in time-averaged form by

$$\overline{C}_{PL} = \overline{C}_D + \overline{C}_N, \tag{3}$$

*Corresponding author: amorim.icaro@usp.br (I. A. Carvalho)

quantifies the effort made by the control system to attenuate mean drag, $\overline{C}_D$, and to counteract shear forces on the $N = 8$ rotating rods

$$C_N = \sum_{n=1}^{N} \frac{p_n}{\rho U_\infty^3 DL/2}, \tag{4}$$

in which

$$p_n = U_n \int_0^{2\pi} \tau_n(\theta)\, \frac{d}{2}\, \mathrm{d}\theta, \tag{5}$$

where $\tau_n(\theta)$ and U_n correspond, respectively, to the shear stress over the surface of the n-th rod and U_n to its tangential velocity. Overlined quantities indicate time-averaging (as described in Section 2 of the paper).

Figure 19 presents $\overline{C}_{PL}$ and its components, $\overline{C}_N$ and $\overline{C}_D$. Shaded areas demarcate the region of complete elimination of vortex shedding, highlighting an earlier occurrence in case 1. The figure anticipates the more power-demanding feature of this new setup, as the curve of $\overline{C}_N$ surpassed that of $\overline{C}_D$ at $\zeta = 2.42$ and 2.10 for cases 0 and 1, respectively.

It becomes evident that in both cases, the value of the power-loss coefficient was below that of the mean drag of the reference case for a range of values (as in Carvalho et al., 2021, in laminar regime). In case 0 this occurred between $\zeta = 1.18$ and 4.06, while in case 1 the same happened within $\zeta = 0.835$ and 3.60.

In a suppressed-wake condition, comparison against the reference case of a bare cylinder shows that the ratio $(\overline{C}_{PL}/\overline{C}_{D,\mathrm{Bare}})_{\mathrm{case\ 0}} = 0.963$ at $\zeta = 4.0$, and $(\overline{C}_{PL}/\overline{C}_{D,\mathrm{Bare}})_{\mathrm{case\ 1}} = 0.596$ at $\zeta = 3.0$, proving the more efficient suppression of vortex shedding provided in case 1. Another aspect that must be retrieved here is that for the same ζ, cases 0 and 1 spent the same input kinetic energy. This enhances the appeal to case 1 for cost-effective vortex-shedding suppression, since $\zeta = 4.0$ required more kinetic energy than $\zeta = 3.0$.

Finally, figure 20 presents the components of $\overline{C}_{PL}$. Dotted vertical lines indicate where the wake was already suppressed. In terms of drag reduction, at the same ζ, case 0 reduced the mean drag to 0.092 (at $\zeta = 4.0$), whereas case 1 reached 0.13 (at $\zeta = 3.0$). This shows a downside of the new configuration for the incipient elimination of the vortex formation (although at lower requirement of input kinetic energy). Comparison of $\overline{C}_D$ and $\overline{C}_N$ outlined in the figure highlights that a suppressed condition may be achieved without additional power-loss. Moreover, a steady condition was achieved with lower power loss than that by mean drag of a bare cylinder, proving

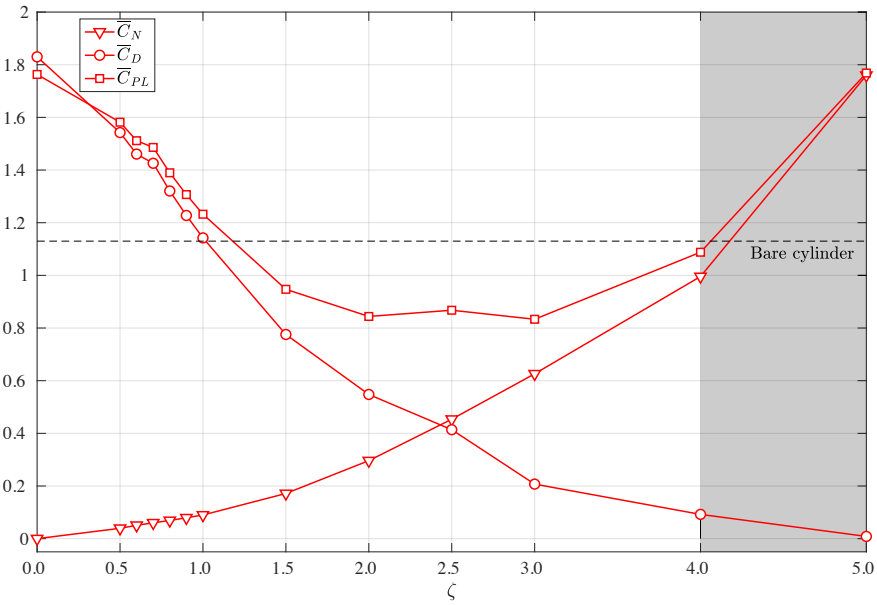

(a) Case 0.

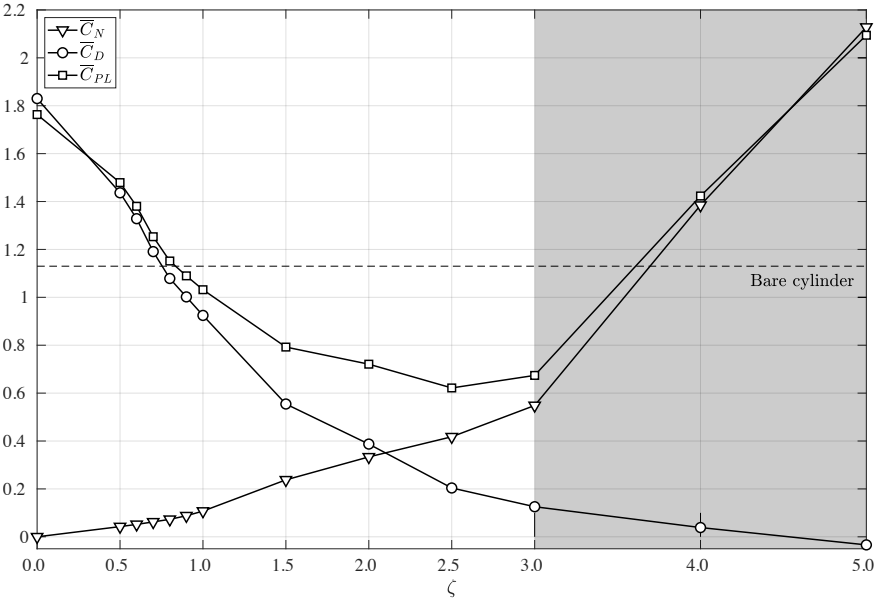

(b) Case 1.

Figure 19: Mean values of the total power-loss coefficient ($\overline{C}_{PL}$) and of its constituents – power-loss due to shear ($\overline{C}_N$) and to drag ($\overline{C}_D$) – for cases 0 and 1. Shading indicates regions of vortex-shedding suppression.

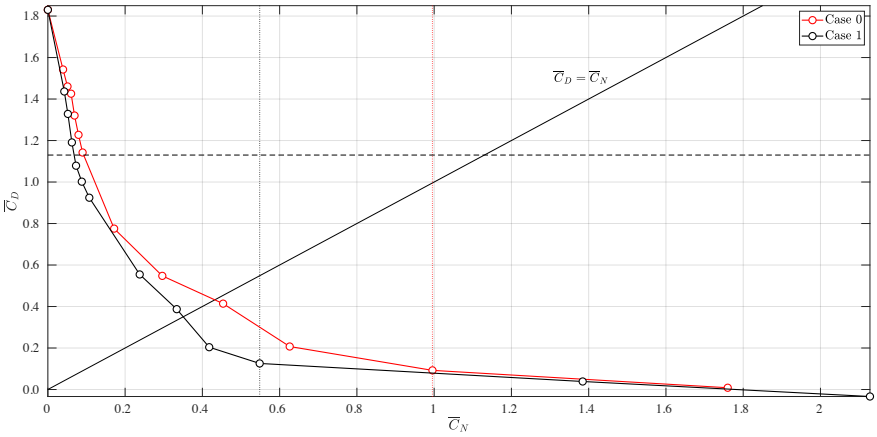

Figure 20: $\overline{C}_D$ vs $\overline{C}_N$. Dotted vertical lines point to the onset of a controlled, steady-wake condition.

the effectiveness of the system (in either configuration, although case 1 was more efficient). Furthermore, the frontier $\overline{C}_D = \overline{C}_N$ divides the figure into drag- and shear-dominated regions. At higher ζ, $\overline{C}_N$ dominated the composition of $\overline{C}_{PL}$ as it can be promptly noted for $\zeta = 5.0$. Unless propulsion is desired, started for $\zeta = 5.0$ in case 1, limiting $\zeta < 5$ as in the scope of this work aptly fulfills the purpose of suppression of vortex shedding with drag reduction.

4. Conclusion

A system comprised of a main cylinder fitted with 8 rotating peripheral rods distanced radially by a gap from the central body was analysed in this paper. DES simulations were conducted in turbulent regime at $Re = 10^3$. Two cases were assessed: case 0, where all rods adopted a uniform absolute speed value $|\omega_n|$; and case 1, where the angular velocities ω_n of the rods were inspired by potential-flow theory, thus weighting the relative position of the rods. The two cases were constrained to the same input kinetic energy. The parameter ζ multiplied the speed of all rods at once to evaluate the effect of the active devices for different rotation rates.

Vortex dynamics showed that the use of the potential-flow-inspired system produced a more effective way to mitigate vortex shedding. In general, mean drag ($\overline{C}_D$) and RMS of the fluctuating lift ($\hat{C}_L$) acting upon the entire system were significantly reduced using the new configuration compared with the uniform setup. This result was associated with a narrower wake and an elongated formation length, leading to increased shedding frequency prior to the transition of the wake to a steady condition.

Besides, it was demonstrated by means of Q-contours of turbulent viscosity that the spinning rods led to a two-dimensional "laminarised" state of the flow, that progressively eliminated turbulent structures. *Vortex dislocations*, in the sense of the vortex-shedding *mode B* of vorticity transfer were detected streamwise, provided the system was supplied with enough actuating power (sufficiently high ζ). One might wonder whether the spinning rods' effect was to "lower the effective Re-regime", taking in consideration that mode B was reported by Williamson (1996) in a wake-transition regime, rather than in a sub-critical regime as in the present work.

Although the loads acting on the group of rods made up by P_n (or, alternatively, by P'_n) seemed insensitive to the distinction between cases 0 and 1, analysis of the individual contributions of the rods showed preference of case 1 to concentrate the effort on the intermediate rods (P_2 and P_3) more intensely than in case 0 for greater ζ, discerning case 1 from case 0 in greater power expenditure. Nevertheless, this behaviour at the upper limit of the velocities hereby analysed was offset by lower $\hat{C}_L$ and $\overline{C}_D$ throughout most ζ-regimes and a more efficient control of the wake. Indeed, because the end rods (P_1 and P_4) were located near stagnation regions, they were expected to interact less with boundary and shear layers. Hence, case 1 anticipated vortex-shedding suppression relative to case 0, thus required lower input kinetic energy and actuating power to control the vortex street.

Concerning the entire system, the present study showed that the power-loss coefficient (that includes power spent to counteract shear and effort to reduce drag) – resulting either from the new configuration or from the uniform-speed one – was able to lower the power-loss coefficient below the value of the mean drag of the reference case of a plain cylinder. Thus, the system proved more efficient than to employ a bare cylinder, because the reduction in mean drag by the rods was accompanied by such small actuating power that cumulatively did not equal the mean drag of the bare body. Furthermore, our results point in the direction that this result is achievable even in a steady condition (although more simulations would be required to corroborate this assertion).

Finally, we were able to show that potential-flow-inspired angular velocities are effective even in turbulent, three-dimensional regime to reduce hydrodynamic loads, and beyond, to suppress vortex shedding entirely. Future work should concern with the system free to respond to vortex-induced vibrations and with multi-objective optimisation of the angular velocities.

References

Carvalho, I.A., Assi, G.R.S., Orselli, R.M., 2021. Wake control of a circular cylinder with rotating rods: Numerical simulations for inviscid and viscous flows. Journal of Fluids and Structures 106, 103385.

Shukla, R.K., Arakeri, J.H., 2013. Minimum power consumption for drag reduction on a circular cylinder by tangential surface motion. Journal of Fluid Mechanics 715, 597–641. doi:10.1017/jfm.2012.537.

Williamson, C.H.K., 1996. Vortex dynamics in the cylinder wake. Annual review of fluid mechanics 28, 477–539.

Physics of Fluids ARTICLE scitation.org/journal/phf

Passive control of vortex-shedding past finite cylinders under the effect of a free surface

Cite as: Phys. Fluids **35**, 015109 (2023); doi: 10.1063/5.0134730
Submitted: 13 November 2022 · Accepted: 14 December 2022 ·
Published Online: 5 January 2023

I. A. Carvalho[1,a] and G. R. S. Assi[2,b]

AFFILIATIONS

[1]Department of Mechanical Engineering, EPUSP, University of São Paulo, São Paulo, Brazil
[2]Department of Naval Architecture & Ocean Engineering, EPUSP, University of São Paulo, São Paulo, Brazil

[a]Author to whom correspondence should be addressed: amorim.icaro@usp.br
[b]Electronic mail: g.assi@usp.br

ABSTRACT

Passive technologies for the control of the flow past bluff bodies have been widely studied. Most of these works have focused on high-aspect-ratio, wall-mounted, or infinitely long cylinders, leaving a gap for low-aspect-ratio bodies fully submerged or under the effect of a free water surface. This is the object of the present work. Detached-eddy simulations at a Reynolds number of 1000 have been carried out for infinitely long (case i) and low-aspect-ratio bodies. For the finite case, two configurations were investigated: bodies fully submerged in the flow, away from surface effects (case ii) and that involving a free surface, here represented by a fixed slip-allowing plane (case iii). These computations were conducted for the bare cylinder and the system is comprised of the same main body fitted with eight wake-control rods uniformly distributed around its perimeter. Results showed that the low-aspect-ratio cases relative to infinitely long structures (1) lowered mean drag and root mean square lift, (2) presented a less coherent wake topology, (3) had frontal rods that concentrated most of the hydrodynamic loads, (4) extended the formation length, and (5) although all cases developed larger hydrodynamic loads when the rods were fitted to the main body compared to the plain cylinder, the finite cases produced a lower increase. We show that these results are intrinsically related to end effects and associated with a less correlated wake lacking coherent vortical structures. Furthermore, we analyze the more accentuated streamwise vortices produced by the presence of the free surface in case iii compared with case ii.

I. INTRODUCTION

Vortex shedding is responsible for cyclic hydrodynamic loads that affect bluff structures. The interplay between opposing vortices shed downstream is the root of vortex-induced vibrations (VIV) that cause the bluff structure to oscillate longitudinally, and principally, transversely to the flow, leading to fatigue and possibly failure. In practice, VIV (sometimes also called VIM for vortex-induced motion of large floating structures) is observed in large offshore platforms with bluff hulls, such as spar and monocolumn platforms. The present study is a part of a research line to develop devices to suppress VIV of floating offshore structures. Knowledge of the physical mechanisms obtained from numerical simulations should help the development of active and passive technologies to control the flow around bluff bodies.

Various methods to eliminate or attenuate vortex shedding have been reviewed by Zdravkovich (1981) and Choi *et al.* (2008). Passive solutions aim at suppressing VIV without any power input. Common examples are shrouds (such as slender cylinders around the main body), near-wake stabilizers (such as end plates and splitter plates), and complex geometrical modifications [like helical strakes recently studied by Assi *et al.* (2022)].

From a physical point of view, this passive category of solutions acts through different mechanisms. One such is through the elimination or delay of vortex shedding farther downstream in the wake, thus diffusing vorticity. It is known from the classic work of Gerrard (1966) that shear layers feed the wake with vorticity and their interaction is of utmost relevance to the shedding mechanism. Hence, other strategies will try to avoid shear layer interaction.

From the seminal paper on the suppression of vortex shedding by a single control rod of Strykowski and Sreenivasan (1990), it is known that the presence of a passive secondary body can attenuate the growth of temporal instabilities and is able to not only reduce vortex shedding but also banish its inception entirely in a limited range of Reynolds numbers ($Re = U_\infty D/\nu$, where U_∞ is the freestream flow velocity, D is the diameter of the main body, and ν is the kinematic viscosity of the fluid). In a more general sense, numerical and experimental results of Strykowski and Sreenivasan (1990) for *Re*

Physics of Fluids ARTICLE scitation.org/journal/phf

comprehended between 40 and 100 showed that local modifications led to global changes in the flow and that in order to control the wake, interaction with the near field is of vital importance.

Experiments with more complex systems subjected to VIV were conducted by Silva-Ortega and Assi (2017; 2018), with 2, 4, and 8 rods in turbulent regime. Drag and response amplitude were assessed regarding changes in the gap between the main body and the fitted rods and their diameters. The authors showed that care must be taken with such a passive device, which may not only increase hydrodynamic loads but also introduce galloping due to directional effects. With an adequate choice of parameters, only residual vibration due to VIV remained for a setup involving eight control rods.

Generally, most of the previous works were concerned with flow control over infinitely long cylinders, in which the end effects were neglected. Relatively, few works were dedicated to the flow behavior past finite cylinders even though the subject dates back to experiments made one century ago by Wieselsberger (1922).

Farivar (1981) experimentally studied the turbulent flow at $Re = 7 \times 10^4$ about cylinders with finite length of different aspect ratios. Supported by the work of Goldstein (1965) on the turbulent flow about a cylinder with different aspect ratios, Farivar (1981) attempted to describe the effect of the free end regarding pressure and drag coefficients. Franzini *et al.* (2013) studied the problem of a bare cylinder subjected to VIV for aspect ratios in the range of 0.3–2.0 and different mass ratios and also reported the lack of studies of cylinders with small aspect ratios. The study of Gonçalves *et al.* (2015) advanced on the matter and evaluated the flow around stationary circular cylinders piercing through the water surface for very low aspect ratios, ranging from $L/D = 0.1$ to 2.0.

Major contributions on finite cylinders are found in the scope of wall-mounted setups. In one of the early works, Kawamura *et al.* (1984) experimentally detected the existence of trailing vortices and downwash and their relation to the formation of the Kármán vortex street. The authors noted that depending on the slenderness parameter L/D (where L is the length of the cylinder), this wake could not form. Rather, for sufficient L/D, the trailing vortices dominated the wake. Later, Luo (1993) pointed out that the formation of a Kármán vortex street for finite cylinders depended on a critical value of the aspect ratio L/D that ranged between 1 and 7 depending on the influence of the plane boundary layer. Working with different L/D, Sumner *et al.* (2004) produced time-averaged velocity and streamwise vorticity contours that showed tip-vortex structures, near-wake recirculations, and downwash. It was also found that the effect of the tip vortices extended into the wake downstream and scaled with the cylinder length. The authors also reported that a coherent Kármán vortex street was not observed for $L/D < 3$. Instead, a symmetric "arch-vortex" dominated the near wake.

Both active and passive solutions have been employed in 2D laminar cases and three-dimensional (3D) fully turbulent cases. Still, there is a lack of research concerning both mechanisms for finite cylinders subjected to end effects. It was remarked by Mittal and Raghuvanshi (2001) that the suppression of vortex shedding (in infinitely long cylinders) by proper placement of a fixed rod near the main cylinder was possible only at low *Re*. Nevertheless, wake control by a passive mechanism is a stepping stone toward more effective solutions, such as active control through the injection of momentum into the boundary layer by spinning the rods (Korkischko and Meneghini, 2012; Assi *et al.*, 2019). The review of Luo *et al.* (1996) is one of the few studies that evaluated the flow interaction between low aspect ratio cylinders; however, the authors were not concerned with a passive mechanism as described above. Rather, the focus was given to the interference between two bodies of sizes of the same order.

As it can be seen, although the problem of the flow past finite cylinders has been explored, particularly for the wall-mounted setup, in general, it is still scarcer in information than that of infinitely long bodies as already anticipated in the work of Sumner *et al.* (2004). At present, no analysis has been made modeling the free surface as a slip surface with a system like the one we propose in this work. Furthermore, fitted rods to the main body have not been employed as a form of passive mechanism of finite bluff bodies.

II. OBJECTIVE

In the present paper, we intend to push forward the literature on the matter of passive control of finite structures by studying free-surface and free-end effects on the vortex shedding mechanism and its suppression with interfering rods. We compare the flow behavior over infinitely long and low-aspect-ratio cylinders.

Configurations of the flow past a plain cylinder and past a system—that involves the main body fitted with peripheral rods—have been considered. The motivation to fit the rods around the main body is to investigate how the entire set [as illustrated in Fig. 1(a)] interacts with the near wake to control vortex shedding. In the scope of finite cylinders, two setups have been studied: one in which the

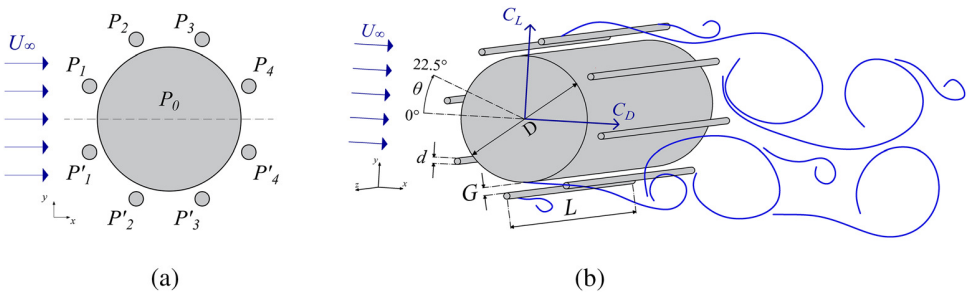

FIG. 1. (a) System comprised of the main cylinder (P_0) and eight rods P_1, P_2, P_3, P_4 and their primed counterparts, symmetrically displayed with respect to the *x*-axis crossing the center of the system. (The figure is not to scale for better visualization.) (b) Parameters of the flow and the system formed by the main cylinder and the eight fitted peripheral rods.

Physics of Fluids ARTICLE scitation.org/journal/phf

system was fully submerged with two free ends and another in which a free surface was attached to one of the ends.

Results from the numerical simulations performed at $Re = 1000$ will be discussed in terms of hydrodynamic loads, wake topology, and wake interaction with the free surface and free-end effects.

III. METHODOLOGY

A. Problem description

The incoming uniform flow with flow speed U_∞ was set past a plain cylinder of diameter D and past a system comprised of the main cylinder (P_0) surrounded by eight peripheral rods (P_n). Figure 1(b) represents the aforementioned system, showing the central body surrounded by eight fixed rods of diameter $d = D/20$. A gap $G = D/100$ was set between the walls of the main cylinder and the rods. This geometry has been deeply studied in other works with and without spinning rods (Assi *et al.*, 2019; Carvalho *et al.*, 2021; Carvalho and Assi, 2022).

It should be noted that designated frontal and rear rods were deliberately displaced away from the stagnation regions of the main body by an angle of 22.5°. In addition, rods were evenly distributed along a circumference of radius $D/2 + G + d/2$ centered at the origin of the entire system (coincident with the center of the main body) apart from one another by 45°.

Regarding the end conditions of the cylinders, three cases have been investigated (shown in Fig. 2):

Case i, infinitely long body: The periodic boundary conditions in the numerical domain guaranteed that no end effects would interfere with the three-dimensional flow, thus producing an infinitely long body (Fig. 2, left).

The next cases employed finite bodies with three-dimensional end effect. A low aspect ratio of $L/D = 2$ was set for all simulations:

Case ii, finite body, fully submerged: Both free ends of the low-aspect-ratio cylinder were exposed to three-dimensional flow. The boundaries of the numerical domain were set sufficiently far apart not to interfere with the flow around the body (Fig. 2, middle).

Case iii, finite body with a free surface: One of the free ends of the cylinder was replaced by a free surface, modeled here as a plane that allowed free slipping of the flow (Fig. 2, right). A two-phase flow has not been considered.

Finally, regarding possible wave interactions on a real free surface, we verified that the Froude number based on the cylinder's length (given by $Fr = U_\infty/\sqrt{gL}$, where g is the gravitational acceleration) was inferior to 0.23. According to Newman (2018), for a subcritical regime of $Fr < 1$, the wave pattern is similar to that expected for deep waters. Generally, for $Fr < 0.5$, water elevation due to free surface effects is deemed negligible. Thus, since wave effects are not significant in the present study, our setup fits well in these conditions and the free surface can be adequately represented by a slip-allowing plane. Gonçalves *et al.* (2018), for example, employed a similar approach for an experimental investigation of floating bluff bodies in a water channel.

B. Finite volume scheme and meshing

The incompressible flow in a turbulent regime was simulated at a Reynolds number $Re = U_\infty D/\nu = 10^3$, based on the main cylinder's diameter D, incoming flow speed U_∞, and fluid viscosity ν. Finite volume simulations were performed in OpenFOAM, an open-source C++ library, to obtain the second-order discretization of the governing equations of mass conservation and momentum transport for incompressible flow and Newtonian fluid, as given by the Navier–Stokes and continuity equations in the differential form below:

$$\rho\left(\frac{\partial U_i}{\partial t} + U_j\frac{\partial U_i}{\partial x_j}\right) = -\frac{\partial p}{\partial x_i} + \mu\frac{\partial^2 U_i}{\partial x_j \partial x_j}, \tag{1}$$

$$\frac{\partial U_j}{\partial x_j} = 0. \tag{2}$$

The left-hand side of the equation was discretized by means of an implicit backward scheme for the Eulerian term and with a second-order blend of the linear upwind and central scheme (with proportion 1:3) for the convective term. Gradients followed a cell-based least squares procedure. Linear interpolation allowed for the computations on the surface of the cells from cell center values. The discretization of the Laplacian term was attained by a surface-normal gradient corrected for non-orthogonality together with the Gauss theorem. All turbulent quantities were subjected to a linear upwind discretization. All terms followed a second-order truncation error.

Coupling between pressure and velocity was made with the transient version of the SIMPLE algorithm of Patankar (1980). This was necessary because there is not a transport equation for the pressure or an equation of state relating pressure and velocity, as it can be

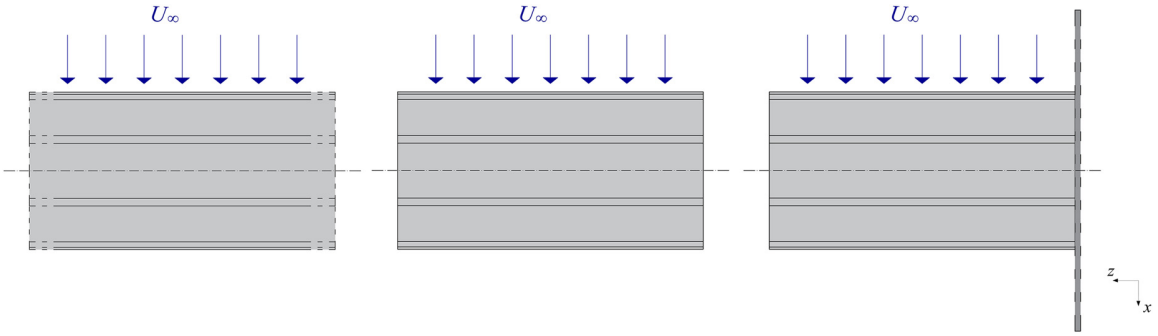

FIG. 2. Three cases regarding end effects: system with nominally infinite span, where end effects are neglected (left), fully immersed finite system (middle), and finite system under the effect of a free surface (right).

Physics of Fluids ARTICLE scitation.org/journal/phf

observed from Eqs. (1) and (2). For the velocity field, a tight tolerance of 10^{-8} was imposed for convergence of each time step. For pressure, the simulation of the bare cylinder of case i was simulated with maximum residual tolerance of 10^{-6}, while other cases adopted 10^{-4}. From Carvalho and Assi (2022), it became clear that this lower tolerance for the pressure did not compromise the results and yet allowed for faster simulations.

Symmetry boundary conditions (no flow across) were applied to the sides of the domain and the free surface of case iii, and no-slip condition was applied to the surfaces of the cylinders. The inflow was specified by the flow velocity U_∞ and zero pressure gradient; the outflow was set at a fixed pressure and null velocity gradient. Inlet and outlet are shown in Fig. 3, in which L_s and L_f represent the distances from the system ends to the sides of the domain.

Case i was reproduced by means of a spanwise length of the bodies $L = \pi D$ (in agreement with Assi *et al.*, 2018), accompanied by periodic boundary conditions on the sides of the domain to simulate the flow over infinitely long bodies. In this case, and using Fig. 3 as a reference, L_s and L_f were set to zero and the width of the domain matched the cylinders' span.

Finite bodies were specified with length $L = 2D$. The immersed bodies of case ii laid distant $L_s = L_f = 8D$ from the sides of the domain.

To simulate case iii—the flow about the bare cylinder and about the entire system with a free surface—one of the sides of the bodies was attached to one a slip surface (at $z = -D$), so, $L_f = 0$ and $L_s = 8D$ were imposed.

In any of these cases, the center of the main cylinder was distant $8D$ from the top and bottom surfaces and the inlet. A greater distance of $20D$ was applied between the main cylinder's center and the outlet downstream. These dimensions for the grid geometry corroborate with the work of Behr *et al.* (1995; 1991), Kim and Mohan (2005), and with Carvalho and Assi (2022)—where a wider domain of the same mesh was investigated—and are, thus, expected to mitigate blockage effects.

Hexahedral and prismatic elements covered the flow domain, and mesh refinement was conducted toward the bodies and in the wake region to capture typical gradients related to vortices and eddies. Away from the cylinders and the wake, the cells were made larger. Figure 4 portrays a cross-section passing through the system for the cases of infinitely long [Fig. 4(a)] and finite bodies [Fig. 4(b)]. (For reference, the set of axis is given in Fig. 3.)

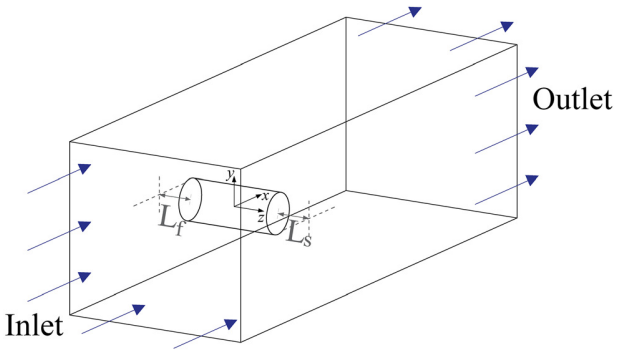

FIG. 3. Numerical domain. Only the main cylinder is represented for clarity.

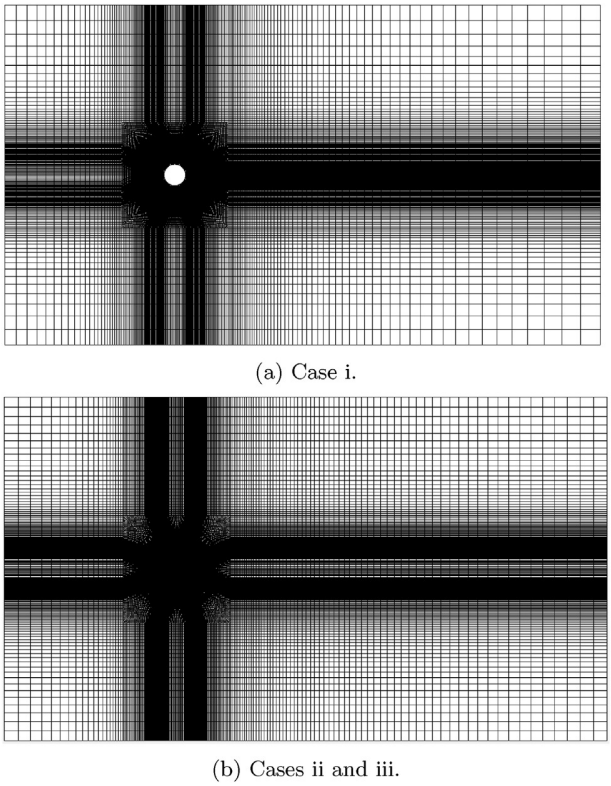

(a) Case i.

(b) Cases ii and iii.

FIG. 4. Meshed domain of the system for cases i (a) and ii and iii (b) for a cross section (z-plane) passing through the system. The flow is in the *x*-direction. (a) Case i. (b) Cases ii and iii.

Exclusively structured and hexahedral elements were used for case i although they were also predominant in the other cases as well. In particular, this type of element was employed to capture boundary layer features. Unstructured, prismatic, elements composed of the cells located on the free ends of the cylinders of cases ii and iii, and the region extruded away to the sides from these surfaces. A planar view of rod P_1 is shown in Figs. 5(a) and 5(b), where triangular elements (of the yet non-extruded mesh) were employed on the free ends of the main cylinder and the rods. Figure 5(c) shows the same rod in a 3D spanwise view and captures its end fixed to the free surface.

For all three cases, the smallest element measured $10^{-3}D$ on the wall of the bare cylinder; for the configurations involving the entire system, it spanned $1.54 \times 10^{-3}D$ for the main body and $3.77 \times 10^{-3}d$ for the rods to ensure quality results near the boundary layer and dispense with wall functions. It must be taken into account that the rods were on the verge of vortex shedding because the Reynolds number based on their diameter $Re_d = Ud/\nu$ was merely 50.

Extrusion of the cases of infinitely long bodies and of the finite bodies are depicted in Fig. 6. For the case of infinitely long cylinders, Fig. 6(a) shows that uniform refinement was applied along the span of the bodies, and their free ends were disregarded. In contrast, the second case [Fig. 6(b)] was refined near the tips of the cylinders, which were closed by a side surface. In particular, this second figure shows

Physics of Fluids ARTICLE scitation.org/journal/phf

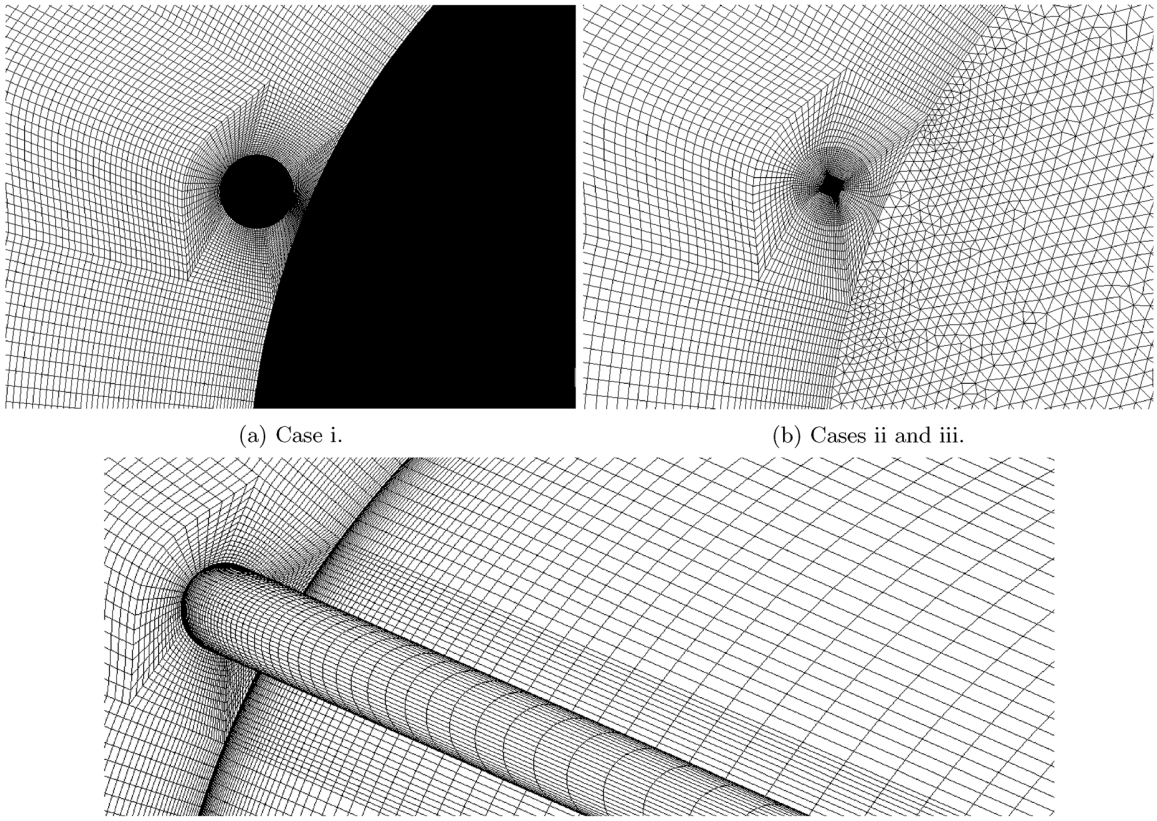

(a) Case i. (b) Cases ii and iii.

(c) Spanwise view near the free surface of case iii.

FIG. 5. Cross section of the meshes for cases i (a), ii and iii (b) showing rod P_1. Grids used for the low-aspect ratio cases required meshing of every cylinder side to capture end effects (b). Spanwise refinement is captured in (c). (a) Case i. (b) Cases ii and iii. (c) Spanwise view near the free surface of case iii.

the triangular-shaped elements that comprised part of the lateral surface of the main cylinder.

C. Turbulence modeling

Note: This section details the approach to turbulence modeling employed in the present investigation, especially considering future works that might advance the numerical scheme. The non-specialized reader may skip this section without losing comprehension of the results.

For cost-effective 3D simulations involving turbulence scales, the detached-eddy simulation (DES) approach was elected (Spalart, 1997) together with the one-equation model of Spalart and Allmaras (1992) for the turbulent viscosity parameter $\tilde{\nu}$ within the resolution of the boundary layer involving such a Reynolds-averaged Navier–Stokes (RANS) model,

$$\frac{\partial \tilde{\nu}}{\partial t} + U_j \frac{\partial \tilde{\nu}}{\partial x_j} = c_{b1}(1 - f_{t2})\tilde{S}\tilde{\nu} + \frac{1}{\tilde{\sigma}}\left\{\frac{\partial}{\partial x_k}\left[(\nu + \tilde{\nu})\frac{\partial \tilde{\nu}}{\partial x_k}\right] + c_{b2}\frac{\partial \tilde{\nu}}{\partial x_k}\frac{\partial \tilde{\nu}}{\partial x_k}\right\} - \left(c_{w1} f_w - \frac{c_{b1}}{\kappa^2} f_{t2}\right)\left(\frac{\tilde{\nu}}{d_{\text{wall}}}\right)^2,$$

where the notation d_{wall} is the distance from the wall. Further constants were set as

$$\tilde{\sigma} = 2/3, \quad \kappa = 0.41, \quad c_{b1} = 0.1355, \quad c_{b2} = 0.622, \quad c_{w2} = 0.3, \quad c_{w3} = 2, \quad c_{v1} = 7.1 c_{w1} = c_{b1}/\kappa^2 + (1 + c_{b2})/\tilde{\sigma}, \quad c_{t3} = 0, \quad c_{t4} = 0.5.$$

Among the following expressions, f_{v2} and f_w are damping functions:

$$\chi = \tilde{\nu}/\nu, \quad f_{t2} = c_{t3} \exp(-c_{t4}\chi^2),$$
$$f_{v1} = \chi^3/(\chi^3 + c_{v1}^3), \quad f_{v2} = 1 - \chi/(1 + \chi f_{v1}),$$
$$\tilde{S} = \max\left\{\left|\frac{\partial U_i}{\partial x_j} - \frac{\partial U_j}{\partial x_i}\right| + \frac{\tilde{\nu}}{\kappa^2 d_{\text{wall}}^2} f_{v2},\ c_s\left(\frac{\partial U_i}{\partial x_j} - \frac{\partial U_j}{\partial x_i}\right)\right\},$$
$$f_w = g\left[\frac{(1 + c_{w3}^6)}{(g^6 + c_{w3}^6)}\right]^{1/6},$$
$$g = r + c_{w2}(r^6 - r), \quad r = \min(\tilde{\nu}/\tilde{S}\kappa^2 d^2,\ 10).$$

The relationship between the turbulent viscosity ν_t and the turbulent viscosity parameter $\tilde{\nu}$ was given by

$$\nu_t = \tilde{\nu} f_{v1}.$$

Physics of Fluids ARTICLE scitation.org/journal/phf

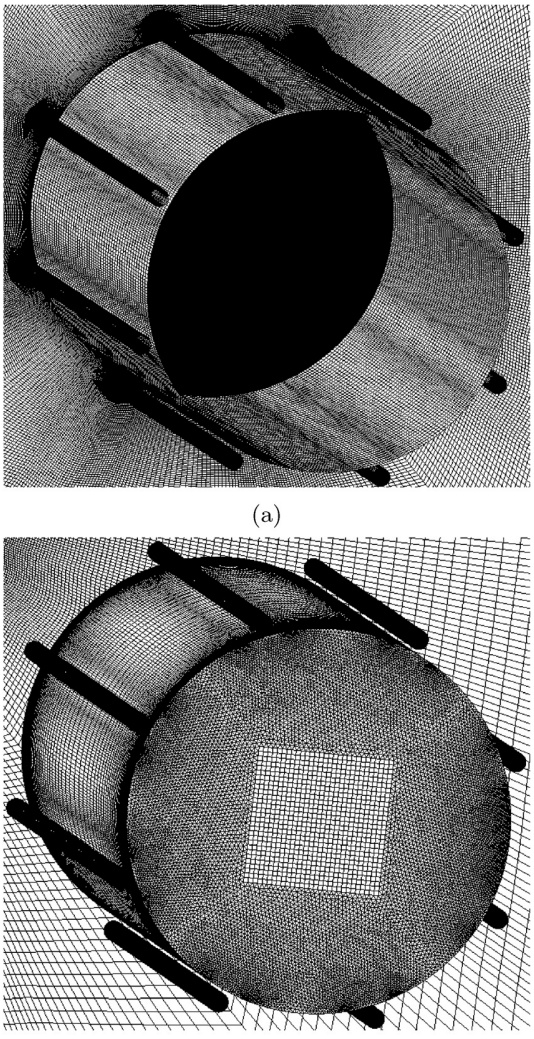

FIG. 6. Extruded meshes for both cases of infinitely long (a) and low-aspect-ratio cylinder (b). In the former, it is seen that spanwise mesh refinement is uniform, whereas refinement is enhanced near the ends of the cylinders for the latter.

A major problem in the DES formulation for the flow about cylindrical structures in a sub-critical regime is that the boundary layer is laminar, whereas the wake is already turbulent (Saltara *et al.*, 2011), and the RANS formulation for the boundary layer is intrinsically turbulent. This downside was circumvented by a low-*Re* correction (Ψ Spalart *et al.*, 2006)

$$\Psi = \min\left\{10^2, \left[1 - \frac{1 - c_{b1}}{c_{w1}\kappa^2 f_w^*}(f_{t2} + (1 - f_{t2})f_{v2})\right] \times \left[f_{v1}\max(10^{-10}, 1 - f_{t2})\right]^{-1}\right\}, \quad (3)$$

so the characteristic length of the DES formulation (l_{DES}) became

$$l_{DES} = \min(\Psi C_{\mathrm{DES}}\Delta,\ d_{\mathrm{wall}}),$$

where Δ is the largest dimension of the cell and the remaining calibrating constants are $C_{\mathrm{DES}} = 0.65$ and $f_w^* = 0.424$. This approach was shown to work well in Carvalho and Assi (2022).

IV. RESULTS

A. Reference simulations

Reference simulations were carried out first for verification, validation, and grid independence test with respect to drag (C_D) and lift (C_L) coefficients, respectively, given by the corresponding loads nondimensionalized by $\rho U^2 DL/2$. For case i, these results are found in Carvalho and Assi (2022) and will not be repeated here for brevity.

For case ii, validation was made with the results substantiated by Goldstein (1965) apud Farivar (1981) for cylinders of finite length, where the authors found that the mean drag was $\overline{C_D} = 0.67$ at $Re = 8.8 \times 10^4$ for an aspect ratio of 1.98. Our simulation at $Re = 10^4$ produced $\overline{C_D} = 0.64$, in agreement with Goldstein (1965) over 95.5%. We disclose that it is, indeed, a feature of this field that recent papers have hardly dealt with measurements over finite cylinders of low aspect ratio with both ends free or under the effect of a water surface. Most of the papers on this matter are from the past century. Recent results either take L/D much greater than 2 or consider another setup, such as wall-mounted bodies or stationary bodies piercing through the water surface.

Table I presents the grid independence test at $Re = 10^3$, in relation to mean drag ($\overline{C_D}$) and root mean square (RMS) lift ($\hat{C}_L$). The highlighted lines correspond to the meshes that will serve as references for cases ii and iii throughout the text. Most quantities showed variance below 10%, thus presenting good convergence, except for the RMS lift coefficient of case iii. However, this greater variance was to be expected for $\hat{C}_L$ of this case as these are small quantities and strongly vary, even after taking a simulation time that spanned $40T_S$ as it was done here. We remark that T_S is the time span of a vortex shedding cycle in the case of the flow past an infinitely long bare cylinder in a subcritical regime.

To further confirm the quality of our meshing, we have verified the convergence of the mean pressure coefficient ($\overline{C_p}$) of case iii. This

TABLE I. Grid independence test with respect to mean drag ($\overline{C_D}$) and RMS lift ($\hat{C}_L$) for cases ii and iii. The highlighted rows show variance below 10% relative to the most refined mesh hereby tested, except for $\hat{C}_L$ of case iii, thus providing a good compromise between computational resources and accuracy.

Bare cylinder					
Case ii (finite)			Case iii (free surface)		
Number of cells	$\overline{C_D}$	$\hat{C}_L$	Number of cells	$\overline{C_D}$	$\hat{C}_L$
4 466 680	0.71	0.0414	3 385 152	0.72	0.0219
6 679 440	0.69	0.0708	4 107 512	0.72	0.0243
8 433 710	0.69	0.0338	4 829 872	0.73	0.0329
10 198 560	0.68	0.0380	5 552 232	0.73	0.0302
12 322 680	0.68	0.0330	6 274 592	0.72	0.0340
15 293 080	0.69	0.0330	8 257 368	0.72	0.0317

Physics of Fluids ARTICLE scitation.org/journal/phf

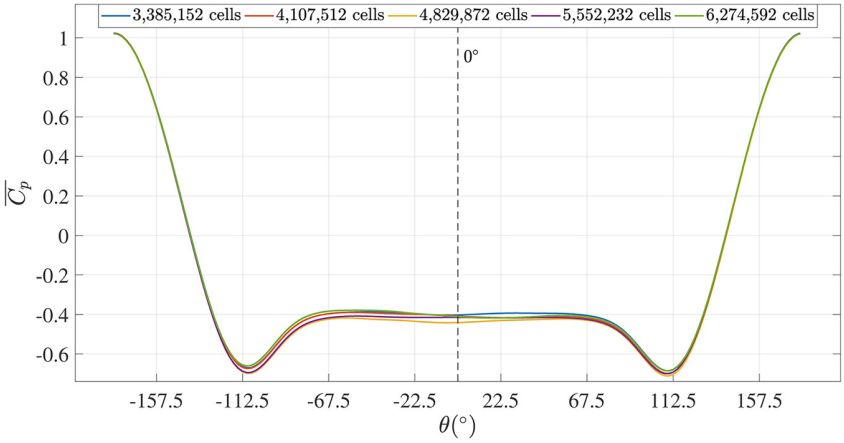

FIG. 7. Case iii mesh convergence study. Mean pressure coefficients $\overline{C_p}$ were taken at different angular positions at $z = L/D$.

analysis was conducted over the circumference of the bare cylinder at different $\theta = \tan^{-1}(y/x)$ angles at $z = L/D$, and it is given in Fig. 7. From the figure, it becomes clear that no significant difference can be ascertained about the mean pressure coefficient among the different levels of mesh refinement.

We note that the mesh used for the system with finite bodies here followed precisely that for the infinitely long system of Carvalho *et al.* (2021) in the same turbulent *Re*-regime and Carvalho and Assi (2022) in the laminar regime, in the sense that the latter structured mesh was merely extruded along the span of the cylinder with refinement toward the tips. About 102 cells described the span of the finite cylinders and 100 represented the flow domain away from the tips (in the spanwise z-direction) of every side. Due to the unstructured mesh applied to the side faces of the cylinders (see Fig. 6), the extruded mesh departing from them was unstructured as well, as it can be visualized by Fig. 4. In total, 30 997 904 and 19 153 204 cells were, correspondingly, used for the entire system of cases ii and iii encompassing prismatic and hexahedral elements altogether.

Finite bodies' simulations require large meshes for adequate representation of the flow. For a cost-effective grid independence study of such systems, only the grid of case iii was assessed. Of course, meshwise, this case also incorporated the stencil features of case ii with respect to the immersed end of the system. Thus, this analysis allowed us to investigate both the convergence of cases ii and iii at once. $40T_S$ were run for each simulation and only the last $20T_S$ were used for the computation of mean and RMS quantities. The grids were constrained to the same size $D/1000$ of the first element near the wall for a fair comparison. Mean drag and RMS lift are presented in Table II. In parenthesis, the percentile difference relative to the reference mesh is given. For the mean drag, the difference between the meshes was below 3%. For lift, the discrepancy was generally greater the coarser the mesh. Still, the table shows that all values were in the same order of magnitude; considering that $\hat{C}_L$ was given by a low value, larger deviance was expected in mesh convergence.

We selected the most refined mesh (highlighted in Table II) to represent the flow about a finite system with a free surface. For case ii, basically, the same mesh was used. The only difference was that the region where there is a free surface in case iii was replaced by an immersed end in case ii (with a symmetrical mesh to that of the immersed end of case iii), thus justifying our mesh convergence procedure.

B. Time histories of hydrodynamic loads

All simulations were left to run for $15T_S$, assumed to be part of the numerical transient that preceded converged and realistic physical results. After this, in order to compute mean and RMS quantities, the simulations spanned at least another 25 additional cycles of vortex shedding, resulting in a total run of at least $40T_S$. T_S here is based on the common assumption that, in agreement with experiments, the Strouhal number can be reasonably approximated by $S_t = (T_S/D/U)^{-1} \approx 0.2$ for an infinitely long fixed cylinder in the subcritical regime, as it can be noted from the compiled results of Norberg (2001).

Thick and thin lines in Fig. 8 correspond to the $25T_S$ converged time histories of lift and drag, respectively. It can be clearly noted that infinitely long cylinders led to the most accentuated hydrodynamic loads and frequency of vortex shedding among the different cases. In any case, the entire system produced greater loads than the plain cylinder. Additionally, attaching a free surface to one end of the cylinders, as in case iii, caused the mean drag to increase compared to the fully immersed system of case ii, see Table III.

A dampening of shedding frequencies is strikingly evident in Fig. 8 for both the setups of a plain cylinder and the entire system in cases

TABLE II. Grid independence test with respect to mean drag ($\overline{C_D}$) and RMS lift ($\hat{C}_L$) for the entire system of case iii.

Entire system (case iii)		
Number of cells	$\overline{C_D}$	$\hat{C}_L$
19 153 204	1.02	0.035
12 017 194	1.02	0.030
9 648 254	0.994	0.033
7 273 476	0.998	0.027
5 372 486	1.00	0.020

Physics of Fluids ARTICLE scitation.org/journal/phf

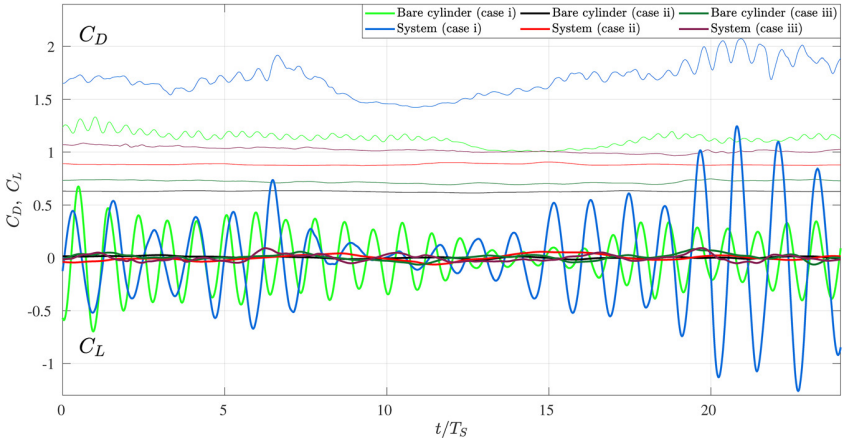

FIG. 8. Converged time histories of lift and drag. The time has been non-dimensionalized by the duration of a vortex-shedding cycle. Thick lines correspond to measurements of lift; thin lines correspond to drag.

ii and iii against case i, followed by their much lower mean coefficients. From $\overline{C_D}$ curves, visual inspection indicates progressive flattening of the fluctuations on the order of cases i, iii, and ii, which is the same order as that where end effects were subsequently incorporated into the system configuration. In case i, end effects were not accounted for; in case iii, only one end was free (as the other was attached to the free surface), and in case ii, both ends interacted with the flow.

Because the bare cylinder presented lower $\hat{C}_L$ than the entire system for any corresponding case (see Table III), a lift increase can be regarded as a consequence of attaching the slender rods to the main body.

C. Vorticity contours

Comparing the setup of the bare cylinder with that of the entire system, the more pronounced drag in the latter might be explained by the relatively greater low-pressure region downstream of the system, produced by the wider wake as revealed by Fig. 9. The figure also shows a less coherent distribution of vortical content within the wake of the finite cases ii and iii that lowered mean drag compared with that of case i, as described below in Sec. IV E.

For case i, the wider wake was accompanied by stronger and larger opposing vortices (first row of Fig. 9) whose response on the structure was translated into greater transversal loads. For cases ii and iii, higher lift due to the presence of the rods is explained by the fact that a wider wake and anticipated roll-up of the shear layers resulted from the presence of the rods (second row of Fig. 9). Of course, vortices are stronger, the nearer they are to the separation point of the shear layer, which acts as their source of vorticity (Gerrard, 1966). As the diffused vortices were shed more distant from the body, the viscosity of the fluid continuously dissipated their strength (from Tennekes and Lumley, 1972, we recall that viscous shear is proportional to velocity gradients, a major feature of the vortices).

Figure 10 supports this argument through Q-contours of high and low levels of vorticity (red and translucent blue-colored), which are evidently associated with small and large coherent vortices, respectively. Turbulent structures carrying high vorticity in case i were ubiquitous and led to a wider wake. The other cases presented weaker vorticity levels and overall more concentrated Q-contours within the shorter wake. From Kawamura *et al.* (1984), for the present L/D value, indeed, the wake was expected to be narrower in finite cases. However, different from these authors, our case involved the interaction of two trailing vortices from the ends of the cylinders instead of that between a trailing vortex (from one free end) and a "necklace vortex" (from the other, wall-mounted, end).

Indeed, the formation length was prolonged by 7.2%, 6.7%, and 12.4% for cases i, ii, and iii, respectively, as the result of the insertion of the rods around the main body, see Fig. 11. We recall that the formation length is defined as the distance from the body to "that point downstream of the body where the velocity fluctuation level has grown to a maximum (and thereafter decays downstream)" (Williamson, 1996). These results are supported by the contours of the time-averaged squared fluctuation of the velocity, as shown in Fig. 12, where the wider wake is highlighted by the enlargement of the spacing between the shear layers detached from the sides (white lines). We note that the boundary and the shear layers were obtained as white contours which corresponded to $0.99U_\infty$, thus justifying the recurrent appearance of the white curve even before the system or, as in case iii, away from the bodies. In the latter, following contours of $0.99U_\infty$, we can note that the wake recovered faster the velocity of the incoming flow past the obstruction of the bodies in comparison with case ii.

It is also worth mentioning that the asymmetry (relative to $x = 0$, see Fig. 3) found in the contours of Fig. 12 derived inherently from the randomness of the turbulent flow. This becomes more evident from comparing the subfigure of the bare cylinder of case i against the other cases. The asymmetry reveals clearer either as a result of end effects (as it will be explored below) or due to the increased complexity of the turbulent flow structures due to the addition of the rods.

TABLE III. Mean and RMS coefficients.

	Bare cylinder		Entire system	
Case	$\overline{C_D}$	$\hat{C}_L$	$\overline{C_D}$	$\hat{C}_L$
i	1.13	0.233	1.71	0.464
ii	0.631	0.0113	0.883	0.0303
iii	0.722	0.0325	1.020	0.0347

Physics of Fluids ARTICLE scitation.org/journal/phf

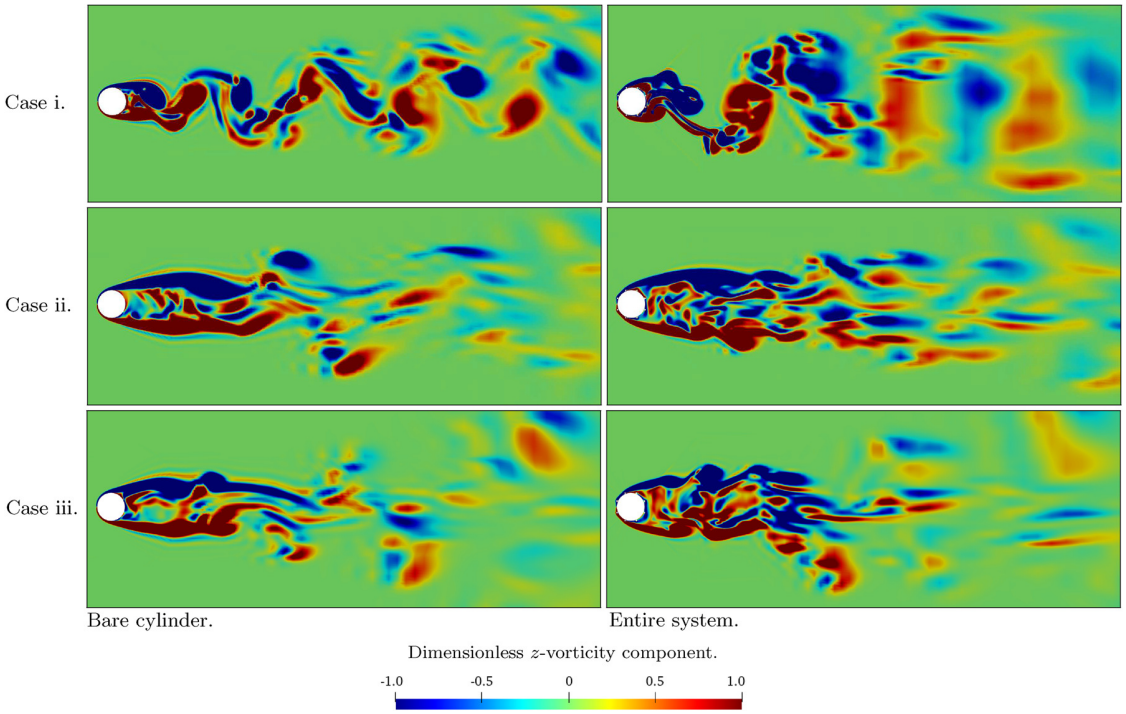

FIG. 9. Dimensionless z-vorticity component, scaled by U_∞/D. Finite cases correspond to the cross-section midway along the cylinders' span. All cases were taken at a positive peak of the lift curve.

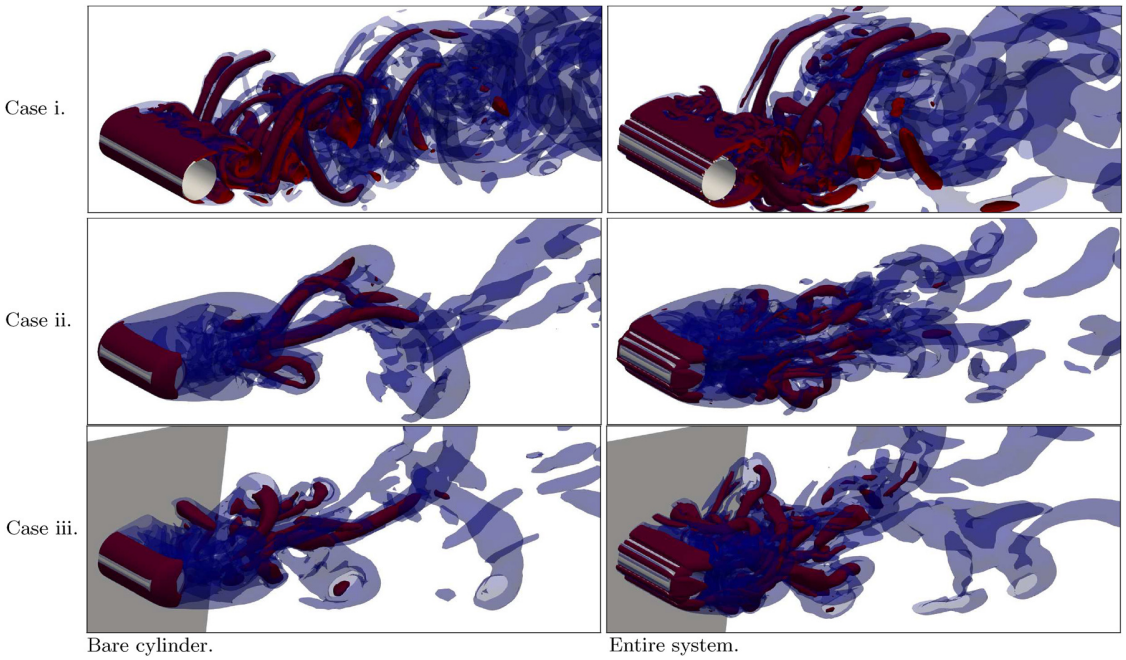

FIG. 10. Q-contours of high and low vorticity at $Q = 2.5$ (red) and $Q = 0.1$ (blue, transparent), respectively. The plain cylinder case is located on the left and the entire system on the right. For ease of visualization, only part of the plane corresponding to the free surface is shown (in gray).

Physics of Fluids ARTICLE scitation.org/journal/phf

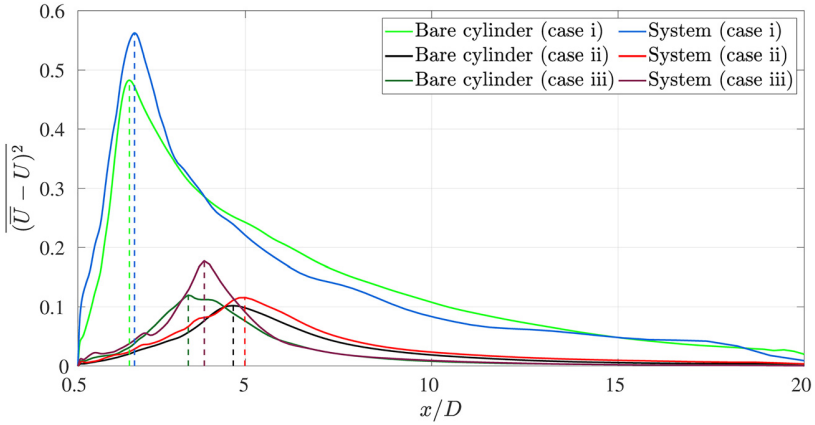

FIG. 11. Increase of mean formation length as the result of fitting the slender rods to the main body. The formation length is marked by x/D, where the mean fluctuation of the velocity was at peak value (abscissae of the dashed lines).

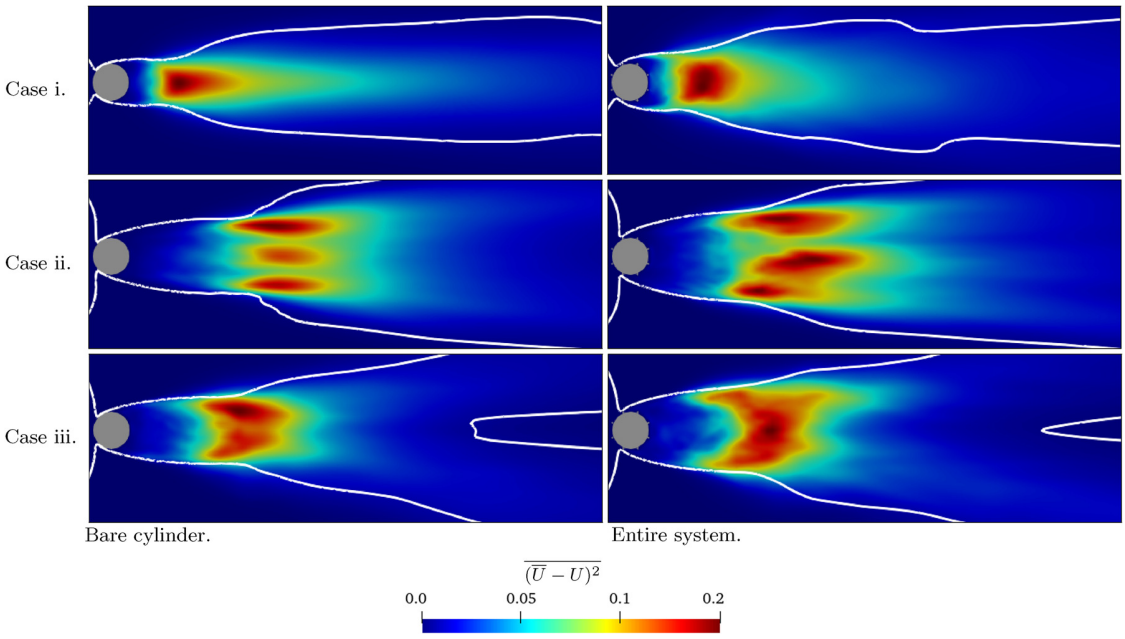

FIG. 12. Contours of the time-averaged square of the mean velocity fluctuations for cases i (top), case ii (middle), and case iii (bottom row) on the plane $z = 0$. The distance from the posterior stagnation point on the system to the location of maximum mean fluctuation defines the formation length.

D. Hydrodynamic loads on each cylinder

One important measure is that of hydrodynamic loads on the main body P_0 to which the passive mechanism was installed. Measurements of mean drag and RMS lift highlight that in case i, changing from the bare cylinder to the entire system increased mean drag by 43.3% and RMS lift by 63.6% for the main body. In case ii, the respective changes were 31.7% and 134%. In case iii, mean drag and RMS lift changed by 33.0% and −5.85%. The actual amounts are provided in Table IV for reference.

TABLE IV. Hydrodynamic coefficients.

	Bare cylinder		P_0	
Case	$\overline{C_D}$	$\hat{C}_L$	$\overline{C_D}$	$\hat{C}_L$
i	1.13	0.233	1.61	0.381
ii	0.631	0.0113	0.826	0.0265
iii	0.722	0.0325	0.960	0.0306

Physics of Fluids ARTICLE scitation.org/journal/phf

In terms of drag, a relative reduction of at least 40.4% was observed for the mean drag of P_0 for the passive mechanism in finite cylinders against its equivalent effect in the infinitely long setup. This can generally be attributed to three-dimensional effects, mainly to the disruption of the greater correlation in wake of the infinitely long case against the finite cases.

On the matter of lift changes, the explanation is less obvious. For case i, the analysis converges to that of Carvalho and Assi (2022), i.e., stronger vortices, a wider wake and more correlated structures along the spanwise direction of the system (due to the assumption of infinitely long cylinders) led to higher RMS lift. For cases ii and iii, similar effects were present, in addition to trailing edge effects as explained in Sec. IV E.

Figures 13(a) and 13(b) show mean drag and lift coefficients that acted on each individual rod, according to their angular positions [refer to Fig. 1(b)]. Rods P_2, P'_2 were subjected to the greater absolute reduction in $\overline{C_D}$ and $\overline{C_L}$ of all rods. Contrarily, rods P_3, P'_3 seemed oblivious to the different approaches. Rods P_1, P'_1 experienced an increase in $\overline{C_D}$ from null value and a decrease in $|\overline{C_L}|$ (with emphasis on case ii for both loads) and P_4, P'_4 shifted with opposite tendencies toward negligible contribution. This is in agreement with Carvalho *et al.* (2021); Carvalho and Assi (2022) in the sense that P_2, P'_2 exceeded the other rods in relevance, as measured by the magnitude of the forces acting on it. In addition, this symmetric set of passive elements was demonstrated to be more sensitive among the different cases than the other rods. Contrary to the aforementioned papers,

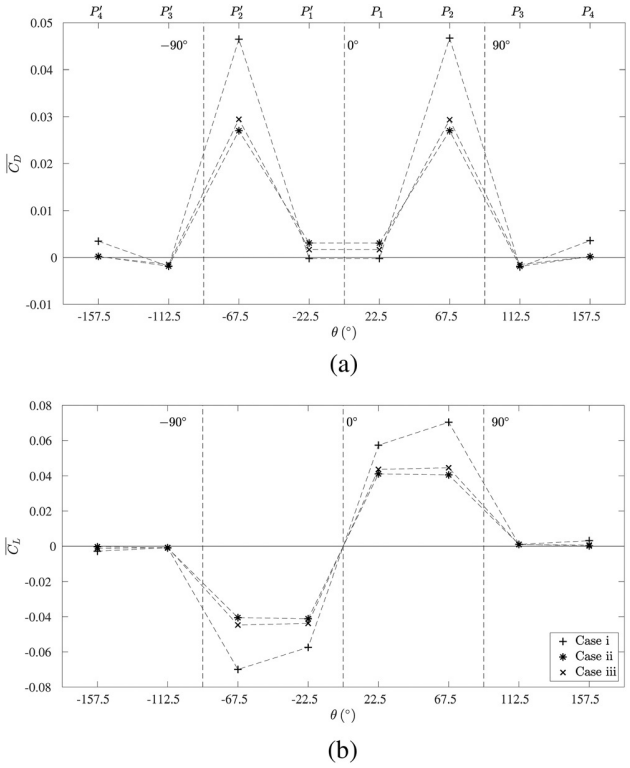

FIG. 13. Mean drag (a) and RMS lift (b) on each of the control rods for both cases of infinitely long cylinders and that of the low aspect ratio (finite cylinders).

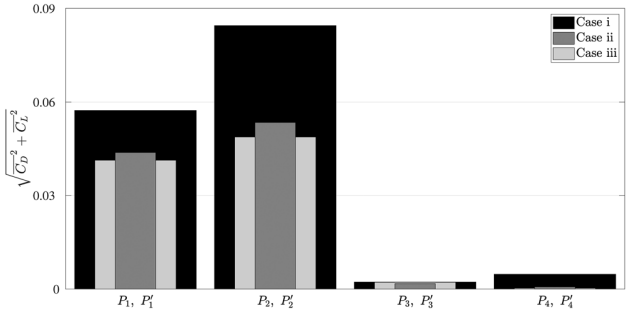

FIG. 14. Total force upon the upper rods of the entire system. By symmetry, their counterparts were subjected to the same loads. Among the different cases, it stands out compared with the previous works that P_4, P'_4 presented negligible loads in finite cases ii and iii compared with the infinitely long case i.

P_1, P'_1 did not carry a negligible mean drag load although it was lower than P_2, P'_2.

The negligible influence of P_4 in Fig. 14 stands out (by symmetry, this applies to P'_4 as well). The previous studies (Assi *et al.*, 2019; Carvalho *et al.*, 2021; Carvalho and Assi, 2022) with infinite cylinders showed that within the scope of a passive mechanism, P_3, P'_3 were affected with lower forces. Here, the opposite is seen. As the rods were modeled finite, P_3, P'_3 remained comparable within cases i, ii, and iii, but, P_4, P'_4 became apparently irrelevant in the latter two cases against the infinitely long case. This draws attention to how these curves would compare with an active mechanism, where all rods would spin to promote the reattachment of the boundary layer, as it was done previously in the literature.

E. End effects

Aside from the aforementioned discussion, there was also a distinct three-dimensional effect contributing to the hydrodynamics of cases ii and iii: that of the free end effects on the flow.

It can be noted from Fig. 16 that the mean velocity vector field projected in the x-plane increased in magnitude on cross-sections passing through the bodies ($x/D = -0.4$ to 0.4), and it swirled around the free end, producing streamwise vortices whose axes were aligned with the x-direction, in the fashion of the upwash- or downwash-like effect. These vortices were barely noticeable in the first cross section, which just past P_1, P'_1, at $x/D = -0.4$. Still, as the flow went around the main body, $x/D = 0$, their formation became clearer. The same analysis is not shown here for the infinite bodies because this flow structure was not observed in such cases.

Between systems of finite length, the main difference was in the faster velocity field of case iii relative to that of case ii along the spanwise direction. The free surface, in blocking the flow that would, otherwise, be directed to one of the ends of the cylinder, sped up the flow in the spanwise z-direction, compared with the former case, as it can be appreciated in the row $x/D = 0.4$ of Fig. 16. This faster velocity field reached the ends of the main body and rods and led to stronger streamwise vortices and a more widespread wake, as presented by Fig. 15. Moreover, the figure also makes clear that the free water surface of case iii amounted to a more significant impact on the streamwise vortices, notably in the number of turbulent eddies with a high

Physics of Fluids ARTICLE scitation.org/journal/phf

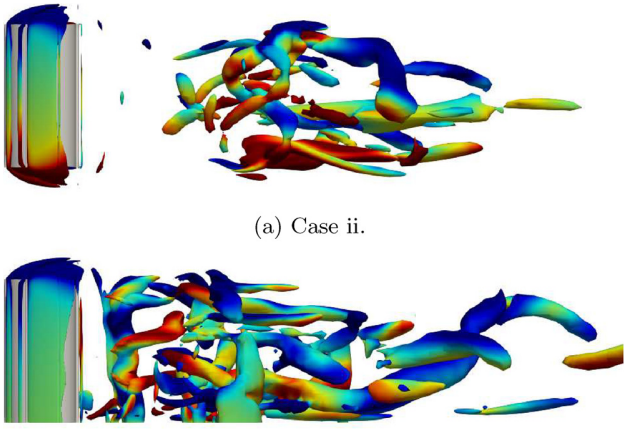

(a) Case ii.

(b) Case iii.

FIG. 15. Contours of dimensionless streamwise vorticity of cases ii (a) and iii (b), nondimensionalized by U_∞/D, ranging from -2.5 (blue) to 2.5 (red). Here, $Q = 2.5$. The represented cross section refers to the plane $y = 0$.

level of vorticity, represented by the presence of Q-contours in the entire wake region, further away into the wake (conversely, for case ii, Q-contours were restricted to a limited and rather intermediate region of the wake).

One of the effects of this three-dimensional phenomenon is how it affected the vortex formation length. Taking into consideration the contribution of Fox and West (1993), the separated flow that left the ends was responsible for delaying the interaction of the vortices and, thus, promoted greater formation length when compared with the respective bare cylinder cases since it led to a "less negative" base pressure. In turn, this culminated in the lower mean drag compared with infinitely long bodies.

Now, it must be acknowledged that between finite systems, in case ii, given sufficient distance away from the system, the vector field projected in the x-plane gradually disappeared, as it is progressively shown in Fig. 16 from $x/D = 0.0$ to $x/D = 1.0$, which is different behavior from that of case iii for the same x-stations: The planar slip-surface allowed streamwise vortices to prevail longer downstream. This is clearly in common with the paragraph above. Higher velocities along the span of the system (as observed for a single cylinder in Kawamura *et al.*, 1984) allowed streamwise vortices to persist long past the system. We further note that this effect was more accentuated for the entire system in comparison with the plain cylinder. This shows that the rods' ends led to a build-up of the vortical effect that would, otherwise, occur for a single cylinder.

Another effect is related to the increase in lift from the bare cylinder to the entire system. When the rods were inserted around the main body, a greater pressure imbalance was established between the upper ($y/D > 0.5$) and the lower ($y/D < 0.5$) parts due to the formation of these trailing vortices. Recall from Figs. 9 and 10 that, in cases ii

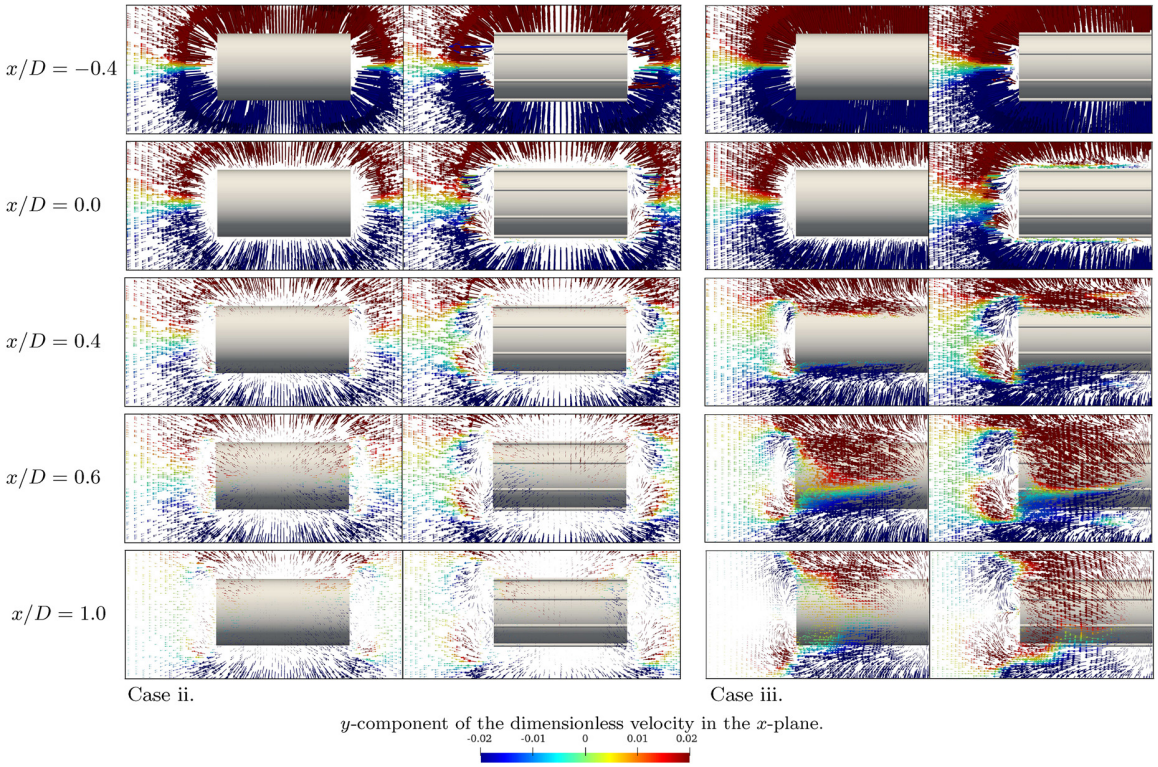

FIG. 16. Mean flow field over finite bodies projected in the yz plane at different stations x in the mean flow direction. Case iii presents a greater increment in upwash and downwash velocities due to the free ends of the cylinders.

Physics of Fluids ARTICLE scitation.org/journal/phf

and iii, the wake of the entire system demonstrated a more chaotic aspect and contained a greater diversity of turbulence scales. This is associated with the assertion by Kawamura *et al.* (1984) that the entire wake of low aspect ratio bodies corresponds with the interaction of trailing vortices in a region that span the entire length of the body (that would behave separately in bodies of high slenderness parameter L/D). Nonetheless, a noticeable feature can be observed from the videos (2D-view) provided in the supplementary material of this paper. The shear layer on one side of the system was partially convected away into the flow in the form of vortices, while the other part was mostly entrained into the wake and dissipated there, and a third very small parcel of one shear layer moved across the wake to cut off the other shear layer. As one of the major parts of the shear layer was dissipated within the wake, this may justify the greater lift as well because a larger region of low pressure was established above and below the entire system intermittently than it would if the contributions were similar to the usual mechanism exhibited in the work of Gerrard (1966).

Neither the absence of coherent vortex structures nor this form of entrainment recollects the typical Kármán vortex street, which is due to the lack of spanwise correlation and end effects. As such, vortex shedding broke away from the usual 2S shedding mode (Williamson and Roshko, 1988) and the part of the shear layer, entrained into the wake, was dissipated there due to viscous effects, leaving no contribution to the interaction and formation of the vortices. We further note that although these mechanisms added to the magnitude of the lift coefficient (from the plain cylinder to the entire system case), the collective effect was still weaker than that instigated by the correlation of case i, where end effects were neglected.

The lower correlation caused the formation of a wake for which spectral analysis did not provide a characteristic Strouhal number. This may also be the result of the low slenderness parameter used in this work, in common with Farivar (1981), as the author observed the appearance of more than one characteristic frequency for high aspect ratio cylinders but could not measure it for $L/D < 7.5$. The same applies here, for the bare cylinder and the entire system with $L/D = 2$. Thus, a lower level of organization in the wake directly associates with the flattening effect highlighted by the curves of Fig. 8. Indeed, the correlation induced by the assumption of a periodic condition to the ends of the body that was made in case i introduced an organizational effect on the wake that resulted in larger hydrodynamic coefficients and fluctuations.

As observed by Fröhlich and Rodi (2004), the resulting wake on a wall-mounted, plain cylinder deviates from a Kármán wake due to the bending and distortion of this well-correlated wake. This distinct behavior of the shear layer interaction with the body and with the wake draws attention to the extension to which an active mechanism of wake control, for example, spinning the rods, could have on vortex shedding of finite bodies of cases ii and iii and beyond, on end effects. An organizational effect has been widely observed for infinitely long cylinders in the literature (Assi *et al.*, 2018; 2019; Carvalho *et al.*, 2021), and it has drawn attention to optimization of systems involving peripheral rods as well (Fan *et al.*, 2020; Bingham *et al.*, 2018; Dehkordi *et al.*, 2018). Considering the dampening of the fluctuation of the hydrodynamic loads, it is an open question whether an active mechanism could be more efficient in low aspect ratio cylinders than in infinitely long ones.

V. CONCLUSION

Finite volume simulations under the turbulent formulation of detached-eddy simulations were conducted at $Re = 1000$. Validation, verification, and grid independence tests indicated a reliable numerical scheme for the computation of the flow about structures with free ends.

Three cases were verified: case i, where the cylinders followed a numerical scheme to simulate an infinitely long system; case ii, where end effects were considered in respect to both ends of the cylinders; and case iii, with one free end, while the other was attached to a slip-surface. Examination of the bare cylinder and of the entire system indicated that the free ends had a decreasing effect in the hydrodynamic loads greater than 40% in mean drag and over 92% in root mean square lift.

Despite the previous studies that ensure the incapacity of a passive mechanism to suppress vortex shedding at sufficiently high Reynolds numbers for infinitely long cylinders (Mittal and Raghuvanshi, 2001; Mittal and Kumar, 2003), the same study was not conducted for a system with free ends or with a free surface such as the present. To fit a circular cylinder with eight slender and passive wake-control rods under uniform flow at $Re = 1000$ proved insufficient to inhibit vortex shedding or to reduce the hydrodynamic loads compared with the plain body. Indeed, the greater obstruction to the flow caused by the surrounding slender bodies caused mean drag and root mean square lift to adopt higher values than those of the corresponding plain cylinder. Nevertheless, end effects promoted lower loads than those found in infinitely long bodies and were responsible for a formation length prolonged by at least 6.7% and weakening of vortex shedding in all cases. These features were shown to be the result of the more chaotic wake topology, which was also associated with end effects.

It was also exposed that the resulting wake was not of the Kármán type. Instead, a rather very small part of one shear layer was responsible for the cutoff of its opposite, and a major fraction of the shear layer was entrained and dissipated, contributing little to the interaction and formation of stronger vortices.

Streamwise vortices were detected in the time-averaged flow of the finite cases, and the absence of this flow structure was noted for infinite bodies. We have demonstrated that these vortices were enhanced cumulatively by the presence of the small rods and the slip-allowing surface (in connection with the increased velocity along the spanwise direction promoted by the blockage of the flow near the free surface).

Greater relevance of the frontal rods and negligible importance of the rear rods were observed in regard to individual contributions of the different rods comprising the passive mechanism, in contrast with Carvalho *et al.* (2021) and Carvalho and Assi (2022) for infinitely long bodies. The present results agree with and expand the knowledge of the previous works employing such a passive mechanism for infinitely long cylinders and pave the way for the application of this system to low aspect ratio structures under an active mechanism of wake control. For example, spinning the rods (Mittal, 2001; Korkischko and Meneghini, 2012) may be able to not only control vortex shedding and vortex-induced vibrations but also further step into the reorganization of the wake into a Kármán street, reduce hydrodynamic loads through, and even eliminate these phenomena entirely in bluff structures of finite length. These matters are left for future work.

SUPPLEMENTARY MATERIAL

See the supplementary material for videos of Q-contours (planar and 3D views) of cases i, ii, and iii.

ACKNOWLEDGMENTS

I.A.C. is grateful to CAPES Brazilian Ministry of Education for his Ph.D. scholarship and the National Laboratory for Scientific Computing (LNCC/MCTI, Brazil) for providing HPC resources of the SDumont supercomputer. G.R.S.A. acknowledges the support of FAPESP, Brazil (No. 2011/00205-6) and CNPq, Brazil (No. 306146/2019-3). We gratefully acknowledge the support of the RCGI Research Centre for Greenhouse Gas Innovation, hosted by the University of São Paulo, Brazil, and sponsored by FAPESP (No. 2020/15230-5) and Shell Brazil.

AUTHOR DECLARATIONS

Conflict of Interest

The authors have no conflicts to disclose.

Author Contributions

Icaro Amorim de Carvalho: Conceptualization (supporting); Data curation (lead); Formal analysis (equal); Investigation (equal); Methodology (equal); Software (lead); Validation (equal); Visualization (equal); Writing – original draft (lead); Writing – review & editing (equal). **Gustavo R. S. Assi:** Conceptualization (lead); Data curation (supporting); Formal analysis (equal); Funding acquisition (lead); Investigation (equal); Methodology (equal); Resources (lead); Software (supporting); Supervision (lead); Validation (equal); Visualization (equal); Writing – review & editing (equal).

DATA AVAILABILITY

The data that support the findings of this study are available from the corresponding author upon reasonable request.

REFERENCES

Assi, G. R. S., Crespi, T., and Gharib, M., "Novel geometries of serrated helical strakes to suppress vortex-induced vibrations and reduce drag," Appl. Ocean Res. **120**, 103034 (2022).

Assi, G. R. S., Orselli, R. M., and Silva-Ortega, M., "Suppression of vortex shedding with rotating wake-control cylinders: Numerical investigation at a moderate Reynolds number," in *International Conference on Offshore Mechanics and Arctic Engineering* (American Society of Mechanical Engineers, 2018), Vol. 51210.

Assi, G. R. S., Orselli, R. M., and Silva-Ortega, M., "Control of vortex shedding from a circular cylinder surrounded by eight rotating wake-control cylinders at Re = 100," J. Fluids Struct. **89**, 13–24 (2019).

Behr, M., Hastreiter, D., Mittal, S., and Tezduyar, T., "Incompressible flow past a circular cylinder: Dependence of the computed flow field on the location of the lateral boundaries," Comput. Methods Appl. Mech. Eng. **123**, 309–316 (1995).

Behr, M., Liou, J., Shih, R., and Tezduyar, T., "Vorticity-streamfunction formulation of unsteady incompressible flow past a cylinder: Sensitivity of the computed flow field to the location of the outflow boundary," Int. J. Numer. Methods Fluids **12**, 323–342 (1991).

Bingham, C., Raibaudo, C., Morton, C., and Martinuzzi, R., "Suppression of fluctuating lift on a cylinder via evolutionary algorithms: Control with interfering small cylinder," Phys. Fluids **30**, 127104 (2018).

Carvalho, I. and Assi, G., "Enhanced control of the turbulent flow past a circular cylinder with rotating rods inspired by an inviscid solution," J. Fluids Struct. **113**, 103652 (2022).

Carvalho, I. A., Assi, G. R. S., and Orselli, R. M., "Wake control of a circular cylinder with rotating rods: Numerical simulations for inviscid and viscous flows," J. Fluids Struct. **106**, 103385 (2021).

Choi, H., Jeon, W.-P., and Kim, J., "Control of flow over a bluff body," Annu. Rev. Fluid Mech. **40**, 113–139 (2008).

Dehkordi, E. K., Goodarzi, M., and Nourbakhsh, S., "Optimal active control of laminar flow over a circular cylinder using Taguchi and ANN," Eur. J. Mech.-B **67**, 104–115 (2018).

Fan, D., Yang, L., Wang, Z., Triantafyllou, M. S., and Karniadakis, G. E., "Reinforcement learning for bluff body active flow control in experiments and simulations," Proc. Natl. Acad. Sci. U. S. A. **117**, 26091–26098 (2020).

Farivar, D., "Turbulent uniform flow around cylinders of finite length," AIAA J. **19**, 275–281 (1981).

Fox, T. A. and West, G., "Fluid-induced loading of cantilevered circular cylinders in a low-turbulence uniform flow. Part 1: Mean loading with aspect ratios in the range 4 to 30," J. Fluids Struct. **7**, 1–14 (1993).

Franzini, G. R., Gonçalves, R. T., Meneghini, J. R., and Fujarra, A. L. C., "One and two degrees-of-freedom vortex-induced vibration experiments with yawed cylinders," J. Fluids Struct. **42**, 401–420 (2013).

Fröhlich, J. and Rodi, W., "Les of the flow around a circular cylinder of finite height," Int. J. Heat Fluid Flow **25**, 537–548 (2004).

Gerrard, J. H., "The mechanics of the formation region of vortices behind bluff bodies," J. Fluid Mech. **25**, 401–413 (1966).

Goldstein, S., *Modern Developments in Fluid Dynamics* (1965), Vol. **2**, p. 439.

Gonçalves, R., Franzini, G., Rosetti, G. F., Meneghini, J., and Fujarra, A., "Flow around circular cylinders with very low aspect ratio," J. Fluids Struct. **54**, 122–141 (2015).

Gonçalves, R. T., Meneghini, J. R., and Fujarra, A. L., "Vortex-induced vibration of floating circular cylinders with very low aspect ratio," Ocean Eng. **154**, 234–251 (2018).

Kawamura, T., Hiwada, M., Hibino, T., Mabuchi, I., and Kumada, M., "Flow around a finite circular cylinder on a flat plate: Cylinder height greater than turbulent boundary layer thickness," Bull. JSME **27**, 2142–2151 (1984).

Kim, S.-E. and Mohan, L. S., "Prediction of unsteady loading on a circular cylinder in high Reynolds number flows using large eddy simulation," in *International Conference on Offshore Mechanics and Arctic Engineering* (ASME, 2005), Vol. 41979, pp. 775–783.

Korkischko, I. and Meneghini, J., "Suppression of vortex-induced vibration using moving surface boundary-layer control," J. Fluids Struct. **34**, 259–270 (2012).

Luo, S., "Flow past a finite length circular cylinder," in *The Third International Offshore and Polar Engineering Conference* (OnePetro, 1993).

Luo, S., Gan, T., and Chew, Y., "Uniform flow past one (or two in tandem) finite length circular cylinder(s)," J. Wind Eng. Ind. Aerodyn. **59**, 69–93 (1996).

Mittal, S., "Control of flow past bluff bodies using rotating control cylinders," J. Fluids Struct. **15**, 291–326 (2001).

Mittal, S. and Kumar, B., "Flow past a rotating cylinder," J. Fluid Mech. **476**, 303–334 (2003).

Mittal, S. and Raghuvanshi, A., "Control of vortex shedding behind circular cylinder for flows at low Reynolds numbers," Int. J. Numer. Methods Fluids **35**, 421–447 (2001).

Newman, J. N., *Marine Hydrodynamics* (The MIT Press, 2018).

Norberg, C., "Flow around a circular cylinder: Aspects of fluctuating lift," J. Fluids Struct. **15**, 459–469 (2001).

Patankar, S. V., *Numerical Heat Transfer and Fluid Flow* (Taylor & Francis, 1980).

Saltara, F., Neto, A., Lopez, J *et al.*, "3D CFD simulation of vortex-induced vibration of cylinder," Int. J. Offshore Polar Eng. **21**, 1–6 (2011); available at https://www.researchgate.net/publication/289347277_3D_CFD_Simulation_of_Vortex-induced_Vibration_of_Cylinder.

Physics of Fluids ARTICLE scitation.org/journal/phf

Silva-Ortega, M. and Assi, G. R. S., "Flow-induced vibration of a circular cylinder surrounded by two, four and eight wake-control cylinders," Exp. Therm. Fluid Sci. **85**, 354–362 (2017).
Silva-Ortega, M. and Assi, G. R. S., "Hydrodynamic loads on a circular cylinder surrounded by two, four and eight wake-control cylinders," Ocean Eng. **153**, 345–352 (2018).
Spalart, P. R., "Comments on the feasibility of les for wings, and on a hybrid rans/les approach," in *Proceedings of First AFOSR International Conference on DNS/LES* (Greyden Press, 1997).
Spalart, P. and Allmaras, S., "A one-equation turbulence model for aerodynamic flows," in *30th Aerospace Sciences Meeting and Exhibit* (AIAA, 1992), p. 439.
Spalart, P. R., Deck, S., Shur, M. L., Squires, K. D., Strelets, M. K., and Travin, A., "A new version of detached-eddy simulation, resistant to ambiguous grid densities," Theor. Comput. Fluid Dyn. **20**, 181–195 (2006).
Strykowski, P. J. and Sreenivasan, K. R., "On the formation and suppression of vortex shedding at low Reynolds numbers," J. Fluid Mech. **218**, 71–107 (1990).
Sumner, D., Heseltine, J., and Dansereau, O., "Wake structure of a finite circular cylinder of small aspect ratio," Exp. Fluids **37**, 720–730 (2004).
Tennekes, H. and Lumley, J. L., *A First Course in Turbulence* (MIT Press, 1972).
Wieselsberger, C., "New data on the laws of fluid resistance," Report No. NACA-TN-84, 1922.
Williamson, C. H. K., "Vortex dynamics in the cylinder wake," Annu. Rev. Fluid Mech. **28**, 477–539 (1996).
Williamson, C. H. and Roshko, A., "Vortex formation in the wake of an oscillating cylinder," J. Fluids Struct. **2**, 355–381 (1988).
Zdravkovich, M. M., "Review and classification of various aerodynamic and hydrodynamic means for suppressing vortex shedding," J. Wind Eng. Ind. Aerodyn. **7**, 145–189 (1981).

Physics of Fluids ARTICLE scitation.org/journal/phf

Active control of vortex shedding past finite cylinders under the effect of a free surface

Cite as: Phys. Fluids **35**, 045130 (2023); doi: 10.1063/5.0147760
Submitted: 25 February 2023 · Accepted: 30 March 2023 ·
Published Online: 13 April 2023

I. A. Carvalho[1,a] and G. R. S. Assi[2,b]

AFFILIATIONS

[1]Department of Mechanical Engineering, EPUSP, University of São Paulo, São Paulo, SP 05508-030, Brazil
[2]Department of Naval Architecture and Ocean Engineering, EPUSP, University of São Paulo, São Paulo, SP 05508-030, Brazil

[a)]Author to whom correspondence should be addressed: amorim.icaro@usp.br
[b)]Electronic mail: g.assi@usp.br

ABSTRACT

This paper presents the analysis of the active flow control promoted by low-aspect-ratio cylinders under the effect of a free surface at a low Froude number, modeled as a slip-allowing plane. To advance the literature in this merit, that is scarce compared with infinitely long and surface-mounted bodies, we carry out Detached-eddy simulations at Reynolds number of 1000 to investigate the active control provided by eight spinning rods surrounding a larger body. One of the ends of this system was immersed in the free stream, while the other was in contact with a free water surface. Our results reveal that when the rods spun with sufficiently large angular velocities, the (non-Kármán) vortex street was progressively organized and the part of the wake associated with the mechanism of vortex formation described by Gerrard ["The mechanics of the formation region of vortices behind bluff bodies," J. Fluid Mech. **25**, 401–413 (1966)] was eliminated. Nevertheless, tip-vortices prevailed throughout the examined range of spinning velocities. We also contrasted drag mitigation with power loss due to viscous traction and found that to reduce the mean drag on the system to a lower value than that of the bare cylinder necessarily required power expenditure. Steady reduction of mean drag and less significant mitigation of root mean square of lift and mean side force were verified to occur for the entire system and for the central body. However, the side force proved less affected by the wake-control mechanism. We demonstrate this to be associated with a novel ring-like vortex that prevailed throughout the simulations. Vortex dynamics and formation of these turbulent structures are explored.

I. INTRODUCTION

It is known that the greater the obstruction a body ("bluffness") causes to the incoming flow, the more likely it is that as the flow attempts to travel about the body, separation will occur due to the formation of a negative pressure gradient. In such cases, the boundary layer detaches from either side of the body in the form of shear layers. For cylinders, the communicating shear layers, with opposite vorticity, roll up and interact in the form of vortices, in a fashion that they draw vorticity from one another, lose some of it to the wake, and are utterly dissipated as they travel downstream away from the structure due to viscous effects (Gerrard, 1966).

Bluff bodies are prone to vortex-induced vibration (VIV), a phenomenon that causes these structures to obey a cyclic motion, both in the direction of the incoming flow and (more intensely) in the transverse direction (Williamson and Govardhan, 2004). Fatigue and failure due to VIV upon offshore structures are some of the undesirable occurrences that pushes forward interest to control the flow, to ultimately prevent or attenuate vibrations. Low-frequency and high-amplitude oscillations are found to occur to large oil rigs that possess an extensive, bluff hull, such as in spar and monocolumn platforms, particularly in activities of the offshore industry devoted to ultra deep water exploration. Within this context, vortex-induced motion (VIM, Gonçalves *et al.*, 2010) is a more common terminology for the fluid–structure interaction, where the amplitude of vibration scales with the characteristic length of the body (Fujarra *et al.*, 2012). Contrarily, for the hydrodynamic power generation, it is often of interest to provide conditions for the motion with non-null, but controlled amplitude. A stepping stone toward VIV suppression or its build-up lies in understanding and controlling vortex dynamics. Thus, vortex-shedding control is a relevant path toward flow control that may directly impact structures subject to vibration.

To achieve flow control, passive technologies have been proposed in the literature (Zdravkovich, 1981). This category comprises shrouds

Physics of Fluids ARTICLE scitation.org/journal/phf

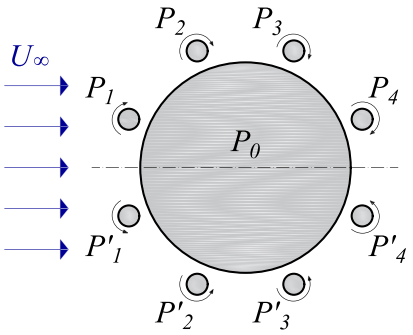

FIG. 1. A cross section of the geometry. The incoming flow at velocity U_∞ reaches the entire system, comprised of the main body denoted P_0, and upper and lower slender rods, respectively, denoted P_n and P'_n, for $n = 1, \ldots, 4$. Frontal rods P_1, P'_1 and rear rods P_4, P'_4 are displaced from stagnation regions by 22.5°. All rods are uniformly distributed about the main body. The figure is not to scale for better visualization.

(Cicolin and Assi, 2017), near-wake stabilizers (Strykowski and Sreenivasan, 1990), and surface protrusions, such as splitter plates and free-to-rotate fairings (Assi *et al.*, 2009; Assi *et al.*, 2014), but the most known are probably helical strakes employed in risers (Korkischko and Meneghini, 2011). These technologies have been vastly studied and have shown to work up to some Reynolds number $Re = U_\infty D/\nu$ (where U_∞ is the free-stream velocity, ν is the kinematic viscosity of the fluid, and D is the dimension of the body). For Re-values below 100, Strykowski and Sreenivasan (1990) showed that a slender rod, properly positioned near the main larger body, was suited to suppress global instabilities of the flow and, thus, precluded the onset of vortex shedding entirely. All of these technologies focused on the reattachment of the shear layers, reduction of their interaction or delayed entrainment of fluid further downstream, so as to dissipate the circulation of the communicating shear layers beforehand.

Active techniques require power input. In doing so, several works showed that technologies of this type have been more apt to control the wake and vortex shedding at higher Re-regimes (Choi *et al.*, 2008). One form that has called attention is that using spinning rods, based on the moving surface boundary-layer control (MSBC), originally from the aerodynamics context. In MSBC, momentum is injected into the near flow to delay separation. To provide the spinning elements with increasingly higher angular velocities proved effective to reduce mean drag and the fluctuating lift and eliminate vortex shedding entirely (Mittal, 2001).

Beyond these results, a configuration where the main and larger body of diameter D is fitted with eight slender rods of diameter d, distant from the main body by a gap G, as shown in Figs. 1 and 2(a) was employed by Assi *et al.* (2019). In such a setup, the active mechanism is characterized by the rotation of the wake-control rods about their own axis. The authors showed that to provide these spinning rods with sufficient actuating power gave rise not only to the results attained by Mittal (2001) with one rod, but extended to produce thrust upon the entire system. Thus, the rotating mechanism promoted a mean drag inversion and released greater flow control than its passive counterpart and the rotating mechanism with fewer spinning elements. Ongoing studies have shown that this system with eight rods behaves omnidirectionally relative to changes in the angle of attack of the incoming flow (Carvalho and Assi, 2023a; Carvalho and Assi, 2023b), in the sense that the same level of wake control and load attenuation were found at different angles of attack of the incoming flow in laminar and turbulent regimes of infinitely long bodies (Carvalho and Assi, 2023a; Carvalho and Assi, 2023b, with an active mechanism as described in Sec. III B), an important feature in considering technological applications, wherein the incoming flow direction might not be aligned with the centerline of the entire system, and the flow control should be desirable.

This technology was found to work with an equivalent system but free to develop VIV (Silva-Ortega and Assi, 2017b), and other arrangements have also been explored with different numbers and locations of the rods (Silva-Ortega and Assi, 2018). However, the configuration with eight rods was less susceptible to the increase in hydrodynamic loads and to galloping.

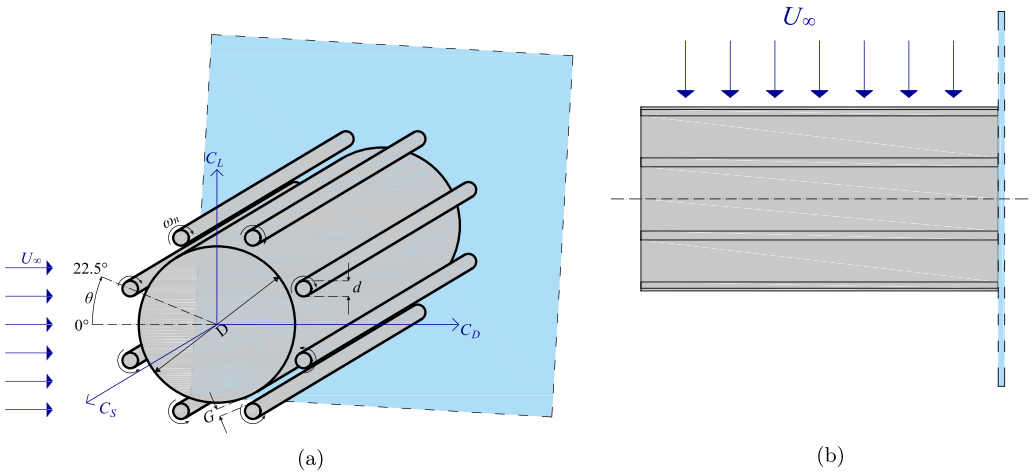

FIG. 2. Geometrical parameters of the entire setup: length (L), gap (G), rods' diameter (d), main body diameter (D), and angle coordinate (θ). Hydrodynamic loads: lift (C_L), drag (C_D), and side forces (C_S). The incoming flow is aligned with the x-direction. Figures are not to scale.

Physics of Fluids ARTICLE scitation.org/journal/phf

Notably, most of previous works have been concerned with infinitely long bodies, where end effects were disregarded, despite the paramount work of Williamson (1996), where the author explicated the relevance of the ends of the body to the three-dimensionality of the flow and to vortex dynamics phenomena, even for long aspect ratio bodies. However, little is found in the literature regarding flow control over these structures. As a matter of fact, as reported by Rosetti *et al.* (2013), a general lack of studies is found for the flow over low aspect ratio bodies (without wake control). Studies with a wake-control device for systems under the effect of a free water surface are even scarcer.

Generally, published works examined the flow over surface-mounted bodies (Sumner, 2013; Gonçalves *et al.*, 2015). Farivar (1981) studied the subcritical flow over a fixed plain cylinder (one without a wake control device) with aspect ratios between 2.78 and 12.5 at $Re = 7 \times 10^4$. The author found that in terms of hydrodynamic loads, the mean effect produced by the ends was in the decrease in the mean drag coefficient (previously noted by Kawamura *et al.*, 1984) as the slenderness parameter (given by the ratio of the length by the diameter of the cylinder, L/D) decreased. Later, this observation was supported by experiments at very low aspect ratio (Gonçalves *et al.*, 2015) and numerical simulations (Palau-Salvador *et al.*, 2010, showed that, through wake topology visualization, this is to be related to downwash vortex formation).

In the scope of a free water surface as the work we propose here, Gonçalves *et al.* (2015) assessed slenderness parameters between 0.1 and 2.0 and observed that monocolumn and spar platforms as well as semi-submersible columns fit into this range. The paper also rendered clear that notwithstanding similarities exist between wall-mounted and free-surface configurations, these setups present flow features of their own due to the different boundary conditions. For example, in free-surface configurations, the cylinder is not immersed in a boundary layer.

We further remark that in spite of these studies, flow control in the form of interference with slender rods is still a field to be unveiled when it comes to finite bodies. As mentioned in Carvalho and Assi (2023c), although the study of Luo *et al.* (1996) assessed the interaction between two low aspect ratio cylinders of sizes of the same order of magnitude, such study was not dedicated to flow control.

As it can be seen, although the problem of the flow past finite cylinders has been investigated, chiefly for the wall-mounted and large aspect ratio setups; in general, flow control of low aspect ratio bodies with a free surface remains vastly unexplored.

II. OBJECTIVE

We intend to advance the current state of information by bringing the MSBC technology, implemented in the form of spinning rods, to comprise an active mechanism of flow control for finite cylinders with a free surface, modeled here a slip-allowing plane. The system is represented in Fig. 2. Some of the matters addressed in this work are (1) the extent of realizable flow control by this active mechanism against end effects and tip-vortex and their suppression; (2) the efficiency of the entire system, assessed through the conflicting goals of mean drag decrease and economical spinning setups; and (3) vortex dynamics interplay and consequent effects upon the structure.

The results from the numerical simulations performed at $Re = 1000$ will be investigated in terms of hydrodynamic loads, wake topology, wake interaction with the free surface, and free-end effects. We compare passive (as in Carvalho and Assi, 2023c) and progressively more power-demanding active mechanisms to one another, as well as with the reference case of a bare cylinder (without wake-control rods).

The present study constitutes part of a research effort to devise suppressing devices to mitigate VIV of floating offshore structures. Knowledge of the physical mechanisms acquired from numerical simulations should help the development of active and passive technologies to control the flow about bluff bodies.

III. METHOD

A. Problem description

We investigate the setup of Fig. 2 (three-dimensional visualization of Fig. 1). An incoming flow U_∞ reaches the arrangement comprised of a main body P_0 of diameter D fitted with an active-control device. The control mechanism is exerted through $N = 8$ slender rods of diameter $d = D/20$ that spin about their respective axes with angular velocities ω_n to inject momentum into the outer flow about the entire system. These rods are distant from the wall of the main body by the gap $G = D/100$. Upper rods $P_1, \ldots, P_4$ spin clockwise with the same magnitude, but opposite direction to that of the lower rods $P'_1, \ldots, P'_4$, so that $\omega_n = -\omega'_n$, $n = 1, \ldots, 4$. Wake-control rods are deliberately positioned away from the stagnation regions by 22.5° and uniformly distributed, so consecutive rods are separated by a 45° angle. The same configuration, but restricted to a passive analysis, was employed earlier in the literature (Carvalho and Assi, 2023c). We emphasize that all cylinders are modeled as finite bodies of low aspect ratio, with length $L = 2D$; thus, end effects are considered. See Fig. 2(a) for the representation of these geometrical parameters. As exhibited by Fig. 2(b), on one end of the entire system is located a free water surface, modeled here an infinitely long slip-allowing plane; and the other end is within the free stream.

This setup was chosen based on previously published results and ongoing work. Silva-Ortega and Assi (2017a) compared different numbers of rods, diameters, and gaps and found that $N = 8$ rods were capable of attenuating VIV amplitude by 99% with $G/D = 0.1$. We used $d/D = 0.1$ (instead of $d/D = 0.08$, as in Silva-Ortega and Assi, 2017a), following Assi *et al.* (2019). For this parameter, it suffices that the rods should be sufficiently small to interact with the shear layers of the larger body. Furthermore, as reviewed in Sec. I, this system has shown an omnidirectional attribute, provided that the angular velocities are defined as in Sec. III B.

Finally, regarding possible wave interactions on a real free surface, we verified that the Froude number based on the cylinder's length (given by $Fr = U_\infty/\sqrt{gL}$, where g is the gravitational acceleration) was inferior to 0.23. According to Newman (2018), for a subcritical regime of $Fr < 1$, the wave pattern is similar to that expected for deep waters. Generally, for $Fr < 0.5$, water elevation due to free surface effects is deemed negligible. Thus, since wave effects are not significant in the present study, our setup fits well in these conditions and the free surface can be adequately represented by a slip-allowing plane. Gonçalves *et al.* (2018), for example, employed a similar approach for an experimental investigation of floating bluff bodies in a water channel.

Physics of Fluids ARTICLE scitation.org/journal/phf

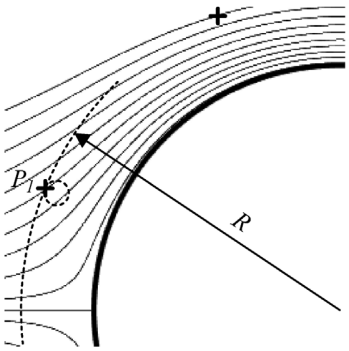

FIG. 3. Potential flow about a bare cylinder. Within this flow configuration, streamwise velocities were computed at polar positions corresponding to the outmost point that will be located on the surface of the rods relative to the center of the entire system in the viscous flow.

B. Definition of rotation rates

The angular velocities imposed to the rods are obtained from a potential-flow analogy, as in previous works (Carvalho *et al.*, 2021; Carvalho and Assi, 2022, although in the context of infinitely long bodies). For this derivation, we consider the polar coordinates $\theta = \pm 22.5 \pm 45°(n-1)$ and $R = D/2 + G + d$ that mark the farthest point located on the surface of the rods relative to the center of the entire system (see Fig. 3 for an example). At these points, streamwise velocity components V_1, V_1', …, V_4, V_4' are calculated from the potential flow about a bare cylinder, as depicted in Fig. 4.

The analytical expression of V_n in the potential flow is given by the following equation:

$$V_n = U_\infty \left\{ \hat{r}[\cos(\theta_n)] \left[1 - \frac{(D/2)^2}{(D/2+G+d)^2} \right] + \hat{\theta}[-\sin(\theta_n)] \left[1 + \frac{(D/2)^2}{(D/2+G+d)^2} \right] \right\} \cdot \hat{\theta}, \quad (1)$$

(for $\zeta = 1.0$, see Carvalho *et al.*, 2021). These same velocities are then imposed in the viscous flow about the entire system, to the control rods in the form of angular velocities $\omega_n = V_n/(d/2)$. To modify these rotation rates proportionally, the parameter ζ was employed so that $\omega_n = \zeta V_n/(d/2)$ for $\zeta = 0.0$ (passive rods), 0.5, 1.0, 2.5, and 3.5.

C. Numerical scheme

The numerical scheme employed in this work is analogous to Carvalho and Assi (2023c). The Navier–Stokes and mass conservation equations, representative of the incompressible flow of a Newtonian fluid,

$$\rho\left(\frac{\partial U_i}{\partial t} + U_j\frac{\partial U_i}{\partial x_j}\right) = -\frac{\partial p}{\partial x_i} + \mu\frac{\partial^2 U_i}{\partial x_j \partial x_j}, \quad (2)$$

$$\frac{\partial U_j}{\partial x_j} = 0, \quad (3)$$

(given in a differential form) were solved through a finite-volume discretization that is described below. In Eq. (3), ρ refers to the fluid density, $\mathbf{U}$ and $\mathbf{x}$ are the velocity field and stations of the flow domain with components indexed by i and j (U_i, U_j, and x_i, x_j), $p = p(\mathbf{x})$ denotes the pressure field, and μ is the dynamic viscosity. We have solved this flow in the open-source C++ library OpenFOAM at a Reynolds number $Re = U_\infty D/\nu = 10^3$ based on the main cylinder's diameter D. We note that this nondimensional based on the rods' diameter is given by $Re_d = U_\infty d/\nu = 50$, at the onset of vortex shedding. Because the rods rotate, and this has shown to interfere with vortex shedding (Mittal and Kumar, 2003), we consider a priori that elements will not produce vortex shedding, thus will not interfere with that sourced from the larger body. This will be confirmed *a posteriori* in Sec. IV.

In order to ensure quality results, all terms hereby discretized followed second-order accuracy interpolants. An implicit backward scheme was employed for the transient term $\partial U_i/\partial t$ of the left-hand side of Eq. (3), while for the Lagrangian convective term $U_j \partial U_i/\partial x_j$, a blend of the linear upwind and central scheme was employed (based 25% on the former, and 75% on the latter), called LUST in the aforementioned library. Least squares were used to calculate gradients. Because our numerical scheme is cell-centered, interpolation of values to the surface of the cells was carried out with linear interpolation. Both structured and unstructured regions contained elements whose centers were not aligned perpendicularly relative to the interface between them; thus, it was necessary to impart a non-orthogonality correction to the surface normal gradient (along with the Gauss theorem). This procedure also allowed computation of the Laplacian term.

A known issue in the numerical solution of incompressible flows is the uncoupled variables velocity and pressure. In fact, Eqs. (2) and (3) rely only on the pressure gradient rather than on the pressure itself;

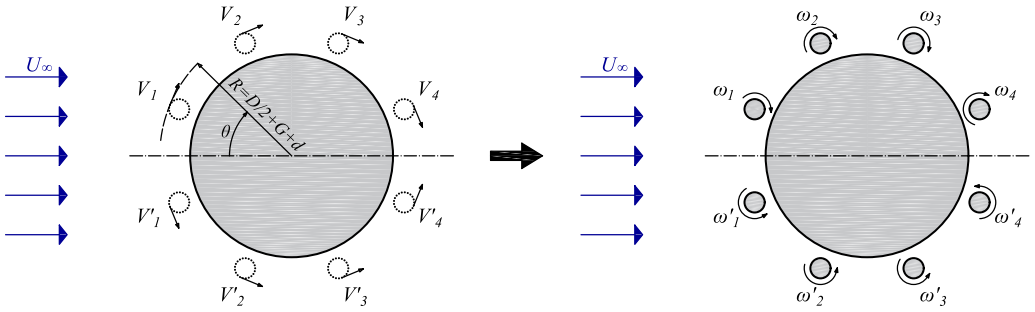

FIG. 4. Velocity vectors computed from the potential-flow field at points located in radial coordinates $R = D/2 + G + d$. $\theta = \pm 22.5° \pm (n-1)45°$, with $n = 1, \ldots, 4$ were assigned as equivalent angular velocities for the rods.

Physics of Fluids ARTICLE scitation.org/journal/phf

thus, these equations may be solved erroneously ignoring the pressure field itself, which is transported through the flow domain. To avoid this issue, these variables were solved together through the unsteady version of the semi-implicit method for pressure-linked equation (SIMPLE) coupling algorithm (Patankar, 1980).

In short, SIMPLE revolves about guessing the pressure field and solving Eqs. (2) and (3) together for the velocity (and turbulence modeling for further variables), where a correction term is found, that is then reapplied in the solution procedure. One of the terms is dropped to ease the solution procedure that would zero in upon convergence. Details of this method are explored in Patankar (1980). Residue tolerances of 10^{-4} for the solution of the pressure and 10^{-8} for the velocity components and other scalars were required for convergence at each time step, with the further requirement of at least 10 outer loops at each time step. The work of Carvalho and Assi (2022) showed that this lower tolerance for the pressure did not compromise the results and yet allowed for faster run times.

Rhie and Chow's interpolation was used to prevent the so-called *checker-board effect*, whereby a third-order pressure term was included for the computation of face velocities (Rhie and Chow, 1983). Among the advantages of this procedure, storage was more efficient, and the second-order accuracy is ensured.

In order to avoid information loss from one time step to another, time step size restrictions were enforced based on the rotation rate of the rods and on the reference vortex shedding cycle of a bare cylinder. Thus, time steps were limited from above by 1/70 of the revolution of the rods and by 1/100 of the timespan of a shedding cycle.

A linear system was obtained after discretization of all terms. After the solution of the linear system, the resultant forces were obtained through integration of viscous effects and pressure distribution over the surface of each body, and the components thereof, lift (F_L), side force (F_S), and drag (F_D), were obtained. Normalization was made by $1/2\rho U_\infty^2 DL$ to get the lift, side force, and drag coefficients C_L, C_S, and C_D, illustrated in Fig. 2.

General details of the finite volume formulation are found in Ferziger *et al.* (2002) and Versteeg and Malalasekera (2007).

D. Boundary conditions and meshing

Symmetry boundary conditions (no flow across) were imposed on the sides of the domain and on the free surface. The walls of the rods adopted the rotation rates explained in Sec. III B for $\zeta \neq 0$, and the no-slip condition was applied to their surfaces in the passive configuration of $\zeta = 0$. For the main body, the no-slip condition was ensured throughout simulations. The inflow was specified by a Dirichlet condition, the far-field flow of fixed velocity U_∞, and a Neumann condition corresponding to fully developed pressure gradient $\nabla p = 0$; conversely, the outflow was prescribed by a Neumann condition on the velocity and Dirichlet's for the pressure. The simplified geometry of the domain, together with the indication of inlet and outlet patches, is given in Fig. 5, in which L_S represents the distance from the system free end to the side of the domain.

From the free end to the farthest side of the numerical domain, an adequate distance $L_S/D = 8$ was imposed to avoid blockage effects. The center of the main cylinder was distant $8D$ from the top and bottom surfaces and from the inlet. A greater distance of $20D$ was applied between the main cylinder's center and the outlet downstream. These dimensions for the grid geometry corroborate with the work of Behr *et al.* (1995), Behr *et al.* (1991), Kim and Mohan (2005), and Carvalho and Assi (2022) for infinitely long bodies. A wider domain was investigated in the latter reference, and no significant changes were observed. In Carvalho and Assi (2023c), this same, but passive, setup was analyzed with the same meshing, and sufficiently accurate results were attained.

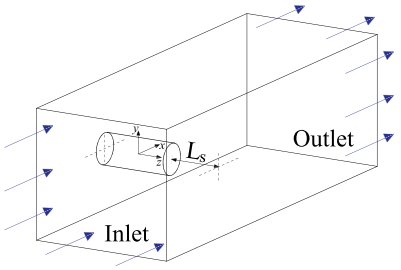

FIG. 5. Simplified geometry of the numerical domain. For clarity, the rods were not represented. As shown, the system is attached to the free water surface at $z = -D$ on one end and its other end, at $z = +D$ is free interacting with the free flow. Sides of the domain correspond to symmetry planes. The origin of the set of axes is placed at the center of the entire system.

Hexahedral and prismatic elements covered the flow domain, and the mesh was the more refined the nearer it was to the bodies or to the wake region, to capture typical gradients of the flow directly associated with vortices and eddies. Away from the cylinders and from the wake are located regions where gradients typically approach null value, and the flow asymptotically assumes fixed and fully developed boundary conditions. Toward these gradient-free locations, the cells were enlarged. Expansion of the cells adopted ratios lower than 10% and 14% for the bare cylinder and system grids, respectively. Figure 6(a) portrays a cross section passing through the system.

Triangular-faced elements can be observed to comprise the part of the lateral surface of the main cylinder in Fig. 6(b). Extrusion of the cylinders is also depicted, as well as the refinement along the span toward the ends of the bodies. It should be noted that it is the extrusion of the sidewall of these cylinders, that contains triangular elements, that led to the need of unstructured, prismatic, cells away from the ends and into the free stream. Nevertheless, predominantly structured and hexahedral elements were used. Near the wall, this choice of element is appropriate because the boundary layer contains a strong velocity gradient transversely to the wall (although weak longitudinally). Cross-sectional and spanwise views of rod P_1 are shown in Figs. 7(a) and 7(b). The latter captures the end fixed to the free surface.

The smallest elements measured $1.54 \times 10^{-3}D$ on the wall of the main body and $3.77 \times 10^{-3}d$ on the wall of the wake-control rods to ensure quality results near the boundary layer and to dispense with wall functions. In total, 19 153 204 cells were employed, comprised 81% of hexahedral elements.

Mesh convergence study was carried out in Carvalho and Assi (2023c) and has shown that our grid was sufficiently refined. For conciseness, this study will not be repeated here.

E. Turbulence modeling

Since the flow about cylinders is laminar for $Re < 190$, our flow at $Re = 1000$ was well into turbulent regime and its behavior was

Physics of Fluids ARTICLE scitation.org/journal/phf

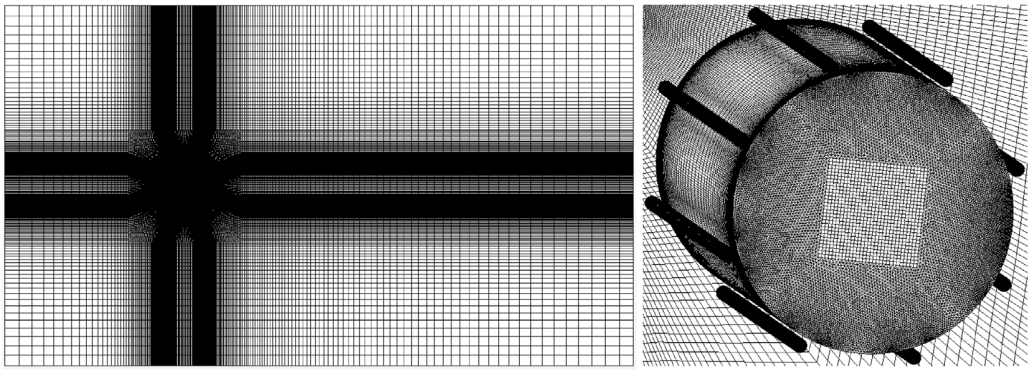

FIG. 6. Different regions of the mesh. (a) Full domain and (b) side of the cylinders.

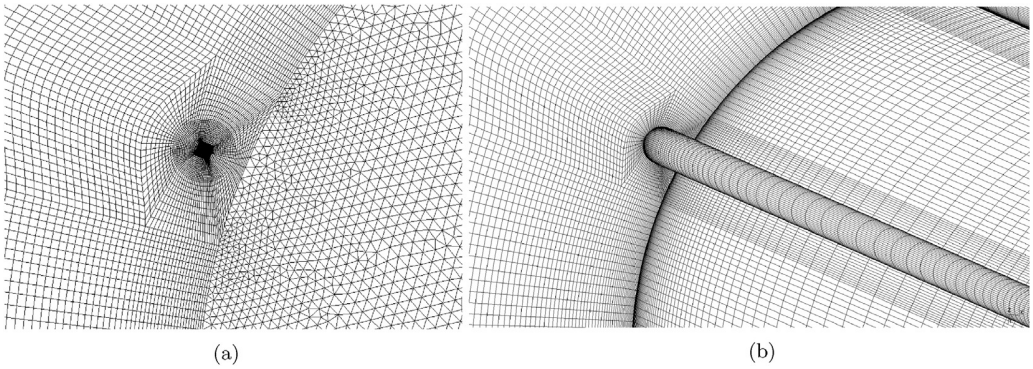

FIG. 7. Close-in view of rod P_1. (a) Cross sectional view and (b) spanwise extruded view.

inherently three-dimensional (3D). Thus, we employed a 3D Detached-eddy simulation (DES, Spalart, 1997) so that large, detached, eddies were fully resolved, while the boundary layer was modeled by means of unsteady Reynolds-averaged Navier–Stokes (URANS) equations. Small, isotropic, and turbulent scales away from the boundary layer were modeled in agreement with the classical work of Smagorinsky (1963). The advantage of this procedure is that, in modeling only the small scales (that approximate better the turbulent universal behavior, Tennekes and Lumley, 1972), this approach has been proven to more computationally efficient (Spalart, 1997).

For the URANS part, we employed the one-equation model of Spalart and Allmaras (1992), which transports the turbulent viscosity parameter $\tilde{\nu}$ and relates it to the turbulent viscosity ν_t. This model has proven able to capture separation points adequately (Travin *et al.*, 2000). The appropriate boundary conditions in this case are those of Spalart (2000) and Vatsa *et al.* (2017),

$$\tilde{\nu}_{\text{wall}} = 0, \tag{4}$$

$$3 < \tilde{\nu}_{\infty}/\nu_{\infty} < 5. \tag{5}$$

For infinitely long and low aspect ratio cases, this approach was successfully verified against other numerical works and validated with experiments Carvalho and Assi (2022) and Carvalho and Assi (2023c).

Further consideration was required because in subcritical flow regime, the wake has transitioned to a turbulent state, whereas the boundary layer is still laminar. Therefore, a low-*Re* correction was necessary (Spalart *et al.*, 2006), because the URANS formulation is intrinsically turbulent and could interfere with the location of the separation points. We anticipate that this was prevented, and all simulations preserved a non-dimensional distance away from the walls of the cylinders $\mathcal{O}(y^+) \sim 1$, so we dispensed with wall functions.

The parameter $\tilde{\nu}$ followed a linear upwind scheme. Turbulence modeling parameters are exposed in Carvalho and Assi (2023c) and will not be repeated here for brevity.

IV. RESULTS

A. Time histories of hydrodynamic loads

Each simulation of the active mechanism was left to run for a timespan corresponding to 28 cycles of vortex shedding based on the flow about an infinitely long bare cylinder in subcritical regime that we shall henceforth denote T_S. For reference, we note that the Strouhal number is given by $S_t = 1/(T_S U_\infty/D) \approx 0.2$, where reasonable approximation is made based on several simulations and experiments (Norberg, 2001).

Physics of Fluids ARTICLE scitation.org/journal/phf

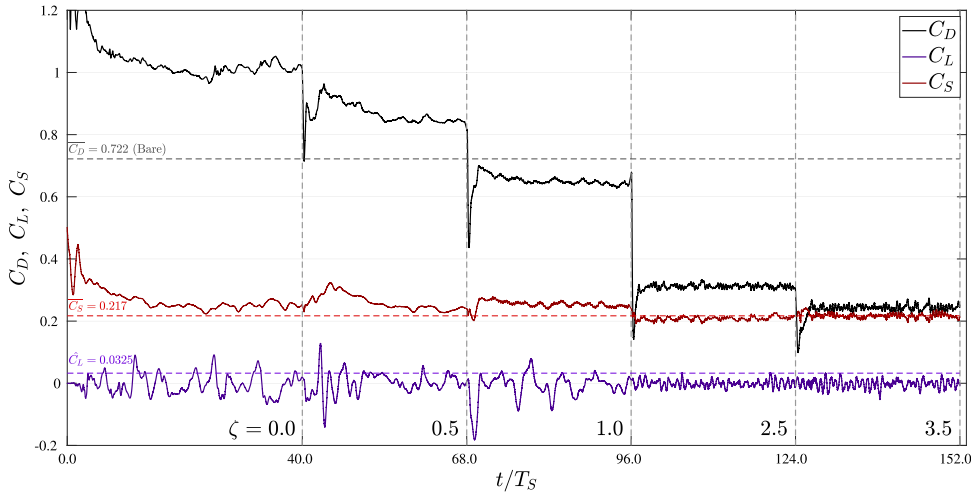

FIG. 8. Time histories of the drag (C_D), lift (C_L), and side force (C_S). Reference values of Eq. (6) for the bare cylinder are represented by dashed lines following the same color scheme.

For the passive setup, the last 25 cycles were assumed converged and, thus, considered for the computation of mean and root mean square (RMS) quantities, whereas for active setups, a timespan of 15 cycles were analogously assessed. The shorter number of cycles and run time of the setups involving spinning rods is justified because these simulations departed from the last time step of the passive setup. This procedure is known to provide faster convergence and was successfully employed in the literature (Mittal, 2001; Goodarzi and Dehkordi, 2017). From a physical standpoint, active setups faced much smoother loads, with lower fluctuation, as the time histories of Fig. 8 show. We anticipate that a simpler wake topology also resulted thereof.

The main trait verified previously from the usage of spinning wake-control rods, that of reduction of drag (C_D) and lift (C_L), is corroborated in Fig. 8. Increasingly higher rotation rates led to steady decrease in C_D. For C_L, perceptible attenuation was only verified for $\zeta \geq 2.5$, but neither a steady shrinkage of the amplitude nor complete elimination was observed as in Carvalho *et al.* (2021) or Carvalho and Assi (2022) for infinitely long bodies, where even its high frequency component faded away, given sufficient actuating power. This was expected for finite cylinders as the present, considering that the free-end is a geometrical singularity susceptible to separation due to its sharp corner. Interestingly, the side force (C_S) was virtually unaffected, except to some slight reduction for $\zeta \geq 2.5$ as in the amplitude of C_L, that might have to do with the increase in correlation of the wake that has been repeatedly shown to happen with sufficiently large rotation rates. These tendencies in the hydrodynamic coefficients of the entire system are quantitatively summarized in Table I. Percentages referring to changes from a ζ value to the passive setup render clear that the mean drag dropped consistently, while the other coefficients adopted an inconsistent trend.

From comparison of reference values of the bare cylinder expressed in Eq. (6) with those of Table I, it is interesting to note that to employ wake-control rods led mean drag ($\overline{C_D}$) and RMS of lift ($\hat{C}_L$) upon the entire system to lower values than those of the bare cylinder. In terms of mean side force ($\overline{C_S}$), the values of the entire system were comparable with $\overline{C_{S,\mathrm{Bare}}}$ in the affected regimes $\zeta \geq 2.5$; while for $\zeta < 2.5$, the rods caused $\overline{C_S}$ to be higher for the entire system,

TABLE I. Mean drag ($\overline{C_D}$), RMS of lift ($\hat{C}_L$), and side force ($\overline{C_S}$) coefficients. A steady trend of decrease in mean drag is observed, while $\hat{C}_L$ and $\overline{C_S}$ reduced only from $\zeta = 1.0$ to $\zeta = 2.5$. Percentages indicate change relative to the passive setup.

	Entire system		
ζ	$\overline{C_D}$	$\hat{C}_L$	$\overline{C_S}$
0.0	1.02 (-)	0.0358 (-)	0.252 (-)
0.5	0.873 (−14%)	0.0283 (−21%)	0.265 (+5.2%)
1.0	0.652 (−36%)	0.0368 (+2.8%)	0.256 (+1.6%)
2.5	0.313 (−69%)	0.0108 (−70%)	0.207 (−18%)
3.5	0.234 (−77%)	0.0158 (+56%)	0.219 (−13%)

$$\begin{aligned} \overline{C_{D,\mathrm{Bare}}} &= 0.722, \\ \hat{C}_{L,\mathrm{Bare}} &= 0.0325, \\ \overline{C_{S,\mathrm{Bare}}} &= 0.217. \end{aligned} \tag{6}$$

B. Vortex dynamics

It is known that as the wake width diminishes, a lower drag is imposed on the structure, because a lower pressure difference occurs between frontal and rear regions. The tendency of decay in $\overline{C_D}$ seen in Fig. 8 may be justified as so. This is pointed out by the vorticity contours of Fig. 9 (Multimedia view) for the cross-section at $z/L = 0$ (see Fig. 5 for the set of axes). The figure shows that the wake expanded with the insertion of passive rods compared with the bare cylinder [Fig. 9(a)], because the fixed rods simply established a larger obstruction to the flow. The wake sustained a similar aspect when the passive system ($\zeta = 0.0$) became just active ($\zeta = 0.5$). Nevertheless, from this

Physics of Fluids ARTICLE scitation.org/journal/phf

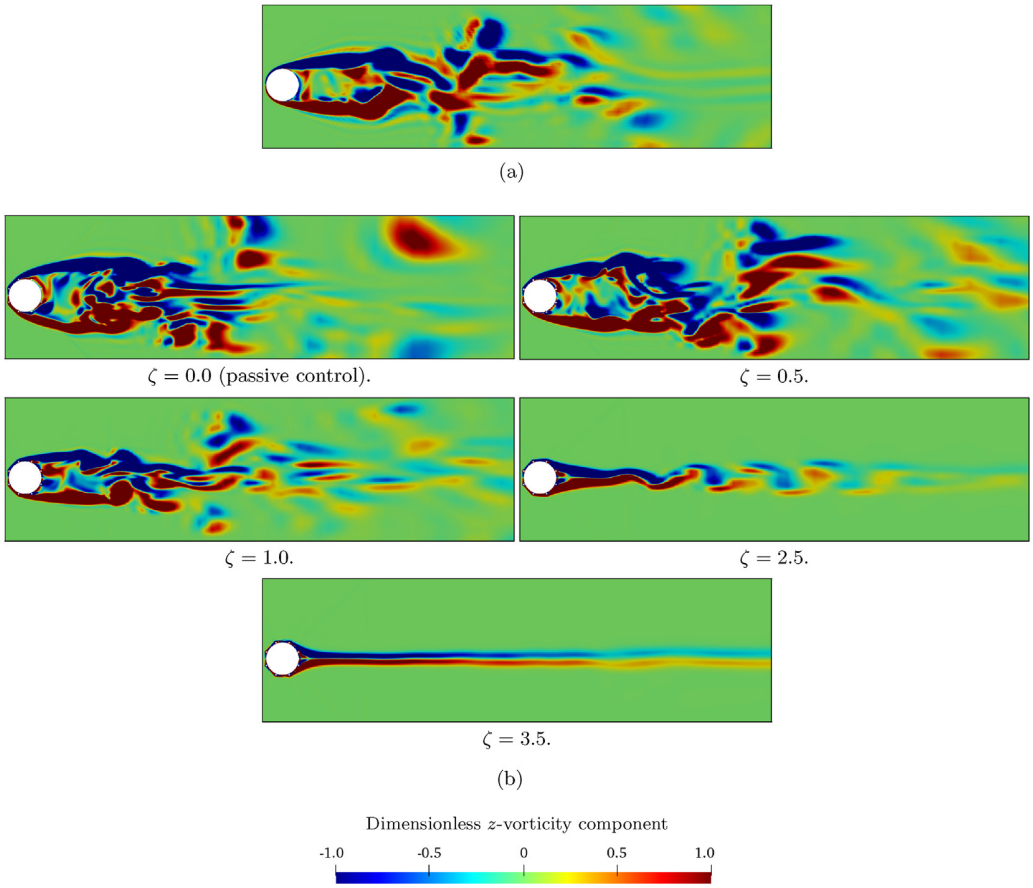

FIG. 9. Vorticity contours at $z/L = 0$ demonstrate the capacity of the active mechanism to attenuate vortex shedding and holistically eliminate the small vortices and turbulent eddies that dominate the wake for the bare cylinder and for the entire system at $\zeta = 0.0$ but that vanish from the flow domain at $\zeta = 3.5$. Instead, at the most active setup, occurred the formation, a very thin wake with rather residual emanation of vortices at a greater distance from the body. (a) Bare cylinder and (b) entire system. Multimedia view: https://doi.org/10.1063/5.0147760.1

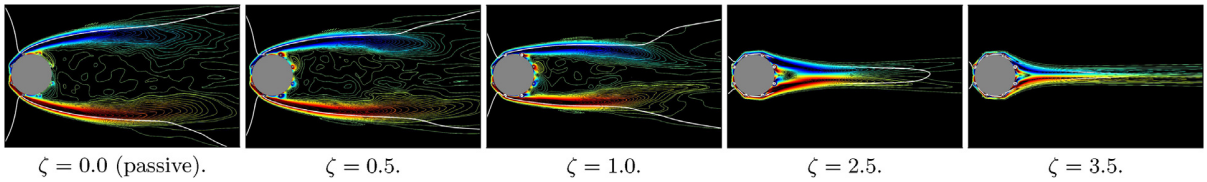

FIG. 10. Time-averaged vorticity contours exhibit progressive concentration of positive and negative vortices in a smaller region as the wake width shortened. This is followed by approaching shear layers (white line).

value of ζ onward, the spinning rods progressively reduced the wake width.

After the wake narrowed (see $\zeta \geq 1.0$ in Fig. 9) and the formation length shortened (as it is discussed below), an intensified interaction between Kármán vortices resulted thereof. Based on the mechanism of formation of vortices explained by Gerrard (1966), the closer the vortices were emanated longitudinally and transversely in the wake, the faster occurred the supply of vorticity from the shear layers to the vortices, their roll-up and shedding from one another. In terms of hydrodynamic loads, this translated into the appearance of the high frequency component of the hydrodynamic loads that is exposed in Fig. 8, particularly for the lift force, directly associated with the regions of low pressure formed interchangeably during their interaction. Vortex shedding was then attenuated and very small scales vanished from the flow domain as $\zeta = 2.5$ was reached. Figure 9 renders this clearer for $\zeta \geq 1.0$.

The reduction in wake width is better seen in Fig. 10 of the time-averaged vorticity contours at the cross section $z/L = 0$. The shear

Physics of Fluids ARTICLE scitation.org/journal/phf

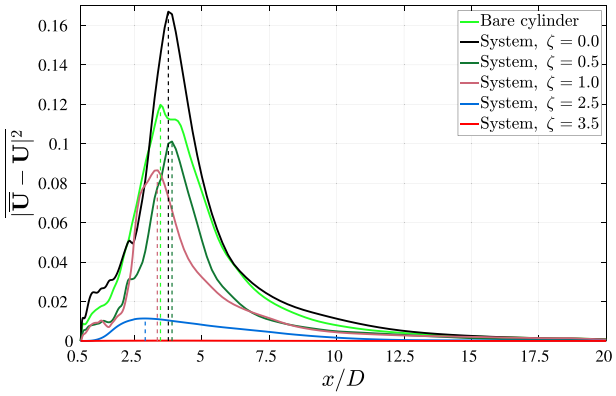

FIG. 11. Curves of $\overline{|\bar{\mathbf{U}} - \mathbf{U}|^2}$ for the bare cylinder and for the entire system. At any level of rotation rates associated with ζ, the peaks were lower than in the bare cylinder case. In general, formation length (associated with the peak x-stations) decreased with higher rotation rates. At $\zeta = 2.5$, the peak was about 1/12 that of the bare cylinder. At $\zeta = 3.5$, the fluctuations were negligible.

layers are highlighted by a white line that corresponds to $0.99U_\infty$. The figure further exhibits that the negative (blue) and positive (red) oriented vorticity contours were confined in a small region past the system for the most active setups.

Figure 11 presents the time-averaged squared fluctuation of the velocity field that was taken along the x-direction in the plane $z/L = 0$. The formation length is highlighted by the dashed vertical lines at the coordinates of the maximum of each setup. We recall that the formation length is measured by the distance from the rear stagnation ($x = 0.5$) region to the point, downstream, where the velocity fluctuation reaches peak value (Williamson, 1996), decaying subsequently. The analysis above of the vorticity contours is corroborated by Fig. 11, which reveals that the insertion of fixed rods amounted to larger velocity fluctuation than that found for the bare cylinder. Contrastingly, the formation length shortened after $\zeta = 0.5$ up to 2.5, an apparently contradicting result when compared with Assi *et al.* (2019); Carvalho and Assi (2022), because as the formation length is prolonged, the viscosity tends to weaken the shear layers that subsequently roll up prior to becoming vortices. It is through this mechanism that splitter plates lead to wake control (Bearman, 1965). The same did not hold for the present active MSBC mechanism as far as shortening formation length is concerned. However, it must be acknowledged that the peaks of the different curves of $|\bar{\mathbf{U}} - \mathbf{U}|^2$ contracted with larger ζ. In fact, already at $\zeta = 0.5$, the system presented a lower peak than the bare cylinder and essentially zeroed in when $\zeta = 3.5$.

Contours of $|\bar{\mathbf{U}} - \mathbf{U}|^2$ of Fig. 12 show that the fluctuations of the flow were cast away, provided the rods spun sufficiently fast and confirm that the passive control led to a larger region of velocity fluctuations (associated with the appearance of turbulent eddies), detected in Carvalho and Assi (2023c). Compared with the vorticity contours of this former work, the disappearance of any red region demonstrates the effectiveness of imposing rotation to the rods, but calls attention to the power expenditure. This topic is discussed in Sec. IV E.

In addition to the aforementioned features, given sufficient angular velocities, the matters of correlation and end effects stood out, as highlighted through Q-contours of vorticity magnitude in the spanwise y-view of Fig. 13 (Multimedia view).

Individually, the wake of the bare cylinder and of the less active setups was comprised of smaller structures near the bodies with greater vorticity content and larger eddies away that traveled throughout the three-dimensional flow domain. As the rods spun faster, the turbulent structures were progressively eliminated, and streamwise vortices became apparent, as depicted for $\zeta = 2.5$. In fact, it is easy to observe in Fig. 13 that in this arrangement, the otherwise correlated vortices were disrupted through the interaction with the tip-vortex of the finite bodies; hence, the well correlated structures observed in laminar and turbulent regimes for infinitely long structures of Carvalho *et al.* (2021) and Carvalho and Assi (2022), respectively, were not detected here.

It may be said that the rods acted on the bidimensional mechanism of vortex formation (Gerrard, 1966, also briefly reviewed in Sec. I) that one verifies to occur in an infinitely long cylinder (and systems with MSBC, Carvalho and Assi, 2022). When the end effects were entailed, instead, the rods were incapable of suppressing the tip-vortex, intrinsically related to a three-dimensional mechanism of vortex formation (Williamson, 1996).

Of course, two-dimensional (2D) contours in cross-sectional planes provide a simple visualization of the features of the rather 3D flow, fully represented in Fig. 14 (Multimedia view). It may be seen that for the bare cylinder much larger, but weaker structures, formed away from the body. For the system, this tendency was followed only for the passive mechanism and for $\zeta = 0.5$. At $\zeta = 1.0$, Q-contours exhibit a wake with fewer coherent structures near and away from the body, while for $\zeta = 2.5$ some correlation is visualized in eddies that emerge with a tube-like format, but that are affected by the tip-vortex. The resulting combination of these structures resemble "arch-vortices"

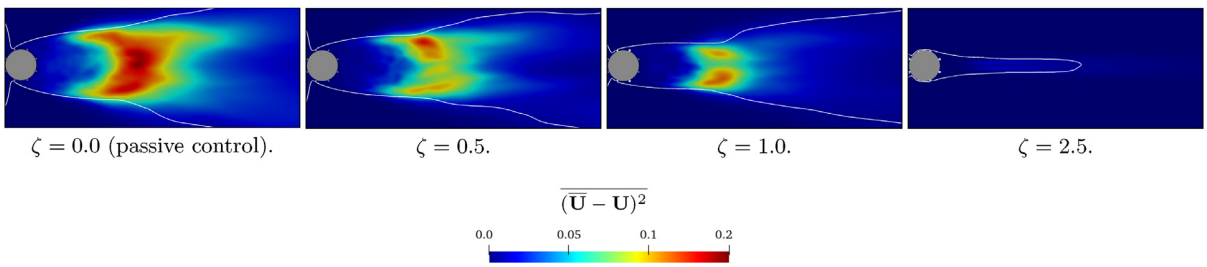

FIG. 12. Time-averaged contours of velocity fluctuation show that to insert fixed rods enlarged the region of high velocity fluctuation, but at any of the active regimes presently considered, this region was strongly weakened down to complete suppression ($\zeta = 2.5$).

Physics of Fluids ARTICLE scitation.org/journal/phf

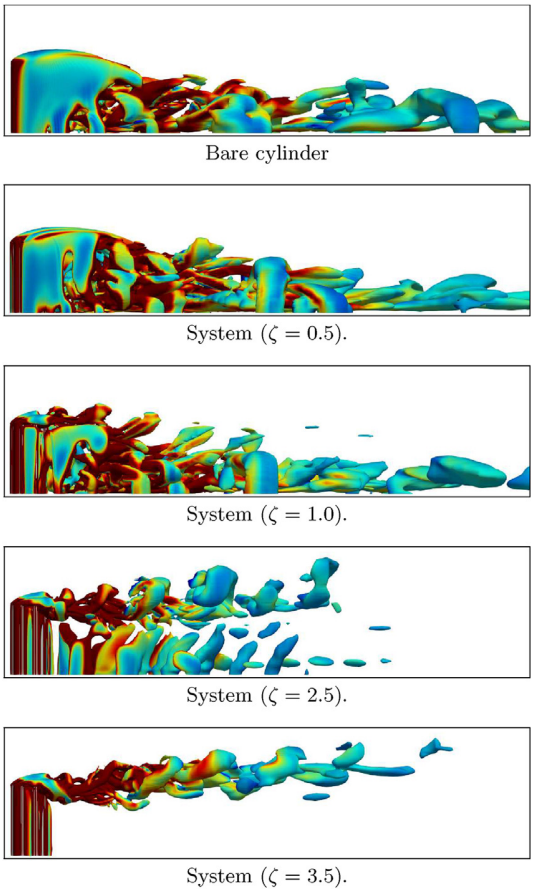

FIG. 13. *Q*-contours seen from a spanwise (*y*-) view. Streamwise vortices that were otherwise made perfectly correlated in laminar and turbulent regimes of infinitely long cylinders by the present system were acted upon by the tip-vortex. Even at $\zeta = 3.5$, tip-vortices remained in the wake with large vortical content. Multimedia view: https://doi.org/10.1063/5.0147760.2

(Taniguchi *et al.*, 1981). It is interesting to note that with this set of rotations, in turbulent infinitely long cases, vortex shedding occurred two-dimensionally, that is, vortices were perfectly correlated spanwise.

At $\zeta = 2.5$, *Q*-contours of high and low values (equal to 2.5, in red; and 0.1 in translucent blue) presented in Fig. 15 (Multimedia view) reveal that the rods were capable of suppressing the wake that originated along the spanwise extension of the cylinders through progressive weakening of the turbulent structures related to the Gerrard's (1966) mechanism of vortex generation in cylinders. This is made clear from the transition in colors. However, as the rods' spanned the passive mechanism toward the most active setups herein analyzed, the tip-vortices not only remained, but their vortical content was unaffected by the wake-control rods. This stands out in Fig. 15(b) ($\zeta = 2.5$): While most vortices were well correlated and with low vorticity (blue), ring-like red vortices (high vorticity) were produced on the free end.

Interestingly, it may be seen from the provided videos that as a result from the interaction of the tip-vortices with those streamwise-oriented, a flow structure reminiscent of the arch-vortices, previously observed in works of wall-mounted bodies, appeared (Sumner *et al.*, 2004). The videos discern, however, that these vortices did not form an arch *per se*, perhaps due to the momentum injected in the *z*-direction by the rods. This behavior differs from the experiments conducted by Sumner *et al.* (2004), where the authors showed that for $L/D < 3$, a symmetric "arch-vortex" dominated the near wake. The difference might lie in the boundary layer as well (as we used a free water surface, whereas there the cylinder was immersed into the boundary layer of the ground).

Clearly, as well, the present wake and the classical von Kármán wake are disparate, in agreement with experiments (Luo *et al.*, 1996; Sumner *et al.*, 2004) that did not detect the coherent wake for low slenderness parameter. Instead, while turbulent eddies lost vorticity by viscous dissipation, they were able to draw vorticity from smaller structures that were carried along. As these incorporated structures weakened and disappeared at the upper end of our ζ-range, tip-vortices approached more clearly a ring shape, particularly at $\zeta = 2.5$. As a matter of fact, for $\zeta = 3.5$, it is seen that streamwise vortices were eliminated from the wake and then only the tip-vortices remained.

In order to further assess end effects, components of the mean velocity field, project in the *y*–*z* plane, are shown in Fig. 16 for different *x*-stations. The first three positions correspond, respectively, to locations past the pair of cylinders P_1, P_1' ($x = -0.4$), P_2, P_2' ($x = 0.0$), and P_3, P_3' ($x = 0.4$); and the last two positions refer to planes that do not cross the system, but are located downstream (therefore past P_4, P_4').

The first column of Fig. 16 refers to the passive mechanism and exhibit the features detected in Carvalho and Assi (2023c). In a nutshell, this includes (1) the vectors representative of the flow from the free water surface (on the right of each figure) to the free end (on the left), (2) tip-vortex formation as the flow course is forced above, below and to the free end of the cylinders, and (3) the sustained vortices past the system, at $x/D = 1$. The other columns refer to the active mechanism ($\zeta = 0.5$, 1.0, 2.5, and 3.5).

Upstream of separation (at $x/D = -0.4$, first row of the figure), the velocity field shows that regardless of power input, the suppressing device did not affect the flow in the *y*–*z* plane substantially, which kept the overall aspect portrayed by Carvalho and Assi (2023c) for the finite bare cylinder under the effect of a free surface. Exception may regard only to some slight reduction in the magnitude of the velocity field distant from the side of the bodies (in the *z*-direction). For the other positions, there was a much more pronounced reduction in the velocity field away from the bodies. For example, it may be seen that, at $x/D = 0$, the flow from the free water surface to the tip of the bodies is gradually eliminated by the effect of the increasing velocities of the rods that might have redirected the flow to adopt the streamwise direction.

Although experimental data about the separation point of such a system are not available, it is reasonable to assume that at $x/D = 0.4$ (equivalent to $\theta > 156°$) separation had already taken place on the basis of (1) the angle of separation of a bare cylinder in the subcritical regime (according to Blevins, 1990, it is greater than 80° but less than 140°) for an infinitely long cylinder, (2) Farivar (1981) measured maximal pressure fluctuations at an angle of 75°, and (3) Figs. 9, 10, and 14 corroborate with this assumption even at the most active arrangements. At this position, we note that as the rods spun faster, the

Physics of Fluids ARTICLE scitation.org/journal/phf

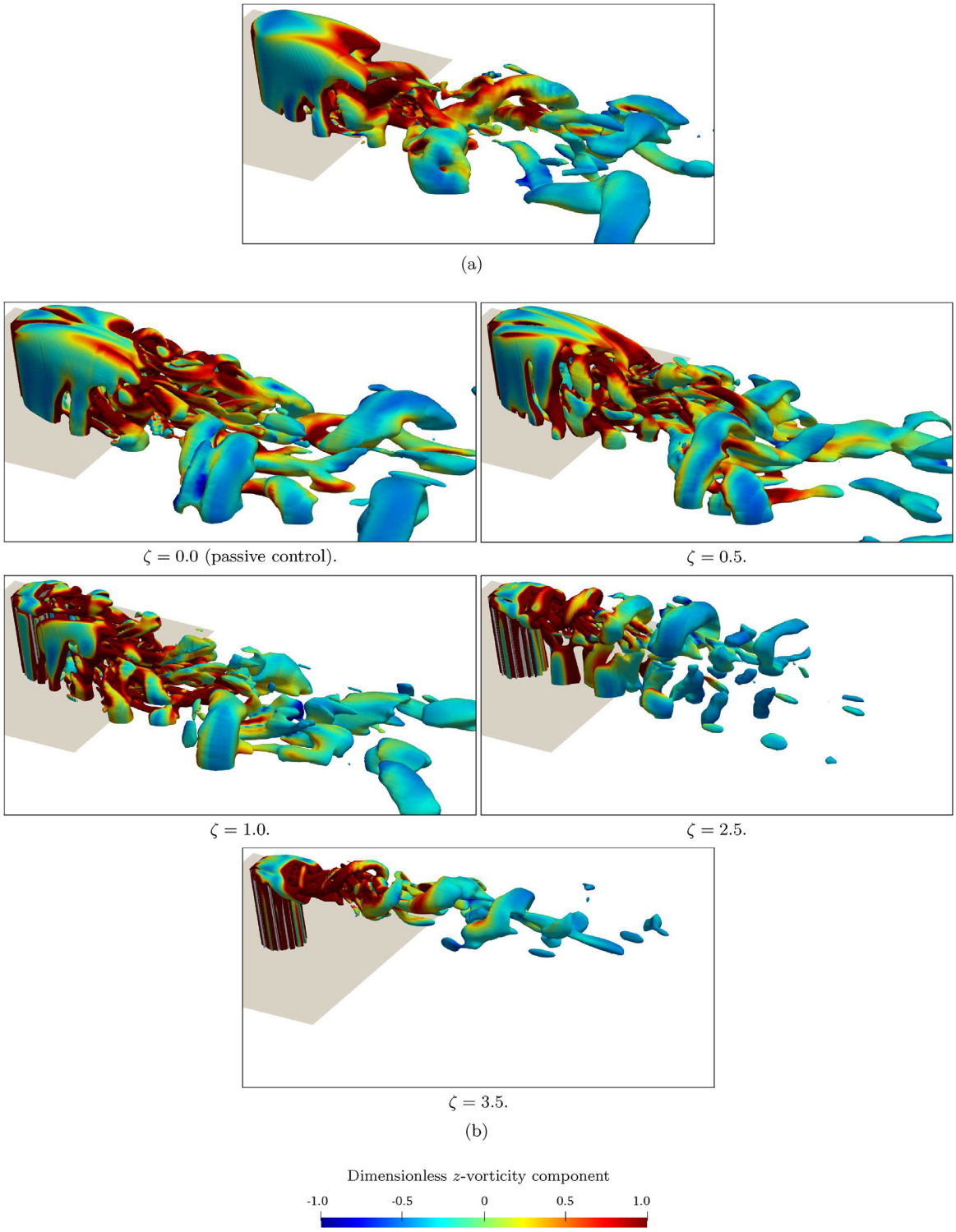

FIG. 14. Q-contours ($Q = 0.1$) present the three-dimensionality of the flow. Active rods suppressed most of the wake, but were unable to eliminate the tip-vortex. Red contours show that these vortices remained strong, even at $\zeta = 3.5$. (a) Bare cylinder and (b) entire system. Multimedia view: https://doi.org/10.1063/5.0147760.3

Physics of Fluids ARTICLE scitation.org/journal/phf

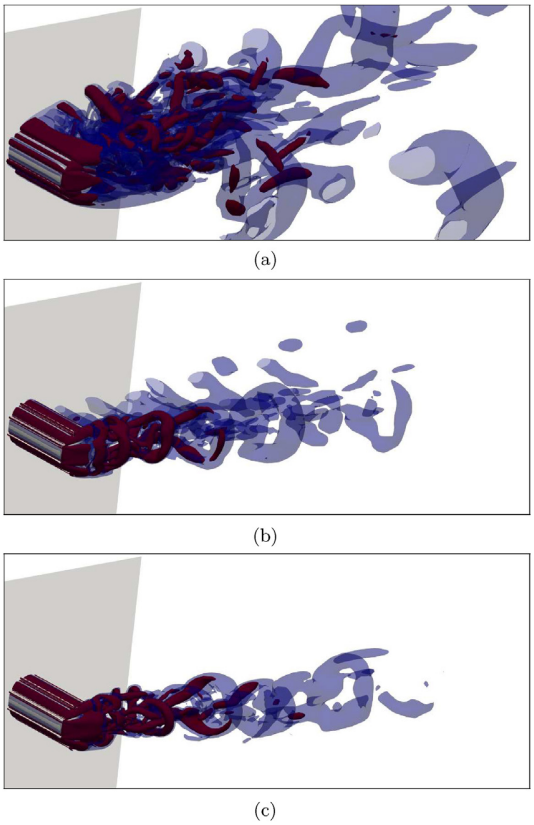

FIG. 15. High and low levels of Q contours corresponding to 2.5 (red) and 0.1 (blue, translucent). (a) Passive mechanism ($\zeta = 0.0$), (b) $\zeta = 2.5$, and (c) $\zeta = 3.5$. Multimedia view: https://doi.org/10.1063/5.0147760.4

orientation of the vectors reversed on the side of the bodies. Whereas in the passive mechanism the flow on the upper part adopted a counterclockwise sense (and the opposite for the lower part) at this position, this direction was gradually reversed. At $\zeta = 3.5$, the figure shows that the flow on the upper part swirled in a clockwise sense instead (and conversely for the lower rods). This means that the rods' spinning motion brought and induced the outer flow to follow the direction imposed by them. Although as a nuance, the same effect took place at $x/D = -0.4$, but there the upper rods P_1, P_1' merely forced the flow upward. This is seen by the rather vertical and parallel vectors along, but perpendicular to, the extension of the bodies. The difference between this effect at $x/D = -0.4$ and at $x/D = 0.4$ lies strictly on the location relative to the separation point.

The same underlying flow behavior was promoted by the rods for the x-stations located in the wake, those of $x = 0.6$ and $x = 1.0$: The flow surrounding the structure, which moved away from the free water surface (recall that the no-penetration condition applied), was pulled by the rods the more the faster they rotated (see these x-stations from left to right in Fig. 16). However, in these cases, a circulatory pattern was found at the fastest configurations, whereby upward and downward vectors represented in the figure mixed across $y = 0$. Yet, above and below $y = 0$, a circulatory pattern remained at $\zeta = 2.5$ and $\zeta = 3.5$ that corresponds to the formation of tip-vortices observed in Figs. 14 and 13, but much more clearly notable in Fig. 15, where the noteworthy ring-like vortex shape is noticeable. This projection of the tip-vortices in the y–z plane was combined and carried along downstream with the bulk of the flow in the x-direction to be later weakened by viscosity, prior to its utter elimination.

Since wake-control rods act in the sense of injecting momentum into the near flow of the entire system in a direction that is tangent to their cross section (in the x–y plane) to principally attenuate z-oriented vortices, it does not come as a surprise that this suppressing mechanism was not able to counteract the formation of tip-vortices, mostly aligned with the x-direction. Indeed, Fig. 8 demonstrates that the side force C_S, that is especially rooted in the tip-vortex, was marginally affected by the presence of the rods.

C. Hydrodynamic loads on the main body

We now quantitatively evaluate the hydrodynamic forces produced as a consequence of the vortex dynamics discussed above. Figure 17 throws some light on whether the insertion of the rods to the main body P_0 reduced mean drag, RMS of lift, and mean side force relative to the plain cylinder, through direct comparison between the loads upon P_0 and the reference values of Eq. (6) related to the bare cylinder.

It is easily seen that the wake-control rods brought significant reduction in the RMS of lift. Overall, the $\hat{C}_L$-curve shows a reduction greater than 23% ($\zeta = 0.5$). At best, we have verified a 75% decrease in $\hat{C}_L$ ($\zeta = 2.5$). At worst, rods' effect in $\hat{C}_L$ was a rather negligible uptick of 0.31% ($\zeta = 1.0$). For the mean drag, decrease was also noted at a less steeper tendency than $\hat{C}_L$, yet steady and monotonic with ζ. At $\zeta = 3.5$, the system was able to produce upon P_0 a mean drag 30% lower than that that affected the bare cylinder. Both the results in terms of $\hat{C}_L$ and $\overline{C_D}$ are directly related to the very essence of the MSBC mechanism: Momentum was transferred to the shear layers that caused their reattachment, as observed in Fig. 10. As a consequence, the thinner wake produced a smaller region of lower pressure past the system, and the difference in pressure fore and aft the system led to lower mean drag. Similarly, vortices were confined to interact in a shorter region, whereby they interacted more frequently. From Gerrard (1966), it is known that a vortex grows until another, opposite vortex, cuts off its vorticity supply. This happens more rapidly in a thin wake.

The same trend did not occur for $\overline{C_S}$, and the reason lies mainly on the mechanism of vortex formation. In lieu of the interaction of opposing vortices that is vital to form a Kármán street, or the present vortex wake of finite bodies shown above, these tip-vortices were rooted in the proneness of flow separation separation due to the geometry of the body. Note that there is a 90° angle between the length of the bodies (aligned with the z-direction) and their sides at the free end (aligned with the x-direction, at $z/L = 1$). The wake-control rods employed here could not affect $\overline{C_S}$ appreciably, as justified in Sec. IV B, but a light decrease in 5.5% was noted at $\zeta = 2.5$.

D. Hydrodynamic loads on each body

Mean force coefficients are represented in Fig. 18 for each rod. In general, it is seen that the mean drag on P_1, P_1' and P_2, P_2' went from positive to negative values, adopting then ever greater propulsion [a

Physics of Fluids ARTICLE scitation.org/journal/phf

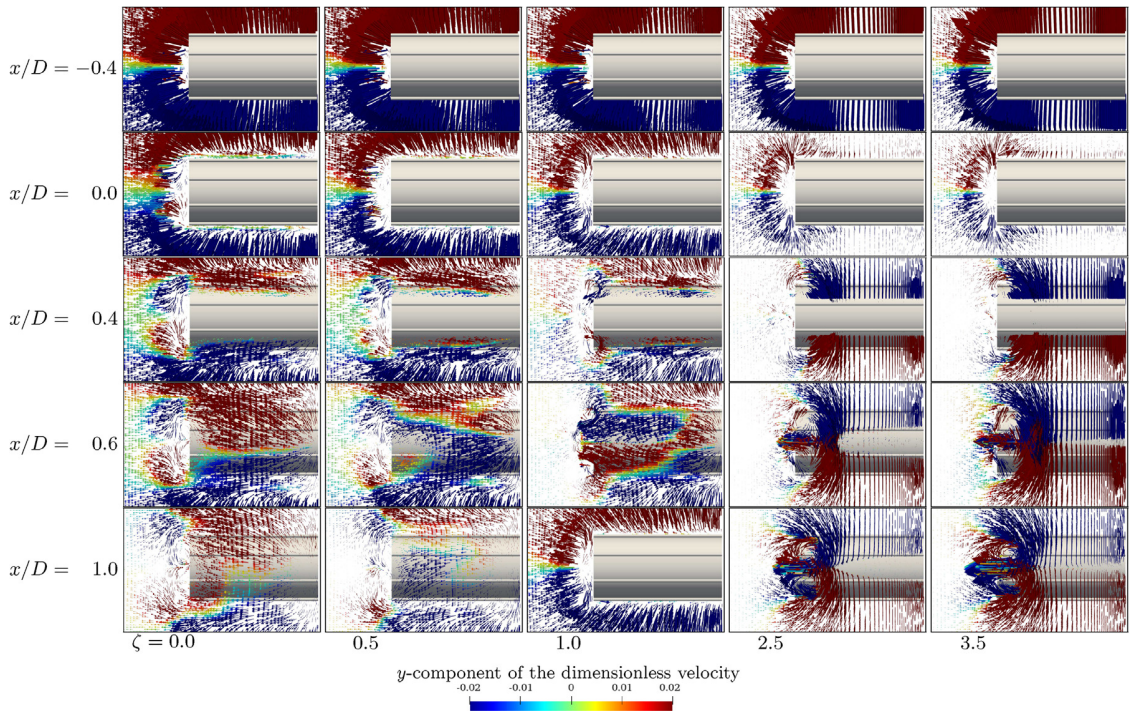

FIG. 16. Mean flow field over finite bodies projected in the *y*–*z* plane at different *x*-stations (lines) with increasingly faster rotation speeds (columns). The *z*-axis spans the length of the body from left to right of each subfigure. Blue and red correspond to upward and downward (in *y*) velocity vectors, respectively.

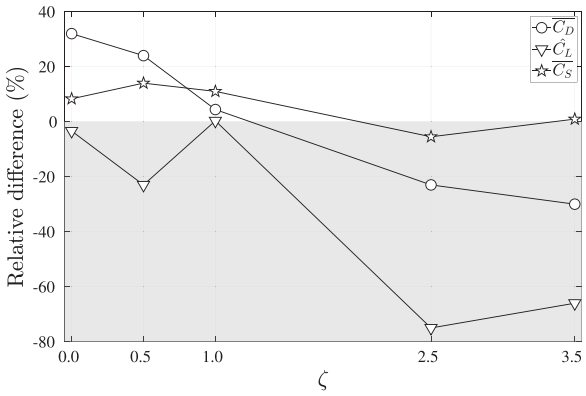

FIG. 17. Comparison between the RMS of lift ($\hat{C}_L$), mean drag ($\overline{C_D}$), and mean side force ($\overline{C_S}$) acting on the main body P_0 relative to the same loads found to act upon the bare cylinder. Shading corresponds to the region of attenuation of these loads.

horizontal force against the direction of the incoming flow, see Fig. 18(a)]. Contrarily, for P_3, P'_3 and P_4, P'_4, the loads generally passed from slightly negative and null values to positive and larger values. These monotonic tendencies seemed to prevail, particularly for the upper end of angular velocities hereby analyzed. The exception was the pair P_3, P'_3, because the loads went from essentially null (passive mechanism) to negative values ($\zeta = 1.0$) and then reversed to larger and positive mean drag ($\zeta = 2.5$ and $\zeta = 3.5$). These features are shared both by this plot and that of Carvalho and Assi (2022). The rods carrying most of the loads acting on the entire structure were the intermediate elements P_2, P'_2 and P_3, P'_3, more distant from stagnation regions, while P_1, P'_1 and P_4, P'_4, located in these regions, were less representative. As seen in the literature, intermediate rods can more easily interact with shear layers and affect separation points (Carvalho *et al.*, 2021; Carvalho and Assi, 2022; Carvalho and Assi, 2023c). This elucidates the far-reaching capacity of MSBC, capable of dealing even with the more complex flow structure of finite bluff bodies.

Difference between these setups lies essentially in the lower magnitudes of the mean loads for the finite bodies. On physical grounds, this difference is the outcome of the lower correlation found for turbulent flows about fully three-dimensional bodies, where end effects are present. In such cases, mean drag and mean lift tend to be lower, as flow modeling prevents information loss from the two-dimensional imposition of periodic boundary conditions on the ends.

In relation to mean lift, represented in Fig. 18(b), it is noted that all rods followed a monotonic tendency with greater angular velocities. The symmetry between positive lift applied on the upper rods and the negative lift on the lower rods led to mean null value of mean lift upon the entire structure and on the main body as in previous works for infinitely long bodies in laminar and turbulent regimes (Assi *et al.*, 2019; Carvalho *et al.*, 2021; and Carvalho and Assi, 2022).

Our data show that time-averaged drag, lift, and side force were comparable in the passive mechanism. However, when the rods were in motion, the $\overline{C_S}$ was broadly one order of magnitude below the other

Physics of Fluids ARTICLE scitation.org/journal/phf

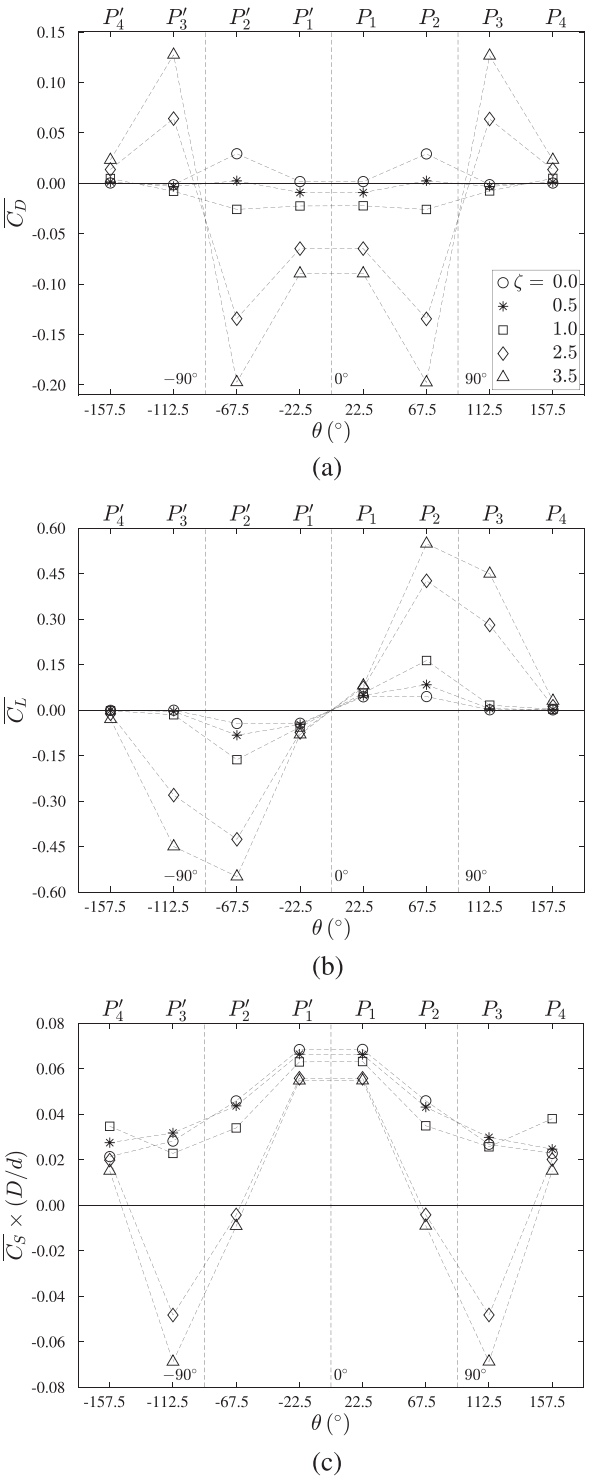

FIG. 18. Loads acting on each rod. (a) Mean drag, (b) mean lift, and (c) mean side force.

loads. For ease of interpretation, Fig. 18(c) represents the side force multiplied by $D/d = 20$. It is seen that the rods broke away from previous behaviors observed for $\overline{C_D}$ and $\hat{C}_L$: P_1 contributed significantly to the side force even at greater angular velocities and remained comparable to the most impacted rod, P_3, in these more power-demanding configurations. P_2 progressively became less relevant, and the same pattern was followed by P_4 (in common with the behavior detected for the other coefficients).

These observations point to the fact that with respect to $\overline{C_S}$, the position of the rods relative to the shear layers was not a key factor in determining their contributions. The $\overline{C_S}$-curves may be jointly analyzed in two groups: one for $\zeta \leq 1.0$ and the other for $\zeta \geq 2.5$, because the curves of these ranges near each other closely. Physically, this division permeates the degree of suppression of vortex shedding. For $\zeta \geq 2.5$ vorticity, contours of section B show that aside from the tip-vortex, the other flow structures in the wake were more strongly correlated than previous active setups, and at $\zeta = 3.5$, only the tip-vortex remained. Therefore, the influence of the rods on $\overline{C_S}$ was not related to the shear–layer interaction, but rather to the state of the wake and its imbalance in pressure along the span of the body. When the wake was not suppressed, a pressure difference along the span of the body amounted to greater $\overline{C_S}$.

This may be noted in Fig. 19, where it is shown that for the lower end of our range of ζ, the mean pressure coefficient gradually decreased toward lower values as it reached the interface between the system and the free stream. Contrarily, for the higher rotation rates, the $\overline{C_p}$ curve was generally flat at higher values until it abruptly lowered to the pressure at the interface. Note that (1) along the system, the values of $\overline{C_p}$ with $\zeta = 2.5$ and 3.5 were much greater than those for $\zeta \leq 1.0$, and these curves reached roughly the same value at the interface. From the high-pressure region (left, see $z/D = -1$) to the low-pressure region ($z/D = 1$), a force was generated in the z-positive direction for all curves. Now, (2) taking into account the free stream, the high pressure region is to the right ($z/D \to 6$ in the plot), asymptotically reaching $\overline{C_p} = 0$, a greater value than that at the interface, so a negative z-oriented force was produced from this pressure imbalance. These two forces summed to give the $\overline{C_S}$ higher for $\zeta \leq 1.0$ and lower otherwise. Further study is required to assess whether greater

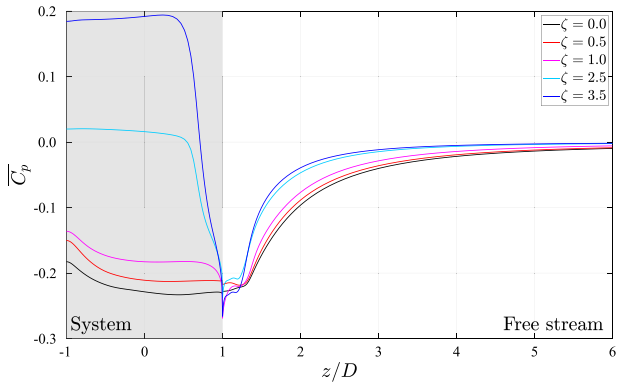

FIG. 19. Mean pressure coefficient along the z-direction, for $x/D = 0.5$ and $y/D = 0$. On the right is the free stream and on the left is the cylinder (shaded region). The interface lies at $z/D = 0$.

Physics of Fluids ARTICLE scitation.org/journal/phf

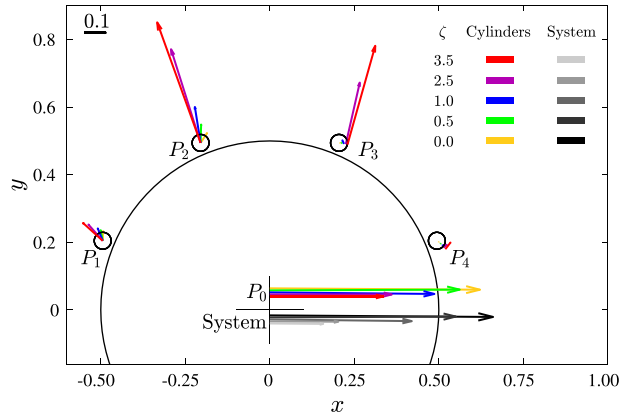

FIG. 20. Total force upon the rods shown by vectors. Groups of bars correspond to $\zeta = 0.0$, 0.5, 1.0, 2.5, and 3.5. Due to the symmetry of the setup in relation to the axial flow, rods P_n, P'_n, $n = 1, \ldots, 4$ were acted upon by the same load magnitudes and were omitted for the sake of conciseness.

angular speeds would be able to maintain this tendency of increase in $\overline{C_p}$ over the cylinder that could eventually eliminate $\overline{C_S}$.

Curiously, present results encompassing all the components of the resultant force on each rod emphasize by and large that P_4 may be less germane to the attenuation of hydrodynamic loads.

The resultant loads on each cylinder (colored) and on the entire system (grayscale) are portrayed qualitatively by Fig. 20 for the upper rods (due to symmetry, the loads on the lower rods are the same, but mirrored with respect to $y = 0$). Because, as explained above, $\overline{C_S}$ was at least an order of magnitude lower than the other loads, the effect of the mean force was relatively negligible in the composition of the total load; thus, we have opted to represent only the x–y plane. General tendencies observed for infinitely long bodies were detected in the loads upon finite bodies: A monotonic increase for all rods (as plotted in Fig. 21); greater relevance of P_2 and P_3, since they concentrated higher loads; inversion in the x-direction of the loads on P_1, P_2, and P_3, while that on P_4 followed a singular direction; consistent reduction in the load upon the entire system, and it was kept essentially aligned with the flow direction (as expected by symmetry). For comparison, these loads were lower than those in the infinitely long case, but still within the same order of magnitude.

E. Power expenditure

Flow control was improved as the rods were put in spinning motion. In order to do so, an actuating power was required. We follow the analysis of Shukla and Arakeri (2013) to assess the effectiveness of the present system. According to these authors, the power loss of the entire system (C_{PL}) may be decomposed into the power spent to counteract the wall shear stress (C_N) and to downsize mean drag (C_D). We employ mean quantities (marked with an overbar) in the following equation:

$$\overline{C_{PL}} = \overline{C_D} + \overline{C_N}, \tag{7}$$

where time-averaging was performed as described in Sec. V. The mean wall shear stress $\overline{\tau_n}$ was integrated over the entire surface of the bodies ($\overline{p_n}$). The first part of the right hand side of the following equation refers to integration over the span, while the second is on the sides of the rods:

$$\overline{p_n} = \omega_n \frac{d}{2}\left\{\int_{-L/2}^{L/2}\left[\int_0^{2\pi}\overline{\tau_n}\,\frac{d}{2}\,\mathrm{d}\theta\right]\mathrm{d}z + \int_0^{D/2}\left[\int_0^{2\pi}\overline{\tau_n}\,r\mathrm{d}\theta\right]\mathrm{d}r\right\}. \tag{8}$$

Normalization is made to get $\overline{C_N}$ is given in the following equation:

$$\overline{C_N} = \sum_{n=1}^{N}\frac{\overline{p_n}}{\frac{1}{2}\rho U_\infty^3 DL}. \tag{9}$$

The curve $\overline{C_D}$ vs $\overline{C_N}$ plotted in Fig. 22 allows to assert that the mean drag upon the entire system was predominant in the components of $\overline{C_{PL}}$ up to $\zeta = 1.0$. The situation reversed for $\zeta \geq 2.5$. This can be viewed from markers to the left and to the right, respectively, of the dashed line plotted after $\overline{C_D} = \overline{C_N}$ in the same figure. Therefore, the presented trend suggests that depending on the amount of power provided to the system, it may occur a situation such that a greater fraction of the actuating power is spent to spin the rods rather than to

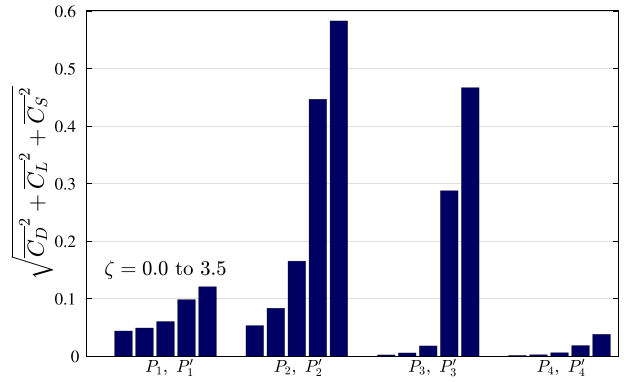

FIG. 21. Bars represent the total force upon the rods. Groups of bars correspond to $\zeta = 0.0$, 0.5, 1.0, 2.5, and 3.5. Due to the symmetry of the setup in relation to the axial flow, rods P_n, P'_n, $n = 1, \ldots, 4$ were acted upon by the same load magnitudes.

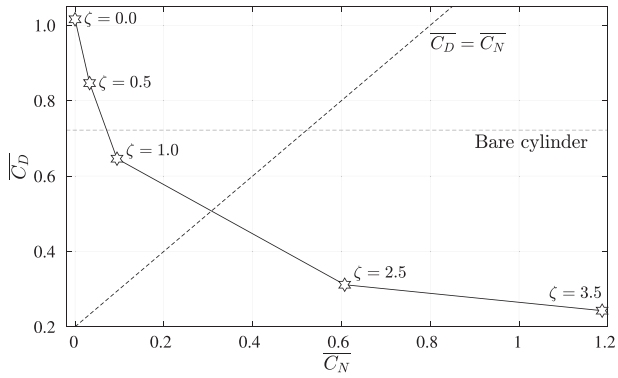

FIG. 22. Time-averaged components of the mean power loss, the mean drag upon the entire system $\overline{C_D}$, and the power-loss due to viscous friction $\overline{C_N}$. Right and left of the dashed line $\overline{C_D} = \overline{C_N}$ indicate two regions, respectively, one where $\overline{C_D}$ and another where $\overline{C_N}$ dominates.

Physics of Fluids ARTICLE scitation.org/journal/phf

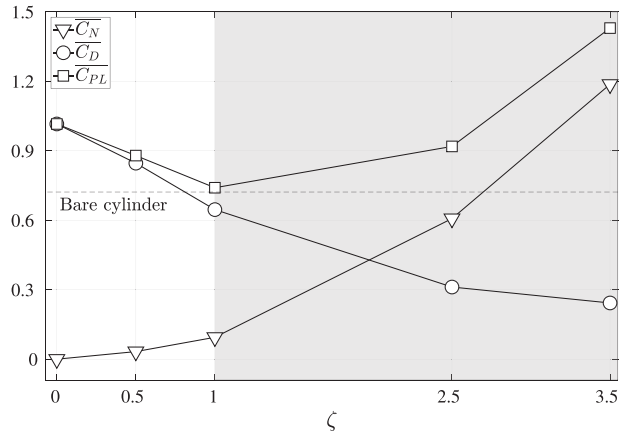

FIG. 23. Mean power-loss coefficient $\overline{C_{PL}}$ and its components $\overline{C_N}$ and $\overline{C_D}$ over the entire system. In the shaded region, $\overline{C_D} < \overline{C_{D,\mathrm{Bare}}}$.

improve flow control (here in the scope of $\overline{C_D}$ attenuation and vortex shedding suppression). These circumstances were not evaluated here, but may be thought of, for example, given $\zeta \geq 3.5$. Vorticity contours shown earlier suggest that wake suppression was maximal in such angular speeds arrangement, and as discussed, one might not expect the rods to eliminate the tip-vortex. Therefore, it seems likely that $\zeta > 3.5$ would correspond to a state of the flow where more power input would not leverage flow control over the tip-vortex, but it may be possible that the system would be submitted to a turnaround where $\overline{C_D} < 0$, as in previous works (Silva-Ortega and Assi, 2017b; Assi *et al.*, 2019; and Carvalho and Assi, 2022).

Equation (7) provides a way to assess the efficiency of the entire system with the computed power-loss coefficient $\overline{C_{PL}}$ plotted in Fig. 23.

The figure outlines that in order to reduce the mean drag over the present system below $\overline{C_{D,\mathrm{Bare}}}$, as it occurred for $\zeta \geq 1.0$, power expenditure is key, since $\overline{C_{PL}} \gtrapprox \overline{C_{D,\mathrm{Bare}}}$. Furthermore, the figure depicts that a steep rise occurred in $\overline{C_N}$, which became the major part of $\overline{C_{PL}}$ already at $\zeta = 2.5$. Indeed, to use this active mechanism for a finite system required more power to counteract viscous traction than for infinitely long bodies. This trade-off between power expenditure and drag reduction establishes an optimization problem that requires further study for a system as the present in the same fashion as those conducted for simpler arrangements, with fewer slender rods (Fan *et al.*, 2020; Bingham *et al.*, 2018).

V. CONCLUSION

Vortex dynamics, hydrodynamic loads, and power efficiency were numerically investigated with respect to finite bodies through Detached-eddy simulations (DES). A bare cylinder (one without flow control device) and a system (as in Silva-Ortega and Assi, 2017b), comprised of this body and eight slender wake-control rods, were analyzed in the turbulent regime at Reynolds number of 1000. Upper and lower rods spun symmetrically, with angular velocities obtained from potential flow about a bare cylinder (Carvalho *et al.*, 2021). The rods rotated faster through the parameter $\zeta = 0.0$ (passive mechanism), 0.5, 1.0, 2.5, and 3.5 that multiplied the velocities. A free water surface, modeled here as a slip-allowing plane, was attached to one end of the cylinders.

Vorticity contours showed that to fit the main body with spinning rods was capable of eliminating the wake originated by a "two-dimensional" mechanism of wake formation (Gerrard, 1966) that consists on vortices produced by separation of the boundary layer as the fluid flows about the bluff body. In order to achieve so, sufficiently large actuating power was given to the system. Nevertheless, separation from the ends of the bodies generated tip-vortices (Kawamura *et al.*, 1984) upon which the active mechanism had little effect and that remained with strong vortical content even at suppression of the other eddies. Spanwise visualization of Q-contours showed that finite bodies' wakes broke away from the perfectly correlated vortex shedding pattern previously found for infinitely long bodies (with large enough angular velocities Carvalho and Assi, 2022).

Flow control released by the active rods with progressively larger angular velocities was accompanied by the contraction of the wake, elimination of mean velocity fluctuations, and reduction of vorticity content within the eddies. Velocity vector field presented for cross sections passing through different streamwise positions revealed that the energy provided to rods' revolutions was translated into momentum injection to a point that the outer flow was induced to adopt the streamwise direction. Furthermore, the recirculation direction was reversed from passive to active mechanism, with threshold detected at $\zeta = 2.5$. This interference with the flow caused the formation of novel ring-like vortices that lasted throughout our range of ζ. At the onset of their formation, these vortices drew smaller vortices, in such a fashion that compensated vorticity loss due to viscosity nearer to the system.

In terms of hydrodynamic loads, addition of the rods led to significant and steady attenuation of mean drag, and light reduction of the root mean square (RMS) of lift and mean side force. These two latter forces were mitigated only more sensibly for $\zeta \geq 2.5$ and 3.5, although these two arrangements differed but marginally. Comparison with the bare cylinder showed that mean drag and RMS of lift reduced by up to 23% and 75%, while the mean side force was negligibly affected.

Efficiency of the entire system analyzed on the basis of power-loss coefficient (Shukla and Arakeri, 2013) rendered clear that in order to mitigate mean drag, power expenditure was key to counteract wall shear stress due to viscous effects. Our analysis also corroborated with previous studies in that this source of power-loss became dominant as the rods spun faster. Power-loss coefficient was 27% and 98% above that of the bare cylinder to reduce the mean drag in 57% and 66%, respectively.

Finally, we remark that to the best of our knowledge, the literature on flow control of finite bodies is scarce, and the present analysis with wake-control rods was not conducted previously. Active control of the wake of stationary bluff bodies is a stepping stone toward more complex configurations, such as that involving vortex-induced vibrations (VIV) of these structures, rooted in the vortex shedding mechanism. Future work should concern with the optimization of the angular velocities ω_n toward drag mitigation, production of a useful hydrodynamic load to maneuver the body or with the system free to oscillate in VIV.

ACKNOWLEDGMENTS

I.A.C. is grateful to CAPES Brazilian Ministry of Education for his Ph.D. scholarship and to the National Laboratory for Scientific

Computing (LNCC/MCTI, Brazil) for providing HPC resources of the SDumont supercomputer. GRSA acknowledges the support of FAPESP, Brazil (No. 2011/00205-6) and CNPq, Brazil (No. 306146/2019-3). We gratefully acknowledge the support of the RCGI Research Centre for Greenhouse Gas Innovation, hosted by the University of São Paulo, Brazil and sponsored by FAPESP (No. 2020/15230-5) and Shell Brazil.

AUTHOR DECLARATIONS

Conflict of Interest

The authors have no conflicts to disclose.

Author Contributions

Icaro Amorim Carvalho: Conceptualization (equal); Formal analysis (equal); Investigation (equal); Methodology (equal); Software (equal); Supervision (equal); Validation (equal); Visualization (equal); Writing – original draft (equal); Writing – review & editing (equal). **Gustavo R. S. Assi:** Conceptualization (equal); Formal analysis (equal); Funding acquisition (equal); Methodology (equal); Resources (equal); Software (equal); Supervision (equal); Visualization (equal); Writing – review & editing (equal).

DATA AVAILABILITY

The data that support the findings of this study are available from the corresponding author upon reasonable request.

REFERENCES

Assi, G. R., Bearman, P. W., and Kitney, N., "Low drag solutions for suppressing vortex-induced vibration of circular cylinders," J. Fluids Struct. **25**, 666–675 (2009).

Assi, G. R., Bearman, P. W., and Tognarelli, M. A., "On the stability of a free-to-rotate short-tail fairing and a splitter plate as suppressors of vortex-induced vibration," Ocean Eng. **92**, 234–244 (2014).

Assi, G. R. S., Orselli, R. M., and Silva-Ortega, M., "Control of vortex shedding from a circular cylinder surrounded by eight rotating wake-control cylinders at Re= 100," J. Fluids Struct. **89**, 13–24 (2019).

Bearman, P., "Investigation of the flow behind a two-dimensional model with a blunt trailing edge and fitted with splitter plates," J. Fluid Mech. **21**, 241–255 (1965).

Behr, M., Hastreiter, D., Mittal, S., and Tezduyar, T., "Incompressible flow past a circular cylinder: Dependence of the computed flow field on the location of the lateral boundaries," Comput. Methods Appl. Mech. Eng. **123**, 309–316 (1995).

Behr, M., Liou, J., Shih, R., and Tezduyar, T., "Vorticity-streamfunction formulation of unsteady incompressible flow past a cylinder: Sensitivity of the computed flow field to the location of the outflow boundary," Int. J. Numer. Methods Fluids **12**, 323–342 (1991).

Bingham, C., Raibaudo, C., Morton, C., and Martinuzzi, R., "Suppression of fluctuating lift on a cylinder via evolutionary algorithms: Control with interfering small cylinder," Phys. Fluids **30**, 127104 (2018).

Blevins, R. D., *Flow-Induced Vibration*, 2nd ed. (Van Nostrand Reinhold, New York, 1990).

Carvalho, I. A. and Assi, G. R. S., "Enhanced control of the turbulent flow past a circular cylinder with rotating rods inspired by an inviscid solution," J. Fluids Struct. **113**, 103652 (2022).

Carvalho, I. A. and Assi, G. R. S., "On the omnidirectionality of a system with eight spinning rods for wake control," J. Fluid Mech. (unpublished).

Carvalho, I. A. and Assi, G. R. S., "On the omnidirectionality of a system with eight spinning rods in controlling the wake of a circular cylinder in a turbulent regime," J. Fluid Mech. (unpublished).

Carvalho, I. A. and Assi, G. R. S., "Passive control of vortex-shedding past finite cylinders under the effect of a free surface," Phys. Fluids **35**, 015109 (2023c).

Carvalho, I. A., Assi, G. R. S., and Orselli, R. M., "Wake control of a circular cylinder with rotating rods: Numerical simulations for inviscid and viscous flows," J. Fluids Struct. **106**, 103385 (2021).

Choi, H., Jeon, W.-P., and Kim, J., "Control of flow over a bluff body," Annu. Rev. Fluid Mech. **40**, 113–139 (2008).

Cicolin, M. M. and Assi, G. R. S., "Experiments with flexible shrouds to reduce the vortex-induced vibration of a cylinder with low mass and damping," Appl. Ocean Res. **65**, 290–301 (2017).

Fan, D., Yang, L., Wang, Z., Triantafyllou, M. S., and Karniadakis, G. E., "Reinforcement learning for bluff body active flow control in experiments and simulations," Proc. Natl. Acad. Sci. U. S. A. **117**, 26091–26098 (2020).

Farivar, D., "Turbulent uniform flow around cylinders of finite length," AIAA J. **19**, 275–281 (1981).

Ferziger, J. H., Perić, M., and Street, R. L., *Computational Methods for Fluid Dynamics* (Springer, 2002), Vol. 3.

Fujarra, A. L., Rosetti, G. F., de Wilde, J., and Gonçalves, R. T., "State-of-art on vortex-induced motion: A comprehensive survey after more than one decade of experimental investigation," in *International Conference on Offshore Mechanics and Arctic Engineering* (American Society of Mechanical Engineers, 2012), Vol. 44915, pp. 561–582.

Gerrard, J. H., "The mechanics of the formation region of vortices behind bluff bodies," J. Fluid Mech. **25**, 401–413 (1966).

Gonçalves, R., Franzini, G., Rosetti, G. F., Meneghini, J., and Fujarra, A., "Flow around circular cylinders with very low aspect ratio," J. Fluids Struct. **54**, 122–141 (2015).

Gonçalves, R. T., Fujarra, A. L., Rosetti, G. F., and Nishimoto, K., "Mitigation of vortex-induced motion (VIM) on a monocolumn platform: Forces and movements," J. Offshore Mech. Arct. Eng. **132**, 041102 (2010).

Gonçalves, R. T., Meneghini, J. R., and Fujarra, A. L., "Vortex-induced vibration of floating circular cylinders with very low aspect ratio," Ocean Eng. **154**, 234–251 (2018).

Goodarzi, M. and Dehkordi, E. K., "Geometrical parameter analysis on stabilizing the flow regime over a circular cylinder using two small rotating controllers," Comput. Fluids **145**, 129–140 (2017).

Kawamura, T., Hiwada, M., Hibino, T., Mabuchi, I., and Kumada, M., "Flow around a finite circular cylinder on a flat plate: Cylinder height greater than turbulent boundary layer thickness," Bull. JSME **27**, 2142–2151 (1984).

Kim, S.-E., and Mohan, L. S., "Prediction of unsteady loading on a circular cylinder in high Reynolds number flows using large eddy simulation," in International Conference on Offshore Mechanics and Arctic Engineering (2005), Vol. 41979, pp. 775–783.

Korkischko, I. and Meneghini, J. R., "Volumetric reconstruction of the mean flow around circular cylinders fitted with strakes," Exp. Fluids **51**, 1109–1122 (2011).

Luo, S., Gan, T., and Chew, Y., "Uniform flow past one (or two in tandem) finite length circular cylinder (s)," J. Wind Eng. Ind. Aerodyn. **59**, 69–93 (1996).

Mittal, S., "Control of flow past bluff bodies using rotating control cylinders," J. Fluids Struct. **15**, 291–326 (2001).

Mittal, S. and Kumar, B., "Flow past a rotating cylinder," J. Fluid Mech. **476**, 303–334 (2003).

Newman, J. N., *Marine Hydrodynamics* (The MIT Press, 2018).

Norberg, C., "Flow around a circular cylinder: Aspects of fluctuating lift," J. Fluids Struct. **15**, 459–469 (2001).

Palau-Salvador, G., Stoesser, T., Fröhlich, J., Kappler, M., and Rodi, W., "Large eddy simulations and experiments of flow around finite-height cylinders," Flow, Turbul. Combust. **84**, 239–275 (2010).

Patankar, S. V., *Numerical Heat Transfer and Fluid Flow* (Taylor & Francis, 1980).

Rhie, C. and Chow, W. L., "Numerical study of the turbulent flow past an airfoil with trailing edge separation," AIAA J. **21**, 1525–1532 (1983).

Rosetti, G. F., Vaz, G., Hoekstra, M., Gonçalves, R. T., and Fujarra, A. L., "CFD calculations for free-surface-piercing low aspect ratio circular cylinder with solution verification and comparison with experiments," in *International Conference on Offshore Mechanics and Arctic Engineering* (American Society of Mechanical Engineers, 2013), Vol. 55416.

Physics of Fluids ARTICLE scitation.org/journal/phf

Shukla, R. K. and Arakeri, J. H., "Minimum power consumption for drag reduction on a circular cylinder by tangential surface motion," J. Fluid Mech. **715**, 597–641 (2013).
Silva-Ortega, M. and Assi, G. R. S., "Flow-induced vibration of a circular cylinder surrounded by two, four and eight wake-control cylinders," Exp. Therm. Fluid Sci. **85**, 354–362 (2017a).
Silva-Ortega, M. and Assi, G., "Suppression of the vortex-induced vibration of a circular cylinder surrounded by eight rotating wake-control cylinders," J. Fluids Struct. **74**, 401–412 (2017b).
Silva-Ortega, M. and Assi, G., "Hydrodynamic loads on a circular cylinder surrounded by two, four and eight wake-control cylinders," Ocean Eng. **153**, 345–352 (2018).
Smagorinsky, J., "General circulation experiments with the primitive equations: I. The basic experiment," Mon. Weather Rev. **91**, 99–164 (1963).
Spalart, P., "Trends in turbulence treatments," in Fluids 2000 Conference and Exhibit, 2000.
Spalart, P. R., "Comments on the feasibility of LES for wings, and on a hybrid RANS/LES approach," in *Proceedings of the First AFOSR International Conference on DNS/LES* (Greyden Press, 1997).
Spalart, P. and Allmaras, S., "A one-equation turbulence model for aerodynamic flows," in 30th Aerospace Sciences Meeting and Exhibit, 1992.
Spalart, P. R., Deck, S., Shur, M. L., Squires, K. D., Strelets, M. K., and Travin, A., "A new version of detached-eddy simulation, resistant to ambiguous grid densities," Theor. Comput. Fluid Dyn. **20**, 181–195 (2006).
Strykowski, P. J. and Sreenivasan, K. R., "On the formation and suppression of vortex shedding at low Reynolds numbers," J. Fluid Mech. **218**, 71–107 (1990).
Sumner, D., "Flow above the free end of a surface-mounted finite-height circular cylinder: A review," J. Fluids Struct. **43**, 41–63 (2013).
Sumner, D., Heseltine, J., and Dansereau, O., "Wake structure of a finite circular cylinder of small aspect ratio," Exp. Fluids **37**, 720–730 (2004).
Taniguchi, S., Sakamoto, H., and Arie, M., "Flow around circular cylinders of finite height placed vertically in turbulent boundary layers," Bull. JSME **24**, 37–44 (1981).
Tennekes, H. and Lumley, J. L., *A First Course in Turbulence* (MIT Press, 1972).
Travin, A., Shur, M., Strelets, M., and Spalart, P., "Detached-eddy simulations past a circular cylinder," Flow, Turbul. Combust. **63**, 293–313 (2000).
Vatsa, V. N., Lockard, D. P., and Spalart, P. R., "Grid sensitivity of SA-based Delayed-Detached-Eddy-Simulation model for blunt-body flows," AIAA J. **55**, 2842–2847 (2017).
Versteeg, H. K. and Malalasekera, W., *An Introduction to Computational Fluid Dynamics: The Finite Volume Method* (Pearson Education, 2007).
Williamson, C. H. K., "Vortex dynamics in the cylinder wake," Annu. Rev. Fluid Mech. **28**, 477–539 (1996).
Williamson, C. H. K. and Govardhan, R., "Vortex-induced vibrations," Annu. Rev. Fluid Mech. **36**, 413–455 (2004).
Zdravkovich, M. M., "Review and classification of various aerodynamic and hydrodynamic means for suppressing vortex shedding," J. Wind Eng. Ind. Aerodyn. **7**, 145–189 (1981).

Physics of Fluids ERRATUM pubs.aip.org/aip/pof

Erratum: "Active control of vortex shedding past finite cylinders under the effect of a free surface" [Phys. Fluids 35, 045130 (2023)]

Cite as: Phys. Fluids **35**, 069901 (2023); doi: 10.1063/5.0159286
Submitted: 22 May 2023 · Accepted: 1 June 2023 ·
Published Online: 13 June 2023

I. A. Carvalho[1,a] and G. R. S. Assi[2,b]

AFFILIATIONS

[1]Department of Mechanical Engineering, EPUSP, University of São Paulo, SP 05508-030, Brazil
[2]Department of Naval Architecture and Ocean Engineering, EPUSP, University of São Paulo, SP 05508-030, Brazil

[a]Author to whom correspondence should be addressed: amorim.icaro@usp.br
[b]Electronic mail: g.assi@usp.br

https://doi.org/10.1063/5.0159286

In Carvalho and Assi (2023), "We used $d/D = 0.1$" should be "We used $d/D = 0.05$."

Carvalho, I. A. and Assi, G. R. S., "Active control of vortex shedding past finite cylinders under the effect of a free surface," Phys. Fluids **35**, 045130 (2023).

10 Papers considered for submission

The following papers are intended to be submitted to an appropriate journal.

On the omnidirectionality of a system with eight spinning rods for wake control of a circular cylinder in laminar regime

I. A. Carvalho[a,*], G. R. S. Assi[b]

[a]*Department of Mechanical Engineering, EPUSP, University of São Paulo, SP, 05508-030, Brazil*
[b]*Department of Naval Arch. & Ocean Engineering, EPUSP, University of São Paulo, SP, 05508-030, Brazil*

Abstract

We have investigated the omnidirectionality of a system comprised of a main circular cylinder fitted with eight rotating rods acting as wake-control devices. Finite-volume simulations were conducted at a Reynolds number of 100 in two configurations: one in which all rods spun with the same angular velocity (case 0); and another in which the rotation speeds were defined based on a potential-flow theory (case 1). We show through the analysis of hydrodynamic coefficients, vorticity contours and power consumption that both configurations reduced mean drag, eliminated the vortex wake, and were negligibly affected in terms of power loss by the angle of attack. Nevertheless, the two cases showed different behaviours regarding omnidirectionality: While case 1 became ever "more omnidirectional" (to be explained in detail) with increasing angular speeds and was capable of balancing vortex contours past the system to render null lift, case 0 produced an imbalanced (yet steady) wake that led to larger absolute values of mean lift at higher speeds. The relative importance of each rod of the system is explained, and it becomes clear that merely introducing actuation power into the rods' motion does not translate directly into better wake control. Rather, it is essential that the rotation speeds are appropriately weighted according to the position of the rods relative to regions of boundary layer and wake of the main body.

Keywords: Vortex-shedding suppression, wake control, drag reduction, bluff body, omnidirectionality.

*Corresponding author: amorim.icaro@usp.br (I. A. Carvalho)

1. Introduction

Bluff bodies have been observed to produce and be subjected to different wakes and motions according to the flow past them. Since its earliest observation over a century ago (Von Kármán, 1954), the typical Kármán-Bénard vortex street has inspired many studies and applications in a multitude of fields. Once the boundary layer separates from the body, it becomes free shear layers influenced by the instabilities of the flow in the near-wake region. These structures carrying high levels of vorticity roll up and subsequently give rise to the alternating *vortex shedding* mechanism (Gerrard, 1966). Consequently, the structure is acted upon by cyclic loads (that may lead to fatigue and failure) with an intensity that depends on the dimension of the body (D), the viscosity of the fluid (ν) and the velocity of the incoming flow (U_∞). As it has been observed, due to transversal and longitudinal components of the resulting load (relative to the direction of the flow, termed *lift* and *drag*, respectively) fluid-structure interaction occurs, represented by low-frequency vortex-induced motion (VIM) and vortex-induced vibrations (VIV), both rooted in the vortex-shedding phenomenon (Blevins, 1990; Williamson and Govardhan, 2004).

Several forms of passive and active actuators have been devised to control vortex shedding according to the need of power input (Zdravkovich, 1981). Whereas in the context of bluff body flows, passive methods are characterised by surface protrusions (e.g., helical strakes, shrouds, fairings and splitter plates Korkischko and Meneghini, 2011; Assi et al., 2014, 2009); active methods (Choi et al., 2008) rely on the power input to spin shrouds, deliberately vibrate the body, blow or suction the flow. Although different mechanisms have been implemented, they generally attempt to enhance flow control through interaction with the boundary or shear layers, or with the developed wake.

One promising approach is that of inserting shrouds around a main body. Strykowski and Sreenivasan (1990) observed that a single (passive) control rod of diameter d significantly smaller than D was able to entirely suppress vortex shedding for appropriate Reynolds numbers ($Re = U_\infty D/\nu$). This limitation was observed by Mittal (2001) and others, who further advanced the subject by employing a spinning rod instead of a passive one. This idea stems from the scope of the Moving Surface Boundary-layer Control (MSBC) technique, originally for aerofoils. For bluff bodies, MSBC implementation aims to use a secondary body to inject momentum into the boundary layer of the larger body and thus move the separation points further downstream (Cicolin et al., 2021). Amongst the benefits, MSBC (i) delays separation, (ii) weakens vortex interaction

within the thinner wake (Gerrard, 1966) and (iii) reduces hydrodynamic loads.

A plethora of (numerical and experimental) studies followed those of Strykowski and Sreenivasan (1990), Mittal (2001) and others for different configurations of spinning rods, varying d/D, gap G/D between the main body and the rods, the number of rods, their relative positions, etc. (Korkischko and Meneghini, 2012; Patino et al., 2017; Silva-Ortega and Assi, 2017b, to cite a few). Recently, the same system was studied in the context of finite cylinders, where end effects were present (Carvalho and Assi, 2022b, 2023). A particular configuration of interest to the present work is that of Silva-Ortega and Assi (2017b) with 8 rods. This study of the passive wake-suppression mechanism showed that this configuration stood out amongst others with two, four and eight rods. Despite a drag increase, this setup mitigated the peak amplitude of VIV utterly when compared with the case of a plain cylinder. Contrarily, the other configurations investigated by Silva-Ortega and Assi (2017b) affected the system with less effective suppression of hydrodynamic loads and response amplitude, or rendered the system more prone to galloping, VIV, or both, cumulatively.

The same setup of 8 rods was later undertaken in the context of an active mechanism (MSBC). Silva-Ortega and Assi (2017a) conducted experiments that presented a reduction in the amplitude of drag and lift; more importantly, they showed that MSBC was able to reduce sustained vibrations (as those of the baseline case). The authors pointed out, however, that changes in the angle of attack (i.e. the orientation of the incoming flow in relation to the device) could affect the performance of the entire system in controlling the hydrodynamic loads.

Advancing on flow topology, incipient numerical simulations of this system evaluated vortex shedding in laminar and turbulent regimes and revealed that the rods effectively eliminated the vortices of the former and subsided in the latter (Assi et al., 2018, 2019). The difference in behaviour was due to the *Re*-regime and its inherent vortex dynamics features. Later, Carvalho and Assi (2022a), based on a potential-flow-inspired setup of rotations (Carvalho et al., 2021), corroborated that indeed the arrangement of 8 rods could eliminate the vortex wake, given sufficient rotation speed to the rods; and, beyond that, exposed that a more efficient system resulted from spinning some rods faster than others. In fact, the authors also remarked that the rods had a similar effect to that of "laminarising" the flow, as the (turbulent viscosity of the) eddies progressively disappeared.

These past studies have advanced in the comprehension of the impact of the system of 8 rods on the flow dynamics, hydrodynamic loads and more particularly, on the interaction of the fitted rods

with the shear layers). Nevertheless, we note that neither experiments nor numerical simulations have tackled the effect of the angle of attack. This was remarked by Silva-Ortega and Assi (2017a). Indeed, previous works were generally concerned with a fixed angle of attack or, when the body was yawed, a suppressing system was not employed (Vakil and Green, 2009) Our study aims to fill this void in the literature for $Re = 100$, varying the angle of attack and the rotation speeds in cases in which the rods spin with the same speed and in which their rotations follow a potential-flow analogy. We further uphold considerations of actuating power required to counteract shear and mean drag.

1.1. Objective

In the present work, we investigate how a system comprised of a main larger body of diameter D fitted with eight slender rods of diameter $d/D = 1/20$ is influenced by the angle of attack α of the incoming flow U_∞. The rotating rods are equally spaced at angular positions θ, at intervals of 45° around the main body, offset by 22.5° from the frontal stagnation point, as presented in figure 1. The gap $G/D = 1/100$ is measured between the walls of the cylinders. Our analysis considers the hydrodynamic loads, wake topology and power spent to rotate the rods. Furthermore, we inspect the individual roles of the rods within the system in terms to lift (C_L) and drag (C_D).

Two cases are considered: (case 0) one in which the rods spin with the same velocity ω_0 (note that upper and lower rods spin in opposite directions), and (case 1) that in which the rods adopt different velocities ω_n, based on the theoretical potential-flow field around a circular cylinder.

2. Method

The incompressible, unsteady flow of a Newtonian fluid is governed by the Navier-Stokes and continuity equations,

$$\rho\left(\frac{\partial U_i}{\partial t} + U_j\frac{\partial U_i}{\partial x_j}\right) = -\frac{\partial p}{\partial x_i} + \mu\frac{\partial^2 U_i}{\partial x_j \partial x_j}, \tag{1}$$

$$\frac{\partial U_j}{\partial x_j} = 0. \tag{2}$$

which were solved by a finite-volume method. Each term followed an appropriate discretisation scheme to mitigate truncation and discretisation errors; and inspired by the physics of the problem, whether the discretised term corresponded to a diffusive or a convective term.

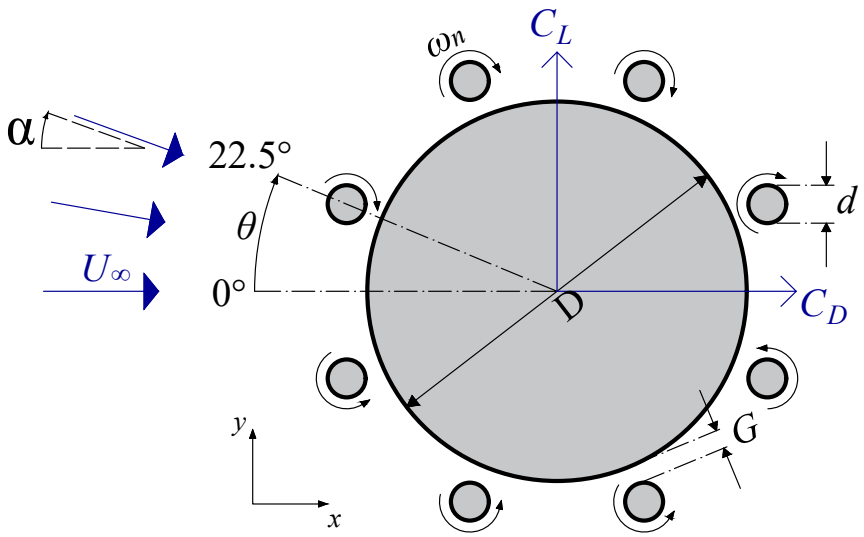

Figure 1: Flow past a system comprised by a main cylinder and rotating control rods under different angles of attack of the incoming flow.

The transient term $\partial U_i/\partial t$ on the left-hand side of equation 1 was discretised according to an implicit backward scheme. The divergence term $U_j \partial U_i/\partial x_j$, representative of the convective flow, was discretised with a linear upwind scheme. Gradients were computed using a least squares method, which entailed the gradient of the pressure term and the Laplacian term on the right-hand side of the same equation (computed as the divergence of the gradient). A non-orthogonality correction was required for the calculation of the Laplacian term whenever the surface of the cells and the line connecting the centres of two adjacent cells were not perpendicular to one another. Interpolations, such as that of cell values from their centres to their edges, were made based on a linear model. Surface normal gradients were determined in the same way as the Laplacian terms.

Equations 1 and 2 were solved at each time step using the aforementioned discretisation scheme and the following boundary conditions: for the incoming flow, far away from the system, the velocity U_∞ and fully developed pressure gradient $\nabla p = 0$ were specified. A no-slip boundary condition was prescribed on the walls of the bodies, either by imposing the tangential velocity of the rotating rod or by zeroing the velocity in the case of the main body. The outflow was given by null pressure and null velocity gradient.

A schematic drawing of the geometry employed in the simulations is shown in figure 2, where the rods were not represented for ease of visualisation. The O-grid topology was selected to enable the variation of the angle of attack α for the incoming flow, and it is fully represented in figure 3,

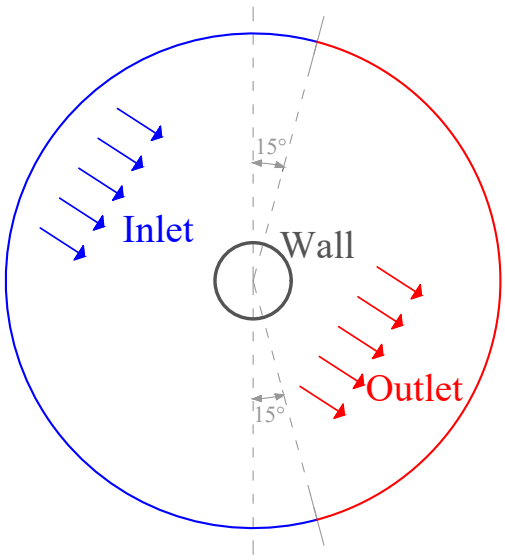

Figure 2: Inlet (blue), outlet (red) and wall (grey) boundary conditions assigned to the O-grid geometry. Only the main body is represented. For the rods, the same condition was applied, however, there the wall rotated with angular velocity ω_n.

where the meshing of different regions are exhibited for clarity.

A pertinent issue in resolving equations 1 and 2 in incompressible flow is that the pressure p and the velocity U_i are neither related by an equation of state, nor there is a transport equation for p. To couple pressure and velocity, the SIMPLE algorithm (Patankar, 1980) iterated the numerical solution at each time step to ensure that the momentum and continuity equations were concurrently satisfied by the resolved field. Tolerances of 10^{-4} and 10^{-8} were respected, respectively, for the determination of the pressure and for the velocity at each time step, looped through for at least 10 iterations. Relaxation factors were not applied.

Provided with the resolved field, pressure and viscous effects were considered over the surface of each body to compute hydrodynamic forces, conveniently decomposed into drag F_D and lift F_L components that were non-dimensionalised into force coefficients $C_D = F_D/(0.5\rho U_\infty^2 D)$ and $C_L = F_L/(0.5\rho U_\infty^2 D)$, respectively, based on the main body's diameter D, freestream flow velocity U_∞ and fluid density ρ.

Input rotation speeds for the control rods were inspired by the commonplace problem of the potential flow around a bare cylinder. At the radial distance $r = D/2 + G + d$ from the centre of the body, the velocities were determined from the potential-flow filed about a plain cylinder,

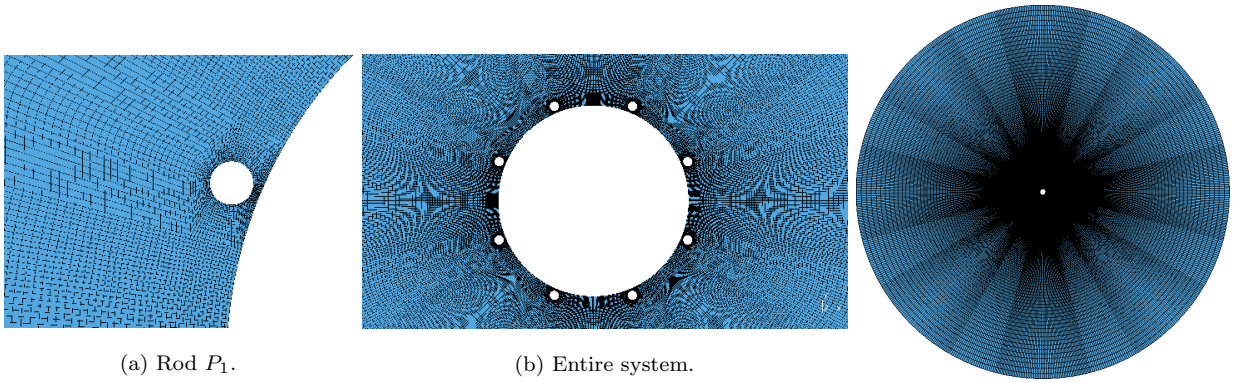

(a) Rod P_1.

(b) Entire system.

(c) Far-field domain.

Figure 3: Different regions of the structured grid.

in directions determined by two points concerning: i) the centre of the entire system and ii) that point coinciding with the location where the centre of the rods would be located. At each of these polar coordinates, the corresponding velocities were obtained from the potential flow. These linear velocities were assigned to each rod in the problem involving the main body and equipped rods (figure 4) following the same procedure performed by Carvalho et al. (2021).

Such definition of the velocities refers to the case hereby denoted *case 1*. Another setup, related to case 1, with the same input kinetic energy, is henceforth denoted *case 0*. The two cases were related in the following manner (Carvalho et al., 2021):

$$\left[\sum \omega_n^2\right]_{\text{case 1}} = \left[8\omega_0^2\right]_{\text{case 0}} \tag{3}$$

In order to speed up or lower the rotations, while keeping their proportionality, the control variable ζ multiplied rotation speeds. This parameter adopted values $\zeta = 0.0$ (passive rods), 0.5, 1.0, 1.5, 2.0 and 2.5 in our analysis. Of course, to impose $\zeta = 0.0$ rendered the system completely passive; and $\zeta = 1.0$ in case 1 imposed the potential-flow velocities. Physical meaning can be attributed to ζ only in case 0, as it coincided with the ratio of the rods' velocities by the incoming flow, $(\omega_0 d/2)/U_\infty$.

For physically-meaningful results, for a given angle of attack and set of rotation speeds, the simulations were advanced with time steps that were limited by three conditions: i) a maximum Courant number below 0.99 in each simulation, ii) at least 70 parts of the revolution of the rods, and iii) 100 parts of a cycle of vortex shedding were captured (the *cycle* here corresponds to that defined by the flow over a bare cylinder, see section 3.1).

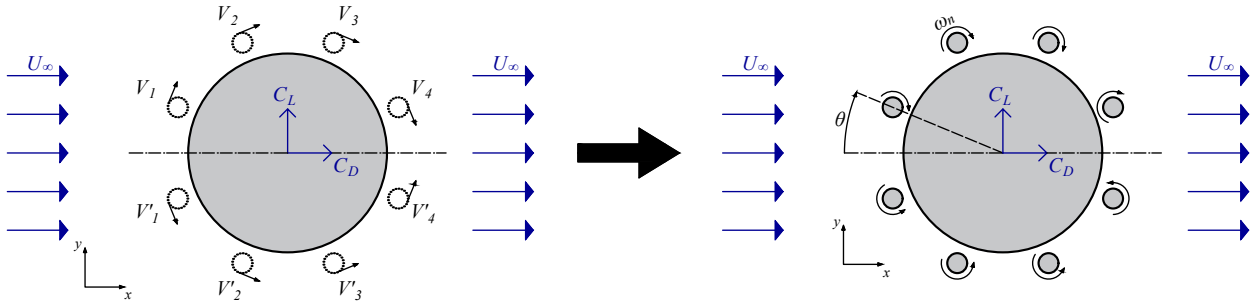

(a) $\alpha = 0°$.

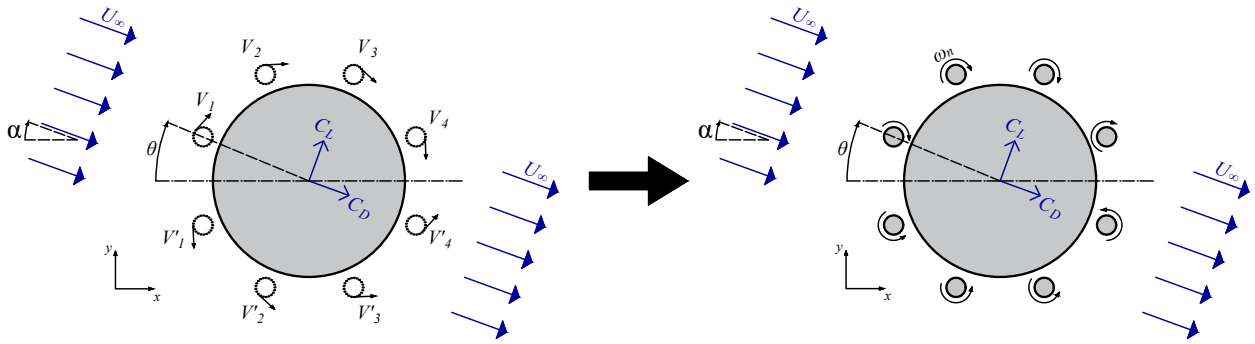

(b) $\alpha = 20°$.

Figure 4: Velocity vectors computed from the potential-flow field at points located in radial coordinates $r = D/2 + G + d/2$. $\theta = \pm\pi/8 \pm n\pi/4$, with $n = 0, \ldots, 3$ were assigned in case 1 as equivalent angular velocities for the rods.

Details of the finite-volume method employed in the present work are described in Ferziger et al. (2002); an analogous numerical scheme, with minor differences, is found in Carvalho et al. (2021).

3. Results

3.1. Grid independence and verification

A grid independence study was performed prior to varying the angle of attack and the rotation speeds of the system through α and ζ. Simulations included the reference configuration of null rotation and null angle of attack of the incoming flow. Each simulation was left to run for $40T_S$, where $T_S = 1/f_S$ corresponds to the inverse of the vortex shedding frequency (f_S) of a bare cylinder in laminar regime, usually defined by the Strouhal number, $S_t \approx 0.2$ (Norberg, 2001), with $S_t = f_S/(U/D)$. The results are shown in table 1. No significant changes occurred in either

Table 1: Mesh convergence study in terms of mean drag ($\overline{C_D}$) and root mean square lift ($\hat{C}_L$). Quantities between parentheses represent the percentage change from the respective mesh relative to the most refined case. We highlight the row of the grid used in this work.

Number of cells	$\overline{C_D}$		$\hat{C}_L$	
83,760	1.469	(0.36%)	0.2759	(0.29%)
110,000	1.473	(0.09%)	0.2771	(0.73%)
123,120	1.473	(0.10%)	0.2808	(2.07%)
132,880	1.473	(0.12%)	0.2778	(0.98%)
143,568	1.472	(0.15%)	0.2767	(0.58%)
146,480	1.473	(0.12%)	0.2776	(0.91%)
174,000	1.474	(0.05%)	0.2768	(0.62%)
179,088	1.474	(0.05%)	0.2748	(0.11%)
185,920	1.474	(-)	0.2751	(-)

$\overline{C_D}$ or $\hat{C}_L$ with increased refinement of the mesh. Even for $\hat{C}_L$, the greatest change was of 2.07% for the mesh with 123,120 cells.

The highlighted O-grid mesh of table 1 was verified with the unstructured grid of Carvalho et al. (2021) (which is not O-grid shaped), with the following results: our $\overline{C_D}$ was 3% and $\hat{C}_L$ was 9.7% below that of the previous work. Considering that the meshes of this work and that of Carvalho et al. (2021) differ qualitatively, the present grid-independence and verification results are judged satisfactory.

3.2. Time histories

Combinations of α and ζ were run in parallel for $40T_S$ for appropriate convergence, which was generally attained after $16T_S$. Time histories of C_D and C_L are plotted together in figures 5a and 5b for cases 0 and 1, respectively. For clarity, only the curves corresponding to $\alpha = 0°$, $10°$, and $20°$ are shown as examples, but all angles of attack mentioned in the methodology section of this work were run as just explained. Figure 5a remarks that in case 0 the parameter ζ matched the ratio of the linear speed applied to the rods ($U_c = \omega_0 d/2$) and the far-field incoming flow (U_∞). This association is not valid for case 1.

Amongst similarities between the two plots, it becomes clear that, given enough rotation speed, the control rods disrupted vortex shedding, observed as a reduction of the fluctuating lift. For $\alpha = 0°$ the amplitude of the lift coefficient was shortened in approximately 4 times from the passive setup to the less energetic configuration with $\zeta = 0.5$. The magnitude of C_D also fell monotonically with the faster spinning of the rods.

Despite these similarities, notably about drag, the two plots show very different behaviours for $\alpha \neq 0°$. Whereas the entire system of case 0 was subjected to strong directional effects in the form of non-zero mean lift – the greater the angle of attack, the greater was the absolute value of the mean lift –, case 1 was generally insensitive to the effect of α, making up for a "more omnidirectional" control arrangement. Besides, complete vortex shedding suppression for $\alpha = 20°$ only occurred at $\zeta = 1.5$ in case 0, instead of $\zeta = 1.0$ as in case 1. Therefore, not only case 0 was more susceptible to lift growth due to increasing α, but it also required greater input kinetic energy (as it can be directly associated with ζ) than case 0 to fully eliminate vortex shedding at higher angles of attack. In addition, for the present range of values of ζ and α, case 0 showed ever greater lift with the increment in any of these two parameters, provided $\alpha \neq 0°$ (in the explored range of α of this work).

3.3. Vortex contours

Instantaneous contours of the z-vorticity component are depicted in figure 6a for case 0, where the snapshot formed by row and column corresponds to a different combination of ζ and α, respectively.

The lines portraying $\zeta = 0.0$ and $\zeta = 0.5$ clearly show an instant in which the blue vortex (negative vorticity) was on the onset of shedding. The figure also shows the directional effect, as the wake aligned with the direction of the incoming flow. It is worth noting that, in spite of the wake topology shown with $\zeta = 1.0$ of figure 6a – which does not allow one to properly visualise vortex shedding –, the oscillation in lift, detected in the corresponding time history of figure 5, reveals that remaining vortex shedding was still present in this configuration.

For higher values of ζ, the vorticity fields corroborate with the preceding time history in that vortex shedding was completely eliminated. Nevertheless, another detail is added: an imbalance occurred between regions of negative (blue) and positive (red) contours within the wake, meaning that a non-zero steady lift was generated.

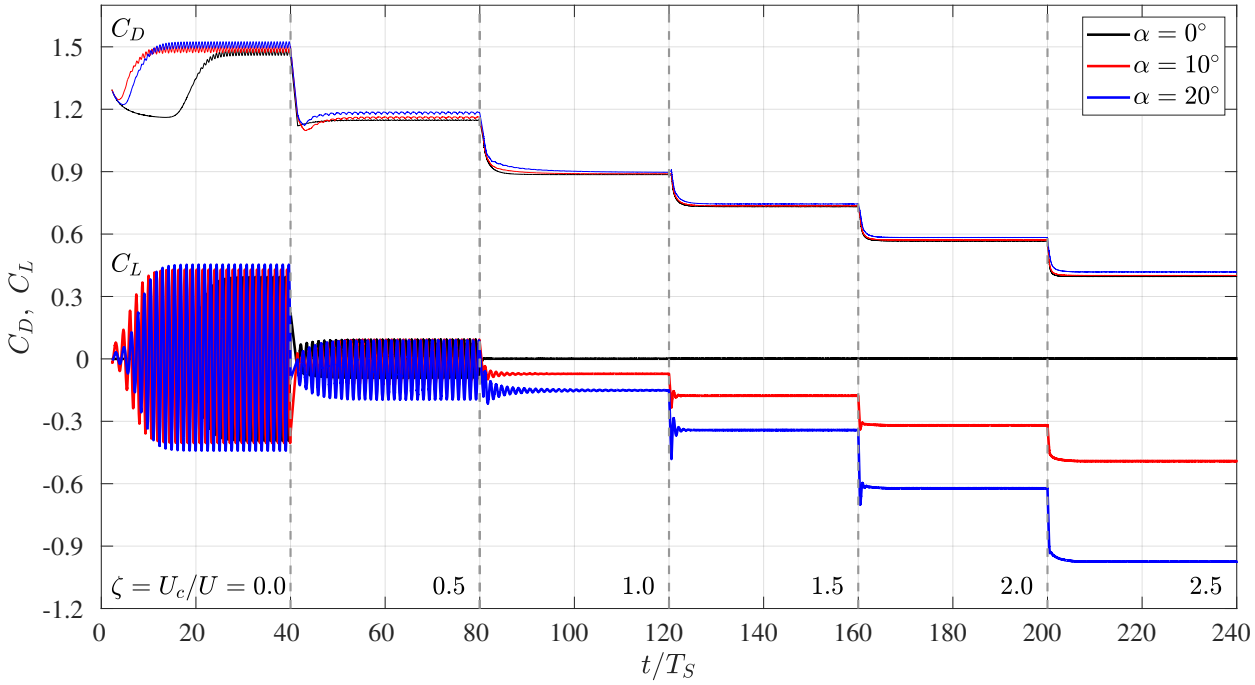

(a) Case 0.

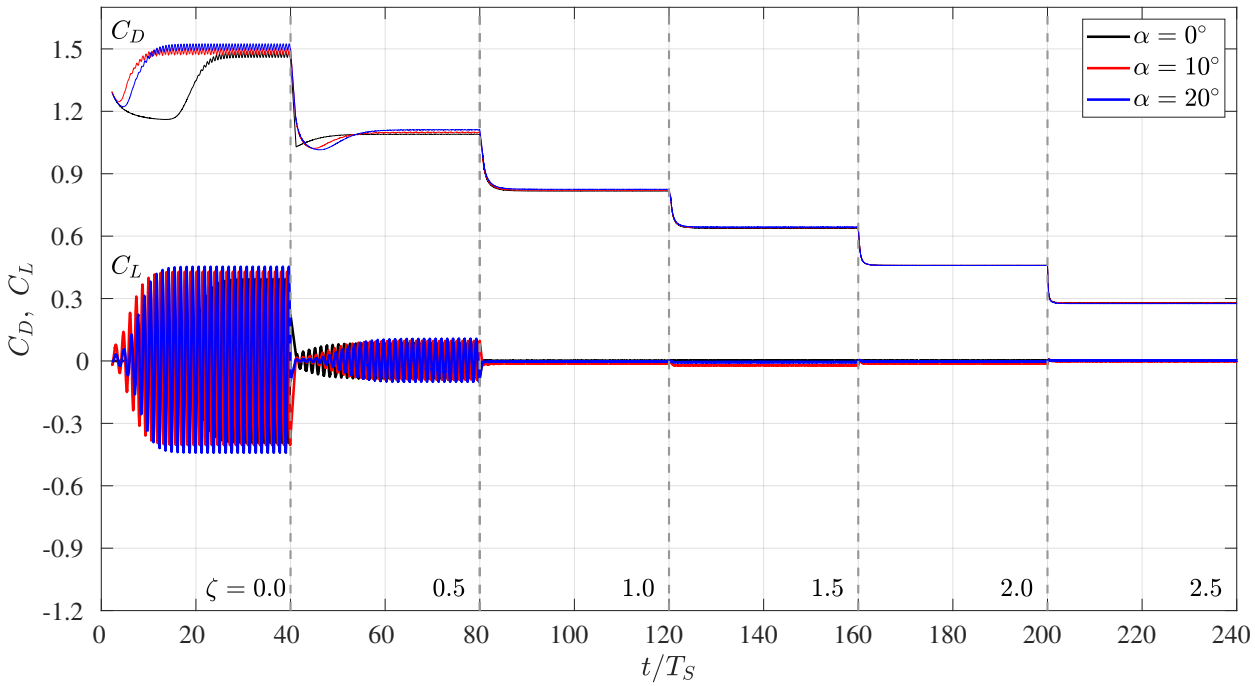

(b) Case 1.

Figure 5: Examples of time histories of drag and lift coefficients for cases 0 and 1.

The fourth row of figure 6a ($\zeta = 2.0$) shows that the magnitude of vorticity of the red region grew ever greater compared with that of the blue region, the more the incoming flow was subjected to higher values of α. For $\zeta = 2.0$ and $\alpha = 20°$ (last column and last row of figure 6a), there were many more contours within the positive-oriented part compared with its blue counterpart (for a symmetrical range of vorticity contours, $\omega/(U_\infty/D) = [-1, 1]$). This indicates that in the vortical composition of the wake, a larger anticlockwise-oriented vorticity region was formed.

This correlates well with the progressively greater lift (in absolute value) pointed out by figure 5. Because the stronger vortex formed past and below the entire system not only produced an imbalance between the two parts, but further created a region of even lower pressure, the resulting lift was directed downwards and it was greater in magnitude than other corresponding cases of lower α.

A similar behaviour was noted in case 1 for low ζ values and $\alpha = 0°$ (first column and first rows of figure 6b). However, as the rotation speeds were set according to potential flow for every angle of attack, the symmetry in the vorticity contours prevailed even for configurations of high ζ and α concurrently, thus corresponding to zero lift. To render this point clearer, figure 7 compares cases 0 and 1 for $\zeta = 2.5$ and $\alpha = 20°$.

3.4. Force coefficients upon the entire system

Coefficients of mean drag and root mean square (RMS) of lift are given in figure 8. As noted in the previous section, lift was one order of magnitude lower in case 1 than in case 0. Therefore, to ensure a better visualisation of its behaviour, the RMS of lift coefficient was multiplied by 25 in figure 8b. In agreement with and complementing the time histories of figure 5 for other angles of attack, figure 8a shows that the mean drag acting on the entire system was generally weakly influenced by changes in α.

Contrarily, however, the resulting RMS of lift of case 0 was affected monotonically by the angle of attack, as demonstrated by figure 8b. Furthermore, the figure reveals that the greater the rotation speeds were (as given by higher ζ), the greater were the inclinations of the curves $\hat{C}_L$ vs α, as exposed by table 2.

For case 1, the $\hat{C}_L$-curves of figure 8b behaved in a parabolic-like fashion, achieving greatest value at $\alpha = 10°$, except for $\zeta = 2.5$, where highest values were concentrated at the extremes $\alpha = 0°$ and $\alpha = 22.5°$. Nonetheless, for this level of rotational speeds this different pattern cannot

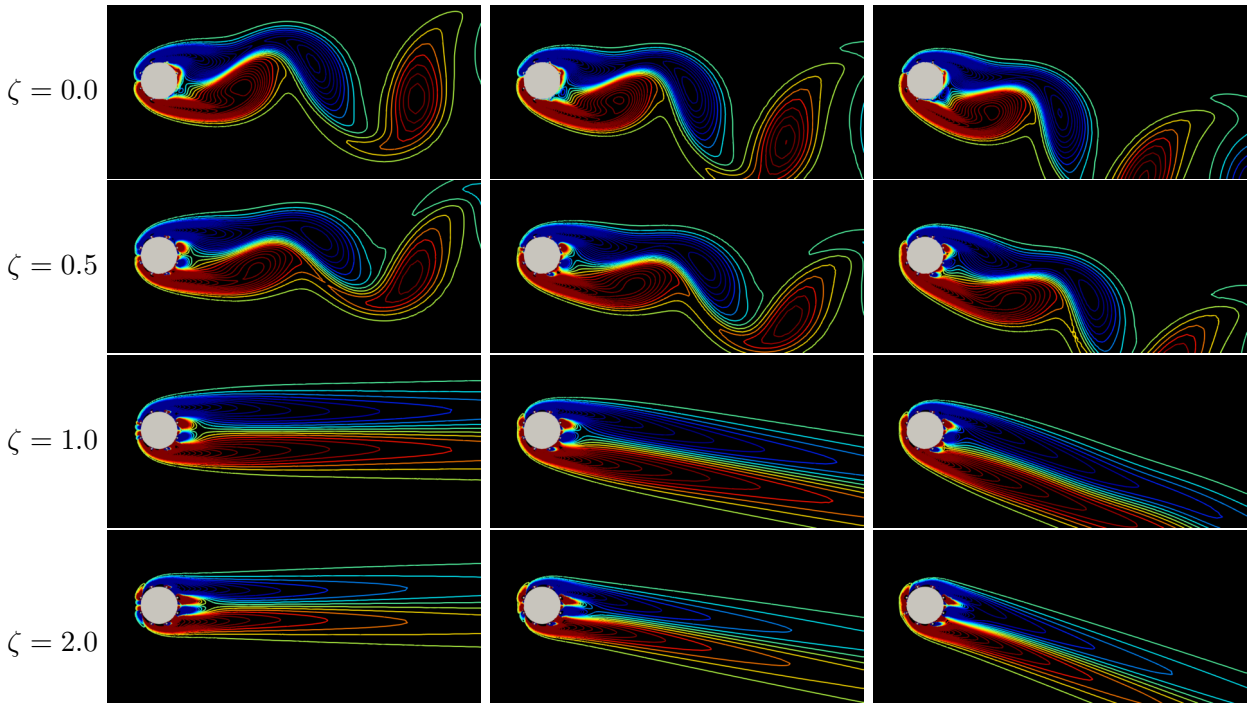

(a) Case 0.

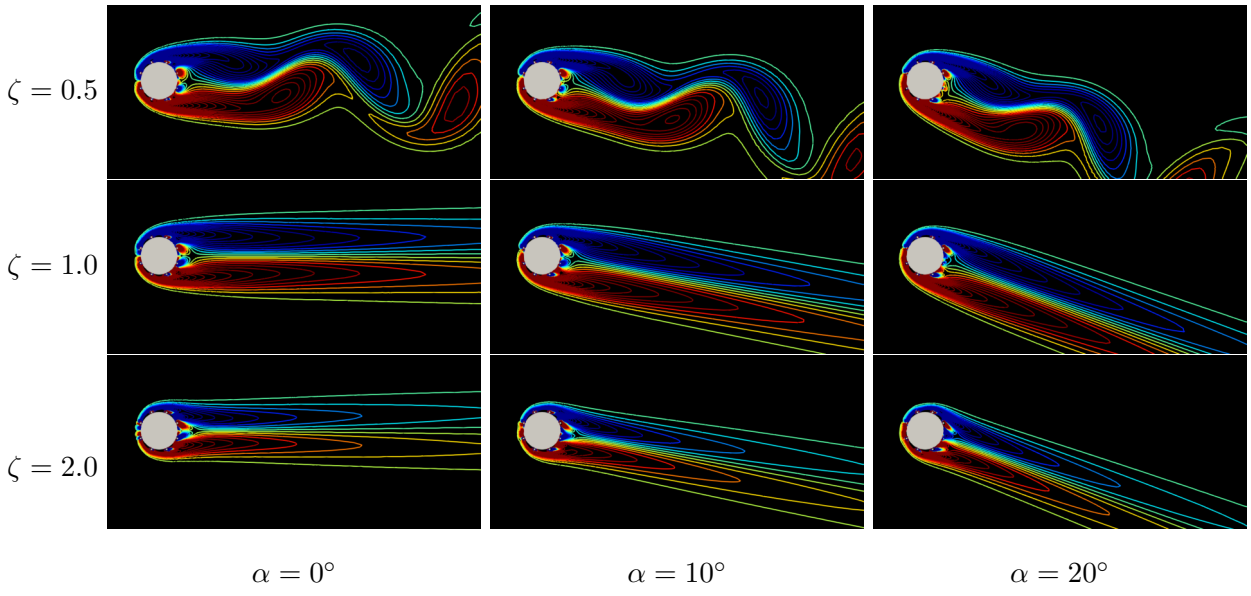

(b) Case 1.

Figure 6: Vorticity contours for different arrangements of rotation speed (ζ) and angle of attack (α).

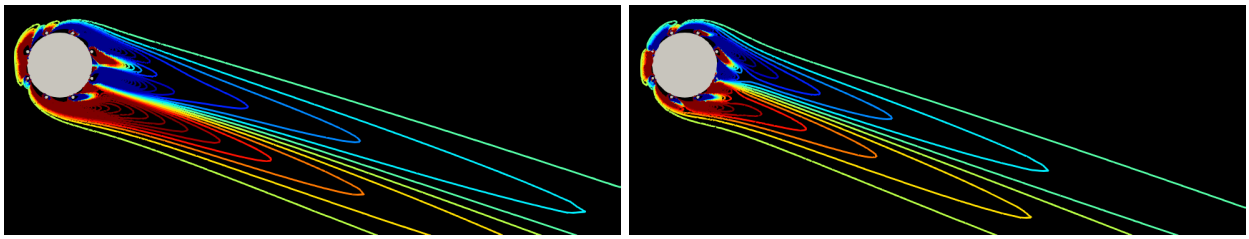

Figure 7: Vorticity contours of cases 0 and 1 for $\zeta = 2.5$. An imbalance was produced between negative (blue) and positive (red) contours of z-vorticity in case 0 that was not present in case 1.

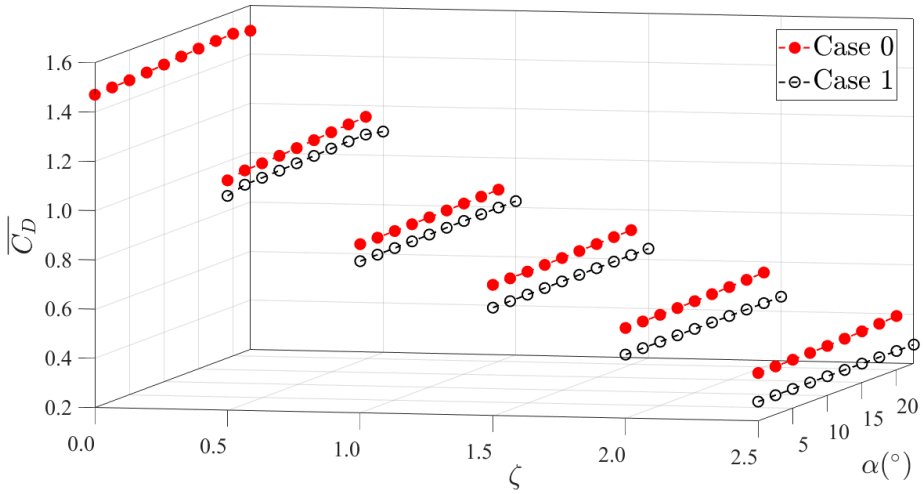

(a) Mean drag coefficient ($\overline{C_D}$).

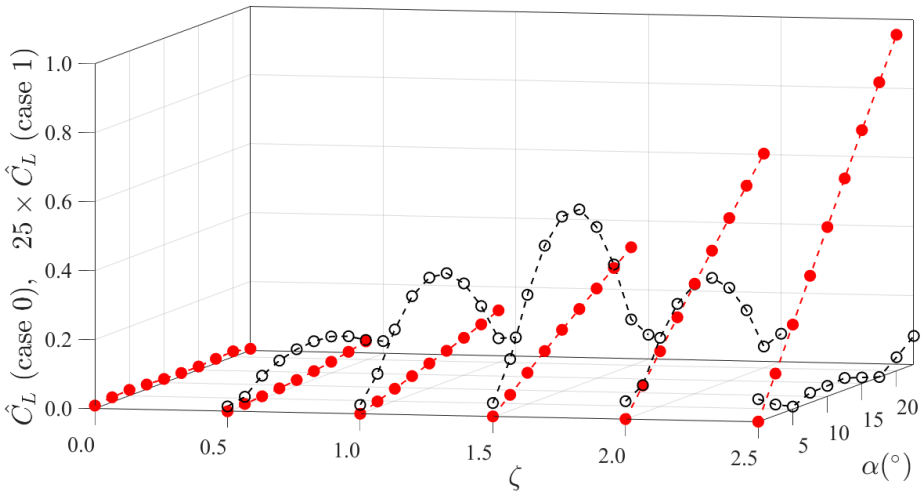

(b) RMS of lift coefficient ($\hat{C}_L$).

Figure 8: Hydrodynamic forces acting on the entire system for cases 0 and 1.

Table 2: Inclination of $\hat{C}_L$ relative to α for different ζ.

ζ	$\tan^{-1}(\hat{C}_L/\alpha)$
0.0	-0.0097
0.5	0.14
1.0	0.38
1.5	0.87
2.0	1.6
2.5	2.5

be considered to be physically meaningful, because the lift is negligible (despite the fact that the lift of this plot was multiplied by 25).

In order to discern whether the aforementioned directional effect stemmed from the entire system, collectively from the rods or from the main body, figures 9a and 9b decompose the mean drag and the mean lift for each of these structures.

In both cases, the previous claim regarding the lack of sensitiveness of the mean drag relative to the angle of attack is supported by figure 9a. For the mean lift, it becomes clear from figure 9b that the rods were generally oblivious to the angle of attack for small ζ in case 0. This behaviour differed as ζ adopted greater values. While in case 0, for a fixed ζ, the curves of $\overline{C_L}$ formed a straight line, in case 1 these curves resembled a parabolic shape.

For the entire system and for the main body of case 0 a steep decrease occurred in the mean lift toward more negative values as α increased. Furthermore, there was a difference in slope between the $\overline{C_L}$-curve for the entire system and for the main body. Generally, $\overline{C_L}$ reduced faster for the entire system compared with that for the main body, justified by the presence of the rods. Therefore, because the rods were progressively affected at higher ζ by the angle of attack, their presence led to a strongly directional system in case 0.

In addition, figure 9 showcases the fact that the root of the non-directional behaviour of case 1 was directly related to the way that the rods' speed were determined, highlighted by figure 10. By adapting the rotation speed according to the potential flow for different angles rendered the system essentially omnidirectional. Furthermore, the system was "more omnidirectional" the greater was the value of ζ in case 1, translated into a flattening effect upon the $\overline{C_L}$-curves observable in figure 11.

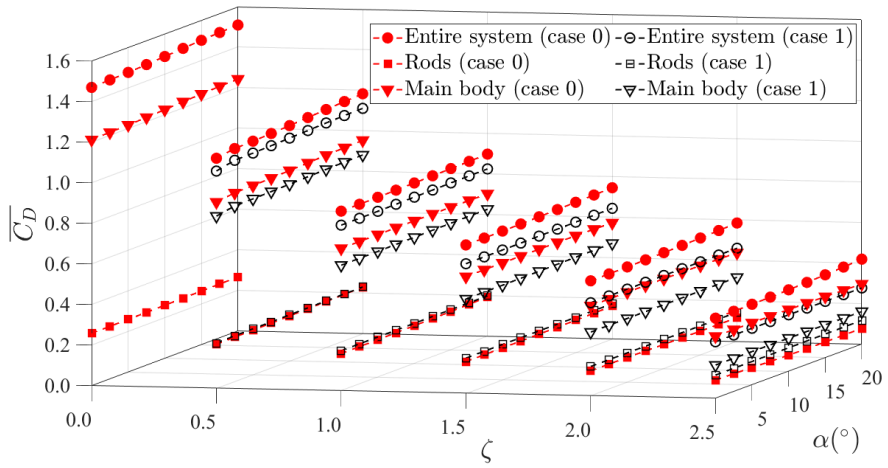

(a) Mean drag coefficient ($\overline{C_D}$).

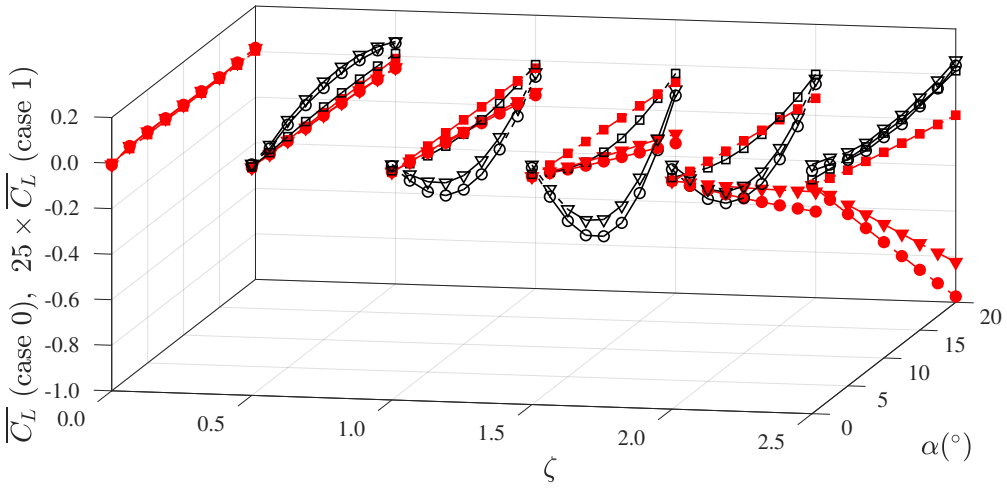

(b) Mean lift coefficient ($\overline{C_L}$).

Figure 9: Mean hydrodynamic forces acting on the main body, on the rods and on the entire system for cases 0 and 1.

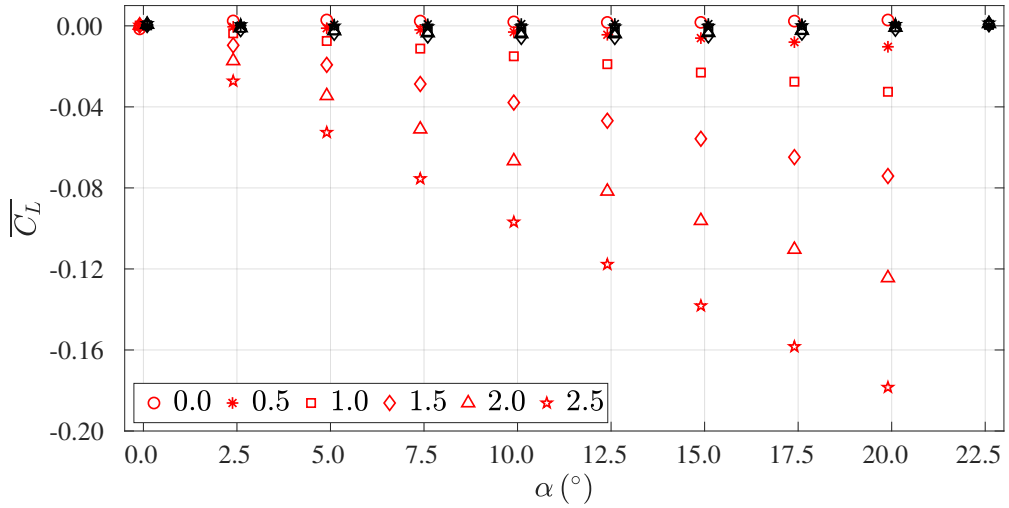

Figure 10: Resultant lift $\overline{C_L}$ from the collective effect of the rods of cases 0 (black) and 1 (red). Strikingly different behaviours justify the omnidirectional quality of each system.

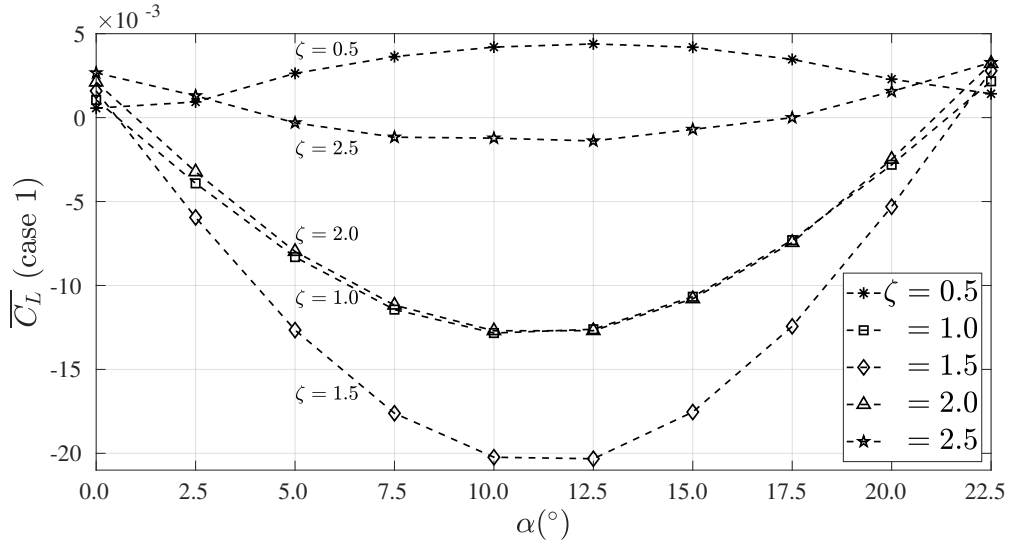

Figure 11: A flattening effect on the curves of the mean lift distribution $\overline{C_L}$ with α on the entire system of case 1 indicates a tendency where the angle of attack α became less important with growing rotation speeds. At any rate, the lift upon the entire system was rather negligible, of the order of 10^{-3}.

The opposite tendency was followed by case 0, proving that to impose a uniform rotation speed to all rods gave rise to an imbalance of lift that was not mitigated by feeding the entire system with a larger amount of kinetic energy. Rather, to diminish or eliminate hydrodynamic loads, each rod's rotation is expected to be weighted properly within the entire setup, to contribute significantly according to the angle of attack of the incoming flow, and depending on its relative position with respect to the boundary layer and to the wake.

3.5. Loads applied on the rods

Figures 12 and 13 present the mean drag and the mean lift acting on each rod for a subset of the α-values investigated in this work. For each of these values, different markers were assigned to convey the effect of the rotation speeds through ζ. The reference configuration of $\alpha = 0°$ was inserted on top of the respective figures.

In terms of mean drag, figure 12a shows that case 0 remained broadly similar to its reference case of figure 12 with 0° with the increase in rotation speeds, with bias toward the lower rods (for negative θ, see figure 4) which were weighted with greater loads. Amongst these rods, P_2' showed the greatest decrease toward a zero value, although this rod was not within the most representative of the system. Upper rods ($\theta > 0$) P_1 and P_4 were subjected to generally lower loads as the incoming flow arrived to the system at higher slope α. Conversely, P_2 developed greater absolute values; while the mean drag on P_3 progressively collapsed to a single value of approximately 0.07 regardless of ζ, pointing to an independence of this parameter at sufficiently high α. Due to these changes – in particular due to those of P_1', P_1 and P_2, which became all negative with increasing ζ at any of these angles of attack – case 0 was able to partially counteract the otherwise produced pressure drag.

Now we turn to the analysis of the mean drag upon the rods of case 1, figure 12b, where the difference of the general tendencies of the dashed lines with respect to the $\alpha = 0°$ case is strikingly evident. For $\alpha > 0$, the loads on P_1, P_3, P_2' and P_4' presented a steady tendency of collapsing to a single value, as it can be perceived from left to right of figure 12b. This set of rods at $\alpha = 20°$ behaved rather symmetrically, with symmetrical pairs given by (P_1, P_4') and (P_3, P_2'), that come from the definition of the potential-flow velocities, which is clearly different from the reference case. As a matter of fact, taking into consideration $\alpha = 20°$ of figure 12b, for $-112.5° < \theta < 112.5°$, the plot is mirrored about 22.5°. Furthermore, the overall mean drag on the system was essentially

attenuated by P_2 and P_1'.

In terms of mean lift applied to individual rods, only slight differences were observed between cases 0 and 1 as seen in figure 13, when compared to the same analysis for the mean drag, and did not stray away from the reference of $\alpha = 0°$ of each respective case (see figure 13). Figures 13a and 13b resemble one another in the following features: i) the load applied to P_1 zeroed as the angle of attack grew, ii) the loads on P_2 and P_3' reduced in magnitude, while those on P_3, P_4 and P_2' amounted to higher levels; iii) the force applied to P_1' grew much faster for higher α (indeed, for $\alpha = 5°$, changes in ζ did not alter significantly the load applied to P_1'), while that on P_4' became insensitive to rotation. The difference between the two cases lied essentially in the greater magnitude of the loads in case 1 against case 0.

As aforementioned, case 1 was able to completely eliminate the mean lift, even at the higher angles of attack of the present analysis. Adversely, case 0 revealed a much "less omnidirectional" quality. As far as lift was concerned, the nuance in these different behaviours allude to the fact that for case 1 there was a rapid increase in this load component exerted on P_3; concomitantly, this configuration reduced the mean lift on P_2. For case 0 this sequence of events occurred for more advanced values of α. The load on P_3 only surpassed that on P_2 for case 0 at $\alpha = 20°$, while for case 1 this occurred at $\alpha = 10°$, as disclosed by figure 13a. Another supporting aspect is that the contributions to the mean lift of the rods for $\theta < 0$ showed lower magnitudes compared with those for $\theta > 0$. Thus, on average, the system of case 1 employed an upward force that counteracted that promoted by the incoming flow, directed downward. This last point is further explored in section 3.7.

3.6. Hydrodynamic coefficients applied on the cylinders and on the entire set

Figure 14 qualitatively exhibits the resultant force applied on each cylinder (coloured) and on the entire system (in greyscale) at different angles of attack of the incoming flow (with direction pointed by the dark blue vector on the left, emphasised by the dashed line). Figure 14a exemplifies the reference case of $\alpha = 0°$. For clarity, the loads applied to the rods located at $y < 0$ were omitted.

The sequence of figures of case 0 singles out that, although the collective contribution from the rods was virtually insensitive to the incoming flow at low angles of attack (as supported by the previous section), each rod was acted upon by resultant forces that were indeed influenced by ζ at

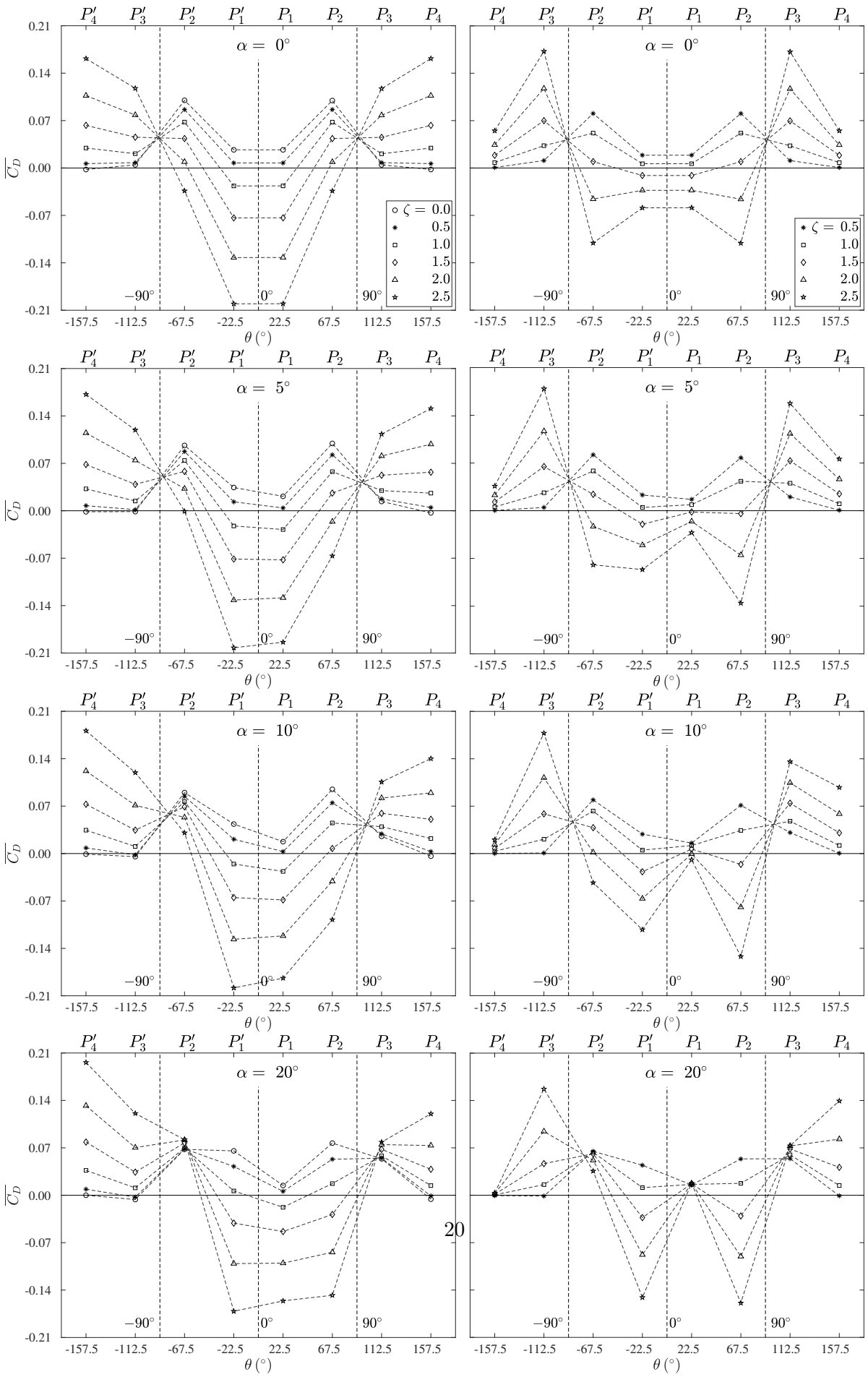

(a) $C_{cyl} = 0$ (b) $C_{cyl} = 1$

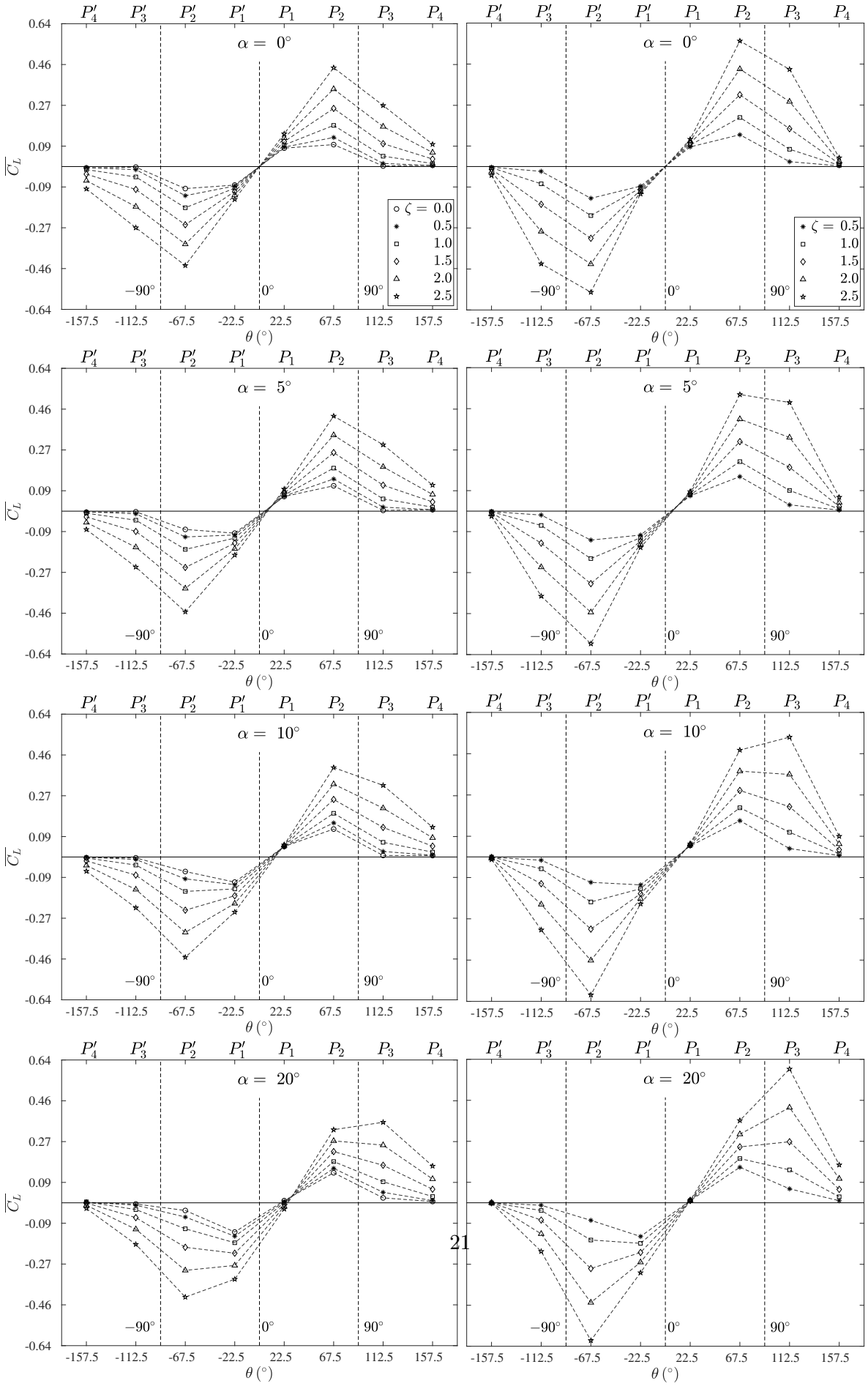

(a) Case 0 (b) Case 1

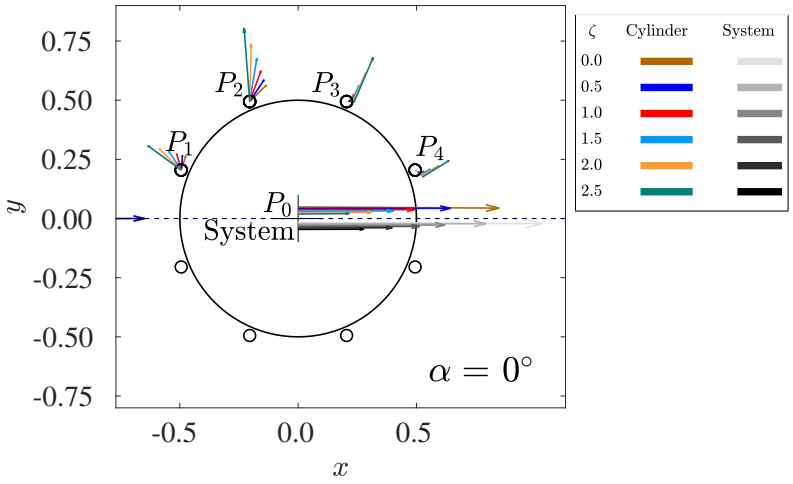

(a) Reference case ($\alpha = 0°$).

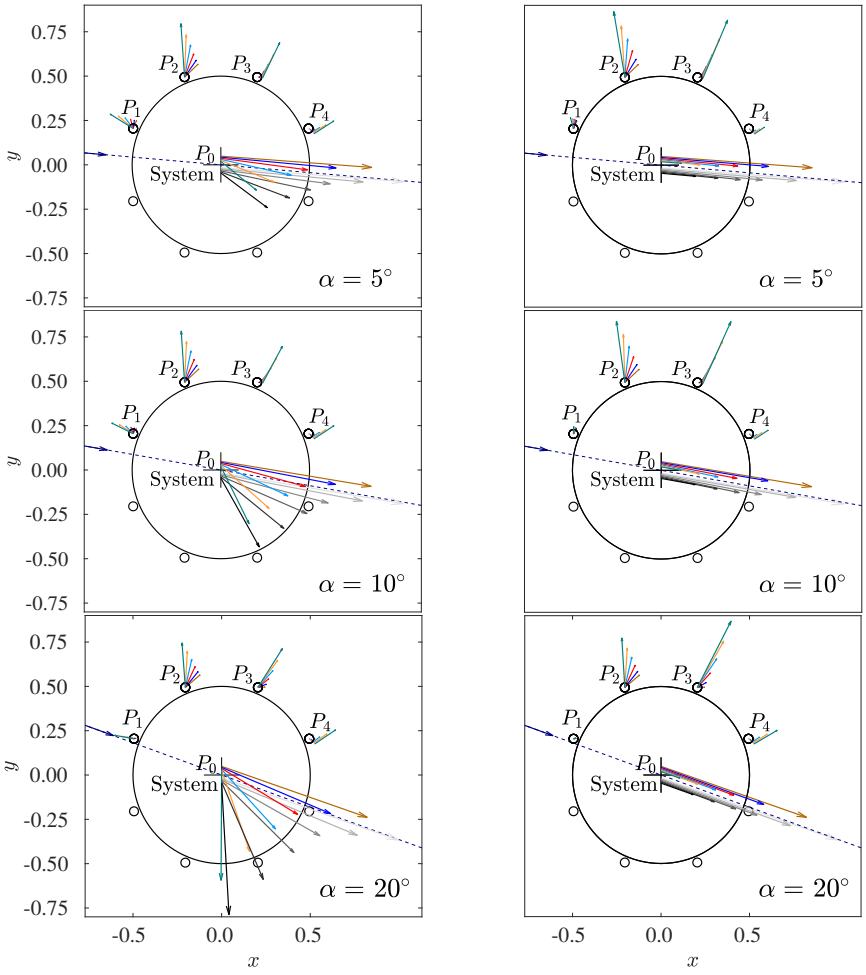

(b) Case 0.

(c) Case 1.

Figure 14: Loads acting on each cylinder (coloured) and on the entire system (greyscale). The incoming flow is represented by the dashed line and the respective vector. The resultant force applied to the main cylinder was slightly moved from the centre of the body, to avoid confusion with that acting on the entire system.

sufficiently high α. Overall, in both cases the forces acting on the rods P_2 and P_4 changed little in direction and magnitude with α; oppositely, the loads applied on P_1 and P_3 were remarkably altered with α.

We first consider the change of the loads with respect to α for cases 0 and 1. For P_1 it is notable that with higher α the resultant forces became smaller and their directions were modified gradually until $\alpha = 20°$, when the forces for each ζ aligned approximately in the same direction as that of $\zeta = 2.5$, except for the loads corresponding to $\zeta = 0.0$ and 0.5. In general, for this angle of attack the loads on P_1 diminished to an almost imperceptible size for different ζ. For P_3 the contrary pattern was followed. For a fixed ζ, as α varied, so did the direction of the load applied to this rod. Collectively, the loads organisation went from a parallel alignment at different ζ when $\alpha = 0°$ to evidently diverging directions when $\alpha = 20°$.

Now we investigate the effect of ζ upon the resulting loads. Taking into consideration the orientation of the resultant force with ζ (for fixed α) of figures 14b and 14c, it can be perceived that with greater angular speeds, the load upon P_1 inverted in the x-direction. With the inversion of its x-component, the load on P_1 started to counteract part of the pressure drag that resulted upon the system due to its obstruction to the incoming flow. Analogously, P_3 opposed the otherwise downward lift as it produced an increasing upward load. For sufficiently large α, it also became evident that the load on P_3 gradually oriented further away from the positive x-direction with the increase in ζ, leaving a more horizontal configuration toward a steeper one. A shift in its x-component did not occur as it happened for P_1 for this range of ζ. Nevertheless, this gradual change in orientation might call attention for increasingly higher speeds, as it may be lead to propulsion of the entire system akin to that investigated by Silva-Ortega and Assi (2017a).

It may be noted from figure 14a that most of the loads were concentrated in magnitude on P_2 and P_3, a tendency that persisted for and became more evident with larger α in cases 0 and 1.

In spite of the commonalities, discrepancies can be noted between cases 0 and 1. The omnidirectional property of case 1 stands out in figure 14c compared with case 0 of figure 14b. Indeed, case 0 was prone to significant lift production as α departed from null value, that is, from its most symmetrical setup relative to the incoming flow. This feature led the two cases to an astounding distinction: Even though both cases reduced drag, only case 1 was capable of eliminating lift. This can be inferred from these qualitative figure. Primarily due to the much larger loads supported by

P_2 and P_3, the resulting forces applied on the entire system in case 1 were well aligned with the dashed line representative of the incoming flow, in clear contrast with case 0. It is worth noting, of course, that case 1 also reduced drag beyond case 0.

3.7. Resultant forces

The previous analysis is now complemented with quantitative results. Figure 15 exhibits the resultant force acting on each rod for both setups herein analysed, for an economical number of plots. Nevertheless, the tendency that is described below was observed for the entire range of α exhibited in section 2. Each group of bars is associated with a pair of rods that were antisymmetrically placed relative to the incoming flow (and thus their rotations were of the same magnitude, given by potential-flow theory). Antisymmetry here is characterised by the rods whose centres were positioned at the same angle relative to the dashed line, e.g., the pairs P_1 and P_4', P_2 and P_3', etc., provided $\alpha > 0$.

From this figure, it can be detected that there was a gradual decrease in the load upon $P_1,\ P_4'$ as α adopted larger values, especially for the fastest rotation rates. As α reached 22.5° (omitted here for brevity), their velocities were set to null value, according to our potential-flow analogy, that led these rods back into a passive behaviour. In this setup, these rods bore virtually negligible loads. The same pattern occurred for rods $P_2,\ P_3'$ although these rods were kept active throughout the different angles of attack. Oppositely, the pairs $P_3,\ P_2'$ and $P_4,\ P_1'$ followed an upward tendency of the resultant forces. Essentially, these two pairs offset the contribution from the former pairs, that decreased.

Cases 0 and 1 essentially followed the same tendency. The difference was concentrated on the adaptability of the system in interacting with the incoming flow. Changes in case 1 advanced much faster, in terms of α, than in case 0.

3.8. Power-loss

It is well known from the work of Korkischko and Meneghini (2012) that increasing the speeds of the rods indefinitely promotes reduction in the mean drag and lift for $\alpha = 0°$. From the paper of Shukla and Arakeri (2013) one can analyse an active system, such as the present, from the point of view of power expended to mitigate the mean drag $\overline{C_D}$ and to counteract the mean shear $\overline{C_D}$

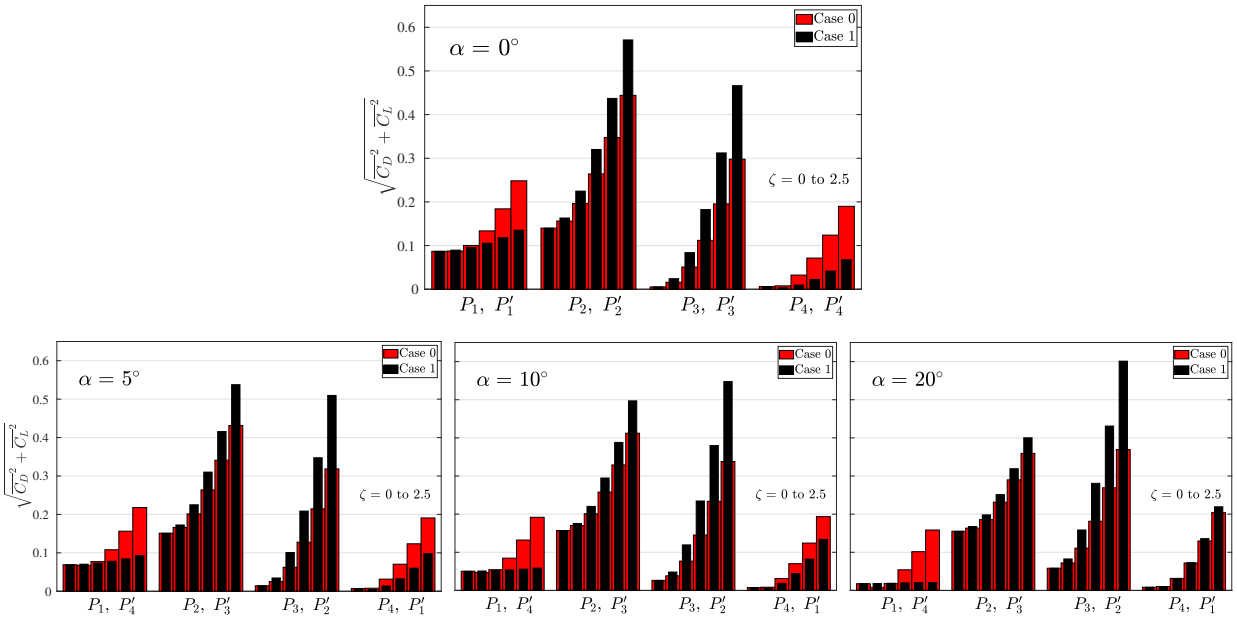

Figure 15: Resultant loads on the rods for different angles of attack. Groups of bars associated to each rod correspond to ζ varying from 0.0 to 2.5 in steps of 0.5. The indicated pairs of rods for each group of bars have symmetrical ($\alpha = 0°$) or antisymmetrical loads ($\alpha \neq 0°$) with equal magnitude.

as the rods rotated about their respective axes, with the following expression

$$\overline{C_{PL}} = \overline{C_N} + \overline{C_D} \tag{4}$$

written in time-averaged form (the bar placed over the variables indicates mean values). With this relationship, the system of cases 0 and 1 can be compared through figure 16. As the figure displays, to subject the entire system to different angles of attack did not output significant difference in power-loss coefficients. Indeed, this result is supported by two considerations: i) the major part of $\overline{C_{PL}}$ at low rotation rates (low C_N) is derived from the mean pressure drag, in particular, that from the main body, which was not strongly affected by the angle of attack of the incoming flow (but rather by pressure difference fore and aft the body) and ii) as ζ increased, from the results of Assi et al. (2019) and Carvalho et al. (2021) it is known that $\overline{C_D}$ becomes less relevant compared with the power required to spin the rods against viscous traction, i.e., $\overline{C_N}$. Neither of these two considerations depend on the angle of the incoming flow, thus they justify that in terms of power consumption, α did not impart significant changes to $\overline{C_{PL}}$, $\overline{C_N}$ or $\overline{C_D}$ as figure 16 confirms.

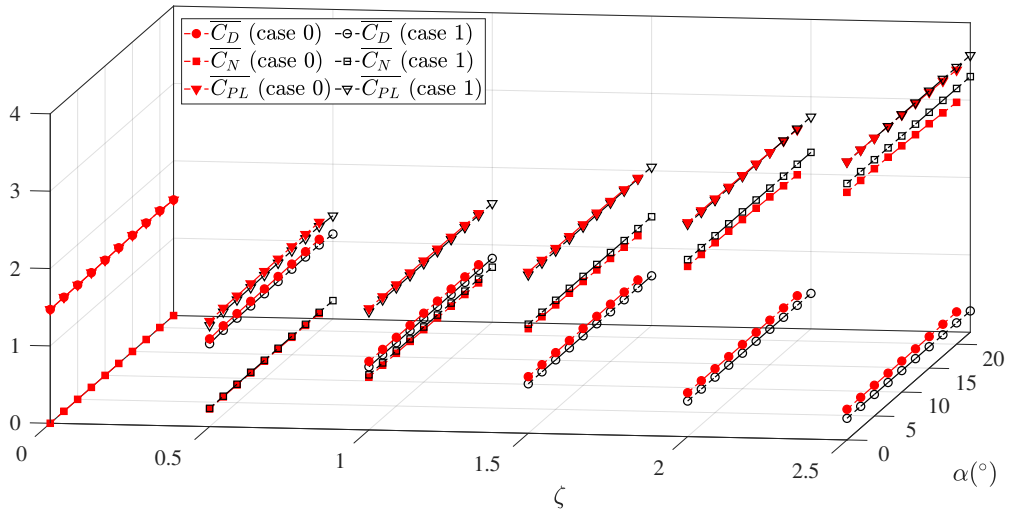

Figure 16: Total mean power-loss coefficients ($\overline{C_{PL}}$) and its components, mean drag ($\overline{C_D}$) and mean shear ($\overline{C_N}$) coefficients.

4. Conclusion

We have investigated whether a system comprised of eight peripheral rotating rods fitted around a main cylinder was capable of reducing hydrodynamic loads and vortex shedding. The system was subjected to different incidence angles of the incoming flow; and the control mechanism functioned with progressively larger levels of actuation. In the active mechanism the wake-control rods were activated to rotate about their own axis. Our comparison involved two angular speed configurations: one in which all rods spun with the same angular velocity (case 0), and another, where their velocities were inspired by the potential-flow field around a bare cylinder (case 1).

Wake topology visualisation through vorticity contours rendered strongly evident that both systems eliminated vortex shedding and reduced wake width. In order to do so, either one of the following conditions were required: 1) appropriate configurations of angle of attack α of the incoming flow together with sufficiently high angular velocities ω_n, represented by $\zeta\omega_n$ were required (ζ ranged from 0 to 2.5 in steps of 0.5 and calibrated the velocities) or 2) to increase $\zeta\omega_n$ indefinitely also caused the Kármán street to completely vanish. These results complement previous analyses that were made exclusively for $\alpha = 0^\circ$ by Assi et al. (2019); Carvalho et al. (2021); Carvalho and Assi (2022a) and further references within these works.

Another common result is the reduction of the mean drag with increasing ζ. Indeed, as the rods spun faster, they injected momentum into the boundary layer and delayed separation, promoting

a smaller region of low pressure aft the system, independently of the angle of attack α. Also, for both cases, the presence of the rods led to mean drag upon the main body lower than that of a plain cylinder under any value of ζ. Investigation of the power consumption, based on the work of Shukla and Arakeri (2013), demonstrated that the power loss coefficient did not to depend on α. The analysis of the hydrodynamic loads upon the rods showed that the inversion of the direction of the loads upon specific rods was fundamental to mitigate mean drag and mean lift.

Aside from these similarities, the two systems produced completely different mean lift. In case 0 the system presented strong directionality and failed to mitigate lift, especially at large angles of attack. In fact, for this system, lift increased monotonically with α. Discrepancy in the number of the vorticity contours of the positive and negative-oriented regions highlighted the imbalance that led to the net lift upon the entire system. Our analysis revealed, in particular, that the non-null lift stemmed from the rods' contributions.

In case 1 the system showed an omnidirectional property: Independently of the angle of attack, case 1 was capable of reducing mean drag and eliminating mean lift. In contrast to case 0, vorticity contours exhibited asymmetry between negative and positive-oriented regions with equal number of contours. Consequently, RMS of lift of case 1 was one order of magnitude lower than in case 0 and vanished more quickly. Furthermore, curves $\overline{C_L} \times \alpha$ followed a tendency of flattening with ζ. Thus, case 1 configuration behaved ever "more omnidirectionally" with faster angular speeds. We have also discerned that the lift of case 0 was not eliminated by feeding the entire system with more actuating power. Rather, it is essential to weight different rods with different velocities in order to achieve this goal.

In practical terms, perhaps anticipating a possible technological application, the present investigation showed that a bluff body surround by 8 rotating rods (45° apart) is capable of mitigating vortex shedding and reduce steady forces by adjusting the rotation speeds of the individual rods in relation to the incoming flow direction. The speed-control approach inspired by the potential-flow velocity field proved to be good enough to achieve wake control. In this sense, the system was shown to be omnidirectional, at least for the current range of Reynolds number. Future research should concentrate on speed optimisation targeting minimum power, drag reduction or even generation of a useful lift force and expand this analysis to higher Reynolds numbers.

Acknowledgments

IAC is grateful to CAPES Brazilian Ministry of Education for his PhD scholarship and to the National Laboratory for Scientific Computing (LNCC/MCTI, Brazil) for providing HPC resources of the SDumont supercomputer. GRSA acknowledges the support of FAPESP, Brazil (2011/00205-6) and CNPq, Brazil (306146/2019-3). We gratefully acknowledge the support of the RCGI Research Centre for Greenhouse Gas Innovation, hosted by the University of São Paulo, Brazil and sponsored by FAPESP (2020/15230-5) and Shell Brasil.

References

Assi, G.R., Bearman, P., Kitney, N., 2009. Low drag solutions for suppressing vortex-induced vibration of circular cylinders. Journal of Fluids and Structures 25, 666–675.

Assi, G.R., Bearman, P.W., Tognarelli, M.A., 2014. On the stability of a free-to-rotate short-tail fairing and a splitter plate as suppressors of vortex-induced vibration. Ocean engineering 92, 234–244.

Assi, G.R.S., Orselli, R.M., Silva-Ortega, M., 2018. Suppression of vortex shedding with rotating wake-control cylinders: Numerical investigation at a moderate reynolds number, in: International Conference on Offshore Mechanics and Arctic Engineering, American Society of Mechanical Engineers. p. V002T08A060.

Assi, G.R.S., Orselli, R.M., Silva-Ortega, M., 2019. Control of vortex shedding from a circular cylinder surrounded by eight rotating wake-control cylinders at Re= 100. Journal of Fluids and Structures 89, 13–24.

Blevins, R.D., 1990. Flow-induced vibration. 2 ed., Van Nostrand Reinhold, New York.

Carvalho, I.A., Assi, G.R.S., 2022a. Enhanced control of the turbulent flow past a circular cylinder with rotating rods inspired by an inviscid solution. Journal of Fluids and Structures 113, 103652.

Carvalho, I.A., Assi, G.R.S., 2022b. Passive control of vortex shedding past finite cylinders under the effect of a free surface. Physics of Fluids 35, 015109.

Carvalho, I.A., Assi, G.R.S., 2023. Active control of vortex shedding past finite cylinders under the effect of a free surface. Accepted for publication by Physics of Fluids .

Carvalho, I.A., Assi, G.R.S., Orselli, R.M., 2021. Wake control of a circular cylinder with rotating rods: Numerical simulations for inviscid and viscous flows. Journal of Fluids and Structures 106, 103385.

Choi, H., Jeon, W.P., Kim, J., 2008. Control of flow over a bluff body. Annu. Rev. Fluid Mech. 40, 113–139.

Cicolin, M.M., Buxton, O.R.H., Assi, G.R.S., Bearman, P.W., 2021. The role of separation on the forces acting on a circular cylinder with a control rod. Journal of Fluid Mechanics 915.

Ferziger, J.H., Perić, M., Street, R.L., 2002. Computational methods for fluid dynamics. volume 3. Springer.

Gerrard, J.H., 1966. The mechanics of the formation region of vortices behind bluff bodies. Journal of fluid mechanics 25, 401–413.

Korkischko, I., Meneghini, J., 2012. Suppression of vortex-induced vibration using moving surface boundary-layer control. Journal of Fluids and Structures 34, 259–270.

Korkischko, I., Meneghini, J.R., 2011. Volumetric reconstruction of the mean flow around circular cylinders fitted with strakes. Experiments in fluids 51, 1109–1122.

Mittal, S., 2001. Control of flow past bluff bodies using rotating control cylinders. Journal of fluids and structures 15, 291–326.

Norberg, C., 2001. Flow around a circular cylinder: aspects of fluctuating lift. Journal of fluids and structures 15, 459–469.

Patankar, S.V., 1980. Numerical heat transfer and fluid flow.

Patino, G.A., Gioria, R.S., Meneghini, J.R., 2017. Evaluating the control of a cylinder wake by the method of sensitivity analysis. Physics of Fluids 29, 044103. doi:10.1063/1.4979482, arXiv:https://doi.org/10.1063/1.4979482.

Shukla, R.K., Arakeri, J.H., 2013. Minimum power consumption for drag reduction on a circular cylinder by tangential surface motion. Journal of Fluid Mechanics 715, 597–641. doi:10.1017/jfm.2012.537.

Silva-Ortega, M., Assi, G., 2017a. Suppression of the vortex-induced vibration of a circular cylinder surrounded by eight rotating wake-control cylinders. Journal of Fluids and Structures 74, 401 – 412.

Silva-Ortega, M., Assi, G.R.S., 2017b. Flow-induced vibration of a circular cylinder surrounded by two, four and eight wake-control cylinders. Experimental Thermal and Fluid Science 85, 354 – 362.

Strykowski, P.J., Sreenivasan, K.R., 1990. On the formation and suppression of vortex shedding at low reynolds numbers. Journal of Fluid Mechanics 218, 71–107.

Vakil, A., Green, S.I., 2009. Drag and lift coefficients of inclined finite circular cylinders at moderate reynolds numbers. Computers & Fluids 38, 1771–1781.

Von Kármán, T., 1954. Aerodynamics: selected topics in the light of their historical development. Cornell University Press.

Williamson, C.H.K., Govardhan, R., 2004. Vortex-induced vibrations. Annu. Rev. Fluid Mech. 36, 413–455.

Zdravkovich, M.M., 1981. Review and classification of various aerodynamic and hydrodynamic means for suppressing vortex shedding. Journal of Wind Engineering and Industrial Aerodynamics 7, 145–189.

On the omnidirectionality of a system with eight spinning rods in controlling the wake of a circular cylinder in a turbulent regime

I. A. Carvalho[a,*], G. R. S. Assi[b]

[a]*Department of Mechanical Engineering, EPUSP, University of São Paulo, SP, 05508-030, Brazil*
[b]*Department of Naval Arch. & Ocean Engineering, EPUSP, University of São Paulo, SP, 05508-030, Brazil*

Abstract

We numerically investigate the attribute of omnidirectionality of the flow-control system comprised of a large circular cylinder equipped with eight spinning rods of smaller diameter, subjected to an incoming flow that adopts different angles of attack. Detached-eddy simulations are employed to compute hydrodynamic loads and to provide flow topology at the Reynolds number of 1000. Two cases are assessed regarding the rods' angular velocities: case 0 - all rods spin with the same angular velocity; and case 1 - with velocities inspired by potential flow around a plain cylinder (without rods) as in Carvalho et al. (2021). The two systems have in common the same input kinetic energy; and velocities are increased proportionally to assess the system response. Both cases succeed in reducing mean drag. However, while case 1 proved to become ever "more omnidirectional" with increasing angular velocities, case 0 demonstrated to be prone to the angle of attack as it was unable to suppress vortex shedding for sufficiently large slopes of the incoming flow or reduce hydrodynamic forces, even at the fastest-spinning configurations. We verify that lift is utterly mitigated in case 1, in contrast to case 0. Even at steady conditions of the flow, the latter produces asymmetric recirculation regions aft the system that drive a pressure imbalance. Reasons for the different outcomes of the two systems are explored, and it is revealed that the omnidirectionality of case 1 is intrinsically related to the emphasis imposed on rotation rates of a shorter set of the eight rods.

Keywords: Vortex-shedding suppression, wake control, drag reduction, bluff body, omnidirectionalityG.

*Corresponding author: amorim.icaro@usp.br (I. A. Carvalho)

1. Introduction

Flow-induced vibration of cylindrical structures is a well-known phenomenon in engineering, especially in the offshore industry, where bluff hulls are used in monocolumn platforms dedicated to ultra-deep water oil exploration and generation of renewable energy. When the incoming flow reaches and is obstructed by these structures, boundary-layer separation occurs at a angle from the frontal stagnation region that depends on the flow regime, i.e., on the dynamic viscosity of the fluid ν, velocity of the incoming flow U_∞ and the characteristic dimension of the body D (that may be the diameter in the case of cylinders). Together, these variables can be collapsed into a single representative nondimensional, the Reynolds number $Re = U_\infty D/\nu$.

It is well known that as early as for $Re \approx 45$ the region past a cylinder becomes unstable. Once this happens, an alternating imbalance in pressure distribution is caused past the body and vortices of opposite orientation are emanated alternatively leeway. When this phenomenon takes place it may trigger vortex-induced vibration (VIV) – a vibrational motion of the structure, especially intense in the transverse direction, that may lead to fatigue and failure, whereby one detaching vortex feeds back on the vorticity of the shear layers to grow and rolls upon itself until the other vortex cuts off its supply of vorticity (Gerrard, 1966). In the context of large offshore structures, these may be put into a low frequency motion, termed *vortex-induced motion* (VIM, Fujarra et al., 2012). When the detached vortex travels downstream, the other one grows and the cycle repeats, producing in the wake the coherent Kármán-Bénard vortex street. VIV is particularly intense when the frequency of vortex shedding nears and locks onto the natural frequency of the body. In such cases, the amplitude significantly increases (Williamson and Govardhan, 2004). With greater Re, transition successively takes place in the wake ($Re \gtrapprox 190$) and in the boundary layer ($Re \gtrapprox 3 \times 10^5$, Blevins, 1990).

Because the root of VIV is in vortex shedding, passive and active methods have been devised to exert some control on the onset of vortex shedding or in its utter elimination (Choi et al., 2008; Zdravkovich, 1981). In the passive context, common strategies involve surface protrusions, commonly exemplified by helical strakes along the cylinder to diminish VIV (Korkischko and Meneghini, 2011), attachment of free-to-rotate fairings to delay interaction between the vortices further downstream (and thus dissipate part of their vorticity in the viscosity of the fluid, Assi et al., 2009, 2014, 2022), or inclusion of secondary smaller bodies, such as slender rods, to prevent

the growth of flow instabilities (Patino et al., 2017). In the seminal paper of Strykowski and Sreenivasan (1990), a single rod was placed near the cylinder, and was apt to prevent vortex shedding. In spite of this advance in suppressing vortex shedding, this passive solution was only capable of handling low Re-regimes (Mittal, 2001). In order to enhance control over the flow and inspired by the Moving Surface Boundary-layer Control (MSBC), otherwise used for airfoils, to actively spin the rods has proven quite effective for cylindrical structures as well, in both laminar and turbulent regimes, justified by the injection of momentum into the adverse pressure gradient. Thus, this technique has allowed to thin the wake, delay vortex interaction with greater formation length and reduce hydrodynamic loads significantly (Assi et al., 2018), and beyond, to suppress the vortex wake entirely (Assi et al., 2019; Carvalho and Assi, 2022a).

Experimentally, Korkischko and Meneghini (2012) noted that the gap between the spinning element and the main body, the diameter of the rod, and the rotation rate were decisive parameters regarding the performance of such a suppressing device. Silva-Ortega and Assi (2017b) extended this technology to involve a greater number of control rods and assessed parametrically how this system affected response amplitude and fluctuating loads. Based on the best setup of this former study in VIV attenuation, Carvalho et al. (2021) and Carvalho and Assi (2022a) assessed the performance of this open-loop system with two arrangements of angular velocities, one in which all rods rotated at the same rate, and another, where rods farther from stagnation region spun faster, and noted that a more cost-effective solution for improving wake-control was related to giving different rods different velocities. The authors noted in this last study that as far as $Re = 1000$ the spinning rods were able to produce a vortex-free wake.

The effectiveness of this MSBC technology has been corroborated in multiple studies. Nonetheless, neither of these past studies have evaluated how the performance of such a system is affected by a different angle of attack, as noted in Silva-Ortega and Assi (2017a). More recently, Carvalho and Assi (2023b) studied the performance of this system with 8 fitted rods subjected to a laminar flow. In the present work we intend to extend the analysis, to incorporate turbulent effects that are commonplace in the offshore environment.

1.1. Objective

We investigate how the system comprised of a main larger body, fitted with eight slender wake-control rods, performs when acted upon by an incoming flow reaching the system from different

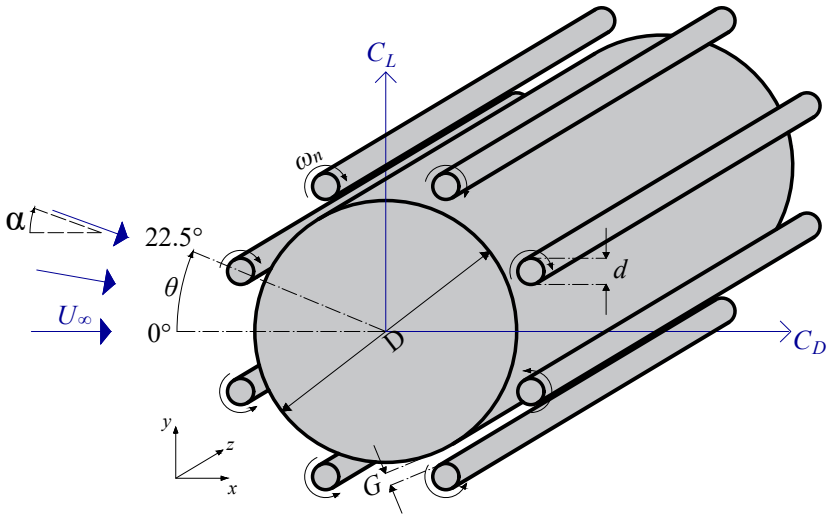

Figure 1: Flow past a system comprised by a main cylinder and rotating control rods under different angles of attack of the incoming flow. (The figure is not to scale for better visualization.)

angles of attack, ranging from 0° to 22.5° (see figure 1). In order to conduct this analysis, the fitted rods spin in two ways: one with uniform angular velocity, and another where their velocities are determined from potential-flow around a bare cylinder (see section 2). Hydrodynamic loads upon the entire system, the main body and all the rods collectively are assessed. The loads supported by each rod are also investigated to explain their individual relevance to the entire setup. Vorticity contours are assessed to explain the underlying physics of the problem and nuances between the cases and power considerations are uphold to assess the efficiency of the system. Moreover, we seek to investigate whether this device inspired by potential-flow velocities behaves omnidirectionally, that is, if this system is robust in its flow control when the angle of attack is modified.

2. Method

The present paper involves the geometry depicted by figure 1. Around the main larger body of diameter D, eight slender rods P_1, ..., P_4 (upper rods), P_1', ..., P_4' (lower rods), of diameter $d/D = 1/20$ are placed, distant from the wall of the main body by a gap $G/D = 1/100$. The rods are separated by an angle of 45°, offset from the frontal stagnation region by 22.5°, at locations $\theta_n = \pm 22.5° \pm (n-1)45°$, with $n = 1, \ldots, 4$ (positive and negative signs correspond to upper and lower rods, respectively). The incoming flow reaches the system with angles of attack α between 0 and 22.5° with velocity U_∞ and Reynolds number based on the main cylinder's diameter, given

by $Re = U_\infty D/\nu = 1000$.

The ratio G/D was selected based on the findings of Silva-Ortega and Assi (2017a), where it mitigated most the VIV response and drag. It is known, in general, that the nearer the rods are to the wall of the main body, the greater is their capacity of reattaching the boundary layer. The rods' diameters were based on Assi et al. (2019), since they allowed sufficient interaction with the shear layer of the main body, and yet, because their Reynolds number was $Re_d = U_\infty d/\nu = 50$, did not produce a vortex street that interfered with that of the main body. And the number of rods corresponded to that which allowed greatest VIV suppression in the parametric study of Silva-Ortega and Assi (2017c).

Two arrangements are considered, concerning the angular velocities ω_n of the rods:

Case 0: all rods spin with a single magnitude of rotation rate (upper rods spin clockwise and lower rods spin counterclockwise), and the same input kinetic energy of case 1 is employed here;

Case 1: the spinning rods rotate with the velocities provided by the potential flow around a bare cylinder (explained below).

The angle of attack α ranged from 0° to 20° in steps of 5° in case 0. In case 1, $\alpha = 22.5°$ was also addressed. A wider range of α would repeat the same results in case 1, because of the uniform distribution of the rods around the central body and the definition of angular velocities seen below.

2.1. Definition of angular velocities

For the definition of the angular velocities of case 1, we have considered the potential flow around a plain cylinder and computed the velocities at polar coordinates $(R, \theta) = (D/2 + G + d,\ \theta_n)$. Once the rods are considered in viscous flow, these computed velocities are then imposed to them. Note that the aforementioned polar coordinates (R, θ) correspond precisely to the location where the outer surface of the rods are located relative to the centre of the entire system, see figure 2 for the example of P_3'. Thus, the streamline velocities from potential flow are imposed in viscous flow to the setup involving the suppressing mechanism in the form of angular velocities. At each angle of attack α of the incoming flow relative to the system, the velocities of case 1 are adjusted following the same procedure, as illustrated by figure 3 for $\alpha = 0°$ and 22.5°. Further details of this potential-flow analogy are found in Carvalho and Assi (2022a).

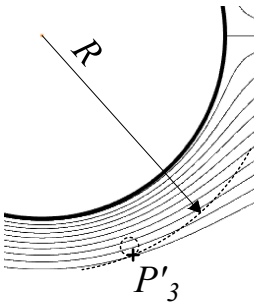

Figure 2: Velocities were obtained in potential flow at polar positions corresponding to the outer surface of the rods.

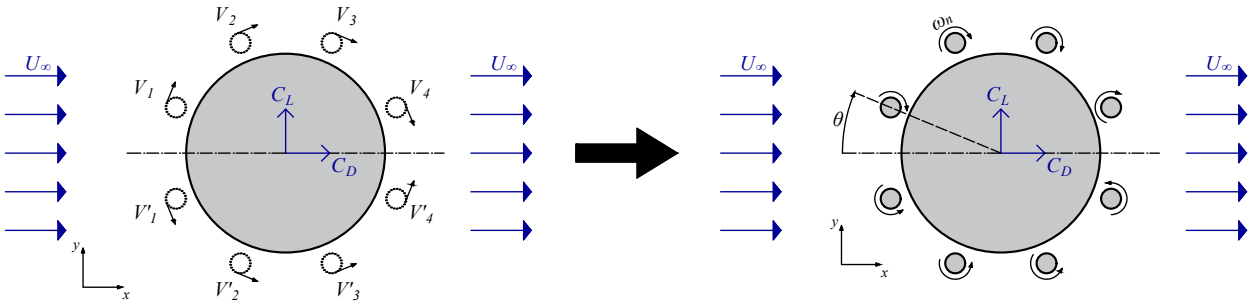

(a) $\alpha = 0°$.

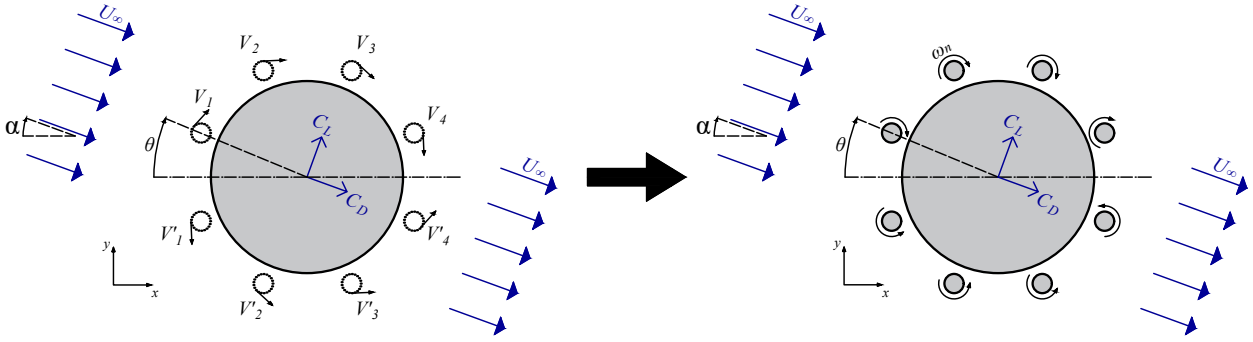

(b) $\alpha = 22.5°$.

Figure 3: Velocity vectors computed from the potential-flow field at points located in radial coordinates $R = D/2 + G + d/2$. $\theta = \pm 22.5° \pm (n-1)45°$, with $n = 1, \ldots, 4$ were assigned in case 1 as equivalent angular velocities for the rods.

For comparison, the system of case 0 is related to case 1 through equal input kinetic energy, expressed as:

$$\left[\sum \omega_n^2\right]_{\text{case 1}} = \left[8\omega_0^2\right]_{\text{case 0}} \tag{1}$$

A gain parameter $\zeta = 0.0,\ 0.5,\ 1.0,\ 1.5,\ 2.0,\ 2.5$ altered the rods' velocities, so that

$$\begin{aligned} \omega_n &\leftarrow \zeta\omega_n \\ \omega_0 &\leftarrow \zeta\omega_0 \end{aligned} \tag{2}$$

Surely, to impose $\zeta = 0.0$ renders the entire system passive (no input kinetic energy) and $\zeta = 1.0$ conveys specifically the velocities from potential flow to the rods of case 1.

2.2. Numerical scheme

Viscous, incompressible, flows of Newtonian fluids are described by the continuity and the Navier-Stokes equations, respectively given by equations 3 and 4 (Einstein's convention notation applies).

$$\frac{\partial U_j}{\partial x_j} = 0. \tag{3}$$

$$\rho\left(\frac{\partial U_i}{\partial t} + U_j\frac{\partial U_i}{\partial x_j}\right) = -\frac{\partial p}{\partial x_i} + \mu\frac{\partial^2 U_i}{\partial x_j \partial x_j}, \tag{4}$$

Numerical methods are required to solve these equations. One such means is to employ a finite volume discretisation of all terms and ensure properties of the flow into the interpolants. So the entire domain is discretised into cells that allow mass fluxes to be conserved in adjacent elements of the grid (Ferziger et al., 2002).

The discretisation of the entire domain into a structured grid of hexahedral elements is portrayed by figure 4. Because of the edges disposed radially from the system at all angles, this grid is commonly termed an "O-grid". Its advantage lies in the ease of performing the simulations with different angles of attack α of the incoming flow. The first subfigure represents the grid near the rod P_1, and highlights the cell dense gap region; the second figure brings the overall aspect of the mesh and cells growth away from the system; the third shows the spanwise aspect of the mesh (uniformly discretised) and the last one portrays the overall flow domain. The full domain measured $32D$, the largest cell near the surface of the rod measured $0.05d$ and that near the wall of the main body measured $0.001D$. Spanwise, the mesh was extruded for an extension of πD

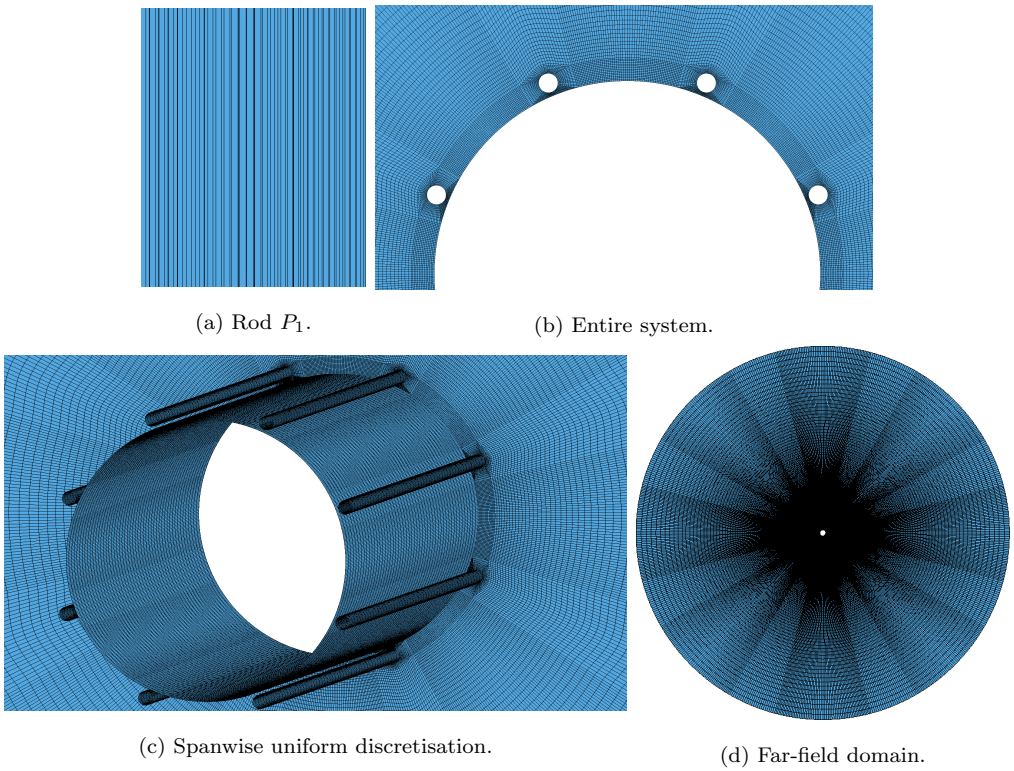

(a) Rod P_1.

(b) Entire system.

(c) Spanwise uniform discretisation.

(d) Far-field domain.

Figure 4: Different regions of the structured grid.

(as in Assi et al., 2018) and discretised by 50 elements. This level of spanwise refinement is in agreement with previous successful works Saltara et al. (2011); Carvalho and Assi (2022a). We have run cell-centred finite volume simulations with the open-source C++ OpenFOAM library.

2.2.1. Pressure-velocity coupling - SIMPLE

One relevant point is the lack of coupling between velocity and pressure in equations 3 and 4 for an incompressible flow, that would otherwise be tackled by means of an equation of state relating the fluid density and the pressure p, which is absent in the first equation. Furthermore, there is not a transport equation for p. Actually, these equations depend only on the pressure gradient; thus, they are oblivious to the pressure field itself which is carried along. Pressure-velocity coupling was dealt with by means of the Semi-Implicit Method for Pressure-Linked Equations (SIMPLE) coupling algorithm (Patankar, 1980).

In a nutshell, a merely guessed pressure field was used initially to solve the Navier-Stokes equations in order to find the guessed velocity field. The continuity equation was then rewritten in terms of pressure correction terms to determine p. Once the correction was found, it was applied to

find the new pressure and later the new velocity and further scalars of interest (such as turbulent ones). In order to find the new velocity field, a correction term was plainly dropped in the Navier-Stokes equations, whose effect was null in the converged situation. The solution procedure then continued, until the iteratively corrected pressure field was such that the velocity field resulting thereof satisfied continuity to a tolerance criterion, here specified as a residual of 10^{-4} for the pressure and 10^{-8} for the other quantities.

To accurately use SIMPLE and avoid the the so-called *checker-board effect* (Patankar, 1980), we used Rhie and Chow's interpolation, whereby a third-order pressure term was included for the computation of face velocities (Rhie and Chow, 1983). Amongst the advantages of this procedure, collocated and body-fitted grids can be used, storage is more efficient, and second-order accuracy is ensured.

The SIMPLE algorithm corresponds to a steady condition of the flow. In comparison with the unsteady case, the steady SIMPLE was applied within each time-step in internal iterations, and then the unsteady version (taking into account the unsteady term in the momentum equations) was used to move the solution to the new time step. In order to prevent information loss from one time step to another, restrictions were imposed on the time step based on the rotation of the rods and based on the reference vortex shedding cycle. Thus, the time step was limited from above by 1/70th of the revolution of the rods and 1/100th of a shedding cycle.

After the solution of the linear system, the resultant force on each body was obtained from viscous effects and pressure distribution, and the components lift F_L and drag F_D were obtained (the former is transversal, and the latter is longitudinal with respect to the incoming flow), that were normalised as follows into lift and drag coefficients:

$$C_L = \frac{F_L}{\frac{1}{2}\rho U_\infty^2 D}, \qquad C_D = \frac{F_D}{\frac{1}{2}\rho U_\infty^2 D} \tag{5}$$

2.2.2. Interpolants

To reach a linear system, the terms of equation 4 were discretised following appropriate second-order schemes to mitigate truncation and discretisation errors. The Eulerian term $\partial U_i/\partial t$ and the divergence term $U_j \partial U_i/\partial x_j$, representative of the convective flow were discretised, respectively, with an implicit backward scheme and with a blend comprised 25% of a linear upwind scheme and 75% of linear scheme. A least squares method allowed the computation of the gradients of the pressure term and the Laplacian term on the right-hand side of equation 4 (computed as the divergence of

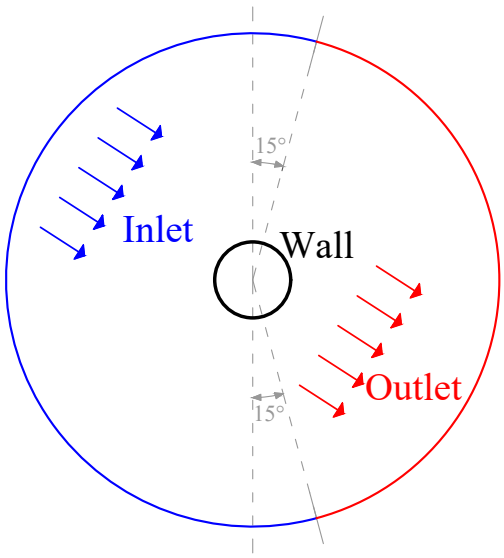

Figure 5: Inlet (blue), outlet (red) and wall (grey) boundary conditions assigned to the O-grid geometry. Only the main body is represented. For the rods, the same condition was applied, however, there the wall rotated with angular velocity ω_n.

the gradient). Correction for non-orthogonality was required for the calculation of the Laplacian term, because the surface of the cells and the line connecting the centres of two adjacent cells were not perpendicular to one another necessarily. Linear interpolations were performed for obtaining face values from cell-centre values. Surface normal gradients were determined analogously as the Laplacian terms.

2.2.3. Boundary conditions

Using the aforementioned discretisation scheme, equations 3 and 4 were solved at each time step. The following boundary conditions were assured: fully developed pressure gradient $\nabla p = 0$ and a fixed velocity U_∞ described the incoming flow away from the system; whereas the flow leaving the domain was imposed with a Dirichlet condition for the pressure and Neumann's for the velocity. The velocity on the walls of the bodies were also prescribed. For fixed bodies, the no-slip boundary condition prevailed; for rotating bodies, velocities $\omega_n d/2$ were ensured. The different regions are schematically illustrated for a cross section in figure 5. For clarity, the rods were not represented. Because this cross section was extruded in the z-direction, front and back patches resulting from this procedure were coupled through a periodic condition, as in Carvalho and Assi (2022a).

2.2.4. Turbulence modelling

Since the flow about cylinders is already turbulent for $Re > 190$, and this flow regime is inherently three-dimensional (3D), we have employed cost-effective 3D Detached-eddy simulations (DES, Spalart, 1997), where the the large (detached) eddies were fully resolved, while the boundary layer was modelled by means of unsteady Reynolds-Averaged Navier-Stokes (URANS) equations. For this latter part, we used the one-equation model of Spalart and Allmaras (1992), which transported the turbulent viscosity parameter $\tilde{\nu}$ and related it to the turbulent viscosity ν_t. For this URANS model, the appropriate boundary condition was that of Spalart (2000) and Vatsa et al. (2017): $\tilde{\nu}_{\text{wall}} = 0$ and $3 < \tilde{\nu}_\infty/\nu_\infty < 5$. This approached was employed successfully in Carvalho and Assi (2022b, 2023a), where further details and parameters are given. Small scales away from the boundary layer followed the classical model of Smagorinsky (1963).

Because $Re = 1000$ is within the subcritical regime, the wake was turbulent, but the boundary layer remained laminar. Since the URANS formulation is inherently turbulent, a low-Re correction was applied (Spalart et al., 2006). All simulations preserved $\mathcal{O}(y^+) \sim 1$, the non-dimensional distance away from the walls of the cylinders.

3. Results

3.1. Grid independence study, verification and validation

To ensure quality results to all simulations described in section 2, a grid independence study was carried out to assess whether mean drag, root mean square (RMS) of lift and the pressure coefficients, respectively denoted, $\overline{C_D}$, $\hat{C}_L$ and $\overline{C_p} = (\overline{p} - p_\infty)/(1/2\rho U D^2)$ at $y/L = 1/2$ (p_∞ is the far-field pressure) approached approximately the same value for different levels of refinement. From table 1 it is clear that neither mean drag nor RMS of lift changed significantly for the different grids relative to the most refined one. In fact, the relative difference in mean drag did not surpass 3.5%. Greater relative differences were found for the RMS of lift. However, most differences stayed under 13%. The exception was the grid with 110,000 cells with 22%. It is worth noting, however, that the RMS of lift values are generally small. Additionally, it is well-known that measurements of the RMS of lift tend to fall short of agreement within distinct grids in numerical analyses and also in physical experiments (Norberg, 2001). To further confirm that our meshing was sufficiently refined, $\overline{C_p}$ represented in figure 6 renders clear that pressure measurements were also in agreement

Table 1: Mesh convergence study in terms of mean drag ($\overline{C_D}$) and root mean square lift ($\hat{C}_L$). Quantities in parentheses correspond to the relative difference from the respective mesh to the most refined one. The highlighted row points to the grid that is referred to throughout this paper.

Number of cells		$\overline{C_D}$	$\hat{C}_L$
Cross-section	Total		
43,360	2,168,000	1.77 (2.9%)	0.67 (12%)
52,880	2,644,000	1.73 (0.58%)	0.58 (3.3%)
83,760	4,188,000	1.67 (2.9%)	0.55 (8.3%)
110,000	5,500,000	1.66 (3.5%)	0.47 (22%)
123,120	6,156,000	1.70 (1.2%)	0.56 (6.7%)
132,880	6,644,000	1.71 (0.58%)	0.58 (3.3%)
143,568	7,178,400	1.74 (1.2%)	0.64 (6.7%)
146,480	7,324,000	1.73 (0.58%)	0.61 (1.7%)
174,000	8,700,000	1.68 (2.3%)	0.52 (13%)
179,088	8,954,400	1.72	0.60

for the different grids, either for the passive mechanism at null incidence angle (figure 6a) or for the most active mechanism at the highest angle of attack evaluated in the present work (figure 6b). For cost-effective computations, we have selected the grid with 83,760 cells on its cross section (that amounts to total of 4,188,000 cells considering the 50 cells along the length of the cylinder).

3.2. Time histories

We take as a time reference the duration of a vortex shedding cycle upon a (plain) circular cylinder under uniform flow in subcritical regime. Under these circumstances, it is well known that the nondimensional Strouhal frequency $S_t = f_S/(U_\infty/D) \approx 0.2$, thus the Strouhal period is given by $T_S = 1/(S_t U_\infty/D)$. Simulations were left to run for $30T_S$ for each set of rotations corresponding to a value of ζ, following the time steps restrictions described in section 2 and imposing that the

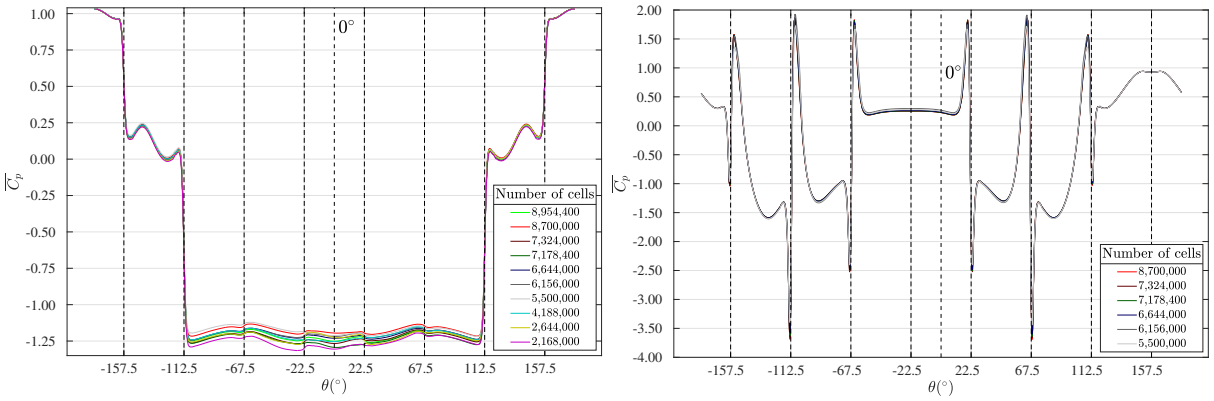

(a) $\zeta = 0.0,\ \alpha = 0.0°$.

(b) $\zeta = 2.5,\ \alpha = 22.5°$.

Figure 6: Mesh convergence of the mean pressure coefficient curve at $z/L = 2$ at different angles. On the left, the passive mechanism at null angle of attack; on the right, the active mechanism at high angle of attack. In the latter, peaks are associated to the regions near the rods where the flow was acted upon by the rods in opposite direction to that of the far-field incoming flow.

Courant number was below 1. Only the last 20 cycles were considered numerically converged. Time histories of drag and lift are represented in figures 7a and 7b, for a rather short selection of α-values, for clarity and conciseness. A tendency of decay in the values of drag and in the amplitude of lift stand out in both plots. In particular, it is evident that the lift amplitude values deeply fell in case 0 for $\zeta = 2.0$ and in case 1 for $\zeta = 1.5$.

Figure 7 corroborates with and expands on the previous study in laminar regime of Carvalho and Assi (2023b) in the observation just made; as well as in the fact that, in terms of ζ, the second case anticipated vortex shedding suppression with a lower requirement of input kinetic energy. Indeed, at $\zeta = 2.0$ the amplitude of the lift curve was null in case 1 (see figure 7b), in contrast with case 0 (figure 7a, for $120 \leq t/T_S \leq 150$). Furthermore, although the lift amplitude of these two cases differed, it is in common that their corresponding mean values at this ζ-regime were slightly offset from null value. This will be investigated more specifically in the following sections. Incidentally, in case 1, after the suppression of vortex shedding at $\zeta = 2.0$, $\overline{C_L}$ was non-null for $\alpha \neq 0$. At an even higher $\zeta = 2.5$, however, figure 7b exhibits that the mean lift curves of the different α narrowed in and approached nulll value. Therefore, to introduce higher rotations to case 1 brought the cumulative effect of a pressure distribution and a viscous traction symmetrical about the body, just as it would be expected for a setup where the angle of attack was $\alpha = 0°$, i.e., with null transverse force relative to the flow.

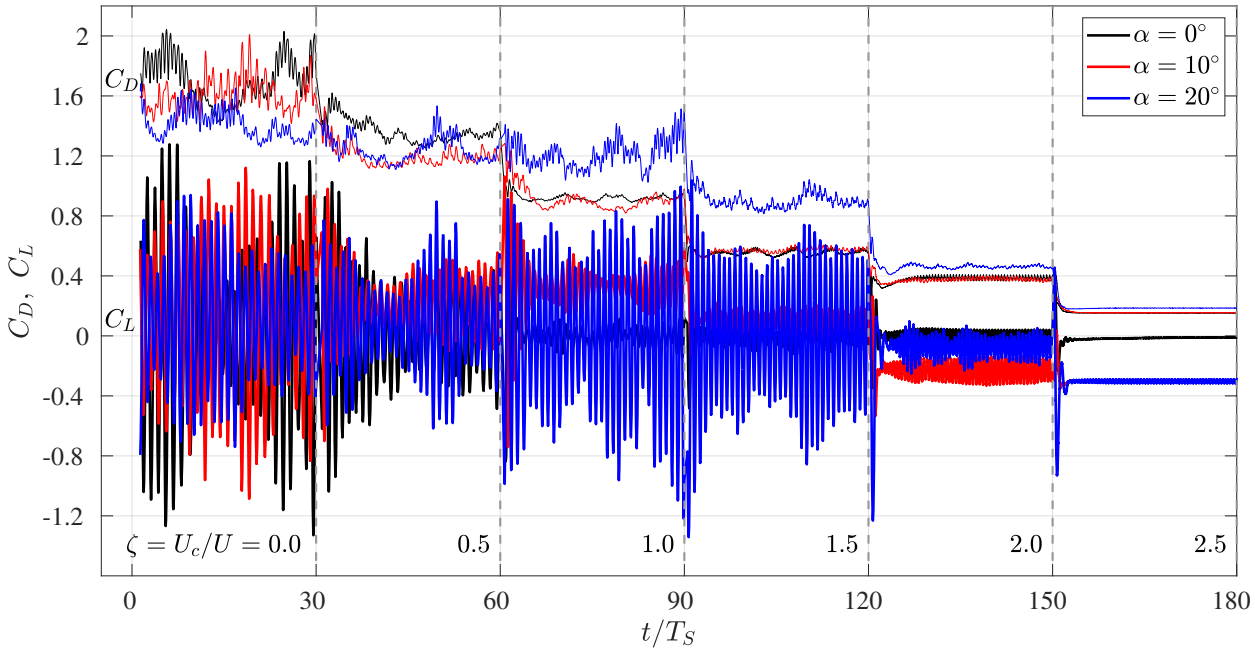

(a) Case 0.

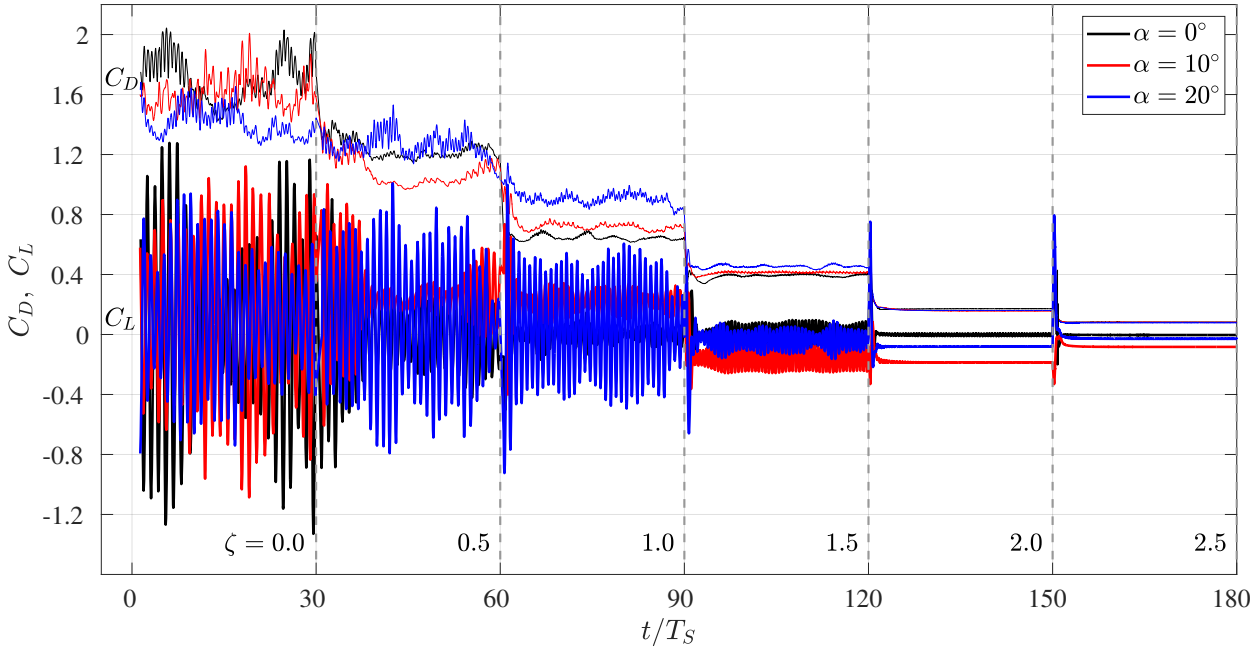

(b) Case 1.

Figure 7: Time histories of cases 0 and 1. Thick lines correspond to lift curves and thin lines to drag. Spurious peaks at the beginning of each regime of ζ are due to the numerical transient at the beginning of each simulation, that is eliminated after convergence of each simulation.

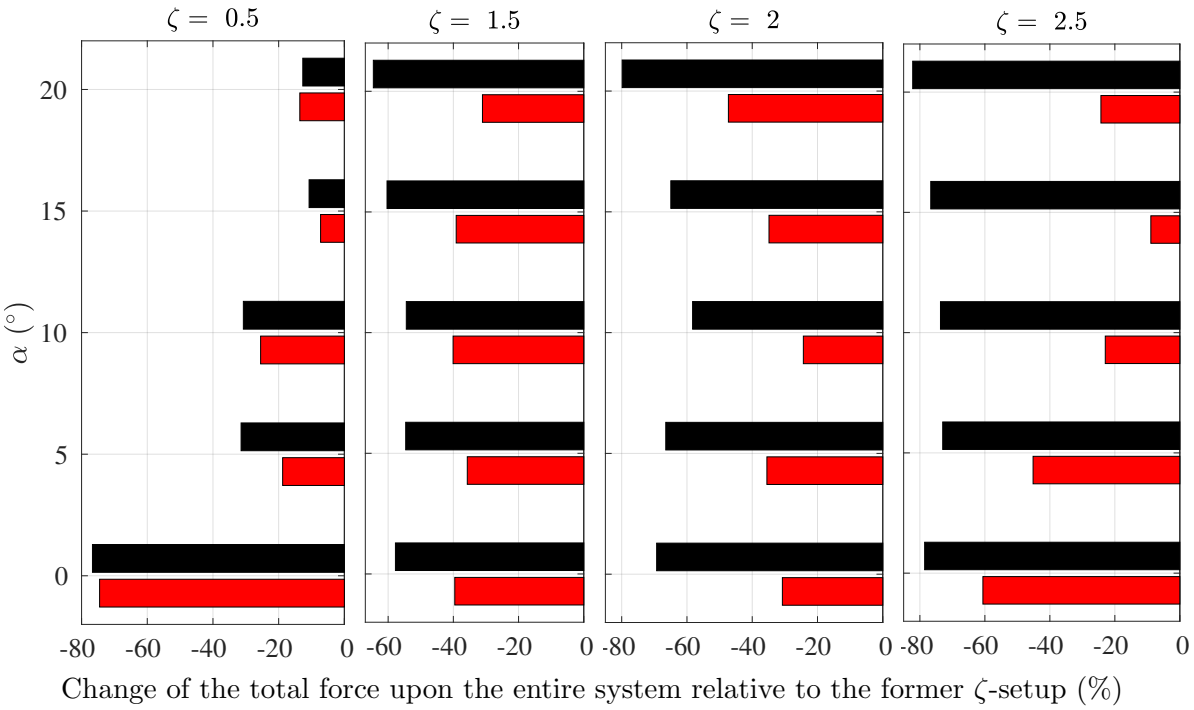

Figure 8: Comparison of the resultant force upon the active system relative to the previous setup for different angles of attack α. Indicated ζ values are compared with the previous setup. E.g., where it indicates $\zeta = 0.5$, this setup is compared with that of $\zeta = 0.0$; $\zeta = 1.5$ is compared with $\zeta = 1.0$, and so on. Our convention is followed here for cases 0 and 1, represented by red and black bars, respectively.

3.3. Attenuation of resultant loads and suppression of the vortex wake

Figure 8 compares cases 0 and 1 for the gradual increase in ζ, i.e., from $\zeta = 0.0$ to $\zeta = 0.5$, then from $\zeta = 0.5$ to $\zeta = 1.0$, etc., regarding the relative change of the mean total force applied on the entire system. The figure highlights that both systems were capable of promoting substantial attenuation of the total force for each increase of ζ, provided α was up to 10°. As the slope of the incoming flow grew steeper, the improvements were drastically reduced for the system of case 0. It can be noted that to rotate the rods faster, from $\zeta = 2.0$ to 2.5, reduced the total force to the most in approximately 20% for case 0 for $\alpha \geq 10$; whereas for case 1, the attenuation of the total force, for the same range of α, consistently surpassed 70%. Incidentally, case 0 only barely reduced the mean total force at a higher rate than case 1 for $\alpha = 20°$ and $\zeta = 0.5$ (relative to $\zeta = 0.0$). In any other case, the configuration of case 1 cut down the mean total load more expressively than that of case 0.

Vorticity contours of figure 9 about the midspan position $z/L = 1/2$ reveal the progressive

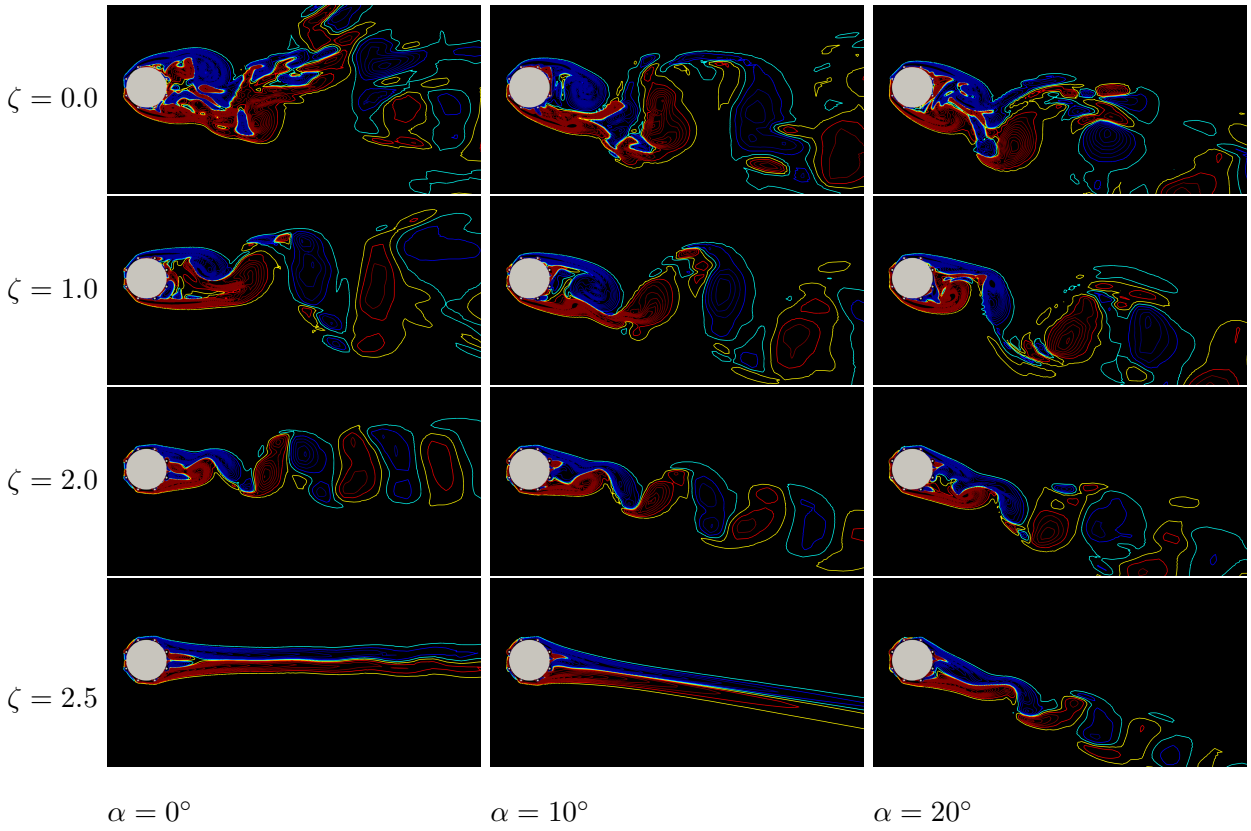

(a) Case 0.

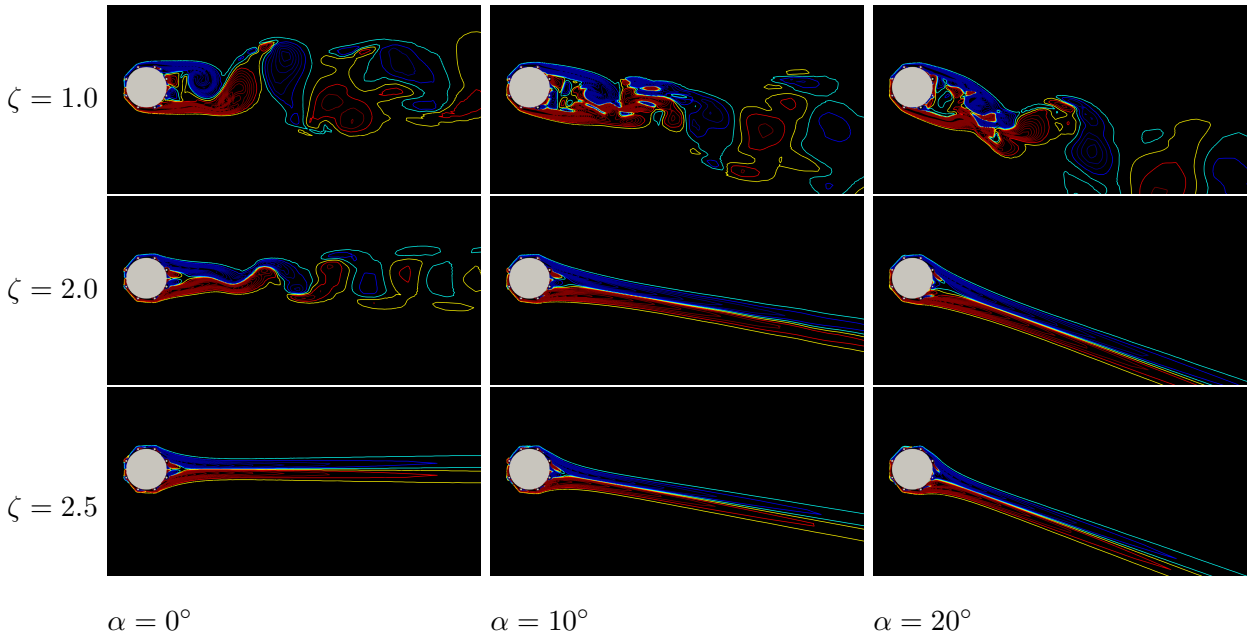

(b) Case 1.

Figure 9: Vorticity contours for different arrangements of rotation speed (ζ) and angle of attack (α).

elimination of the vortex wake with increasing rotation speeds, in either case 0 or case 1. However, it may be acknowledged that even at $\zeta = 2.5$ the flow past the system of case 0 was still subjected to weak oscillation for $\alpha = 20°$, as figure 9a shows. From the trend exhibited by figure 9a one might ascertain that this system can suppress vortex shedding entirely, provided with higher rotation speeds. However, one might wonder whether case 0 promotes the formation of a flow configuration that allows zeroing the mean lift. Of course, vorticity contours of case 1 (see figure 9b) exhibited a thinner wake at a lower ζ, which led to faster vortex shedding suppression. It is well known that the phenomenon of vortex shedding depends on the interaction between oppositely oriented-vortices (Gerrard, 1966), and that their interaction is increased in a thinner wake, and at greater formation length (Williamson, 1996), which leads to weaker vortices, as one vortex rapidly disrupts the supply of vorticity from its counterpart.

The three-dimensional aspect of the wake of case 1 is displayed by Q-contours ($Q = 0.1$) in figure 10 at different sets of combinations of ζ and α. Progressive increase in correlation of the wake can be qualitatively observed for $\alpha = 0°$ with higher rotation rates. For this angle of attack, at $\zeta = 2.0$ the contours present a bi-dimensional aspect. For higher slopes, $\zeta = 2.0$ completely eliminated the vortex-wake.

3.4. Mean drag and RMS of lift upon the entire system, rods and main body

A monotonic decay in the mean drag can be observed for the entire system of cases 0 and 1. At any given ζ of figure 11a, it becomes clear that case 1 was more apt to reduce mean drag than case 0. For the RMS of lift, the same can be generally stated, except for $\zeta = 1.5$. The compilation of Carvalho and Assi (2022a) of $\overline{C_D}$ values at this Re-regime shows that for a bare cylinder, generally $\overline{C_{D,\text{bare}}} \geq 1$ from previous works. Therefore, a circular cylinder fitted with spinning rods at $\zeta = 1.0$ can already reduce the mean drag below that of a bare cylinder. We note that the α-axis of figure 11 ranges from 0° to 20° for case 0 and from 0° to 22.5° for case 1. Stands out in this plot the case $\zeta = 2.5$. Indeed, in such case, the mean drag of the two cases neared one another.

However, the RMS of lift were strongly far apart for $\alpha \neq 0$ proving the susceptibility of case 0 relative to the direction of the incoming flow. Overall, we note that the $\hat{C}_L \times \alpha$ curves behaved essentially parabolically, with peaks located at $\alpha = 10°$. The peak of this curve shifted to $\alpha = 15°$ for case 0 with $\zeta = 2.5$, in connection with figure 9a: although the vortex shedding was eliminated at $\alpha = 10°$, it still provided higher RMS of lift than $\alpha = 0°$, where the wake was merely residual.

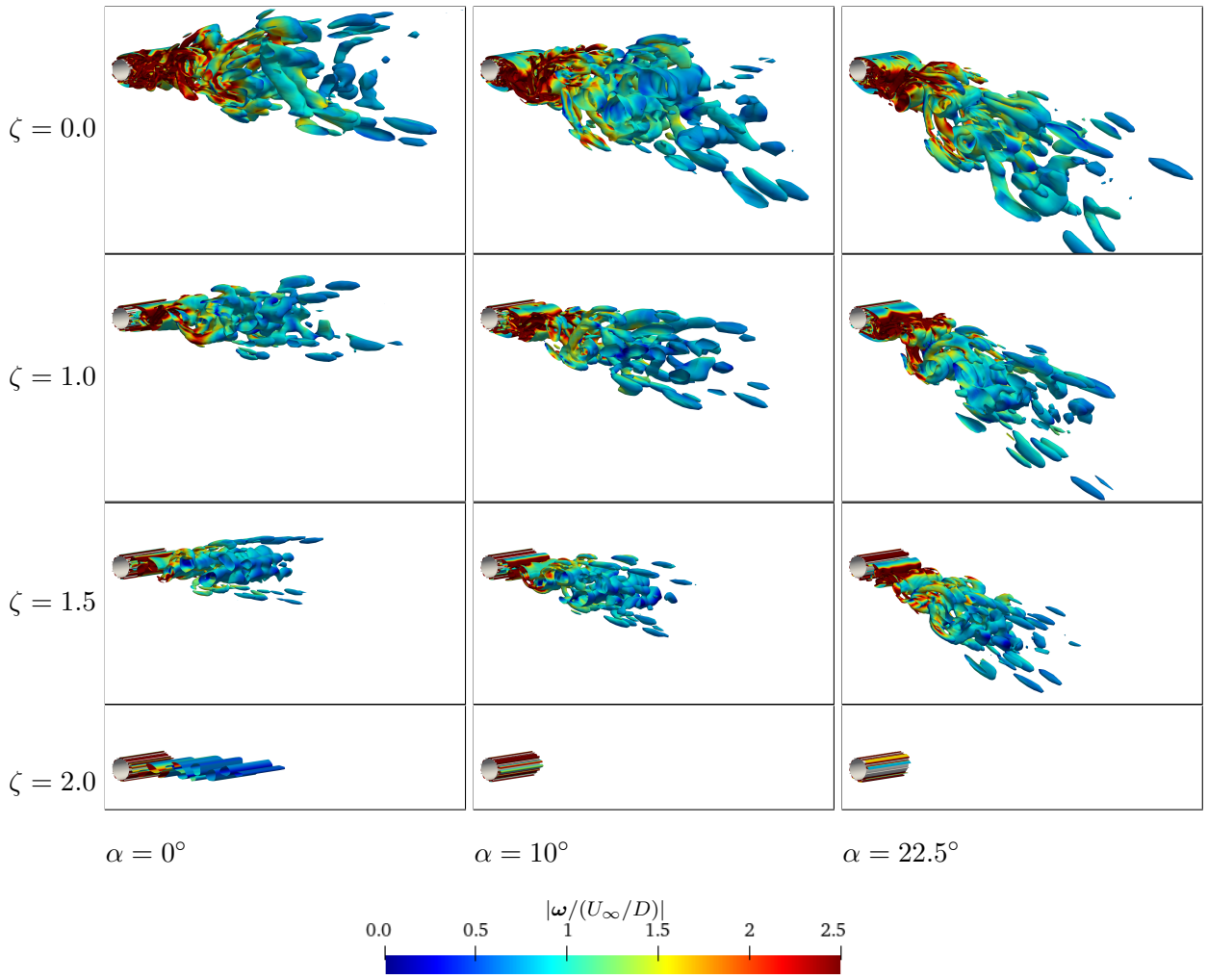

Figure 10: Q-contours ($Q = 0.1$) coloured by non-dimensional vorticity magnitude $\boldsymbol{\omega}/(U_\infty/D)$ at different slopes and rotation rates of case 1.

This might be the result of an imbalance of vorticity distribution around the body, that is higher at $\alpha = 10^{\circ}$ than for 0°. Furthermore, comparison with the data of $\hat{C}_L$ of a plain cylinder reveals that the fitted rods lowered RMS of lift below the value of a plain cylinder.

Figure 12a presents the mean drag acting on the entire system, collectively on the rods and on the main body. It may be drawn that in general, for a fixed ζ, the main body was affected by a higher mean drag than the entire system or by the rods. Surely, the rods' effect was partially to counteract the mean drag imposed by the incoming flow so the entire system was less affected by it. Additionally, the loads were significantly lower for the entire system and for the main body in case 1 compared with case 0. As for the rods, the mean drag acting on them was merely slightly different between the cases, with more prominent discrepancies at the higher rotation rates of $\zeta = 2.0$ (case 0 with lower loads) and 2.5 (case 1 with lower loads). Now, to consider different regimes of ζ, renders clear that higher rotation rates were responsible for the mitigation of the mean drag for all (sets of) bodies of figure 12a.

In terms of mean lift, the system of case 1 was more efficient in attenuating $\overline{C_L}$ over the entire system and upon the main body, as displayed by figure 12b. Aside from $\zeta = 1.5$, to impose potential-flow-inspired rotations brought the mean lift in case 1 closer to null values than in case 0. In order to ensure this for $\zeta = 2.0$, the rods supported larger mean lift in case 1. For higher angle of attack of the incoming flow, the situation reversed: the load upon the rods in case 1 was smaller for $\zeta = 2.5$ with more attenuated mean lift over the entire system and over the main body than in case 0. The difference in the latter configuration is that, although the rods withstood much higher lift contributions in case 0, the entire system and the main body were subjected to higher loads. Therefore, the rods of case 0 did not counteract lift in the same measure as in case 1. It is notable that at fixed ζ in figures 12a and 12b the curves $\overline{C_L} \times \alpha$ present a complex behaviour when contrasted with that merely linear found in the work of Carvalho and Assi (2022a), that may be attributed to the laminar regime there. Nevertheless, these plots of mean hydrodynamic loads along with the vorticity contours delineate that for the present range of data the system of case 1 was more capable of mitigating drag and lift, and in suppressing vortex shedding.

In Carvalho and Assi (2023b), the $\hat{C}_L \times \alpha$ curves for the entire system showed a trend of flattening with higher rotation rates for lift values of the order of 10^{-3} in case 1. In figure 13b we confirm that this effect also occurred in turbulent regime for higher mean lift, but strictly in

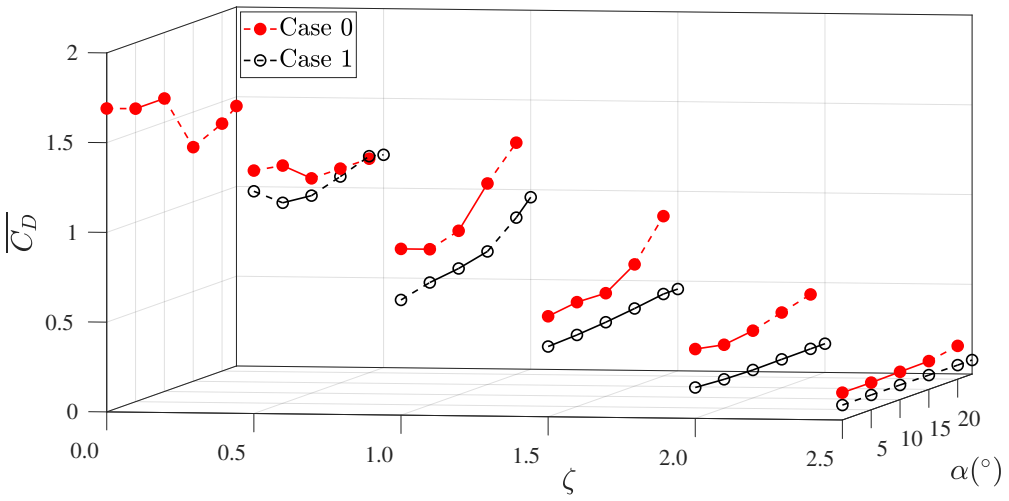

(a) Mean drag ($\overline{C_D}$).

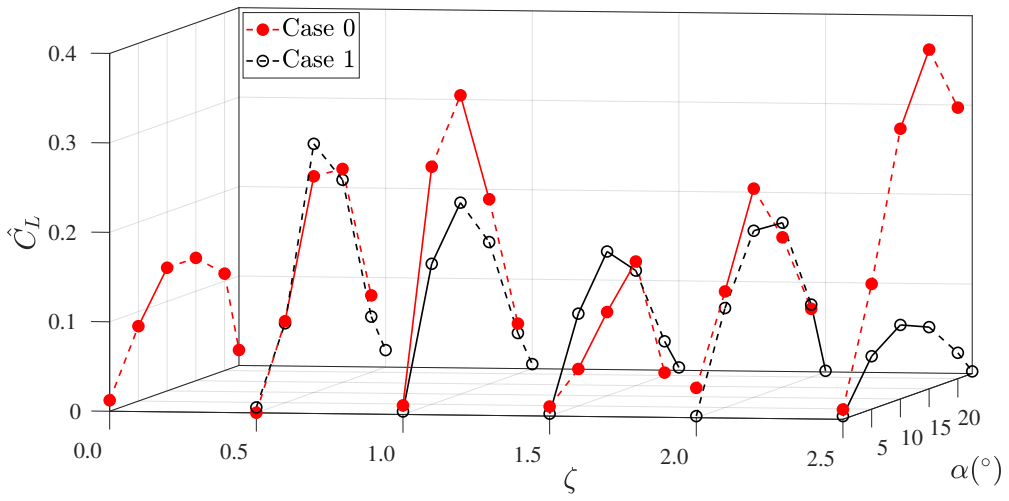

(b) RMS of lift ($\hat{C}_L$).

Figure 11: Hydrodynamic forces acting on the entire system of cases 0 and 1.

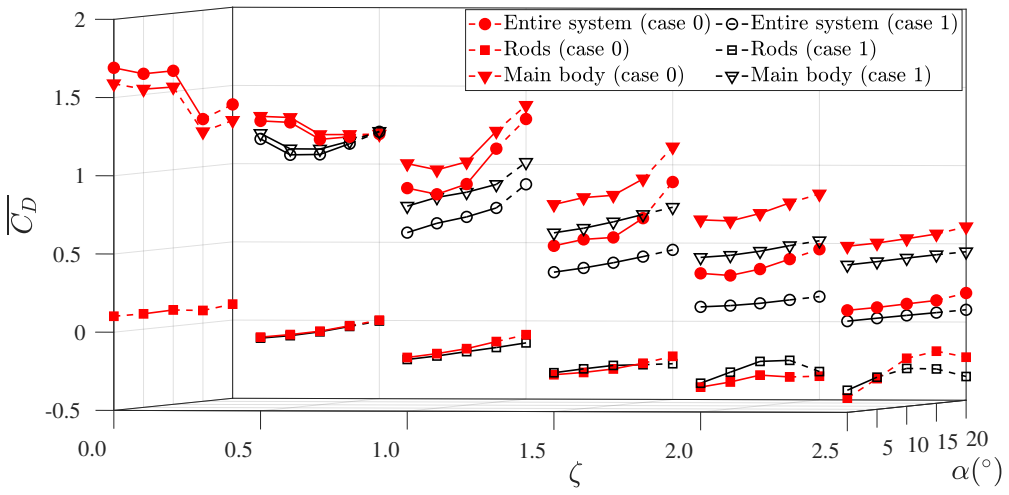

(a) Mean drag $\overline{C_D}$.

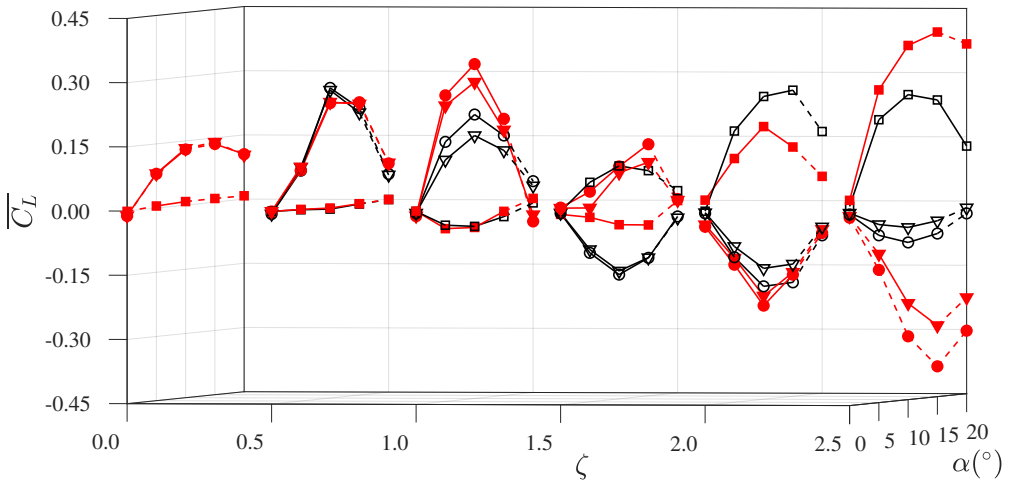

(b) Mean lift $\overline{C_L}$.

Figure 12: Mean hydrodynamic forces acting on the main body, on the rods and on the entire system of cases 0 and 1.

case 1. In case 0 the same tendency was not detected (figure 13a). This shows that potential-flow inspired rotations rendered the system "more omnidirectional", i.e., turned the fixed setup of bodies capable of controlling the flow regardless of the different slopes of the incoming flow, sufficing for so to arrange an adequate configuration of rotation rates. This is confirmed in figure 14.

When the rods were spinning with relatively lower rotation rates, lift curves corresponding to the collective contribution of the rods were either flat ($\zeta = 0.5$) or comprised of negative values ($\zeta = 0.5$) in both cases. However, as $\zeta \geq 1.0$, figure 14 shows that case 1 went from negative to positive values when ζ reached 1.5; the same occurred in case 0 only at $\zeta = 2.0$. Another difference between the cases is in how the two systems progressed toward and into vortex shedding suppression. Case 1 suffered but a slight shift around $\alpha = 10°$, as the mean lift at $\zeta = 2.0$ was lower than at $\zeta = 2.5$ for $\alpha \leq 10°$, but higher for $\alpha \geq 10°$. Notwithstanding this, it must emphasised that these were rather short differences in $\overline{C}_L$. The maximum values of the lift curves at $\zeta = 2.0$ and 2.5 were, respectively, 0.2651 ($\alpha = 15°$) and 0.2626 ($\alpha = 10°$), a decrease of 0.94%.

Of course, to employ these systems to reduce hydrodynamic loads requires actuating power to spin the rods. This is analysed in section 3.6.

3.5. Loads applied on the rods

We now investigate the individual contributions of each rod to understand their roles and their implications to the main body and to the entire system that were analysed in the previous section. From the outset, from 0° to a 5° angle of attack, figure 15a exhibits very different sets of curves for the systems of cases 0 and 1. The former setup promoted but a gradual change in the mean drag acting on all rods. In particular, P_1 was the most affected. The latter setup, on the other hand, led the mean lift curves to adopt very different shapes through more intense attenuation in P_1 than in case 0, increase in the magnitude of $\overline{C_D}$ of P_2', P_3', P_2 and reduction in P_4'.

For case 0, figure 15a reveals that a single trend was followed: increase in the magnitude of P_2, P_1' and P_4', while for P_4, P_3, P_1, P_2' and P_3' the absolute value of mean drag diminished.

Although generally the loads upon the rods of case 1 obeyed the same pattern, the loads upon P_4 and P_4' differed from the previous case. P_4 increased quickly from 5° to 20°, while the curves of different ζ converged to null value for $\alpha = 0°$ and $\alpha = 10°$. As for P_4', mean drag maintained steadily null throughout the α values. It is easily discerned that P_1 and P_2' supported progressively subdued mean drag as α increased, because P_1 was progressively immersed into a frontal stagnation

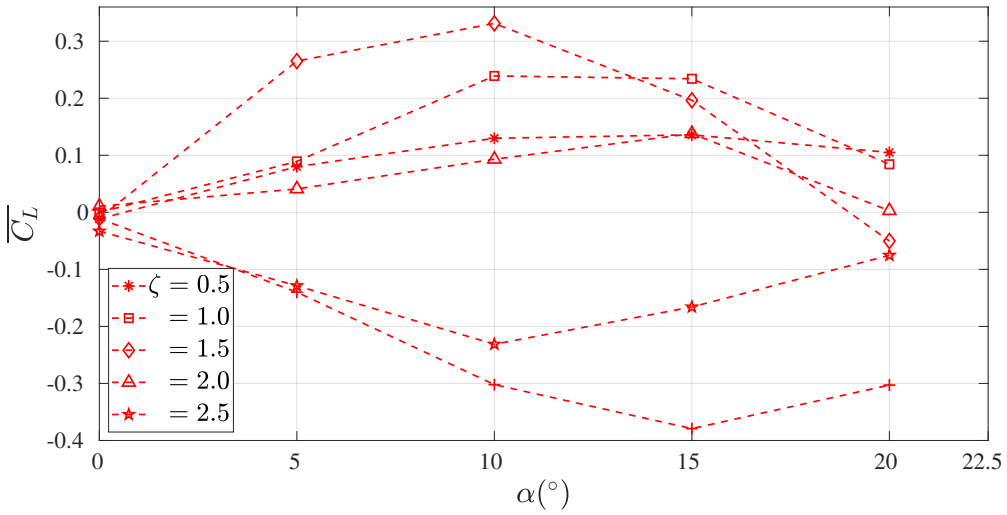

(a) Case 0.

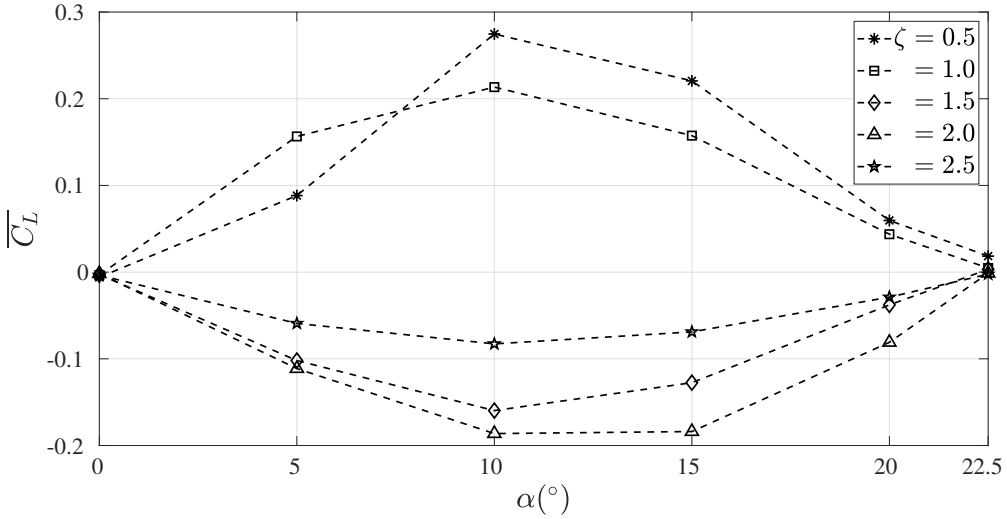

(b) Case 1.

Figure 13: Mean lift coefficient upon the entire system of cases 0 and 1 at different slopes of the incoming flow. A flattening effect on the curves of the mean lift distribution $\overline{C_L}$ with α on the entire system of case 1 indicates a tendency where the angle of attack α became less important with growing rotation speeds, in stark contrast with case 0, where the same was not detected.

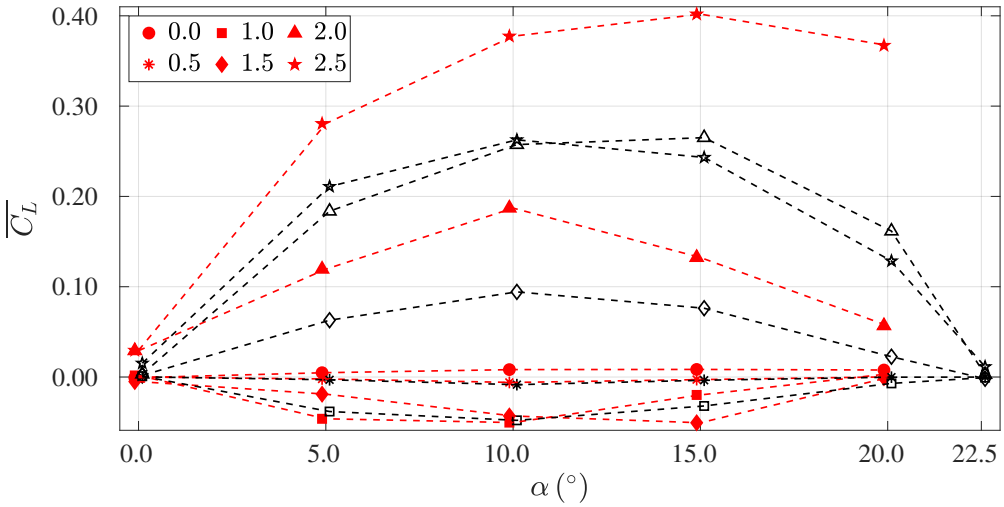

Figure 14: Resultant lift $\overline{C_L}$ from the collective effect of the rods of cases 0 (black) and 1 (red). Strikingly different behaviours justify the omnidirectional quality of each system.

zone, while P_2' was located within a wake-forming region. Both of these rods, therefore, did not have an impact into the shear layer around the system. Thus they were barely affected in terms of mean drag and, concurrently, did not contribute to the control of vortex shedding significantly.

Now, for the rods whose absolute value of mean drag rise were more accentuated in the two arrangements, P_2 and P_1', the rightmost plots of figures 15a and 15b reveal that case 0 caused the absolute value of the mean drag upon P_1' to grow beyond that of P_2. The opposite occurred in case 1, principally because the adjustment of the rotation rates by potential-flow theory took into account that P_2 was located at a greater angle than P_1'. In doing so, P_2 and P_1' corresponded, respectively, to higher and lower rotation rates than those of the corresponding rods in case 0. The lower angle at which P_1' was positioned placed this rod nearer to a stagnation region, thus limiting the interaction between the rotating surface of the rod and the flow, and vice-versa for P_2. The same analysis applies to P_4 in the two cases, but at a much lower relevance in the scope of the entire system, since the mean drag on this rod was approximately 1/3 those of P_2 and P_1'. As for P_4, although its value was more expressive at $\zeta = 2.5$, it did not strongly impact the mitigation of mean drag of the setup of case 1, because it was in a wake region, thus did not impart a relevant control of the wake. Therefore, with a greater interaction with the flow and at a higher angular velocity, P_2 was key in lowering drag in case 1 beyond case 0 for the entire system, as explicited in the time histories of figure 7.

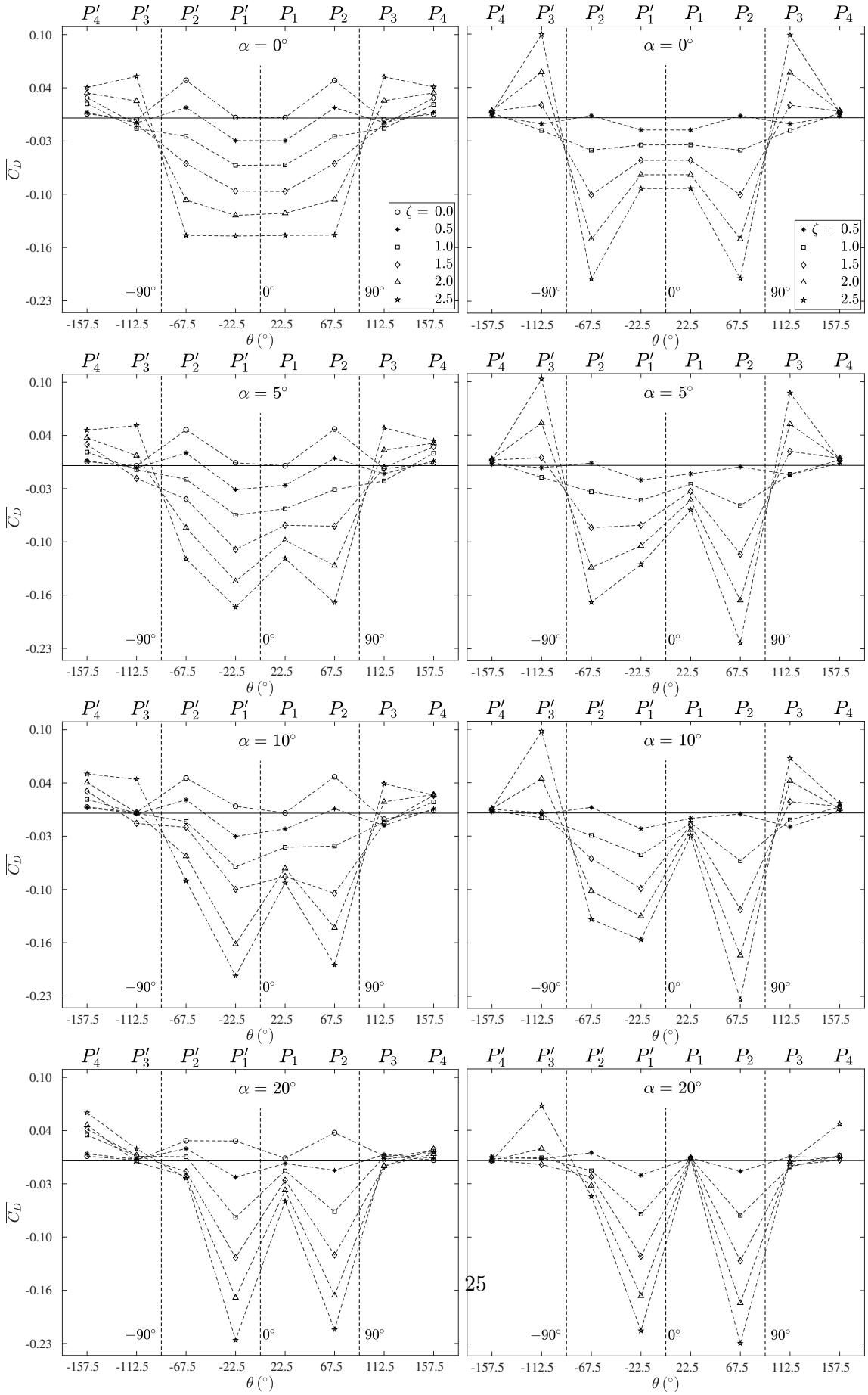

(a) Case 0.

(b) Case 1.

Lift curves for different α of figure 16 presented a similar trend for cases 0 and 1, which include: 1) a rise in the mean lift upon P_3 and P_2' to achieve the highest magnitudes for our range of α, 2) shortening of $\overline{C_L}$ upon P_1 toward null value, 3) mean lift development upon P_1', 4) stable null load upon P_4' and 5) contraction of the loads upon P_2 and P_3'. We can understand that case 1 was more able to counteract the downward force impressed by the flow through the upward lift promoted by P_3 with a slight contribution from P_4, which only adopted positive values in case 1 (but remained steadily close to zero in case 0). Although case 0 followed the same trend, it seemed "delayed" in α relative to case 1: figure 16b illustrates that whereas in case 1 the load upon P_3 overcame that upon P_2 at $\alpha = 10°$, this only happened in case 0 for $\alpha = 20°$ (figure 16a).

Notwithstanding the mean lift of case 1 was non-null for the upper end of angles of attack even at higher ζ (see time histories of figure 7b), it was much closer to zero, compared with setups with lower rotation rates and against case 0. Case 1 made up for a better arrangement to reduce the mean lift upon the entire system. Considering that the Reynolds number of the present analysis is 10 times higher than that of Carvalho and Assi (2023b) and the turbulent features incorporated to the flow tend to "delay" lift mitigation to higher ζ (in common with Mittal (2001)), it is expected that the system of case 1 will be able to completely eliminate the mean lift at ζ values close to and above our upper limit of 2.5; whereas the configuration of case 0 might be utterly incapable of doing so (Carvalho and Assi, 2023b).

This tendency is exemplified by figure 17. The coloured arrows, corresponding to P_0, P_1, ..., P_4 leave strikingly clear that whereas P_2 was prime to counteract mean drag, P_3 was key to balance downward lift. At the same time, it also shows that the load upon P_3 lightly inclined to the right with higher ζ for $\alpha = 5°$ and $10°$, dampening partially the role of P_2 in opposing drag increase. However, as α reached $20°$, the resultant load upon P_3 essentially grew monotonically and did not change orientation, while P_2 shifted from right to left. P_4 supported progressively larger loads with the increase in α and ζ. However, P_1 seemed to lose relevance as α was concerned, principally in case 1. This makes sense, as this rod approached a frontal stagnation region with steeper slope of α. However, as this happened, drag became mitigated particularly by P_2. Comparison of figures 17b and 17c at any α with sufficiently high ζ illustrates that the potential-flow-inspired case 1 neared an "omnidirectional" system capable of downsizing lift and drag given enough actuation power. In particular, at $\alpha = 20°$ the vectors acting on the main body P_0 and the greyscale vectors

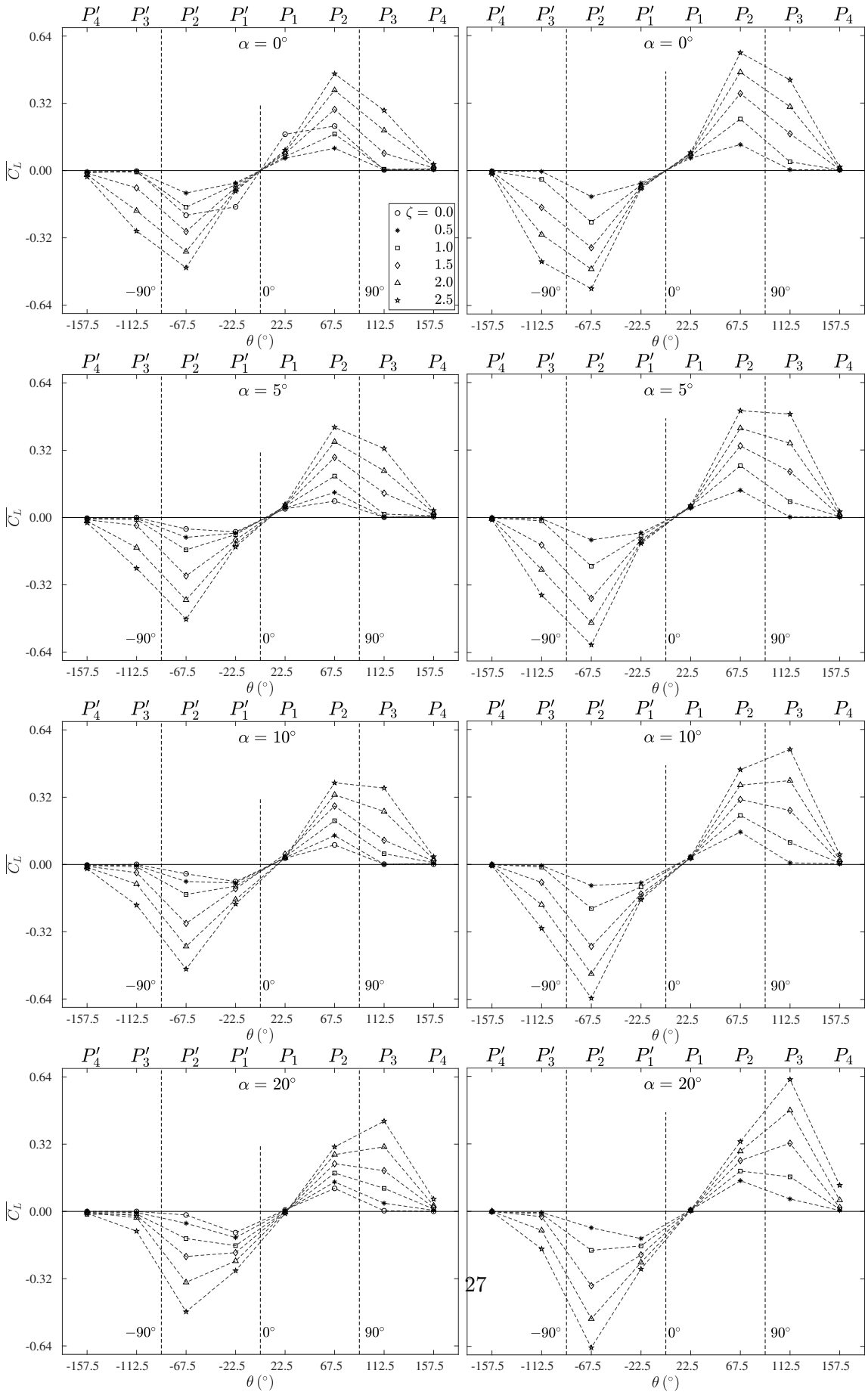

(a) Case 0.

(b) Case 1.

corresponding to the entire system nearly aligned with the direction of the incoming flow.

The aforementioned analysis can also be extended to the lower rods P_1', ..., P_4', requiring only that the asymmetric pairs are taken into account: ($P_1,\ P_4'$), ($P_2,\ P_3'$), ($P_3,\ P_2'$) and ($P_4,\ P_1'$). These pairs have the same angular distance from the centre of the rod to the blue dashed line of figure 17 (passing through the centre of the system in the direction of the incoming flow).

To substantiate the former qualitative analysis on the individual contributions of the rods to the total force on the entire system, figure 18 shows the mean total force coefficients acting on each pair of rods that were either symmetric (for $\alpha = 0°$) or asymmetric (for $\alpha \neq 0$) for the same exemplary α values. It can be noted that as α adopted larger values, an upturn occurred in the loads upon the pairs $P_3,\ P_2'$ and $P_4,\ P_1'$, whereas a downturn took place upon the resultant mean loads upon $P_1,\ P_4'$ and $P_2,\ P_3'$. Therefore, in general, rear rods gained importance, in contrast to frontal rods. Besides, intermediate rods kept overall larger loads. From a physical viewpoint, this indicates that those rods at intermediate positions harnessed higher control over the loads acting on the entire system. Indeed, these rods are more distant from stagnation regions and nearer to a point where the boundary layer would separate from the body (in this subcritical regime, roughly around 90° from the frontal stagnation region).

Although the frontmost and rearmost rods $P_1,\ P_4$ or $P_1',\ P_4'$ withstood the lowest hydrodynamic forces, their alternating contributions were still significant in the extremes of $\alpha = 0°$ and 20° and compensated one another. Indeed, taking case 1 as reference for its "more omnidirectional" property, the loads upon $P_1,\ P_1'$ in the reference figure 18 reached 0.17, whereas $P_4,\ P_4'$ contributed with barely null total force coefficient. At $\alpha = 22.5°$, conversely, P_4 reached 0.16 and then $P_1,\ P_4'$ contributed negligibly, that is, the situation was basically reversed. Using the potential-flow analogy, $P_1,\ P_1'$ and $P_4,\ P_4'$ showed to be complementary to one another. To remove one of these rods might lead the system to an imbalance that requires further study and may even impair some of the omnidirectional quality discussed above.

3.6. Power loss

In addition to uphold vortex dynamics and hydrodynamic coefficients discussions, the system employed in this work draws attention to power expenditure. To assess the power loss of the entire system, C_{PL}, one must take into account that this coefficient is composed of two parts: one is that required to counteract mean drag $\overline{C_D}$; another is to spin the rods against viscous traction C_N

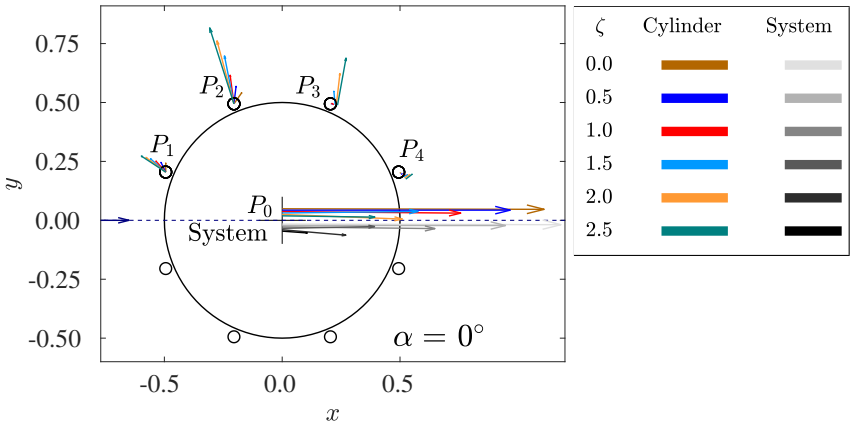

(a) Reference case ($\alpha = 0$).

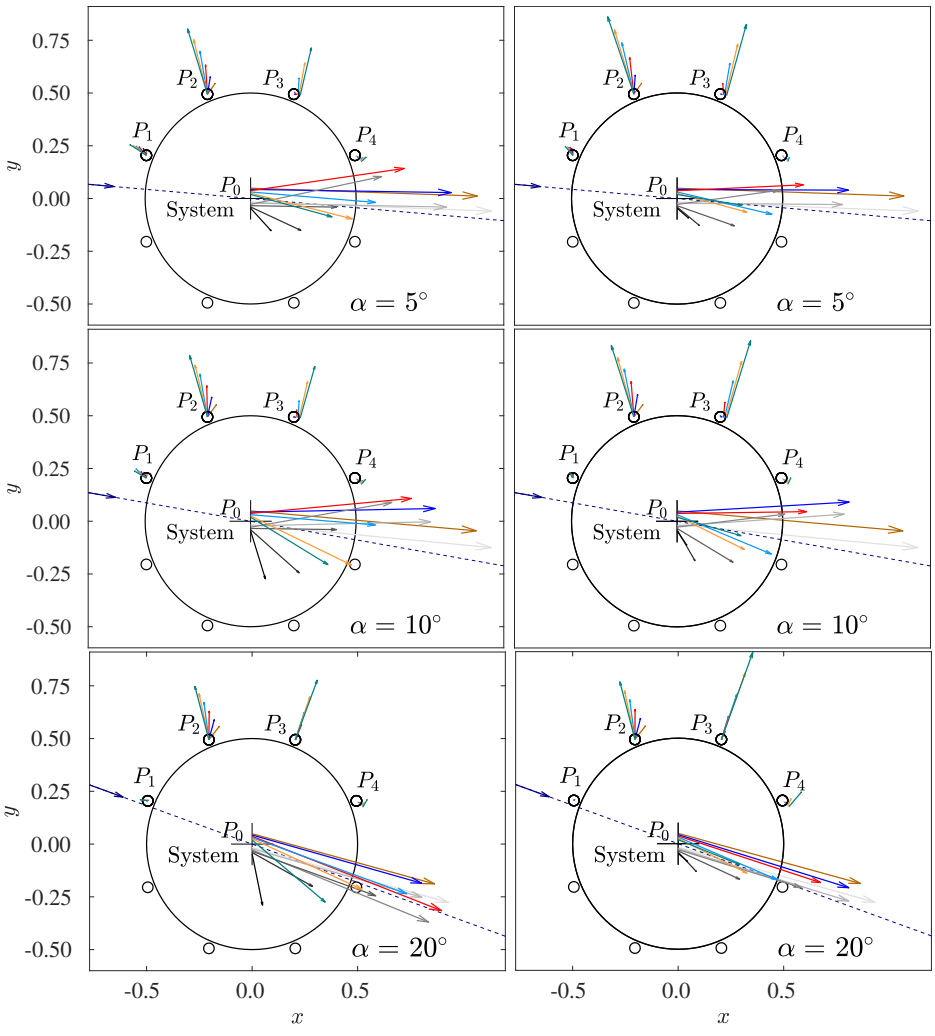

(b) Case 0.

(c) Case 1.

Figure 17: Diagrams show the loads acting on each cylinder (coloured) and on the entire system (greyscale) of cases 0 and 1. The direction of the incoming flow is shown through the dashed line and the respective vector. For clarity, the resultant force applied to the main cylinder P_0 was slightly translated from the centre of the body, so as not to be confused with that acting on the entire system.

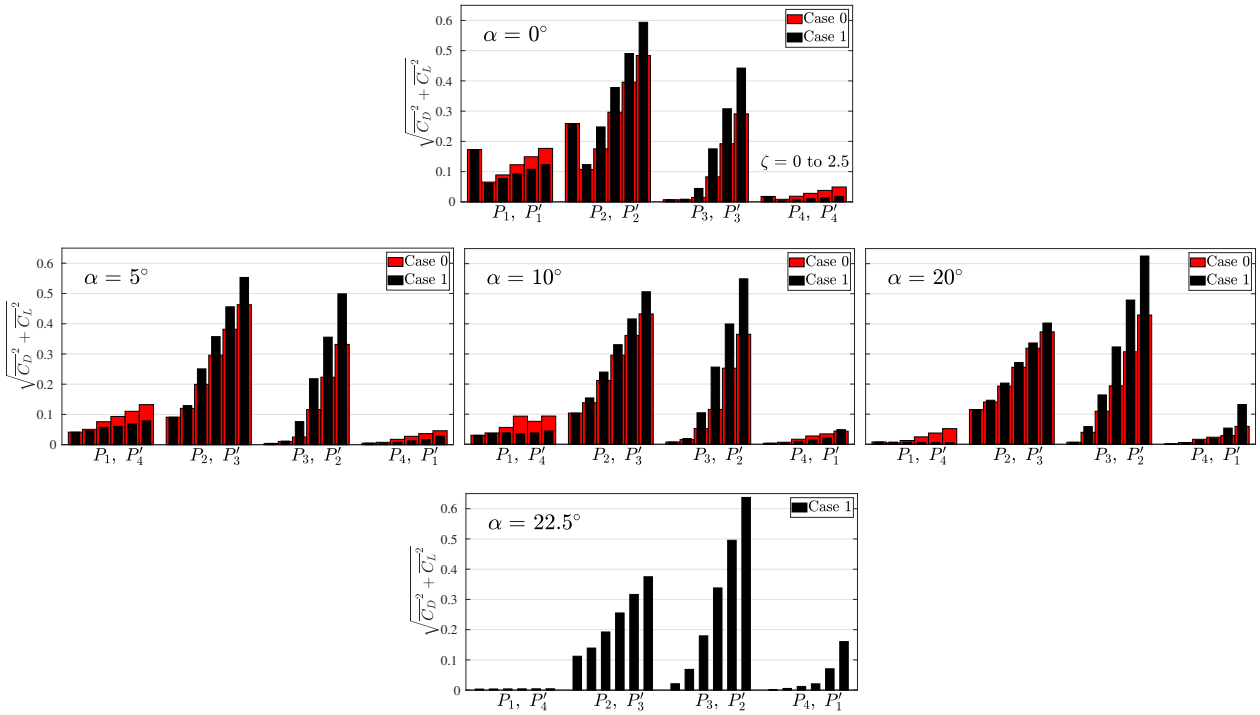

Figure 18: Resultant loads on the rods for different angles of attack. Groups of bars associated to each rod correspond to ζ varying from 0.0 to 2.5 in steps of 0.5.

(Shukla and Arakeri, 2013). In time-averaged form,

$$\overline{C_{PL}} = \overline{C_D} + \overline{C_N} \tag{6}$$

where

$$\begin{aligned} C_N &= \sum_{n=1}^{8} \frac{p_n}{\rho U^3 D L/2} \\ p_n &= \left(\omega_n \frac{d}{2}\right) \int_0^L \left[\int_0^{2\pi} \overline{\tau}\, \frac{d}{2} \mathrm{d}\theta\right] \mathrm{d}z \end{aligned} \tag{7}$$

where mean quantities (with overbar) were computed only with converged time steps (see sections 2 and 3.2), and $\overline{\tau} = \overline{\tau}(\theta, z)$ is mean wall shear stress. It is well known that to spin the rods with progressively larger angular velocities allows the system to exert greater control over the surrounding flow (Korkischko and Meneghini, 2012); nevertheless, for practical purposes this is only justified if the required power is not prohibitive. Figure 19 presents data of $\overline{C_{PL}}$ and its components. Considering that the lower end of mean drag values found for the bare cylinder is $\overline{C_{D,\mathrm{bare}}} \approx 1$, the figure depicts that under most configurations the arrangement with spinning rods

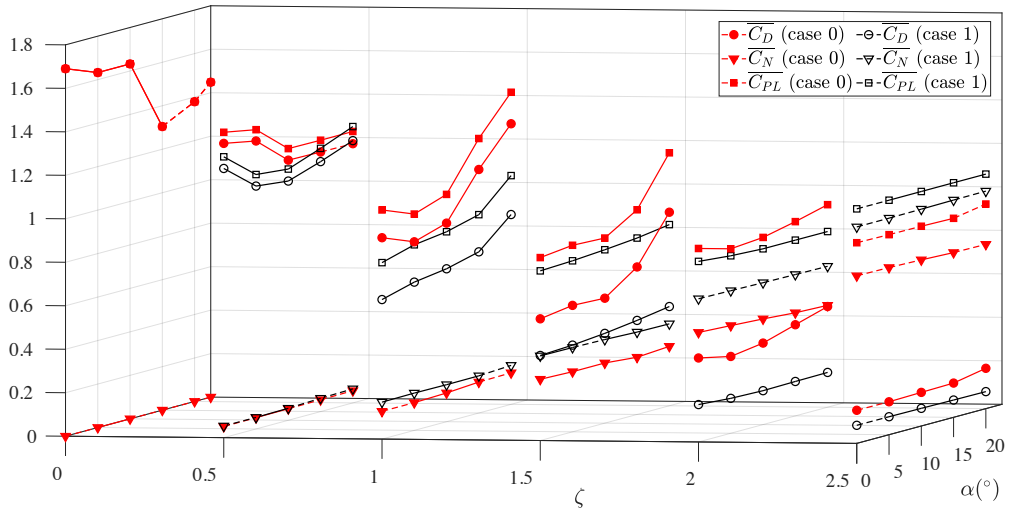

Figure 19: Total mean power-loss coefficients ($\overline{C_{PL}}$) and its components, mean drag ($\overline{C_D}$) and mean shear ($\overline{C_N}$) coefficients.

will be sufficiently efficient, so that a surplus in power will not be required to attenuate the mean drag of a bare cylinder, because generally $\overline{C_{PL}} \leq \overline{C_{D,\text{bare}}}$ for any α and $\zeta > 1$ for both systems, as far as our range of analysis of ζ is concerned. We remind, of course, that the system of case 0 was not as effective as case 1, because it was more sensible to changes in α, and vortex shedding suppression was not achieved at higher ζ and α compared with case 1. Furthermore, comparison of cases 0 and 1 indicates that the latter configuration becomes progressively more power-consuming (up to 1.0 against 2.5 in case 0). At any rate, for $\zeta \geq 2.0$ it becomes evident that $\overline{C_N}$ comprised the majority of $\overline{C_{PL}}$. Optimisation of the present system might indicate more economical setups by reaching optimal values of the gap, angular speeds and rods' diameters, as these parameters are known to have direct impact in the performance of this system, even under VIV (Silva-Ortega and Assi, 2017c,a).

4. Conclusion

Turbulent, Detached-eddy, simulations were carried out at Reynolds number 1000 for a flow-control system comprised of a main circular cylinder fitted with eight slender wake-control rods. As the rods spun about their axis with increasingly higher rotation speeds, the more they exerted control on the nearby flow. In order to assess the performance of such a device, we have considered two cases. One in which all rods spun with the same angular velocity (case 0), and another where

rod's rotation rates stemmed from the canonical case of potential flow around a plain cylinder (case 1). The two cases were constrained to the same input kinetic energy, and their velocities were updated according to a gain parameter, $\zeta = 0.0, \ldots, 2.5$ (in steps of 0.5), which multiplied all rods' angular velocities. The incoming flow reached the system at different angles of attack $\alpha = 0°, \ldots, 20°$ (and in case 1, $\alpha = 22.5°$ was also assessed, when one of the rods was kept aligned with the frontal stagnation region).

It was perceived that both configurations of cases 0 and 1 were able to reduce mean drag and suppress vortex shedding, for sufficiently high ζ. However, it stood out that case 1 was able to produce these effects for lower ζ compared with case 0. And more importantly, case 1 demonstrated to be more robust when α was altered, whereas case 0 was prone to be less effective in suppressing the wake and in mitigating hydrodynamic loads when α was greater than 10°. We say that case 1 proved to be "more omnidirectional" than case 0. As a matter of fact, vorticity contours showed that an imbalance occurred past the system of case 0, that was responsible for the generation of regions of different pressure distributions relative to the incoming flow. Consequently, significant mean lift was produced, even when the suppressing device had already eliminated the Kármán-Bénard vortex street in its entirety.

Case 1 released greater control over the resultant load upon the entire structure. Furthermore, our computations showed that to increase ζ (e.g., from 0.5 to 1.0, or from 1.5 to 2.0, etc.) for this arrangement improved mitigation of the resultant force beyond 50%, at any angle of attack α. For case 0, a lower, but comparable level of improvement was only attained at lower slopes of the incoming flow. For $\alpha > 10°$ the same did not occur for case 0; rather, the reduction was as low as a 10% in the total load for $\alpha = 15°$ when ζ was increased from 2.0 to 2.5. Beyond this, in agreement with the previous study conducted in laminar regime of Carvalho and Assi (2023b), it was noted that the mean lift acting on the entire system became progressively less dependent on the angle of attack for case 1 and the curves became essentially flat with more actuating power.

In addition to the analysis of the entire system, the main body and all rods collectively were assessed with respect to the hydrodynamic loads to find that the main body was subjected to larger mean drag than the entire system and than the rods for the active mechanism, especially at greater incidence angle.

To understand the different behaviours of cases 0 and 1, each rod was investigated with respect

to mean lift and drag. We have found that the intermediate rods played a paramount role in ensuring attenuation of the hydrodynamic loads. We also detected that rearmost and frontmost rods, in spite of generally contributing less to the total loads, interchanged contributions when the angle of attack advanced to extreme values $\alpha = 0°$ and $20°$, and might have an important role in an optimised setup, because this nuance mattered significantly into the diverging responses of cases 0 and 1.

In practical applications, perhaps anticipating a possible implementation of this device, our study showed that a bluff body surrounded by 8 rotating rods (45° apart) is capable of mitigating vortex shedding and turbulence effects, and of reducing mean forces through proper adjustment of the angular velocities of the individual rods in relation to the incoming flow direction. Moreover, we showed that this level of flow control was achieved with reduction in the mean drag without requiring additional power to counteract the viscous traction as the rods spun; and the power loss, following the analysis of Shukla and Arakeri (2013) was below the mean drag of a bare cylinder. The present control approach inspired by the potential-flow velocity field proved to be good enough to achieve wake control. Therefore, the setup was shown to be omnidirectional, as far as our flow regime is concerned. Future investigation should focus on optimisation of these angular velocities targeting minimal power, drag reduction (or thrust, such as in Silva-Ortega and Assi, 2017a), or generation of a useful lift force.

Acknowledgments

IAC is grateful to CAPES Brazilian Ministry of Education for his PhD scholarship and to the National Laboratory for Scientific Computing (LNCC/MCTI, Brazil) for providing HPC resources of the SDumont supercomputer. GRSA acknowledges the support of FAPESP, Brazil (2011/00205-6) and CNPq, Brazil (306146/2019-3). We gratefully acknowledge the support of the RCGI Research Centre for Greenhouse Gas Innovation, hosted by the University of São Paulo, Brazil and sponsored by FAPESP (2020/15230-5) and Shell Brasil.

References

Assi, G.R., Bearman, P., Kitney, N., 2009. Low drag solutions for suppressing vortex-induced vibration of circular cylinders. Journal of Fluids and Structures 25, 666–675.

Assi, G.R., Crespi, T., Gharib, M., 2022. Novel geometries of serrated helical strakes to suppress vortex-induced vibrations and reduce drag. Applied Ocean Research 120, 103034.

Assi, G.R.S., Bearman, P.W., Tognarelli, M.A., 2014. On the stability of a free-to-rotate short-tail fairing and a splitter plate as suppressors of vortex-induced vibration. Ocean Engineering 92, 234 – 244.

Assi, G.R.S., Orselli, R.M., Silva-Ortega, M., 2018. Suppression of vortex shedding with rotating wake-control cylinders: Numerical investigation at a moderate reynolds number, in: International Conference on Offshore Mechanics and Arctic Engineering, American Society of Mechanical Engineers. p. V002T08A060.

Assi, G.R.S., Orselli, R.M., Silva-Ortega, M., 2019. Control of vortex shedding from a circular cylinder surrounded by eight rotating wake-control cylinders at Re= 100. Journal of Fluids and Structures 89, 13–24.

Blevins, R.D., 1990. Flow-induced vibration. 2 ed., Van Nostrand Reinhold, New York.

Carvalho, I.A., Assi, G.R.S., 2022a. Enhanced control of the turbulent flow past a circular cylinder with rotating rods inspired by an inviscid solution. Journal of Fluids and Structures 113, 103652.

Carvalho, I.A., Assi, G.R.S., 2022b. Passive control of vortex shedding past finite cylinders under the effect of a free surface. Physics of Fluids 35, 015109.

Carvalho, I.A., Assi, G.R.S., 2023a. Active control of vortex shedding past finite cylinders under the effect of a free surface. Accepted for publication by Physics of Fluids .

Carvalho, I.A., Assi, G.R.S., 2023b. On the omnidirectionality of a system with eight spinning rods for wake control of a circular cylinder in turbulent regime.

Carvalho, I.A., Assi, G.R.S., Orselli, R.M., 2021. Wake control of a circular cylinder with rotating rods: Numerical simulations for inviscid and viscous flows. Journal of Fluids and Structures 106, 103385.

Choi, H., Jeon, W.P., Kim, J., 2008. Control of flow over a bluff body. Annu. Rev. Fluid Mech. 40, 113–139.

Ferziger, J.H., Perić, M., Street, R.L., 2002. Computational methods for fluid dynamics. volume 3. Springer.

Fujarra, A.L.C., Rosetti, G.F., de Wilde, J., Gonçalves, R.T., 2012. State-of-art on vortex-induced motion: A comprehensive survey after more than one decade of experimental investigation, in: Proceedings of the OMAE International Conference on Offshore Mechanics and Arctic Engineering, pp. 561–582.

Gerrard, J.H., 1966. The mechanics of the formation region of vortices behind bluff bodies. Journal of fluid mechanics 25, 401–413.

Korkischko, I., Meneghini, J., 2012. Suppression of vortex-induced vibration using moving surface boundary-layer control. Journal of Fluids and Structures 34, 259–270.

Korkischko, I., Meneghini, J.R., 2011. Volumetric reconstruction of the mean flow around circular cylinders fitted with strakes. Experiments in fluids 51, 1109–1122.

Mittal, S., 2001. Control of flow past bluff bodies using rotating control cylinders. Journal of fluids and structures 15, 291–326.

Norberg, C., 2001. Flow around a circular cylinder: aspects of fluctuating lift. Journal of fluids and structures 15, 459–469.

Patankar, S.V., 1980. Numerical heat transfer and fluid flow.

Patino, G.A., Gioria, R.S., Meneghini, J.R., 2017. Evaluating the control of a cylinder wake by the method of sensitivity analysis. Physics of Fluids 29, 044103. doi:10.1063/1.4979482, arXiv:https://doi.org/10.1063/1.4979482.

Rhie, C., Chow, W.L., 1983. Numerical study of the turbulent flow past an airfoil with trailing edge separation. AIAA journal 21, 1525–1532.

Saltara, F., Neto, A., Lopez, J., et al., 2011. 3D CFD simulation of vortex-induced vibration of cylinder. International Journal of Offshore and Polar Engineering 21.

Shukla, R.K., Arakeri, J.H., 2013. Minimum power consumption for drag reduction on a circular cylinder by tangential surface motion. Journal of Fluid Mechanics 715, 597–641. doi:10.1017/jfm.2012.537.

Silva-Ortega, M., Assi, G., 2017a. Suppression of the vortex-induced vibration of a circular cylinder surrounded by eight rotating wake-control cylinders. Journal of Fluids and Structures 74, 401 – 412.

Silva-Ortega, M., Assi, G.R.S., 2017b. Flow-induced vibration of a circular cylinder surrounded by two, four and eight wake-control cylinders. Experimental Thermal and Fluid Science 85, 354–362.

Silva-Ortega, M., Assi, G.R.S., 2017c. Flow-induced vibration of a circular cylinder surrounded by two, four and eight wake-control cylinders. Experimental Thermal and Fluid Science 85, 354 – 362.

Smagorinsky, J., 1963. General circulation experiments with the primitive equations: I. the basic experiment. Monthly weather review 91, 99–164.

Spalart, P., 2000. Trends in turbulence treatments, in: Fluids 2000 conference and exhibit, p. 2306.

Spalart, P., Allmaras, S., 1992. A one-equation turbulence model for aerodynamic flows, in: 30th Aerospace Sciences Meeting and Exhibit, p. 439.

Spalart, P.R., 1997. Comments on the feasibility of les for wings, and on a hybrid rans/les approach, in: Proceedings of first AFOSR international conference on DNS/LES, Greyden Press.

Spalart, P.R., Deck, S., Shur, M.L., Squires, K.D., Strelets, M.K., Travin, A., 2006. A new version of detached-eddy simulation, resistant to ambiguous grid densities. Theoretical and computational fluid dynamics 20, 181–195.

Strykowski, P.J., Sreenivasan, K.R., 1990. On the formation and suppression of vortex shedding at low reynolds numbers. Journal of Fluid Mechanics 218, 71–107.

Vatsa, V.N., Lockard, D.P., Spalart, P.R., 2017. Grid sensitivity of SA-based Delayed-Detached-Eddy-Simulation model for blunt-body flows. AIAA Journal 55, 2842–2847.

Williamson, C.H.K., 1996. Vortex dynamics in the cylinder wake. Annual review of fluid mechanics 28, 477–539.

Williamson, C.H.K., Govardhan, R., 2004. Vortex-induced vibrations. Annu. Rev. Fluid Mech. 36, 413–455.

Zdravkovich, M.M., 1981. Review and classification of various aerodynamic and hydrodynamic means for suppressing vortex shedding. Journal of Wind Engineering and Industrial Aerodynamics 7, 145–189.

References

Ali, U., Islam, M., Janajreh, I., Fatt, Y., Alam, M., et al. (2021). "Flow-induced vibrations of single and multiple heated circular cylinders: A review". In: *Energies* 14.24, p. 8496.

Anderson, J. D. (1995). *Computational Fluid Dynamics. The Basics with Applications.* Vol. 1. McGraw-Hill Education.

Assi, G. R. S. (2009). "Mechanisms for flow-induced vibration of interfering bluff bodies". PhD thesis. Department of Aeronautics, Imperial College London.

Assi, G. R. S., Bearman, P. W., and Kitney, N. (2009). "Low drag solutions for suppressing vortex-induced vibration of circular cylinders". In: *Journal of Fluids and Structures* 25.4, pp. 666–675.

Assi, G. R. S., Bearman, P. W., Kitney, N., and Tognarelli, M. A. (2010). "Suppression of wake-induced vibration of tandem cylinders with free-to-rotate control plates". In: *Journal of Fluids and Structures* 26.7-8, pp. 1045–1057.

Assi, G. R. S., Bearman, P. W., and Tognarelli, M. A. (2014). "On the stability of a free-to-rotate short-tail fairing and a splitter plate as suppressors of vortex-induced vibration". In: *Ocean engineering* 92, pp. 234–244.

Assi, G. R. S., Crespi, T., and Gharib, M. (2022). "Novel geometries of serrated helical strakes to suppress vortex-induced vibrations and reduce drag". In: *Applied Ocean Research* 120, p. 103034.

Assi, G. R. S., Orselli, R. M., and Silva-Ortega, M. (2018). "Suppression of vortex shedding with rotating wake-control cylinders: Numerical investigation at a moderate Reynolds number". In: *International Conference on Offshore Mechanics and Arctic Engineering.* Vol. 51210. American Society of Mechanical Engineers, V002T08A060.

Assi, G. R. S., Orselli, R. M., and Silva-Ortega, M. (2019). "Control of vortex shedding from a circular cylinder surrounded by eight rotating wake-control cylinders at Re= 100". In: *Journal of Fluids and Structures* 89, pp. 13–24.

Bearman, P. W. (1984). "Vortex shedding from oscillating bluff bodies". In: *Annual Review of Fluid Mechanics* 16.1, pp. 195–222.

Behr, M., Hastreiter, D., Mittal, S., and Tezduyar, T. E. (1995). "Incompressible flow past a circular cylinder: dependence of the computed flow field on the location of the lateral boundaries". In: *Computer Methods in Applied Mechanics and Engineering* 123.1-4, pp. 309–316.

Behr, M., Liou, J., Shih, R., and Tezduyar, T. E. (1991). "Vorticity-streamfunction formulation of unsteady incompressible flow past a cylinder: Sensitivity of the computed flow field to the location of the outflow boundary". In: *International Journal for Numerical Methods in Fluids* 12.4, pp. 323–342.

Bingham, C., Raibaudo, C., Morton, C., and Martinuzzi, R. (2018). "Suppression of fluctuating lift on a cylinder via evolutionary algorithms: Control with interfering small cylinder". In: *Physics of Fluids* 30.12, p. 127104.

Bird, R. B., Stewart, W. E., and Lightfoot, E. N. (2006). *Transport Phenomena*. Vol. 1. John Wiley & Sons.

Bishop, R. E. D. and Hassan, A. Y. (1964). "The lift and drag forces on a circular cylinder oscillating in a flowing fluid". In: *Proceedings of the Royal Society of London. Series A. Mathematical and Physical Sciences* 277.1368, pp. 51–75.

Blanchard, A., Bergman, L. A., and Vakakis, A. F. (2020). "Vortex-induced vibration of a linearly sprung cylinder with an internal rotational nonlinear energy sink in turbulent flow". In: *Nonlinear Dynamics* 99.1, pp. 593–609.

Blevins, R. D. (1990). *Flow-induced vibration*. 2nd ed. New York: Van Nostrand Reinhold.

Cantwell, B. and Coles, D. (1983). "An experimental study of entrainment and transport in the turbulent near wake of a circular cylinder". In: *Journal of Fluid Mechanics* 136, pp. 321–374.

Carmo, B. S. and Meneghini, J. R. (2006). "Numerical investigation of the flow around two circular cylinders in tandem". In: *Journal of Fluids and Structures* 22.6-7, pp. 979–988.

Carvalho, I. A. and Assi, G. R. S. (2022). "Enhanced control of the turbulent flow past a circular cylinder with rotating rods inspired by an inviscid solution". In: *Journal of Fluids and Structures* 113, p. 103652. ISSN: 0889-9746. DOI: https://doi.org/10.1016/

j.jfluidstructs.2022.103652. URL: https://www.sciencedirect.com/science/article/pii/S0889974622000913.

Carvalho, I. A. and Assi, G. R. S. (2023a). "Active control of vortex shedding past finite cylinders under the effect of a free surface". In: *Physics of Fluids* 35.4. 045130, p. 045130. ISSN: 1070-6631. DOI: 10.1063/5.0147760. eprint: https://pubs.aip.org/aip/pof/article-pdf/doi/10.1063/5.0147760/16831213/045130_1_5.0147760.pdf. URL: https://doi.org/10.1063/5.0147760.

Carvalho, I. A. and Assi, G. R. S. (2023b). "On the omnidirectionality of a system with eight spinning rods for wake control". Under revision of the Journal of Fluid Mechanics.

Carvalho, I. A. and Assi, G. R. S. (2023c). "On the omnidirectionality of a system with eight spinning rods in controlling the wake of a circular cylinder in a turbulent regime". Considered for publication in the Journal of Fluid Mechanics.

Carvalho, I. A. and Assi, G. R. S. (2023d). "Passive control of vortex-shedding past finite cylinders under the effect of a free surface". In: *Physics of Fluids* 35.1. 015109. ISSN: 1070-6631. DOI: 10.1063/5.0134730. eprint: https://pubs.aip.org/aip/pof/article-pdf/doi/10.1063/5.0134730/16778152/015109_1_online.pdf. URL: https://doi.org/10.1063/5.0134730.

Carvalho, I. A., Assi, G. R. S., and Orselli, R. M. (2021). "Wake control of a circular cylinder with rotating rods: Numerical simulations for inviscid and viscous flows". In: *Journal of Fluids and Structures* 106, p. 103385. ISSN: 0889-9746. DOI: https://doi.org/10.1016/j.jfluidstructs.2021.103385. URL: https://www.sciencedirect.com/science/article/pii/S0889974621001687.

Choi, H., Jeon, W. P., and Kim, J. (2008). "Control of flow over a bluff body". In: *Annual Review of Fluid Mechanics* 40, pp. 113–139.

Cicolin, M. M. and Assi, G. R. S. (2017). "Experiments with flexible shrouds to reduce the vortex-induced vibration of a cylinder with low mass and damping". In: *Applied Ocean Research* 65, pp. 290–301.

Cicolin, M. M., Buxton, O. R. H., Assi, G. R. S., and Bearman, P. W. (2021). "The role of separation on the forces acting on a circular cylinder with a control rod". In: *Journal of Fluid Mechanics* 915, A33.

Coutanceau, M. and Bouard, R. (1977). "Experimental determination of the main features of the viscous flow in the wake of a circular cylinder in uniform translation. Part 1. Steady flow". In: *Journal of Fluid Mechanics* 79.2, pp. 231–256.

Dolci, D. I. and Carmo, B. S. (2019). "Bifurcation analysis of the primary instability in the flow around a flexibly mounted circular cylinder". In: *Journal of Fluid Mechanics* 880, R5.

Fan, D., Yang, L., Wang, Z., Triantafyllou, M., and Karniadakis, G. (2020). "Deep reinforcement learning for bluff body active flow control in experiments and simulations". In: *APS Division of Fluid Dynamics Meeting Abstracts*, R01–010.

Farivar, D. J. (1981). "Turbulent uniform flow around cylinders of finite length". In: *AIAA journal* 19.3, pp. 275–281.

Feng, C. (1968). "The measurement of vortex induced effects in flow past stationary and oscillating circular and D-section cylinders". PhD thesis. University of British Columbia.

Ferziger, J. H., Perić, M., and Street, R. L. (2002). *Computational Methods for Fluid Dynamics*. 3rd ed. Springer.

Fielding, S. M. (2005). *Laminar Boundary Layer Theory*. Available at: https://community.dur.ac.uk/suzanne.fielding/teaching/BLT/sec4c.pdf. Autumn semestre course notes from Dunham University. Accessed in: 05 May 2020.

Franzini, G. R., Gonçalves, R. T., Meneghini, J. R., and Fujarra, A. L. C. (2013). "One and two degrees-of-freedom Vortex-Induced Vibration experiments with yawed cylinders". In: *Journal of Fluids and Structures* 42, pp. 401–420.

Freire, C. M. (2015). "Estudo experimental do fenômeno de vibração induzida por vórtices em cilindro rígido livre para oscilar com dois graus de liberdade." PhD thesis. Universidade de São Paulo.

Gad-el-Hak, M. (2000). *Flow Control: Passive, Active, and Reactive Flow Management*. Cambridge University Press.

Gandra, A. (2020). *Produção no pré-sal passa de 70% do petróleo e gás extraídos no país*. Available at: https://agenciabrasil.ebc.com.br/economia/noticia/2020-08/producao-no-pre-sal-passa-de-70-do-petroleo-e-gas-extraidos-no-pais. Agência Brasil. Accessed in: 05 May 2020.

Germano, M., Piomelli, U., Moin, P., and Cabot, W. H. (1991). "A dynamic subgrid-scale eddy viscosity model". In: *Physics of Fluids A: Fluid Dynamics* 3.7, pp. 1760–1765.

Gerrard, J. H. (1966). "The mechanics of the formation region of vortices behind bluff bodies". In: *Journal of Fluid Mechanics* 25.2, pp. 401–413.

Geuzaine, C. and Remacle, J. F. (2009). "Gmsh: A 3-D finite element mesh generator with built-in pre-and post-processing facilities". In: *International journal for numerical methods in engineering* 79.11, pp. 1309–1331.

Goldstein, S. (1965). *Modern Developments in Fluid Dynamics*. Vol. 2. Dover Publications Inc., New York, p. 439.

Gonçalves, R. T., Franzini, G. R., Rosetti, G. R., Meneghini, J. R., and Fujarra, A. L. C. (2015). "Flow around circular cylinders with very low aspect ratio". In: *Journal of Fluids and Structures* 54, pp. 122–141.

Griffin, O. M. and Ramberg, S. E. (1974). "The vortex-street wakes of vibrating cylinders". In: *Journal of Fluid Mechanics* 66.3, pp. 553–576.

Hay, A. D. (1947). *Flow about semi-submerged cylinders of finite length*. Princeton University Report, New Jersey.

Hess, J. L. and Smith, A. M. O. (1967). "Calculation of potential flow about arbitrary bodies". In: *Progress in Aerospace Sciences* 8, pp. 1–138.

Kärrholm, F. P. (2006). "Rhie-chow interpolation in OpenFOAM". In: *Department of Applied Mechanics, Chalmers University of Technology: Goteborg, Sweden*.

Kawamura, T., Hiwada, M., Hibino, T., Mabuchi, I., and Kumada, M. (1984). "Flow around a finite circular cylinder on a flat plate: Cylinder height greater than turbulent boundary layer thickness". In: *Bulletin of JSME* 27.232, pp. 2142–2151.

Kawamura, T., Mayer, S., Garapon, A., and Sørensen, L. (2002). "Large eddy simulation of a flow past a free surface piercing circular cylinder". In: *Journal of Fluids Engineering* 124.1, pp. 91–101.

Khalak, A. and Williamson, C. H. K. (1999). "Motions, forces and mode transitions in vortex-induced vibrations at low mass-damping". In: *Journal of fluids and Structures* 13.7-8, pp. 813–851.

Kim, S. E. and Mohan, L. S. (2005). "Prediction of unsteady loading on a circular cylinder in high Reynolds number flows using large eddy simulation". In: *International Conference on Offshore Mechanics and Arctic Engineering*. Vol. 41979, pp. 775–783.

Korkischko, I. and Meneghini, J. R. (2012). "Suppression of vortex-induced vibration using moving surface boundary-layer control". In: *Journal of Fluids and Structures* 34, pp. 259–270.

Korkischko, I. and Meneghini, J. R. (2011). "Volumetric reconstruction of the mean flow around circular cylinders fitted with strakes". In: *Experiments in fluids* 51.4, pp. 1109–1122.

Krajnović, S. (2011). "Flow around a tall finite cylinder explored by large eddy simulation". In: *Journal of Fluid Mechanics* 676, pp. 294–317.

Krazer, A. (1904). *Verhandlungen des dritten Internationalen Mathematiker-Kongresses in Heidelberg: vom 8. bis 13. August 1904*. BG Teubner.

Kuethe, A. M., Chow, C., and Fung, Y. C. (1987). *Foundations of Aerodynamics, Bases of Aerodynamics Design*. John Wiley & Sons, Inc.

Lindefjeld, R. and Randulff, B. (2020). *Equinor's Aasta Hansteen Spar Offers Insight into FPSO Design Choices*. Available at: https://www.equinor.com/energy/aasta-hansteen. Accessed in: 13 May 2020.

Luo, S. C. (1993). "Flow past a finite length circular cylinder". In: *The Third International Offshore and Polar Engineering Conference*. OnePetro.

Luo, S. C., Gan, T. L., and Chew, Y. T. (1996). "Uniform flow past one (or two in tandem) finite length circular cylinder (s)". In: *Journal of wind engineering and industrial aerodynamics* 59.1, pp. 69–93.

Marquet, O., Sipp, D., and Jacquin, L. (2008). "Sensitivity analysis and passive control of cylinder flow". In: *Journal of Fluid Mechanics* 615, pp. 221–252.

Menter, F. R. (1992). "Influence of freestream values on k-omega turbulence model predictions". In: *AIAA journal* 30.6, pp. 1657–1659.

Menter, F. R. (1994). "Two-equation eddy-viscosity turbulence models for engineering applications". In: *AIAA journal* 32.8, pp. 1598–1605.

Menter, F. R., Kuntz, M., and Langtry, R. (2003). "Ten years of industrial experience with the SST turbulence model". In: *Turbulence, heat and mass transfer* 4.1, pp. 625–632.

Mittal, S. (2001). "Control of flow past bluff bodies using rotating control cylinders". In: *Journal of fluids and structures* 15.2, pp. 291–326.

Mittal, S. and Kumar, B. (2003). "Flow past a rotating cylinder". In: *Journal of Fluid Mechanics* 476, pp. 303–334.

Mittal, S. and Raghuvanshi, A. (2001). "Control of vortex shedding behind circular cylinder for flows at low Reynolds numbers". In: *International journal for numerical methods in fluids* 35.4, pp. 421–447.

Modi, V. J. (1997). "Moving surface boundary-layer control: a review". In: *Journal of fluids and structures* 11.6, pp. 627–663.

Morais, J. M. (2013). "Petróleo em águas profundas: uma história tecnológica da Petrobras na exploração e produção offshore". In:

Newman, J. N. (2018). *Marine hydrodynamics*. The MIT press.

Niemann, H. J. and Hölscher, N. (1990). "A review of recent experiments on the flow past circular cylinders". In: *Journal of Wind Engineering and Industrial Aerodynamics* 33.1-2, pp. 197–209.

Norberg, C. (2001). "Flow around a circular cylinder: aspects of fluctuating lift". In: *Journal of Fluids and Structures* 15.3-4, pp. 459–469.

Okamoto, T. and Yagita, M. (1973). "The experimental investigation on the flow past a circular cylinder of finite length placed normal to the plane surface in a uniform stream". In: *Bulletin of JSME* 16.95, pp. 805–814.

Palau-Salvador, G., Stoesser, T., Fröhlich, J., Kappler, M., and Rodi, W. (2010). "Large eddy simulations and experiments of flow around finite-height cylinders". In: *Flow, turbulence and combustion* 84, pp. 239–275.

Park, C. W. and Lee, S. J. (2004). "Effects of free-end corner shape on flow structure around a finite cylinder". In: *Journal of Fluids and Structures* 19.2, pp. 141–158.

Patankar, S. V. (1980). *Numerical heat transfer and fluid flow*.

Patankar, S. V. and Spalding, D. B. (1972). "A calculation procedure for heat, mass and momentum transfer in three-dimensional parabolic flows". In: *Numerical prediction of flow, heat transfer, turbulence and combustion* 15, p. 1787.

Patino, G. A., Gioria, R. S., and Meneghini, J. R. (2017). "Evaluating the control of a cylinder wake by the method of sensitivity analysis". In: *Physics of Fluids* 29.4, p. 044103.

Reichl, P., Hourigan, K., and Thompson, M. C. (2005). "Flow past a cylinder close to a free surface". In: *Journal of Fluid Mechanics* 533, pp. 269–296.

Rhie, C. M. and Chow, W. L. (1983). "Numerical study of the turbulent flow past an airfoil with trailing edge separation". In: *AIAA journal* 21.11, pp. 1525–1532.

Roache, P. J. (1976). “Computational Fluid Dynamics”. In: *Hermosa, Albuquerque*.

Roache, P. J. (1997). “Quantification of uncertainty in computational fluid dynamics”. In: *Annual Review of Fluid Mechanics* 29.1, pp. 123–160.

Roshko, A. (1961). “Experiments on the flow past a circular cylinder at very high Reynolds number”. In: *Journal of Fluid Mechanics* 10.3, pp. 345–356.

Rostamy, N., Sumner, D., Bergstrom, D. J., and Bugg, J. D. (2012). “Local flow field of a surface-mounted finite circular cylinder”. In: *Journal of Fluids and Structures* 34, pp. 105–122.

Saltara, F., Neto, A. D. A., and Lopez, J. I. H. (2011). “3D CFD simulation of vortex-induced vibration of cylinder”. In: *International Journal of Offshore and Polar Engineering* 21.03.

Scarborough, J. B. (1958). *Numerical Mathematical Analysis*. Johns Hopkins University Press.

Schlichting, H. (1982). *Boundary-layer theory. Grenzschicht-Theorie*.

Shukla, R. K. and Arakeri, J. H. (2013). “Minimum power consumption for drag reduction on a circular cylinder by tangential surface motion”. In: *Journal of Fluid Mechanics* 715, pp. 597–641.

Silva-Ortega, M. and Assi, G. R. S. (2017a). “Flow-induced vibration of a circular cylinder surrounded by two, four and eight wake-control cylinders”. In: *Experimental Thermal and Fluid Science* 85, pp. 354–362.

Silva-Ortega, M. and Assi, G. R. S. (2017b). “Suppression of the vortex-induced vibration of a circular cylinder surrounded by eight rotating wake-control cylinders”. In: *Journal of Fluids and Structures* 74, pp. 401–412.

Silva-Ortega, M. and Assi, G. R. S. (2018). “Hydrodynamic loads on a circular cylinder surrounded by two, four and eight wake-control cylinders”. In: *Ocean Engineering* 153, pp. 345–352.

Silva-Ortega, M., Orselli, R. M., and Assi, G. R. S. (2014). “Control of rotating cylinders as suppressors of vortex-induced vibration of a bluff body”. In: *Congresso Nacional de Transporte Aquaviário, Construção Naval e Offshore*. Sobena.

Silva-Ortega, M., Assi, G. R. S., and Cicolin, M. M. (2015). “Hydrodynamic Force Measurements on a Circular Cylinder Fitted With Peripheral Control Cylinders: Preliminary Results on the Development of VIV Suppressors”. In: *International Conference*

on Offshore Mechanics and Arctic Engineering. Vol. 56482. American Society of Mechanical Engineers, V002T08A062.

Smagorinsky, J. (1963). "General circulation experiments with the primitive equations: I. The basic experiment". In: *Monthly weather review* 91.3, pp. 99–164.

Spalart, P. R. (2000). "Trends in turbulence treatments". In: *Fluids 2000 conference and exhibit*, p. 2306.

Spalart, P. R. (2009). "Detached-eddy simulation". In: *Annual Review of Fluid Mechanics* 41, pp. 181–202.

Spalart, P. R. and Allmaras, S. (1992). "A one-equation turbulence model for aerodynamic flows". In: *30th Aerospace Sciences Meeting and Exhibit*, p. 439.

Spalart, P. R., Deck, S., Shur, M. L., Squires, K. D., Strelets, M. K., and Travin, A. (2006). "A new version of detached-eddy simulation, resistant to ambiguous grid densities". In: *Theoretical and Computational Fluid Dynamics* 20.3, pp. 181–195.

Spalart, P. R., Jou, W. H., Strelets, M., and Allmaras, S. (Jan. 1997). "Comments on the Feasibility of LES for Wings, and on a Hybrid RANS/LES Approach". In: *Proceedings of first AFOSR international conference on DNS/LES*. Greyden Press.

Spalding, D. B. (1961). "A single formula for the "law of the wall"". In: *Journal of Applied Mechanics* 28, pp. 455–458.

Stevens, W., Goradia, S., Braden, J., and Morgan, H. (1971). "Mathematical model for two-dimensional multi-component airfoils in viscous flow". In: *10th Aerospace Sciences Meeting*, p. 2.

Strykowski, P. J. and Sreenivasan, K. R. (1990). "On the formation and suppression of vortex 'shedding' at low Reynolds numbers". In: *Journal of Fluid Mechanics* 218.1, pp. 71–107.

Sumner, D. (2013). "Flow above the free end of a surface-mounted finite-height circular cylinder: a review". In: *Journal of Fluids and Structures* 43, pp. 41–63.

Sumner, D., Heseltine, J. L., and Dansereau, O. J. P. (2004). "Wake structure of a finite circular cylinder of small aspect ratio". In: *Experiments in Fluids* 37.5, pp. 720–730.

Sweby, P. K. (1984). "High resolution schemes using flux limiters for hyperbolic conservation laws". In: *SIAM journal on numerical analysis* 21.5, pp. 995–1011.

Tennekes, H. and Lumley, J. L. (1972). *A first course in turbulence*. MIT press.

Travin, A., Shur, M., Strelets, M., and Spalart, P. R. (2000). "Detached-eddy simulations past a circular cylinder". In: *Flow, turbulence and combustion* 63.1, pp. 293–313.

van Dyke, M. (1982). *An album of fluid motion*. Vol. 176. Parabolic press Stanford.

Vatsa, V. N., Lockard, D. P., and Spalart, P. R. (2017). "Grid sensitivity of SA-based Delayed-Detached-Eddy-Simulation model for blunt-body flows". In: *AIAA Journal* 55.8, pp. 2842–2847.

Versteeg, H. K. and Malalasekera, W. (2007). *An introduction to computational fluid dynamics: the finite volume method*. Pearson education.

von Kármán, T. (1954). *Aerodynamics: selected topics in the light of their historical development*. Cornell University Press.

Weller, H. G., Tabor, G., Jasak, H., and Fureby, C. (1998). "A tensorial approach to computational continuum mechanics using object-oriented techniques". In: *Computers in physics* 12.6, pp. 620–631.

Wieselsberger, C. (1922). *New data on the laws of fluid resistance*. Tech. rep.

Wilcox, D. C. (1998). *Turbulence modeling for CFD*. Vol. 2. DCW industries La Canãda, CA.

Wilcox, D. C. (2008). "Formulation of the kw turbulence model revisited". In: *AIAA journal* 46.11, pp. 2823–2838.

Willden, R. H. J. and Graham, J. M. R. (2006). "Three distinct response regimes for the transverse vortex-induced vibrations of circular cylinders at low Reynolds numbers". In: *Journal of Fluids and Structures* 22.6-7, pp. 885–895.

Williamson, C. H. K. (1996). "Vortex dynamics in the cylinder wake". In: *Annual Review of Fluid Mechanics* 28.1, pp. 477–539.

Williamson, C. H. K. and Roshko, A. (1988). "Vortex formation in the wake of an oscillating cylinder". In: *Journal of Fluids and Structures* 2.4, pp. 355–381.

Williamson, C. H. and Govardhan, R (2004). "Vortex-induced vibrations". In: *Annual Review of Fluid Mechanics* 36, pp. 413–455.

Zdravkovich, M. M. (1981). "Review and classification of various aerodynamic and hydrodynamic means for suppressing vortex shedding". In: *Journal of Wind Engineering and Industrial Aerodynamics* 7.2, pp. 145–189.

Zdravkovich, M. M. (1998). *Flow Around Circular Cylinders: Volume 1: Fundamentals*. Oxford university press.

Zhu, H., Chu, X., Yan, Z., and Gao, Y. (2021). “Coupling response of flow-induced oscillating cylinder with a pair of flow-induced rotating impellers”. In: *Physics of Fluids* 33.8, p. 083608.

APPENDIX A - Vortex-panel method

Implementation details of the vortex-panel method applied in the published work of section 9.1 are presented in this section. Figure A.1 exemplifies the employed discretisation using merely 20 panels to represent a control rod. For the case with N peripheral rods, each of which discretised by m panels, the velocity potential at the control points in a Cartesian system (x, y) is given by

$$\phi(x_i, y_i) = U(x_i \cos\theta + y_i \sin\theta) - \sum_{k=0}^{N} \sum_{j_{i,k}}^{j_{f,k}} \int_0^{S_j} \frac{\gamma(s_j)}{2\pi} \tan^{-1}\left(\frac{y_i - y_j}{x_i - x_j}\right) ds_j, \qquad \text{(A.1)}$$

where $k = 0$ corresponds to the main cylinder and $k = 1, 2, ..., N$ corresponds to the rotating rods. The index $i = 1, 2, ..., (N+1)m$ counts the number of control points and $j = 1, 2, ..., N(m+1) + m$ refers to the boundary points; $j_{i,k}$ and $j_{f,k}$, with $j_{f,k} > j_{i,k}$, denote initial and final values of j corresponding to the boundary points in the k^{th} cylinder. The length of each panel is run by s_j, from 0 to S_j (total length of the panel). The integration is performed over the entire panel and the circulation varies linearly as

$$\gamma(s_j) = \gamma_j + (\gamma_{j+1} - \gamma_j) s_j / S_j, \qquad \text{(A.2)}$$

where $\gamma(s_j)$ corresponds to the circulation density over the panel delimited by the boundary points j and $j+1$. To impose null velocity across the control points i, the condition

$$\frac{\partial}{\partial \eta_i} \phi(x_i, y_i) = 0 \qquad \text{(A.3)}$$

is met for every panel, where η_i denotes the normal direction relative to the panel. The differentiation and expansion steps of (A.3), incorporating (A.1) and (A.2), are detailed in Kuethe, Chow, and Fung (1987).

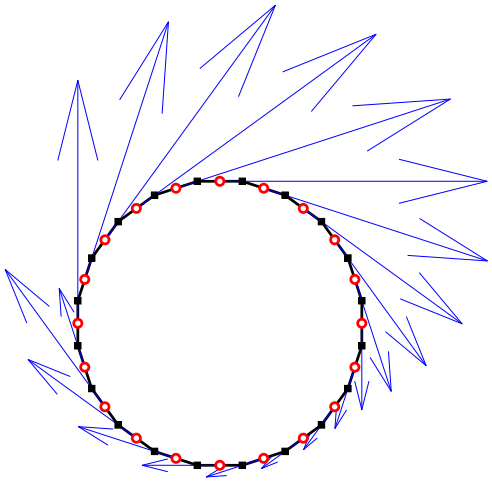

Figure A.1: Control points (red circles) in the middle of the panel and boundary points (black squares) at the extremities. A low number of panels was used for clarity purposes.

The total circulation of the k^{th} cylinder

$$\Gamma_k = -\int_k \mathbf{v}_{surf} \cdot d\mathbf{s} = -\frac{\pi \omega_k D_k^2}{2} \tag{A.4}$$

is related to its angular velocity, where $\mathbf{v}_{surf}$ is the velocity at the surface of the k^{th} cylinder and D_k is its diameter, i.e., $D_0 = D$, and $D_k = d$ for $k = 1, 2, ..., N$. Then, for the k^{th} cylinder

$$\left\{ \sum_{j=j_{i,k}}^{j_{f,k}} \int \gamma(s_j)\ ds_j \right\}_{j \text{ in } k} = -\frac{\pi \omega_k D_k^2}{2}. \tag{A.5}$$

Equation (A.5) along with (A.2) yield, for every cylinder,

$$\left\{ \gamma'_{j_{i,k}} S_{j_{i,k}} + \left[\sum_{j>j_{i,k}}^{j_{f,k}} \gamma'_{j+1}(S_j + S_{j+1}) \right] + \gamma'_{j_{f,k}} S_{j_{f,k}-1} \right\}_{j \text{ in } k} = -\frac{\omega_k D_k^2}{2U}, \tag{A.6}$$

where $\gamma' = \gamma/(2\pi U)$.

An algebraic system is provided by the expansion of (A.1). In conjunction with (A.6), the circulation of the boundary points is derived.

The Biot-Savart Law is applied to solve for the entire velocity field induced by the circulations placed over the panels. Associated with the pressure, from Bernoulli's equation, the force $\mathbf{F} = -\iint p\ d\mathbf{S}$ is computed and, consecutively, normalised by $\frac{1}{2}\rho U^2 D$ to give C_L and C_D.

APPENDIX B - Reference simulations for infinitely-long cylinders

Here we present some verification and validation results that complement those in the main body of this thesis, as well as in its constituent papers. Analogous, but shorter analyses, were conducted for finite bodies and are presented in sections 9.3 and 9.4.

The number of cells, the size of the smallest element on the wall and some dimensions are presented in table B.1. For the entire system with such a narrow gap, the smallest element is always located between the peripheral rod and the main cylinder. All meshes are structured and were designed with Gmsh (Geuzaine and Remacle, 2009). The simulation setup employed here is described in section 6.4. These grids are shown in section 9.2.

We merely note that time steps were set to capture at least 100 times the Strouhal period of any cylinder or 70 parts of the rotation of the rods, whichever corresponded to the lowest time step. As a matter of fact, for large values of angular velocity the flow tended to become smoother (with shedding suppression), that justifies the lower requirement for capturing rotations. Periodic regime was awaited for all simulations, and at least 15 cycles of vortex shedding were considered for mean and RMS values. Maximum Courant number stayed below 0.95.

All laminar flow simulations were two-dimensional and used the mesh with 130,004 elements. However, due OpenFOAM's requirement of a 3D mesh, the mesh had to be extruded for an arbitrary length and an empty condition was imposed on the extruded parts to retrieve a 2D problem. For turbulent regime simulations, the same setup was generally used as in the previous sections, except for the changes below:

- the same mesh for the bare cylinder was used, but extruded 48 times, summing up

Table B.1: Mesh information.

	Cell count	Minimum size (units of D)		ℓ_u/D	ℓ_d/D	h/D
		Main cylinder	Control rods			
Bare cylinder	49,204	1.00×10^{-3}	-	8	20	16
System	72,910	8.29×10^{-4}	7.23×10^{-4}	8	30	16
	78,152	8.29×10^{-4}	7.23×10^{-4}	8	20	16
	98,330	6.77×10^{-4}	2.61×10^{-4}	8	30	16
	108,150	7.05×10^{-4}	8.01×10^{-4}	8	20	16
	109,710	7.13×10^{-4}	8.01×10^{-4}	8	20	16
	130,004	8.29×10^{-4}	7.23×10^{-4}	8	20	16
	1,235,788	6.00×10^{-4}	7.53×10^{-5}	8	30	16

2,361,792 elements. Spanwise lengths were $L/D = 5$ in URANS and $L/D = \pi$ in DES;

- Spalding's continuous wall function was used (Spalding, 1961) in the SST k-ω model;
- momentum equations were discretised with the LUST scheme of section 6.4, while in laminar regime liner upwind was used;
- equation 5.8 was used, including the DES filter and the low-Reynolds correction of equations 5.16 and 5.17, since the boundary layer is laminar for $Re = 10^3$ and $Re = 10^4$. Equation 5.8 was iterated to maximum tolerance of 10^{-8}, and discretisation was made with the linear upwind scheme of equation 4.3;
- boundary conditions, in addition to those of chapter 5, followed equations 5.4-5.7 for SST k-ω RANS model; and equations 5.14 and 5.15 for DES.

Mesh convergence tests were performed with the structured grids of table B.1 in laminar and turbulent regimes. It is widely accepted that the flow past a cylinder can be characterised by $\overline{C}_D$, $\hat{C}_L$ and S_t (Behr et al., 1991; Behr et al., 1995). Very often C_p is used, but it was not considered in this section.

In laminar regime of $Re = 100$, this rationale motivated the analysis of table B.3. As it can be noticed, insignificant difference is perceived in $\overline{C}_D$ for the case of a bare cylinder, and the variation in S_t can be shown to be of at most 2.9% between the mesh with 49,204 elements and that of Assi, Orselli, and Silva-Ortega (2019). $\hat{C}_L$, on the

Table B.2: Comparison of the mesh with 72,910 elements with results given by section 9.1.

ζ	$\overline{C}_D$		Residual (%)
	9.1	Mesh with 72,910 cells	
0.0	1.57	1.55	1.02
0.5	1.25	1.23	1.53
1.0	0.971	0.955	1.66
1.5	0.808	0.800	0.99
2.0	0.660	0.650	1.50
2.5	0.515	0.500	2.87

Table B.3: Mesh convergence and comparison with previous results for $Re = 10^2$. Cell count corresponds to transverse section of the extruded cylinder.

	2D cell count	$\overline{C}_D$	$\hat{C}_L$	S_t
Bare cylinder	49,204	1.41	0.241	0.172
Blanchard, Bergman, and Vakakis (2020)		1.39	0.242	0.170
Assi, Orselli, and Silva-Ortega (2019)		1.40	0.227	0.175
System	72,910	1.23	0.095	0.170
	98,330	1.22	0.084	0.170
	108,150	1.22	0.082	0.169
	130,004	1.22	0.102	0.169
	1,235,788	1.23	0.086	0.169

other hand, presented a wider deviation of 6.2% between the mesh of this work and that of Blanchard, Bergman, and Vakakis (2020). However, it still agreed well with Assi, Orselli, and Silva-Ortega (2019). This mesh was advantageously used for bare cylinder simulations.

Additionally, the results for the mesh with 72,910 were compared with a previous work in another mesh, that of section 9.1, and residuals are given accordingly in table B.2 for different ζ values, all under 2.87%, which justified our numerical scheme in a simple setup for the entire system, allowing for fast simulations and tight tolerance criterion. The visual aspect of the results of such simulations were exactly the same as those of section 9.1 (that was conducted with a different mesh and numerical scheme, but at the same Re).

For grid independence study, we compared the individual contributions of the rods in

Table B.4: Mesh convergence with respect to individual cylinders, comparing $\overline{C}_D$ and $\hat{C}_L$ between those meshes with 72,910 and 130,004 cells.

Mesh	Cylinder								
	P_0	P_1	P_2	P_3	P_4	P_5	P_6	P_7	P_8
					$\overline{C}_D$				
72,910	0.99	0.022	0.089	0.0071	-0.0065	0.022	0.089	0.0072	-0.00070
130,004	0.98	0.022	0.091	0.097	-0.00027	0.022	0.091	0.0097	-0.00033
					$\hat{C}_L$				
72,910	0.081	0.091	0.14	0.016	0.0050	0.091	0.139	0.016	0.0052
130,004	0.087	0.092	0.14	0.015	0.0045	0.092	0.139	0.015	0.0046

table B.4 for different mesh refinements.

Turbulent simulations were also conducted. For the bare cylinder, the mesh with 49,204 crosswise elements was used. URANS and DES simulations began with the boundary conditions mentioned in section 6.4, however the DES simulation started from a mapped condition, i.e., from another simulation where a periodic regime had already been installed, as it was done in Mittal and Raghuvanshi (2001), for faster convergence.

Time histories of lift and drag are shown in figures B.1a and B.1b. The progressive difference in periodic behaviour from 2D URANS, 3D URANS to DES is striking. This trait comes from their different formulations, as explained below.

Main quantities of interest are summarised in table B.5 for verification and validation purposes. Mesh convergence for the bare cylinder is given in section 9.2.

Now digression of the discrepancies are in order. In URANS simulations, the dependence of the large scales on the boundary conditions is not well represented, and a general formulation applied to all scales allows for too high a spanwise correlation. This is principally observed for the 2D URANS case, as it builds up to perfect correlation, leading to overestimated hydrodynamic coefficients. Another consideration is that on the use of Spalding's wall function, which is bound to be imprecise. Since the boundary layer is laminar, URANS usage without wall functions ignores the low-Re condition, and resolves it as turbulent, delaying further the separation. The benefits of wall functions in general are offset by their calibration, usually made by means of curve fitting based on zero-pressure-gradient flow over flat plate boundary layers. These arguments explain the difference found between quantities of interest in this simulation and experimental data

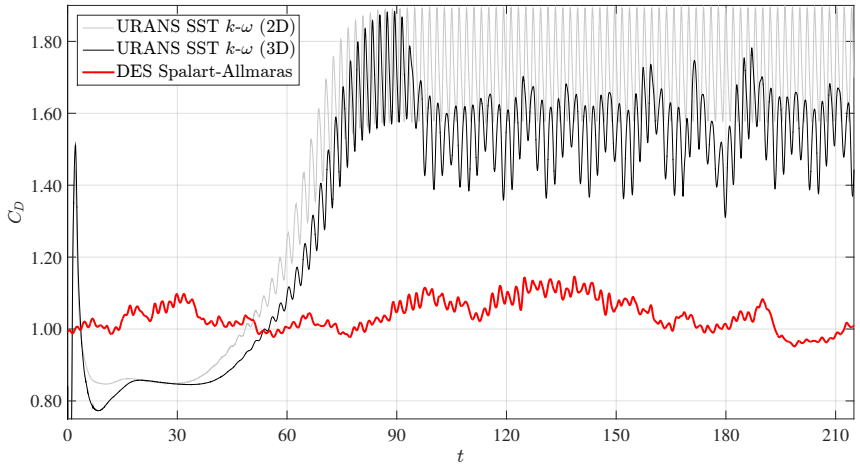

(a)

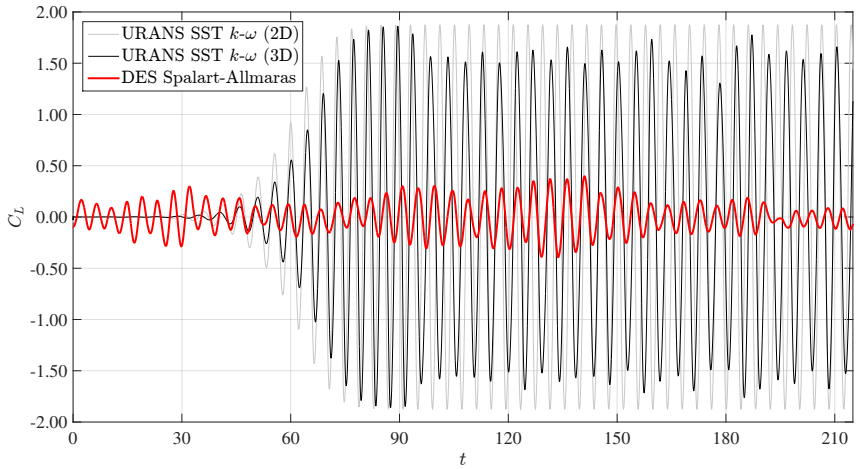

(b)

Figure B.1: (a) C_D and (b) C_L using different turbulence formulations. DES started from another converged simulation, hence the rapid convergence.

Table B.5: Validation of turbulent flow simulations for a bare cylinder using 2,361,792 cells (49,204 crosswise). Only the maximum value of y^+ in time and space is shown.

	$\overline{C}_D$	$\hat{C}_L$	S_t	$y^+_{\max}$
$Re = 10^3$				
URANS 2D	1.41	0.83	0.23	0.16
URANS 3D	1.41	0.83	0.23	0.16
DES (Spalart-Allmaras)	1.13	0.24	0.22	0.16
Norberg (2001) (experiments)		0.10-0.30	0.21	
Cantwell and Coles (1983) (experiments)	1.0			
Schlichting (1982) (experiments)	1.00			
$Re = 10^4$				
URANS 2D	1.72	1.32	0.24	1.00
URANS 3D	1.56	1.12	0.22	1.1
DES (Spalart-Allmaras)	0.99	0.11	0.22	0.88
Saltara, Neto, and Lopez (2011) (DES)	1.18	0.41	0.21	
Silva-Ortega, Assi, and Cicolin (2015) (experiments)	1.50	0.25		
Norberg (2001) (experiments)		0.25-0.50	0.20	
Cantwell and Coles (1983) (experiments)	1.0-1.25			
$Re = 10^6$				
DES (Spalart-Allmaras)	0.46	0.044	0.36	48
Cantwell and Coles (1983) (experiments)	0.25-0.40			
Roshko (1961) (experiments)	0.36		0.3	
Niemann and Hölscher (1990) (experiments)	0.22-0.52	0.04		

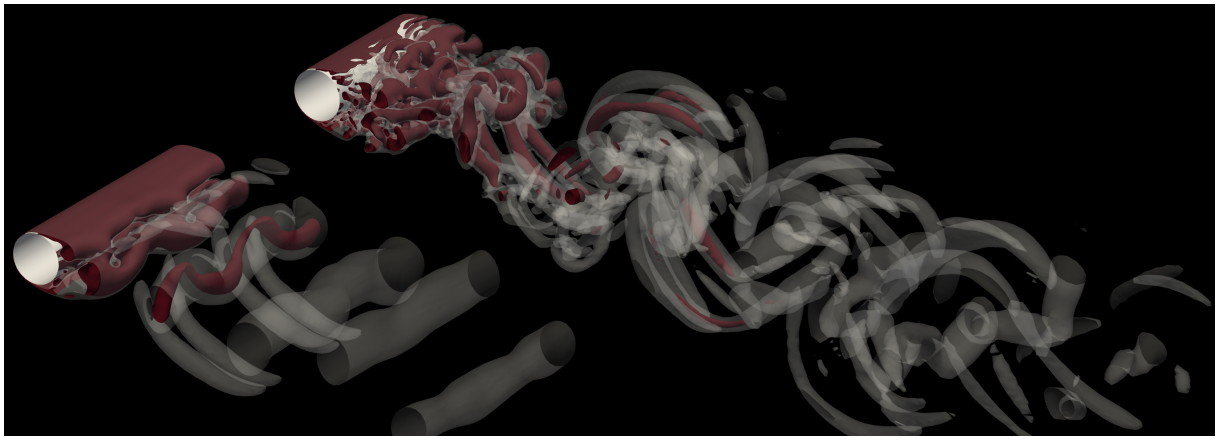

Figure B.2: Eddies shown with the support of Q-contours related to small eddies ($Q = 5$, red) and large eddies ($Q = 0.5$, transparent) at $Re = 10^4$. DES on the right and URANS on the left.

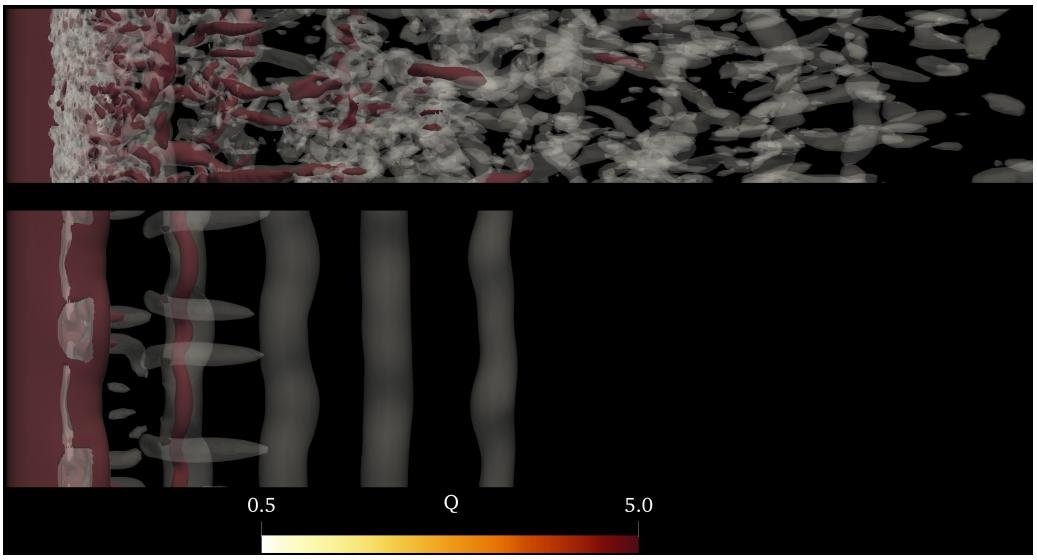

Figure B.3: Q-contours of spanwise eddies. Small eddies ($Q = 5$, red) and large eddies ($Q = 0.5$, transparent) are represented at $Re = 10^4$. DES on the top and URANS below.

of table B.5, as well as the visual aspect portrayed by figures B.2 and B.3[1]. In the former, one can easily see that the vorticity of the eddies shed by the cylinder prevailed for a larger extent downstream in the resolution provided by DES. However, eddies resulting from closure models are dissipated sooner, both in examination of large and smaller eddies. This is expected. URANS simulations treat all eddies uniformly. Therefore, large eddies' inviscid behaviour was not accounted for properly. The latter figure emphasises this aspect, and brings out the relevance of DES to capture small structures.

The Spalart and Allmaras (1992) model for DES adjusts the flow in laminar regions with a low-Re correction. Wall functions were not necessary, because $y^+_{\max} < 0.849$ for

[1]We remark that $L/D = 5$ in the URANS formulation and $L/D = \pi$ in DES.

Table B.6: Assessment of blockage effects for a wider flow domain. DES formulation with the Spalart-Allmaras turbulence model was used for all simulations.

Re	ℓ_d/D	h/D	$\overline{C}_D$	$\hat{C}_L$	S_t	$y^+_{\max}$
10^3	20	16	1.13	0.24	0.22	0.16
	30	32	1.08	0.22	0.22	0.15
10^4	20	16	0.99	0.11	0.22	0.88
	30	32	0.96	0.12	0.23	0.86

the entire simulation, due to mesh refinement. Furthermore, the determination of large scales in DES benefits from the LES approach, and Smagorinsky's SGS model, used for the small scales away from the wall.

From table B.5, $\overline{C}_D$ from DES simulations were in agreement with experiments performed by Cantwell and Coles (1983), and URANS results presented a deviation of at least 24.8% (3D case), which is expected for turbulence modelling for reasons discussed above.

$\hat{C}_L$ measurements tend to be problematic in simulations and experiments alike, in terms of Re, extending from Reynolds regimes of 200 to 10000 (Norberg, 2001).

Blockage effects were assessed shortly and the results are presented in table B.6. These are commented in section 9.2.